Liu, Deyun (2013) Advances in beam propagation method for facet reflectivity analysis. PhD thesis, University of Nottingham.

Access from the University of Nottingham repository:
http://eprints.nottingham.ac.uk/13491/1/Deyun__Liu%27s_Thesis.pdf

Copyright and reuse:

The Nottingham ePrints service makes this work by researchers of the University of Nottingham available open access under the following conditions.

- Copyright and all moral rights to the version of the paper presented here belong to the individual author(s) and/or other copyright owners.
- To the extent reasonable and practicable the material made available in Nottingham ePrints has been checked for eligibility before being made available.
- Copies of full items can be used for personal research or study, educational, or not-for-profit purposes without prior permission or charge provided that the authors, title and full bibliographic details are credited, a hyperlink and/or URL is given for the original metadata page and the content is not changed in any way.
- Quotations or similar reproductions must be sufficiently acknowledged.

Please see our full end user licence at:
http://eprints.nottingham.ac.uk/end_user_agreement.pdf

A note on versions:

The version presented here may differ from the published version or from the version of record. If you wish to cite this item you are advised to consult the publisher's version. Please see the repository url above for details on accessing the published version and note that access may require a subscription.

For more information, please contact eprints@nottingham.ac.uk

Advances in Beam Propagation Method for Facet Reflectivity Analysis

By Deyun Liu, MEng

Thesis submitted to the University of Nottingham for the degree of

Doctor of Philosophy, July, 2013

Acknowledgements

It is a pleasure to thank all of those who made this thesis possible. First of all, I wish to thank my academic supervisor Professor Phillip Sewell, Dr. Ana Vukovic, and Professor Trevor Benson for their enthusiastic guidance and patient support and encouragement throughout the time of this project. I am also grateful to Dr. Ken Chan for his assistance and many useful discussions. It has been a great pleasure working with the people in George Green Group. This thesis would not have been completed without the input from all of them.

The moral support from my family and friends has motivated me and I would like to show my gratitude to my whole family for their wonderful love and support. I sincerely thank my parents and my wife, who have always been there for me. Many thanks must go to my dear friends who have made my life rather interesting throughout this period.

Finally, I also wish to thank the school of Electrical and Electronic Engineering – the University of Nottingham (Tower Innovation Scholarship) who provided the financial support that made this project possible.

Abstract

Waveguide discontinuities are frequently encountered in modern photonic structures. It is important to characterize the reflection and transmission that occurs at the discontinuous during the design and analysis process of these structures. Significant effort has been focused upon the development of accurate modelling tools, and a variety of modelling techniques have been applied to solve this kind of problem. Throughout this work, a Transmission matrix based Bidirectional Beam Propagation Method (T-Bi-BPM) is proposed and applied on the uncoated facet and the single coating layer reflection problems, including both normal and angled incident situations.

The T-Bi-BPM method is developed on the basis of an overview of Finite Difference Beam Propagation Method (FD-BPM) schemes frequently used in photonic modelling including paraxial FD-BPM, Imaginary Distance (ID) BPM, Wide Angle (WA) BPM and existing Bidirectional (Bi) BPM methods. The T-Bi-BPM establishes the connection between the total fields on either side of the coating layer and the incident field at the input of a single layer coated structure by a matrix system on the basis of a transmission matrix equation used in a transmission line approach. The matrix system can be algebraically preconditioned and then solved by sparse matrix multiplications. The attraction of the T-Bi-BPM method is the potential for more rapid evaluation without iterative approach. The accuracy of the T-Bi-BPM is verified by simulations and the factors that affect the accuracy are investigated.

List of Principal Symbols

D	Electric displacement (Cm^{-2})
B	Magnetic flux density (T)
E	Electric field (Vm^{-1})
H	Magnetic field (Am^{-1})
ψ	Envelope of the field
J	Electric current density
$\mu, \mu_0 \mu_r$	Dielectric permeability, permeability of free space, relative permeability (Hm^{-1})
$\varepsilon, \varepsilon_0, \varepsilon_r$	Dielectric permittivity, permittivity of free space, relative permittivity (Fm^{-1})
n	Material refractive indices
n_{core}	Refractive indices of the core
$n_{cladding}$	Refractive indices of the cladding
n_{eff}	Effective index of simulation / structure
λ	Wavelength
k	Wavenumber
β	Propagation constant
x, y, z	Co-ordinates of the Cartesian co-ordinate system
t	Time
Δ	Cell size

List of Acronym

2D	Two dimensional
3D	Three dimensional
ADI	Alternating Direction Implicit
Bi-BPM	Bidirectional Beam Propagation Method
BI-CGSTAB	Bi-Conjugate Stable
BPM	Beam Propagation Method
CN	Crank-Nicolson
FD	Finite Difference
FD-BPM	Finite Difference Beam Propagation Method
FDTD	Finite Difference Time Domain
FE	Finite Element
FFT	Fast Fourier Transform
FSRM	Free Space Radiation Mode
GMRES	Generalized Minimal Residual
ID-BPM	Imaginary Distance Beam Propagation Method
PDE	Partial differential equation
PML	Perfectly Matched Layer
SVEA	Slowly Varying Envelope Approximation
SP	Surface Plasmon
SPP	Surface Plasmon Polariton

TBC	Transparent Boundary Condition
T-Bi-BPM	Transmission Matrix Based Bidirectional Beam Propagation Method
TD	Time Domain
WA	Wide Angle

Contents

Chapter 1: Introduction

1.1 Background and Motivation

In the second half of the 20th century, the improvement of the understanding and manipulation of light lead to a new technology revolution. Typically related to the electromagnetic or quantum properties of light, this revolution encompasses the areas of both optical science and optical engineering. Nowadays, photonic devices have been widely applied in information transmission over long distances and high bandwidth communications [1]. However, the hybrid application of the electrical components and the optical components in optoelectronic hybrid circuits requires a conversion between the optical and electrical signals, which is a time-consuming and expensive process. In order to eliminate this negative effect, all-optical networks (AONs) which eliminate the optical-to-electrical-to-optical conversion have become a new research target. The idea of AONs is to replace the electrical components in the integrate circuit by photonic components of the same functionality. Components such as switch and memory which are currently operating in the electrical domain are potentially to be replaced by equivalent photonic components, so that the operations are conducted completely within the optical domain [2, 3]. With the ongoing research toward photonic components, their application also extends to the area of quantum computing and bio-sensing [4, 5].

Optical waveguides are the basic building blocks in integrated photonics [6]. As the transmission medium, their main function is to confine and guide electromagnetic waves to different optical devices. Silicon (Si) and semiconductors belonging to III-V group are traditional materials used for waveguides fabrication. Dielectric waveguides can be fabricated in different configurations such as straight waveguides, S-bends, Y branches, and Arrayed Waveguide Grating (AWG) [7, 8]. They guide optical light relying exclusively on total internal reflection. In recent years, Photonic Bandgap (PBG) Waveguides are becoming more popular due to their ability to guide optical light in photonic crystal fibers, along narrow channels and around very tight bends, with no losses [9]. Furthermore, with the development of nanoscale fabrication and characterization techniques, Surface Plasmon (SP) waveguides have attracted much interest because of its ability to guide electromagnetic energy within nanostructures [10]. In Chapter 2 of this thesis, typical optical waveguides and materials will be introduced in details.

The advance of integrated optics poses new challenges in the design, optimisation and fabrication of the increasingly complex individual devices and whole circuits. In practice, the design and optimisation processes are ideally to be proceeded by means of computer simulation, before embarking upon costly and time consuming experimentation. Therefore, accurate and efficient analysis methods which can reduce both the cost and the length of the design cycle are required. To date, a variety of simulation methods have been reported which can be globally classified into three categories, namely analytical, semi-analytical and numerical methods. Analytical methods provide accurate results but their application is limited to simple cases of layered slab waveguides. Semi-analytical methods simplify a problem by introducing acceptable approximations in the light of physical analysis. They tend to be not very numerically intensive providing a fast solution of good accuracy. Typical representatives for semi-analytical methods are Effective Index (EI) Method [11], Mode Matching Method [12], Spectral Index (SI) Method [13] and Free Space Radiation Mode (FSRM) Method [14]. Typical structures analysed using semi-analytical methods are rib waveguides, buried waveguides, tapers and directional couplers [15-17]. Nevertheless, the application of semi-analytical methods is restricted to relatively simple structures where approximations have to rely on a priori knowledge of physical fields. In contrast, numerical methods are versatile and can be applied to any type of structures. Typical numerical methods, such as Finite Difference (FD) method [18], Finite Element Method (FEM) [19], Finite Difference Time Domain Method (FDTD) and Finite Difference Beam Propagation Method (FD-BPM) [20], provide flexible platforms for modelling a wide range of modern photonic devices starting from rib waveguides and extending to PBG, photonic crystal and plasmonic waveguides. By means of the discretization of the physical space, they can be readily applied to complicated problems with complex cross-section. However, the generality of numerical methods comes at the expense of high computational demand, which means large memory requirements and long computation time. Generally, numerical methods fall into time domain methods or frequency domain methods. The former, such as FDTD [21], simulate the transmission of signals through the optical structure in time. They can be used to simulate structures made with time dependent or dispersive materials. The main disadvantage of these approaches is computational efficiency, requiring direct discretization of the full spatial domain and by virtue of their explicit nature, using small time steps leading to long overall run times [22]. On the other hand, frequency domain methods such as FE and FD-BPM model propagation of signals with steady state behaviour at one particular frequency. A brief introduction of the commonly used analysis methods will be given in Chapter 3.

The FD-BPM has been proved as an invaluable tool to design integrated photonics in the last decade. It is suitable for majority of photonic devices for which Slowly Varying Envelope Approximation (SVEA) can be applied. SVEA assumes slow changes in the envelope of the field containing a fast varying carrier. The FD-BPM describes the evolution, ie. the envelope, of the total field rather than the carrier. Therefore, it is much more computationally efficient compared to time domain methods. Its simplicity, flexibility and accuracy make it popular to provide practically useful simulations of arbitrary optical waveguides and large structures such as Y-junctions, tapers, bends and gratings [22]. By different approximation schemes, FD-BPM can be divided into paraxial algorithm and wide angle (WA) algorithm.

Paraxial BPM uses a paraxial wave equation which assumes the incident wave is inclined by a small angle with respect to the axis of the propagation direction [23]. It is a convenient tool in simulation for most forward propagation problems, which means that the wave travels in an invariant structure along the propagation direction and no reflections need to be considered. The paraxial approximation greatly simplifies the wave equation for computational modeling but limits applications of this method. Paraxial BPM is not suitable for the structures where the beam propagates in directions that make large angles with respect to the axis of propagation. On the other hand, wide angle BPM (WA-BPM) removes the paraxial approximation and enables simulation of structures where the field propagates at an angle to propagation axis. The detailed information of the paraxial BPM and the WA BPM will be presented in Chapter 3 and Chapter 4, respectively.

Compared to the paraxial BPM, the WA-BPM has another important application, which is to be the foundation of bidirectional BPM (Bi-BPM) for solving bidirectional propagation problems. Bidirectional propagation problems are frequently encountered in the investigation of modern integrated photonics systems. Many practical optical devices involve laser facets, taper structures, multiple dielectric layers, waveguide ends and junctions between different waveguides. In these devices, the material of the guiding structure changes along the propagation direction and reflections occur on the interface between different materials. During the analysis of this kind of problems, it is often of crucial importance to characterize the reflection and transmission that occurs at these interfaces. Typically, it is desired that facet reflections are minimized to avoid resonances within amplifiers and similar integrated devices and, of equal importance, that the transmission is maximized to obtain superior system performance. In practice, facets are angled in order to redirect reflected light away from the waveguides, therefore reducing coupling back into their guided modes [24, 25]. Furthermore, the use of optical antireflection, AR, coatings provides enhanced transmission as well as reducing the total quantity of reflected light [26, 27] and in practice, facets that are both coated and angled are employed [28-30]. In order to solve these kinds of problems, a connection between the fields on either side of the discontinuity interface needs to be set up. This work cannot be easily done by the convenient paraxial FD-BPM. Again, this is the scenario where the wide angle FD-BPM shows the advantage. So far, various Bi-BPM algorithms based on the WA scheme have been proposed for handling the single facet reflection problems [31-33] and the coating layer reflection problems [34-37].

The objective of the work presented in this thesis is to develop and improve FD-BPM for analysis of bidirectional propagation. A novel BPM method, the Transmission matrix Based Bi-BPM (T-Bi-BPM), to assess the reflection problems of the facet and the single coating layer structures will be developed and investigated. This new scheme aims to derive a matrix equation that establishes the connection between the fields on either side of the coating layer by using the well-known transmission matrix analysis. By suitable mathematical derivation, the matrix can be arranged into a sparse matrix form that is convenient to solve. The following outlines the organization of the work contained in this thesis.

1.2 Thesis Organization

Chapter 2 presents different design technologies in integrated photonics, including Planar Lightwave Circuit (PLC), Photonic Integrated Circuit (PIC) and Optoelectronic Integrated Circuit (OEIC), together with the introduction of typical optical materials used and different configurations of optical waveguides including traditional dielectric waveguides, PBG waveguides and SP waveguides. This chapter also presents the basic electromagnetic principles of wave optics starting from the Maxwell's Equations for isotropic dielectric media. The boundary conditions at material interfaces are introduced and the wave equations are derived in Cartesian coordinates for full-vectorial, semi-vectorial and scalar field solutions. These concepts form the basis of computational modeling.

Chapter 3 provides an overview of various semi-analytical and numerical modeling methods commonly used in modern optics, including the discussion of features of each method. Special emphasis is placed on the review of the developments and applications of paraxial FD-BPM because it is the basic BPM scheme which is considered as the foundation of other developed BPM schemes. Important concepts in the application of FD-BPM such as SVEA are presented. The Crank-Nicolson scheme, which will be used as the discretization scheme along the propagation direction throughout this thesis, will also be introduced in this chapter. Moreover, boundary conditions frequently applied in BPM simulations such as Neumann and Dirichlet Boundary Condition, Transparent Boundary Condition (TBC), Perfectly Matched Layers Boundary Condition (PLM) and the periodic boundary condition, are discussed. The Alternation-Direction Implicit (ADI) scheme is also described. Finally, the imaginary distance BPM (IDBPM) is described as an effective mode solver. It will be used to calculate the effective refractive index of the modelling structures and to obtain the fundamental mode of incident field for all the simulations presented in this thesis.

The bidirectional BPM schemes are derived on the basis of the wide angle BPM scheme. The techniques frequently used in wide angle scheme, such as the Padé approximation and the multistep method， are also applied to solve the bidirectional problems. Therefore, before the investigation of the bidirectional BPM, the wide angle BPM is introduced in Chapter 4. Important concepts including Padé approximation, Multistep method and Rotated Branch Cut Approximation are overviewed. Test simulations using the WA FD-BPM are implemented for 2D and 3D forward propagation problems, and the simulation results are compared with those obtained using the paraxial scheme. In Chapter 5, the FD-BPM theory is extended to the bidirectional propagation problems based on the wide angle wave equation. An overview of the existing Bidirectional BPM (Bi-BPM) schemes for the facet reflection problems and the coating layer reflection problems is given in details.

In Chapter 6, the T-Bi-BPM scheme is proposed according to the transmission matrix used in the transmission line theory. The T-Bi-BPM method is especially applicable for a special case where the waveguide has a cladding or an interlayer along the propagation direction. The difficulty of this kind of problems is that the structure contains more than one interface so that multi-reflection will occur. The T-Bi-BPM method considers the incident and the reflected fields of either side of the coating layer as a whole and establishes the connection between the total fields on either side of the coating layer by a matrix operator in order to avoid the analysis of the multi-reflection between the interfaces, and therefore, simplifies the problem. Moreover, the T-Bi-BPM method is also considered as a potential approach to solve the uncoated facet reflection problems. The benefit of T-Bi-BPM is that it describes a bidirectional propagation problem by an algebraically preconditioned matrix system, which can be calculated by a matrix solver without iterative process. This leads to more rapid evaluation. The assessment of the performance of T-Bi-BPM is implemented and discussed for the case of normal and angled incident waveguide. In each case facet is considered to be uncoated and coated with a single coating layer.

Finally, Chapter 7 concludes the thesis, together with a discussion about possible further work.

1.3 References

1. Lifante, G., Integrated Photonics Fundamentals. 2003.
2. Martin T. Hill, A fast low-power optical memory based on coupled micro-ring lasers. Nature, 2004. **432**(206-209).
3. Battestilli, T. and Perros. H., An introduction to optical burst switching. Communications Magazine, IEEE, 2003. **41**(8): p. S10-S15.
4. Kaminow, I., Optical Integrated Circuits: A Personal Perspective Lightwave Technology. Journal of Lightwave Technology, 2008. **26**: p. 994-1004.
5. Luff B. J., Integrated Optical Mach–Zehnder Biosensor. Journal of Lightwave Technology, 1998. **16**: p. 583-592.
6. Adams, M.J., An introduction to optical waveguides. Wiley, 1981.
7. J. Salzmanl, H.O., A. Mprller-Larsen, O. Albrektsen, J. Hanberg, J. Norregaard and B. Tromborg, The S-bent waveguide distributed feedback laser. in 14th IEEE International Semiconductor Laser Conference, 1994: p. 57-58.
8. McGreer, K.A., Arrayed waveguide gratings for wavelength routing. Communications Magazine, IEEE, 1998. **36**(12): p. 62-68.
9. J.D.Joannopoulos, Photonic crystals: putting a new twist on light. Nature, 1997. **386**: p. 143-149.
10. Junxi Zhang, Surface plasmon polaritons: physics and applications. JOURNAL OF PHYSICS D: APPLIED PHYSICS, 2012.

11. Buus, J., The effective index method and its application to semiconductor lasers. Quantum Electronics, IEEE Journal of, 1982. **18**(7): p. 1083-1089.

12. Chew Weng Cho,Waves and Fields in Inhomogenous Media, Chapter 6:Mode Matching Method 1995.

13. P. N. Robson, Rib Waveguide Theory by the Spectral Index Method. 1990.

14. Smartt, C.J., T.M. Benson, and P.C. Kendall, `Free space radiation mode' method for the analysis of propagation in optical waveguide devices. Optoelectronics, IEE Proceedings J, 1993. **140**(1): p. 56-61.

15. Burke, S.V., Spectral index method applied to coupled rib waveguides. Electronics Letters, 1989. **25**(9): p. 605-606.

16. Van Der Tol, J.J.G.M. and N.H.G. Baken, Correction to effective index method for rectangular dielectric waveguides. Electronics Letters, 1988. **24**(4): p. 207-208.

17. Vukovic, A., Fourier Transformation Analysis of Optoelectronic Components and Circuits. Thesis submitted to the University of Nottingham for the degree of Doctor of Philosophy, 2000.

18. Sadiku, M.N.O., Numerical Techniques in Electromagnetics. 1992.

19. Davies, A.J., the Finite Element Method: an Introduction with Partial Differential Equations. 1980.

20. Chung, Y. and N. Dagli, An assessment of finite difference beam propagation method. Quantum Electronics, IEEE Journal of, 1990. **26**(8): p. 1335-1339.

21. Taflove, A., Computational Electrodynamics: the Finite-Difference Time

Domain Method. 1996.

22. T M Benson, B Hu, A Vukovic, P Sewell, What is the future for beam propagation methods? 2004.

23. Haus, H.A., Waves and fields in optoelectronics. 1984: p.99-103.

24. C.E. Zah, et al., Fabrication and performance of 1.5μm GaInAsP travelling-wave laser amplifiers with angled facets. Electronics Letters, 1987. **23**(19): p. 990-992.

25. Rideout, W., et al., Ultra-low-reflectivity semiconductor optical amplifiers without antireflection coatings. Electronics Letters, 1990. **26**(1): p. 36-38.

26. T. Mukai, and O. Mikami, Theoretical analysis and fabrication of antireflection coatings on laser-diode facets. Lightwave Technology, Journal of, 1985. **3**(2): p. 288-293.

27. Olsson, N.A., et al., Ultra-low reflectivity 1.5 μm semiconductor laser preamplifier. Electronics Letters, 1988. **24**(9): p. 569-570.

28. Buus J., M.C. Farries, and D.J. Robbins, Reflectivity of coated and tilted semiconductor facets. Quantum Electronics, IEEE Journal of, 1991. **27**(6): p. 1837-1842.

29. C. E. Zah, 1.3 μm GaInAsP near-travelling-wave laser amplifiers made by combination of angled facets and antireflection coatings. Electronics Letters, 1988. **24**(20): p. 1275-1276.

30. Barnsley, P.E., J.J. Isaac, and D.J. Elton, Ultra-low reflectivity broadband 1.5 mu m GaInAsP semiconductor optical amplifiers. Electronics Letters, 1990.

26(12): p. 825-827.

31. Yih-Peng, C. and C. Hung-Chun, Analysis of optical waveguide discontinuities using the Pade approximants. Photonics Technology Letters, IEEE, 1997. **9**(7): p. 964-966.
32. Yevick, C.Y.a.D., application of the bidirectional parabolic equation method to optical waveguide facets J. Opt. Soc. Amer. A, 1997. **14**: p. 1448–1450.
33. El-Refaei, H., I. Betty, and D. Yevick, The application of complex Pade approximants to reflection at optical waveguide facets. Photonics Technology Letters, IEEE, 2000. **12**(2): p. 158-160.
34. Hongling, R., R. Scarmozzino, and R.M. Osgood, Jr., A bidirectional beam propagation method for multiple dielectric interfaces. Photonics Technology Letters, IEEE, 1999. **11**(7): p. 830-832.
35. Ya Yan, L. and W. Su Hua, A new iterative bidirectional beam propagation method. Photonics Technology Letters, IEEE, 2002. **14**(11): p. 1533-1535.
36. El-Refaei, H., D. Yevick, and I. Betty, Stable and noniterative bidirectional beam propagation method. Photonics Technology Letters, IEEE, 2000. **12**(4): p. 389-391.
37. Pui Lin, H. and L. Ya Yan, A stable bidirectional propagation method based on scattering operators. Photonics Technology Letters, IEEE, 2001. **13**(12): p. 1316-1318.

Chapter 2: Basic Electromagnetic Theory

This chapter overview typical optical waveguides and materials used in optics. The Maxwell's equations for a linear non-dispersive medium are given together with the boundary conditions for optical waveguides. The chapter also derives full-vectorial, semi-vectorial and scalar wave equations and overviews the mode classification.

2.1 Optical Waveguides and Materials

The realisation of the required functions of photonic devices is reliant on planar dielectric material systems. The material used, the physical shape and dimensions of the component structure are the main factors to affect the behaviour of an optical device. The main types of technologies in integrated photonics are divided into Planar Lightwave Circuit (PLC), Photonic Integrated Circuit (PIC) and Optoelectronic Integrated Circuit (OEIC). The first one is the simplest type to fabricate because it only consists of passive optical components. Typically silica based material, being the most common and favorable semiconductor material, is widely used due to its attractive properties including low propagation and insertion loss, stable physical and chemical characteristics [1]. In comparison with PLCs, PICs consist of active and passive components on the same substrate, and allow optical systems to be more compact and achieve higher performances. The fabrication process of PICs is more complicated than that of PLCs and the material is limited to III-IV group of compounds such as Gallium Arsenide (GaAs) and Indium Phosphide (InP) [2-4]. PICs can be integrated with Electronic Integrated Circuits (EICs) to form Integrated Optoelectronic Circuits (OEICs), a hybrid integration of optical and electronic components, which provide increased functionality.

Optical waveguides are the transmission medium in photonic integrated circuits to confine and guide electromagnetic waves [5]. A slab waveguide is the simplest waveguide consisting of three layers of materials with different refractive indices, as shown in Fig. 2.1. The middle layer, n_{core}, has a larger refractive index than the surrounding layers, $n_{cladding}$, to confine the wave in one dimension by total internal reflection [6].

Figure 2.1: slab waveguide

A strip waveguide is a strip of the guiding layer confined between cladding layers which confines the light in both transverse directions. A strip or several strips can be superimposed onto a slab to form a rib waveguide. Various strip-line waveguides are shown in Fig. 2.2, namely (a) embedded strip waveguide, (b) strip waveguide, (c) rib waveguide and (d) strip loaded waveguide [5].

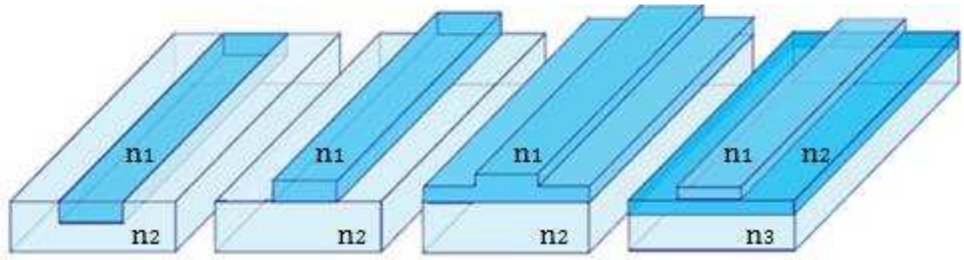

(a) (b) (c) (d)

Figure 2.2: Various waveguide geometries: (a) Embedded strip, (b) Strip, (c) Rib, (d) Strip loaded. The darker the shading, the higher the refractive index is.

Waveguides that confine light in both transverse directions are also used as S-bends, Y branches, couples, Mach-Zehnder interferometers or intersections, as illustrated in Fig. 2.3. Two waveguides in close proximity, or intersecting, can exchange power and may be used as directional couplers. S-bends can be used to control Bragg wavenumber for laser cavity [7, 8]. During the propagation, unwanted leakage can occur where the bends are sharp. The Y branch plays the role of a beamsplitter or combiner. It can be designed either symmetrically to equally separate the input wave at the output port, or asymmetrically to create bias at the output port [9]. Two Y branches can be used to make a Mach–Zehnder interferometer which is used as an intensity modulator, where output from one arm can be altered by applying electric voltage to create phase shift. When signal from two arms meet, they can interference constructively or destructively [10-12].

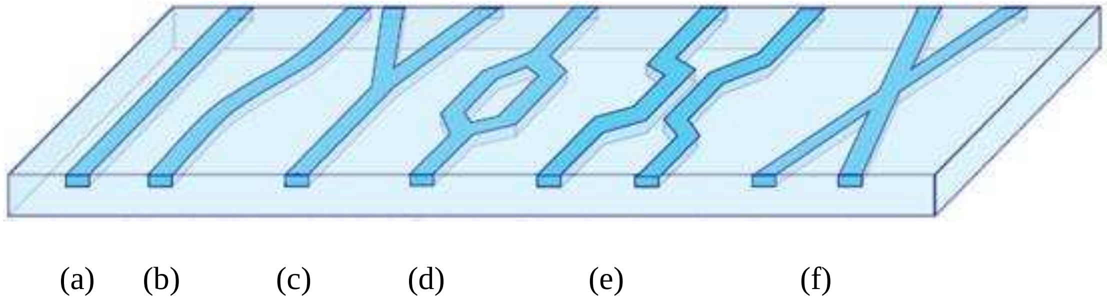

Figure 2.3: Different configurations for embedded-strip waveguides: (a) straight, (b) S-bend, (c) Y branch, (d) Mach–Zehnder, (e) directional coupler, (f) intersection.

The drive for miniaturization has meant that dimensions of standard waveguides are reduced bellow μm range. One of the first waveguides with cross section reaching nano-scale range is a Silicon wire based on SiO_2 technology [13]. In order to reduce the waveguide dimensions even further, a range of PBG waveguides and devices, which are on the basis of photonic crystals, are introduced [14]. Photonic crystals are composite of two materials with different refractive indices. One material is patterned with a periodicity on the other material. This structure creates a range of 'forbidden' frequencies called a photonic bandgap. Light with frequencies in this range is forbidden to exist within the interior of the crystal so that photons with energies cannot propagate through the medium. If there is a defect in the periodicity, it could lead to localized photonic states in the gap. The shapes and properties of the localized photonic states would be determined by the nature of the defect. This ability to manipulate a photon provides a new dimension to control the properties of light [14]. If there is a line defect in the periodicity, the structure works like a waveguide. Light with a frequency within the bandgap of crystal is confined within the defect and propagates along the waveguide. Compared to the traditionally optical waveguides relying on the total internal reflection to propagate light, PBG waveguides have a significant advantage. If the traditionally optical waveguides, such as an optical fiber, curve tightly, the incidence angle is too large to satisfy the condition of total internal reflection, hence light would escape at the corners and serious loss is unavoidable. PBG waveguides could continue to confine light within the gap even around tight corners [14]. Fig.2.4 presents an example of light guided in a bended PBG waveguide. A 1.55μm optical signal is launched into a 90^o bended PBG waveguide as in Fig.2.4 (a) and propagates long the gap with little loss as in Fig.2.4 (b) [15].

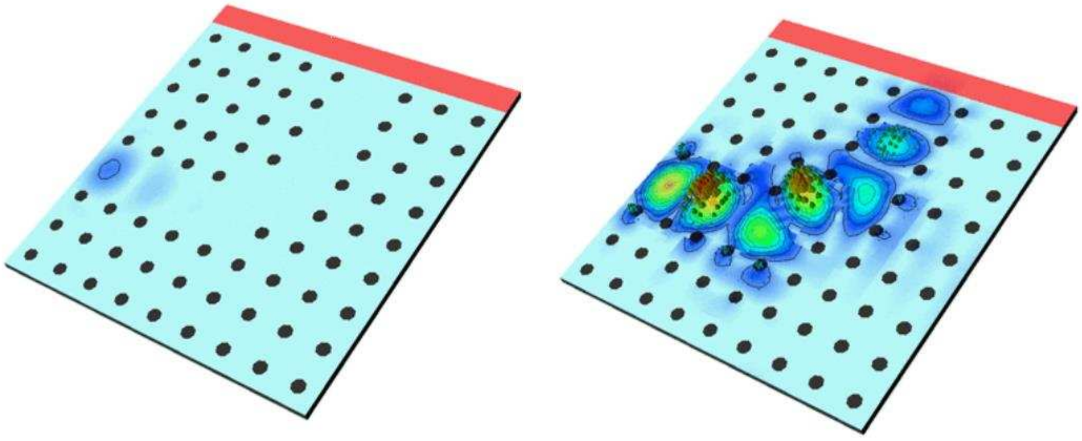

(a) (b)

Figure 2.4: The electric field of a 1.55μm optical signal traversing the bend of a PBG waveguide: (a) the single is launched into the waveguide; (b) the single propagates along the gap with little loss.

Another new waveguide, the SP waveguide which uses the interface between a metal and a dielectric to guide the signal, has attracted much recent interest for its good ability in guiding electromagnetic energy within nanostructures [16]. SPs wavegudies are named after Surface Plasma Polaritons (SPPs) which are collective coherent oscillations occurring and existing at the interface between metal and dielectric materials at optical frequencies. SPPs can propagate along the surface of a metal over a short distance (couple of hundreds μm), with fields that peak at the interface and decay exponentially away from the interface [17]. The SP waveguides are used for highly integrated photonic signal-processing systems, and as nano-resolution optical imaging sensors [16, 18]. Moreover, SP waveguides are to sense very small dielectric constant changes of molecules on its surface and are used in chemistry and biology area. For example, based on surface plasmon resonance (SPR) phenomenon, SPR microscope is invented for the medical and bio-sensing science [19]. The basic SP waveguide is a thin metal film of a certain thickness laying on a dielectric substrate, covered by a dielectric cladding or air. The thickness of the metal film is normally around dozens to hundreds of nanometers. Metals at optical frequencies behave as lossy dielectrics with negative dielectric constant. The typical metals which yield negative dielectric constants at optical wavelengths are gold, silver, and copper [20]. Only optical fields polarized perpendicular to the metal-dielectric interface can excite SPP waves. A schematic illustration of a classic SPP waveguide is shown in Fig. 2.5 [21]. The waveguide is composed of a thin silver (Ag) film located above a dielectric substrate. SPP waveguide supports surface electromagnetic waves at the interface between dielectric material and metal film, where the charge density oscillations are supported [22]. This surface localization has the potential for transporting and sensing information via guided polariton modes with small spatial extents [21].

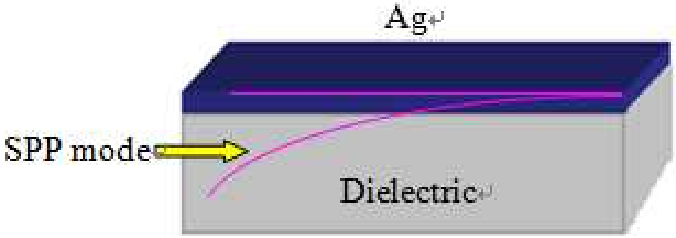

Figure 2.5: Illustration of a SPP waveguide structure and its mode (red curve) guided between the interface of silver (Ag) film and the dielectric.

There are four parameters associated with the SPP modes, including the SPP wavelength (λ_{spp}), the SPP propagation distance (δ_{spp}), and the penetration depths of the field associated with the SPP into the dielectric (δ_d) and metal media (δ_m) that bound the interface to support the SPP [23]. Fig. 2.6 illustrates different length scales of SPP parameters [23] and shows that these length scales span seven orders of magnitude. It can be seen that the SPP penetration depth into the metal is in the range of dozens of nanometers, the SPP penetration depth into the dielectric and the SPP wavelength is around hundreds of nanometers, and the SPP propagation length spans from dozens of micrometers to about one centimeter. It should be noted that the SPP propagation length is significantly greater than the SPP wavelength. This fact means that wavelength scale gratings and other periodic surface structures can be used to manipulate SPPs since the modes are able to interact over many periods of such a structure [23].

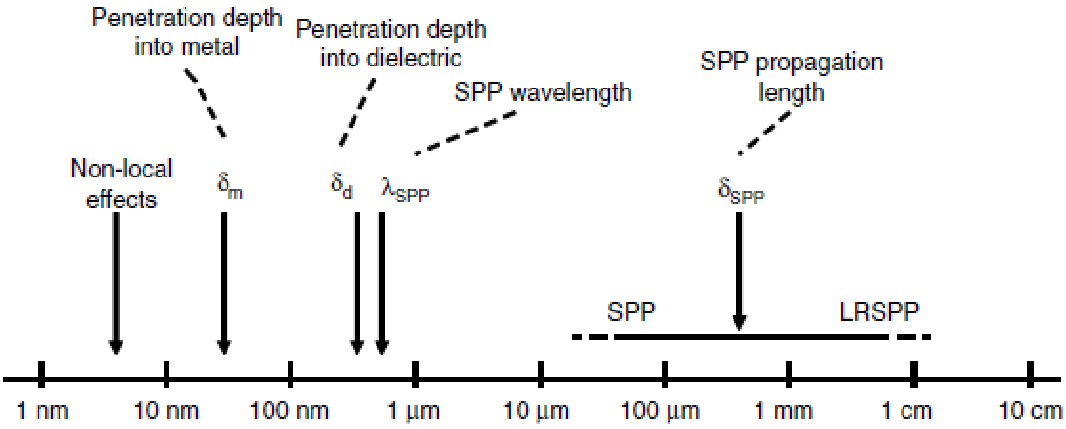

Figure 2.6: The different length scales of importance for surface plasmon-polaritons in the visible and near-infrared are indicated on a logarithmic scale. [23]

In terms of materials, semiconductors belonging to III-V group are generally used to fabricate both active and passive waveguides [24]. The typical representatives of this category are InP- and GaAs- based technologies, both of which are suitable for high frequency and high power applications. However, these two technologies work at slightly different frequencies: InP technology works in the 1.3-1.5 µm wavelength range in which single mode optical fiber exhibits small losses, while GaAs technology works in the 0.8 λm wavelength range [25]. However, III-V semiconductor waveguides have several common characteristics: (a) they have relatively large refractive index differences, typically in the ratio of 3:1, so that an air-semiconductor boundary can exist near a guiding region; (b) the dimension of the waveguides is about one micrometer in the vertical direction and approximately a couple of micrometers in the lateral direction, leading to an elliptic mode profile which is not matched to the circular fiber mode. To alleviate this, particular waveguides known as mode spot converters are used to couple a rib waveguide to a fiber. These converters are specially designed rectangular waveguides buried deeply in the substrate or close to the air-semiconductor boundary, such as buried rectangular waveguides, diffused waveguides, or air-clad rib waveguides. [24].

Silicon (Si) is the most common and economical semiconductor device material that has played a crucial role in large scale manufacture of monolithic optoelectronic integrated circuits. Traditionally, Si is used for passive components over a wide optical communication range from 1.3 to 1.55μm [26]. Recent development in active Si based material alloys, such as SiGe [27, 28], has extended the application of Si to active photonic components. Experimentally, light can be propagated within four types of Group IV waveguides, including lightly doped silicon on heavily doped silicon, epitaxial $Si_{1-x}Ge_x$ on Si, silicon-on-sapphire, and silicon-on-insulator [26]. The combination of materials normally exhibits a large refractive index difference and provides a possibility to achieve low-loss optical waveguide. For instance, waveguides can be fabricated using silicon-on-insulator (Si-SiO_2 or SOI) technique, in which the refractive index of silicon is around 3.5 but that of silica is around 1.5 [29].

Furthermore, Lithium niobate ($LiNbO_3$) crystal that belongs to III-V group is another important electro-optic material. Over the past twenty years, the fabrication and application of $LiNbO_3$ structures has attracted a lot of attention, and fiber and waveguide forms of $LiNbO_3$ have played increasingly important role [30]. It is widely used for optical waveguides and optical modulators where non-linear interaction between the signal and material is required. For instance, $LiNbO_3$ modulators using the electro-optic effect is a very important device for optical communications as it is used for Mach-Zehnder interferometer (MZI) [30].

2.2 Maxwell's Equations

An optical field is a time dependent electromagnetic wave and is completely described by Maxwell's equations [31]. The differential form of Maxwell's equations in a source free region is given as:

$$\nabla \times \vec{E} = -\frac{\partial \vec{B}}{\partial t}, \tag{2.2.1}$$

$$\nabla \times \vec{H} = \frac{\partial \vec{D}}{\partial t}, \tag{2.2.2}$$

$$\nabla \cdot \vec{D} = 0, \tag{2.2.3}$$

$$\nabla \cdot \vec{B} = 0. \tag{2.2.4}$$

where, $\vec{E}$ and $\vec{H}$ denote the electric and magnetic field vectors respectively, $\vec{D}$ denotes the electric displacement vector and $\vec{B}$ denotes the magnetic flux density. Eq. (2.2.1) and Eq. (2.2.2) are vector equations which relate time and space derivatives of the field quantities, and Eq. (2.2.3) and Eq. (2.2.4) are scalar equations to express Gauss's law for the electric and magnetic field.

For a linear and isotropic medium, electric displacement vector is given as

$$\vec{D} = \varepsilon_0 \vec{E} + \vec{P_L}, \qquad (2.2.5)$$

where $\vec{P_L}$ is the polarisation density of the linear non-dispersive material and is given as:

$$\vec{P_L} = \varepsilon_0 \chi_e \vec{E} = \varepsilon_0 (n_r^2 - 1)\vec{E}, \qquad (2.2.6)$$

where χ_e is electric susceptibility, and n_r is the refractive index which is related to the relative dielectric permittivity ε_r as $n_r = \sqrt{\varepsilon_r}$.

Therefore, the relationships between $\vec{D}$ and $\vec{E}$, $\vec{H}$ and $\vec{B}$, in a phasor form are defined as:

$$\vec{D} = \varepsilon_0 n_r^2 \vec{E} \qquad (2.2.7)$$

$$\vec{B} = \mu_0 \mu_r \vec{H} \qquad (2.2.8)$$

In the context of this work, only non-magnetic materials are considered, and $\mu_r = 1$. The free space permittivity is $\varepsilon_0 \approx 8.85\times10^{-12}$ and the free space permeability is $\mu_0 = 4\pi\times10^{-7}$.

2.3 Boundary Conditions at Material Interfaces

Maxwell's equations, as stated in Eq.(2.2.1) to Eq.(2.2.4), hold true for homogenous regions with continuous physical properties. In the case where the properties of the material changes abruptly, the solution to Maxwell's equations have to satisfy boundary conditions across the interface separating different media. An interface plane between two dielectric regions with refractive indices n_{r1} and n_{r2} is illustrated in Fig. 2.7. $\vec{E}_1$ and $\vec{H}_1$ denote the electric and magnetic field vectors in medium 1 of refractive index n_{r1}. $\vec{E}_2$ and $\vec{H}_2$ denote the corresponding field vectors in medium 2 of refractive index n_{r2}, and $\vec{n}$ is the unit normal to the interface between these two media.

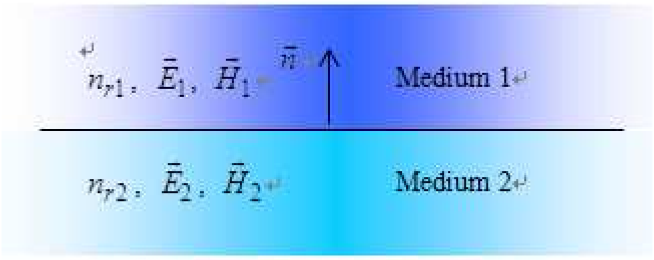

Figure 2.7: An interface between two dielectric materials.

In the absence of surface charges and surface currents, the boundary conditions are reduced to four conditions, namely [32]:

(i) Tangential components of electric fields are continuous:

$$\vec{n} \times \vec{E}_1 = \vec{n} \times \vec{E}_2 . \qquad (2.3.1)$$

(ii) Tangential components of magnetic fields are continuous:

$$\vec{n}\times\overrightarrow{H_1}=\vec{n}\times\overrightarrow{H_2}. \tag{2.3.2}$$

(iii) Normal components of electric flux are continuous:

$$\vec{n}\cdot\vec{D}_1=\vec{n}\cdot\vec{D}_2. \tag{2.3.3}$$

(iv) Normal components of magnetic flux are continuous:

$$\vec{n}\cdot\vec{B}_1=\vec{n}\cdot\vec{B}_2. \tag{2.3.4}$$

For non-magnetic media, $\mu_{r1}=\mu_{r2}=1$. Eq. (2.3.4) is reduced to

$$\vec{n}\cdot\overrightarrow{H_1}=\vec{n}\cdot\overrightarrow{H_2}. \tag{2.3.5}$$

These equations allow the boundary conditions for the normal ($\perp$) and tangential (||) field components to be expressed explicitly as:

$$E_{1||}=E_{2||} \tag{2.3.6}$$

$$H_{1||}=H_{2||} \tag{2.3.7}$$

$$n_{r1}^2E_{1\perp}=n_{r2}^2E_{2\perp} \tag{2.3.8}$$

$$H_{1\perp}=H_{2\perp} \tag{2.3.9}$$

It is observed that the tangential components of the electric and magnetic fields, $E_{||}$ and $H_{||}$, are continuous, and so is the normal component of the magnetic field, $H_{\perp}$.

However, the normal component of the electric field, $E_{\perp}$, is subject to a step-change due to the discontinuity in the refractive indices of the media.

2.4 Wave Equations

In this section Maxwell's equations are used to derive wave equations for the full-vectorial, semi-vectorial and scalar fields. From Maxwell's equations, a general vector wave equation can be derived in terms of only electric or magnetic field components. Time-harmonic electric and magnetic fields can be expressed as [33]:

$$\vec{E}(x, y, z; t) = \vec{E}(x, y, z)\exp(j\omega t) \qquad (2.4.1)$$

$$\vec{H}(x, y, z; t) = \vec{H}(x, y, z)\exp(j\omega t) \qquad (2.4.2)$$

where ω is the angular frequency.

Substituting Eq. (2.2.8) and Eq.(2.2.7) into Eq. (2.2.1) and Eq. (2.2.2) gives

$$\nabla\times\vec{E} = -\frac{\partial(\mu_0\vec{H})}{\partial t}, \qquad (2.4.3)$$

$$\nabla\times\vec{H} = \frac{\partial(\varepsilon_0 n_r^2\vec{E})}{\partial t}. \qquad (2.4.4)$$

For time harmonic form of electric and magnetic fields it follows that $\frac{\partial}{\partial t} = j\omega$, and previous equations reduce to:

$$\nabla\times\vec{E} = -j\omega\mu_0\vec{H}, \qquad (2.4.5)$$

$$\nabla\times\vec{H} = j\omega\varepsilon_0 n_r^2\vec{E}\ . \tag{2.4.6}$$

Taking the curl of Eq. (2.4.5) and replacing time derivatives with the term *jω* gives:

$$\nabla\times(\nabla\times\vec{E}) = \nabla\times(-j\omega\mu_0\vec{H}) = -j\omega\mu_0(\nabla\times\vec{H})$$

$$= -j\omega\mu_0\bullet j\omega\varepsilon_0 n_r^2\vec{E} = \omega^2\varepsilon_0\mu_0 n_r^2\vec{E}\ , \tag{2.4.7}$$

or
$$\nabla\times(\nabla\times\vec{E}) = k_0^2 n_r^2\vec{E}\ , \tag{2.4.8}$$

where k_0 is the wave number in free space and is given as $k_0 = \omega\sqrt{\varepsilon_0\mu_0}$.

On the other hand, the angular frequency is $\omega = 2\pi f$ and the speed of light in vacuum is $c = \frac{1}{\sqrt{\varepsilon_0\mu_0}}$. Therefore, the wavenumber in free space can be expressed as:

$$k_0 = \omega\sqrt{\varepsilon_0\mu_0} = \frac{2\pi f}{c} = \frac{2\pi}{\lambda}\ , \tag{2.4.9}$$

where λ is the free space wavelength.

Using the vector identity in Eq. (2.4.10)

$$\nabla\times\nabla\times\vec{E} = \nabla(\nabla\cdot\vec{E}) - \nabla^2\vec{E}\ . \tag{2.4.10}$$

Eq.(2.4.8) can be rewritten as

$$\nabla^2\vec{E} - \nabla(\nabla\cdot\vec{E}) + k_0^2 n_r^2\vec{E} = 0\ . \tag{2.4.11}$$

For the source free region, the relationship $\nabla\cdot\vec{D} = \nabla\cdot(n_r^2\vec{E}) = 0$ is satisfied. Using the identity

$$\nabla\cdot(n_r^2\vec{E}) = n_r^2\nabla\cdot\vec{E} + \vec{E}\cdot\nabla n_r^2 = 0 \quad , \tag{2.4.12}$$

gives

$$\nabla\cdot\vec{E} = -\frac{\vec{E}\cdot\nabla n_r^2}{n_r^2} \quad , \tag{2.4.13}$$

and substituting Eq. (2.4.13) into Eq. (2.4.11), the general vector wave equation for the electric field is obtained as:

$$\nabla^2\vec{E} + \nabla\left(\frac{\vec{E}\cdot\nabla n_r^2}{n_r^2}\right) + k_0^2 n_r^2\vec{E} = 0 \quad . \tag{2.4.14}$$

The general vector wave equation for the magnetic field may be derived in a similar manner by eliminating the electric field and is

$$\nabla^2\vec{H} + \frac{\nabla n_r^2}{n_r^2}\times\left(\nabla\times\vec{H}\right) + k_0^2 n_r^2\vec{H} = 0 \, . \tag{2.4.15}$$

Eq. (2.4.14) and Eq. (2.4.15) are only valid in regions of continuous refractive index. For the case that the refractive indices are discontinuous, appropriate boundary conditions need to be applied. Because the solution for either the electric field or the magnetic field can be used to calculate the other field components via Maxwell's equations, only one wave equation needs to be analysed. In this thesis, the wave equation for electric field will be applied for most modelling and simulations.

2.4.1 Vectorial Wave Equation

For most photonic components and waveguides, the refractive indices of the structures are longitudinally invariant or slowly changing along the propagation direction, conventionally the z direction, and the derivative of the refractive index with respect to z direction can be neglected. The second term in the left-hand side of Eq. (2.4.14) can be rewritten as:

$$\begin{aligned}\nabla(\frac{\vec{E}\cdot\nabla n_r^2}{n_r^2}) &= \nabla[\frac{\vec{E}}{n_r^2}(\frac{\partial n_r^2}{\partial x}\vec{i}+\frac{\partial n_r^2}{\partial y}\vec{j}+\frac{\partial n_r^2}{\partial z}\vec{k})] \\ &= \nabla[\frac{1}{n_r^2}(\frac{\partial n_r^2}{\partial x}E_x+\frac{\partial n_r^2}{\partial y}E_y+\frac{\partial n_r^2}{\partial z}E_z)]\end{aligned} \qquad (2.4.16)$$

For longitudinally invariant waveguides,

$$\frac{\partial n_r^2}{\partial z} \simeq 0 \, ,$$

the electric field in Eq. (2.4.15) can be expressed in terms of transverse components E_x and E_y as:

$$\nabla^2 E_x + \frac{\partial}{\partial x}(\frac{1}{n_r^2}\frac{\partial n_r^2}{\partial x}E_x) + \frac{\partial}{\partial x}(\frac{1}{n_r^2}\frac{\partial n_r^2}{\partial y}E_y) + k_0^2 n_r^2 E_x = 0 \qquad (2.4.17)$$

$$\nabla^2 E_y + \frac{\partial}{\partial y}(\frac{1}{n_r^2}\frac{\partial n_r^2}{\partial x}E_x) + \frac{\partial}{\partial y}(\frac{1}{n_r^2}\frac{\partial n_r^2}{\partial y}E_y) + k_0^2 n_r^2 E_y = 0 \qquad (2.4.18)$$

Furthermore, the following equations are valid:

$$\begin{aligned}\frac{\partial}{\partial x}[\frac{1}{n_r^2}\frac{\partial}{\partial x}(n_r^2 E_x)] &= \frac{\partial}{\partial x}[\frac{1}{n_r^2}(\frac{\partial n_r^2}{\partial x}E_x + \frac{\partial E_x}{\partial x}n_r^2)] \\ &= \frac{\partial}{\partial x}(\frac{1}{n_r^2}\frac{\partial n_r^2}{\partial x}E_x) + \frac{\partial^2 E_x}{\partial x^2}\end{aligned} \qquad (2.4.19)$$

$$\begin{aligned}\frac{\partial}{\partial x}[\frac{1}{n_r^2}\frac{\partial}{\partial y}(n_r^2E_y)] &= \frac{\partial}{\partial x}[\frac{1}{n_r^2}(\frac{\partial n_r^2}{\partial y}E_y+\frac{\partial E_y}{\partial y}n_r^2)] \\ &= \frac{\partial}{\partial x}(\frac{1}{n_r^2}\frac{\partial n_r^2}{\partial y}E_y)+\frac{\partial^2 E_y}{\partial x\partial y}\end{aligned} \tag{2.4.20}$$

$$\begin{aligned}\frac{\partial}{\partial y}[\frac{1}{n_r^2}\frac{\partial}{\partial y}\left(n_r^2E_y\right)] &= \frac{\partial}{\partial y}[\frac{1}{n_r^2}(\frac{\partial n_r^2}{\partial y}E_y+\frac{\partial E_y}{\partial y}n_r^2)] \\ &= \frac{\partial}{\partial y}(\frac{1}{n_r^2}\frac{\partial n_r^2}{\partial y}E_y)+\frac{\partial^2 E_y}{\partial y^2}\end{aligned} \tag{2.4.21}$$

$$\begin{aligned}\frac{\partial}{\partial y}[\frac{1}{n_r^2}\frac{\partial}{\partial x}\left(n_r^2E_x\right)] &= \frac{\partial}{\partial y}[\frac{1}{n_r^2}(\frac{\partial n_r^2}{\partial x}E_x+\frac{\partial E_x}{\partial x}n_r^2)] \\ &= \frac{\partial}{\partial y}(\frac{1}{n_r^2}\frac{\partial n_r^2}{\partial x}E_x)+\frac{\partial^2 E_x}{\partial y\partial x}\end{aligned} \tag{2.4.22}$$

Based on these identities, the full-vectorial wave equations Eq. (2.4.17) and Eq. (2.4.18) can be rewritten as [34]:

$$\frac{\partial}{\partial x}[\frac{1}{n_r^2}\frac{\partial}{\partial x}(n_r^2E_x)]+\frac{\partial^2 E_x}{\partial y^2}+\frac{\partial^2 E_x}{\partial z^2}+\frac{\partial}{\partial x}[\frac{1}{n_r^2}\frac{\partial}{\partial y}(n_r^2E_y)]-\frac{\partial^2 E_y}{\partial x\partial y}+k_0^2n_r^2E_x=0\,, \tag{2.4.23}$$

$$\frac{\partial^2 E_y}{\partial x^2}+\frac{\partial}{\partial y}[\frac{1}{n_r^2}\frac{\partial}{\partial y}\left(n_r^2E_y\right)]+\frac{\partial^2 E_y}{\partial z^2}+\frac{\partial}{\partial y}[\frac{1}{n_r^2}\frac{\partial}{\partial x}\left(n_r^2E_x\right)]-\frac{\partial^2 E_x}{\partial y\partial x}+k_0^2n_r^2E_y=0\,. \tag{2.4.24}$$

2.4.2 Semi-vectorial Wave Equation

For a strongly polarised wave along either of the transverse direction, the coupling terms of the transversal components E_x and E_y can be neglected and the corresponding terms in the wave equation, $\frac{\partial}{\partial x}[\frac{1}{n_r^2}\frac{\partial}{\partial y}(n_r^2E_y)]$, $\frac{\partial^2 E_y}{\partial x\partial y}$, $\frac{\partial}{\partial y}[\frac{1}{n_r^2}\frac{\partial}{\partial x}\left(n_r^2E_x\right)]$ and $\frac{\partial^2 E_x}{\partial y\partial x}$, are assumed to be zero. In this case, the vectorial wave equations are simplified into the semi-vectorial wave equations.

In this thesis, The TE mode is defined in the condition that the component E_x is assumed to be zero and then the field components are $\vec{E}(x, y, z) \equiv (0, E_y, E_z)$; the TM mode is defined in the condition that the component E_y is assumed to be zero and then the field components are $\vec{E}(x, y, z) \equiv (E_x, 0, E_z)$, as shown in Fig. 2.8. Therefore, the wave equations Eq. (2.4.23) and Eq. (2.4.24) are simplified into the TM semi-vectorial wave equation with dominant E_x field component as

$$\frac{\partial}{\partial x}[\frac{1}{n_r^2}\frac{\partial}{\partial x}(n_r^2 E_x)] + \frac{\partial^2 E_x}{\partial y^2} + \frac{\partial^2 E_x}{\partial z^2} + k_0^2 n_r^2 E_x = 0, \qquad (2.4.25)$$

and TE semi-vectorial wave equation with dominant E_y field component as

$$\frac{\partial^2 E_y}{\partial x^2} + \frac{\partial}{\partial y}[\frac{1}{n_r^2}\frac{\partial}{\partial y}\left(n_r^2 E_y\right)] + \frac{\partial^2 E_y}{\partial z^2} + k_0^2 n_r^2 E_y = 0. \qquad (2.4.26)$$

The semi-vectorial equations only solve the dominant field component for each corresponding polarisation and thus significantly simplify the simulation algorithm and reduce the computation time [35]

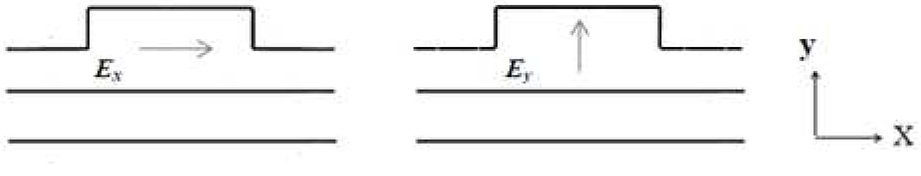

(a) (b)

Figure 2.8: Principal electric field components for the (a) TM mode (b) TE mode.

2.4.3 Scalar Wave Equation

Further simplification of the wave equation is possible when polarisation is not of interest or in case of waveguides with very small refractive index difference. Mathematically, this means that the term $\nabla n^2 \cong 0$ and the vector field $\vec{E}$ can be replaced by a scalar quantity ψ. This leads to scalar Helmholtz formulation in the form of:

$$\frac{\partial^2 \psi}{\partial x^2} + \frac{\partial^2 \psi}{\partial y^2} + \frac{\partial^2 \psi}{\partial z^2} + k_0^2 n_r^2 \psi = 0 \qquad (2.4.27)$$

In the scalar approximation, both the field and its derivative are required to be continuous across the dielectric boundary.

So far, the approaches to solve the wave propagation problem have fallen into three classes: (1) vectorial, (2) semi-vectorial, and (3) scalar. For the waveguide with high refractive index contrast or longitudinally variant structures such as bends and Y-junctions, significant coupling occurs between electric and magnetic field polarisations. In this case, the full vectorial wave equations are required for accurate modelling. On the other hand, for weakly guiding structures with low refractive index contrasts, the propagating fields can be regarded as uncoupled, in which case the semi-vectorial or the scalar wave equation can be used for efficient modelling. These wave equations will be considered as the foundation for further development of analysis tools.

2.5 Waveguide Modes Classification

The solutions of a waveguide are given by a complete set of functions describing the modes supported by the waveguide. As dielectric waveguides are open structures, the modes that exist in a waveguide can be divided into two classes: a discrete set of bound modes and a continuum of radiation modes [36]. The differences between these two types of modes can be distinguished from the perspective comparison, which between the propagation constants of the modes and the refractive indices of the materials forming the waveguide. For simplicity this is illustrated for the case of an asymmetric 3-layer slab waveguide in Fig. 2.9, where the refractive indices of the cladding, the core and the substrate satisfy the relationship $n_{core} > n_{substrate} > n_{cladding.}$

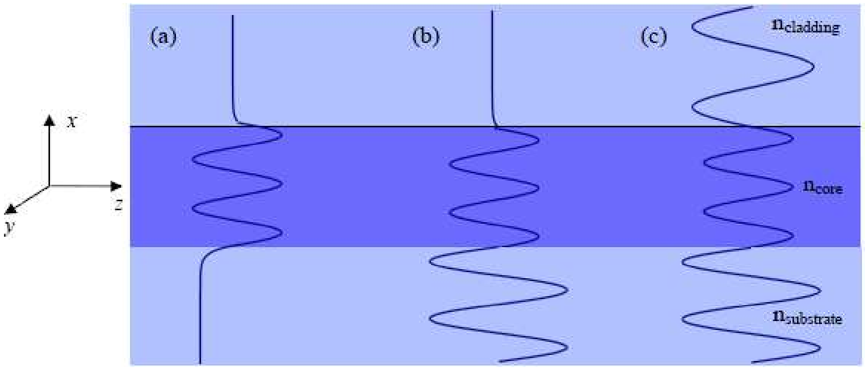

Figure 2.9: The modes supported by a 3-layer asymmetric slab waveguide: (a) guided mode, (b) substrate radiation mode and (c) substrate-cladding mode.

Propagation constants β of the bound modes are purely real and lie within the range $k_0 n_{substrate} < \beta < k_0 n_{core}$. These modes are oscillatory within the core region and exponentially decay in the cladding and substrate regions [37], hence bound modes are known as guided modes, as shown in Fig.2.9(a). A guided mode, normally the fundamental mode, is used to transmit the information.

The total radiation field is comprised of radiation modes and leaky modes. Propagation constants of radiation modes are below the cut-off for bound modes. If $k_0 n_{cladding} < \beta < k_0 n_{substrate}$, the modes are known as substrate radiation modes, as shown in Fig.2.9(b). If $0 < \beta < k_0 n_{cladding}$, the modes are known as cladding-substrate radiation modes, as shown in Fig.2.9(c). Leaky modes are characterised by discrete solutions that yield complex propagation constants below cut off which lose power into the cladding as they propagate.

2.6 References

1. Okamoto K., Advances in Silica Planar Lightwave Circuits. Journal of Lightwave Technology, 2006. **24**: p. 4763-4789.
2. Stefano Bottacchi, Advanced Photoreceivers for High-Speed Optical Fiber Transmission Systems. Journal of Selected Topics in Quantum Electronics, 2010. **16**: p. 1099-1112.
3. Albrecht P., Monolithically integrated transceivers on InP: the development of

a generic integration concept and its technological challenges. International Conference on Indium Phosphide and Related Materials, 1998: p. 431-434.

4. Hamacher M., Monolithic integration of lasers, photodiodes, waveguides and spot size converters on GaInAsP/InP for photonic IC applications. International Conference on Indium Phosphide and Related Materials, 2000: p. 21-24.
5. Adams, M.J., An introduction to optical waveguides. Wiley, 1981.
6. Richard Syms, Optical Guided Waves And Devices. McGraw-Hill International (UK) Ltd, 1992.
7. J. Salzmanl, H.O., A. Mprller-Larsen, O. Albrektsen, J. Hanberg, J. Norregaard and B. Tromborg, The S-bent waveguide distributed feedback laser. in 14th IEEE International Semiconductor Laser Conference, 1994: p. 57-58.
8. Salzman, J., Distributed Feedback Lasers with an S-Bent Waveguide for High-Power Single-Mode Operation. IEEE Journal of Selected Topics in Quantum Electronics, 1995. **1**(2): p. 346-354.
9. R. Krähenbühl, M.M.H., J. Dubinger, and A. S. Greenblatt, Performance and Modeling of Advanced Ti : LiNbO3 Digital Optical Switches. JOURNAL OF LIGHTWAVE TECHNOLOGY, 2002. **20**(1): p. 95-99.
10. K. JINGUJI, N.T., A. SUGITA, M. KAWACHI, Mach-Zehnder Interferometer Type Optical Waveguide Coupler With Wavelength-Flattened Coupling Ratio. Electronic Letters, 1990. **26**(17): p. 1326-1327.
11. Robert A. Mayer, K.H.J., W. D. Lee, Dim-Lee Kwong, and Joe C. Campbell,

Thin-film thermo-optic Ge.Sil-. Mach-Zehnder interferometer. OPTICS LETTERS 1992. **17**: p. 1812-1814.

12. B. J. Luff, J.S.W., Jacob Piehler, Uwe Hollenbach, Jan Ingenhoff, and Norbert Fabricius, Integrated Optical Mach–Zehnder Biosensor. JOURNAL OF LIGHTWAVE TECHNOLOGY, 1998. **16**: p. 583-592.
13. Pieter Dumon, e.a., Low-Loss SOI Photonic Wires and Ring Resonators Fabricated With Deep UV Lithography. PhotonicsTechnology Letter, 2004. **16**: p. 1328-1330.
14. J.D.Joannopoulos, P.R.V.a.S.F., Photonic crystals: putting a new twist on light. Nature, 1997. **386**: p. 143-149.
15. Laboratory,T.w.o.L.L.N., https://www-eng.llnl.gov/emsolve/emsolve_results_waveguides.html.
16. Junxi Zhang, Surface plasmon polaritons: physics and applications. Journal of Lightwave Phycisc D: Applied Physics, 2012.
17. Boardman, A.D., Electromagnetic Surface Modes. 1982.
18. bozhevolnyi, plasmonics beyond the diffraction limit. nature photonics, 2010. **4**: p. 83-91.
19. Thomas Wilkop, Ian L Alberts, Joost D de Bruijn and Asim K Ray, Surface Plasmon Resonance Imaging for Medical and Biosensing. IEEE SENSORS 2009 Conference, 2009.
20. American Institute of Physics Handbook. 1972.
21. Hu, B., "Advanced Beam Propagation Methods for the Analysis of Integrated

Photonic Devices",PhD Thesis, University of Nottingham. 2006.

22. R. Zia, M. L. Brongersma, Dielectric waveguide model for guided surface polaritons. Opt. Lett, 2005. **30**: p. 1473-1475.

23. W.L. Barnes, Surface plasmon–polariton length scales: a route to sub-wavelength optics. Journal of Optics A: Pure and Applied Optics, 2006: p. S87-S93.

24. I. Moerman, P. M. Demeester, A review on fabrication technologies for the monolithic integration of tapers with III-V semiconductor devices. IEEE Journal of Selected Topics in Quantum Electronics, 1997.

25. Vukovic, A., Fourier Transformation Analysis of Optoelectronic Components and Circuits. Thesis submitted to the University of Nottingham for the degree of Doctor of Philosophy, 2000.

26. SOREF, R.A., Silicon-Based Optoelectronics. PROCEEDINGS OF THE IEEE, 1993. **81**: p. 1687-1706.

27. Bernd Schiippert, Integrated Optics in Silicon and SiGe-Heterostructures. Journal of Lightwave Technology, 1996. **14**: p. 2311-2323.

28. L. Naval, L. Gomelsky, and J. M. Liu, Optimization of Si_1-xGe_x/Si Waveguide Photodetectors Operating at A = 1.3 pm. JOURNAL OF LIGHTWAVE TECHNOLOGY, 1996. **14**: p. 787-797.

29. E. Cortesi, R. A. Soref, Novel silicon-oninsulator structures for silicon waveguide. in Proc. 1989 IEEE SOSISOI 89 Technology Conf 1989.

30. Shizhuo Y., Lithium niobate fibers and waveguides: fabrications and

applications. Proceedings of the IEEE, 1999. **87**(11): p. 1962-1974.

31. R.F. Harrington, Time harmonic electromagnetic fields. 1961.
32. M.B. Wolf, Principles of Optics. 1993.
33. J. Yamauchi,, Propagation Beam Analysis of Optical Waveguide. 2003.
34. J. Yamauchi, G. Takahashi, and H. Nakano, Full-vectorial beam-propagation method based on the McKee-Mitchell scheme with improved finite-difference formulas. Lightwave Technology, Journal of, 1998. **16**(12): p. 2458-2464.
35. M.S. Stern, Semivectorial polarised finite difference method for optical waveguides with arbitrary index profiles. Optoelectronics, IEE Proceedings J, 1988. **135**(1): p. 56-63.
36. T.Rozzi, Open electromagnetic waveguides. 1997.
37. A.W.Snyder, Optical Waveguide Theory. 1983.

Chapter 3: Overview of Analysis Tools for Photonic Devices

The developments of optical waveguide based technologies require powerful tools for the designing and testing of the photonic devices. With the improvements of computer capabilities, Computer-Aided Design (CAD) has played an increasingly important role in the design process. To date, a variety of CAD simulation packages and methods exist. They can be classified into three main groups: (1) Analytical methods, (2) Semi-analytical methods, and (3) Numerical methods.

This chapter will review typical analysis methods used in modelling of photonic devices, and concentrate on their characteristics, advantages and disadvantages. Semi-analytical methods such as Marcatili's method, the Effective Index (EI) Method and the Spectral Index Method are presented. Classic numerical methods including the Finite Element (FE) Method, the Finite Difference (FD) Method and Finite Difference Time Domain (FDTD) are described. The chapter focuses on the overview of the FD-BPM method and the derivation of the paraxial FD-BPM wave equation. Boundary conditions used to terminate the simulation window in FD-BPM method are also outlined. Finally the chapter presents the approach based on Imaginary Distance (ID) BPM that is used for solving for the propagation modes, together with the test simulation results of the mode solver.

3.1 Analytical and Semi-Analytical Methods

Analytical methods provide accurate results that are limited to simple structures, such as homogenous medium or slab waveguide structures. In other words, they are not valid for practical waveguide structures with a complex refractive index distribution.

The semi-analytical methods were popular tools for simulation before the advent of modern computers. They simplify the problem by applying certain approximations to the structure, and then solve the modified structure analytically. Nowdays, they are still highly valuable for the design of optical waveguides such as rib and buried waveguides. Semi-analytical methods provide good accuracy and are not numerically intensive. This makes them efficient and easy to implement. However, the semi-analytical methods often involve extensive mathematical manipulations in order to obtain the simplified solutions of the practical problems for further process, and their range of applications are limited to certain types of problems [1].

This section will overview the most commonly used semi-analytical methods including Marcatili's [2], Effective index [3] and Spectral index [4] methods.

3.1.1 Marcatili’s Method

Marcatili’s Method is one of the first semi-analytical methods for analysis of a buried rectangular waveguide surrounded by dielectric material [2]. This method is restricted to waveguides having large dimensions and small refractive index contrast between the core and the cladding materials. The principle of the Marcatili’s Method is schematically shown in Fig. 3.1. Firstly, the whole cross section of the waveguide is divided into nine regions belonging to three different types:

(1) the core region;

(2) four neighbouring cladding regions obtained by extending in turn the height and width of the core region to infinity;

(3) four corner regions.

Secondly, the field in each region is considered separately. The field in the corner regions is assumed to be negligible and taken as zero; the field in the neighbouring cladding regions is assumed to vary exponentially; the field in the core region is assumed to vary sinusoidally. Finally, two transcendental slab equations are solved simultaneously so that the propagation constant is obtained.

The weakness of Marcatili’s method is that it is not valid for waveguides operating near cut-off region when the field in the corners cannot be neglected.

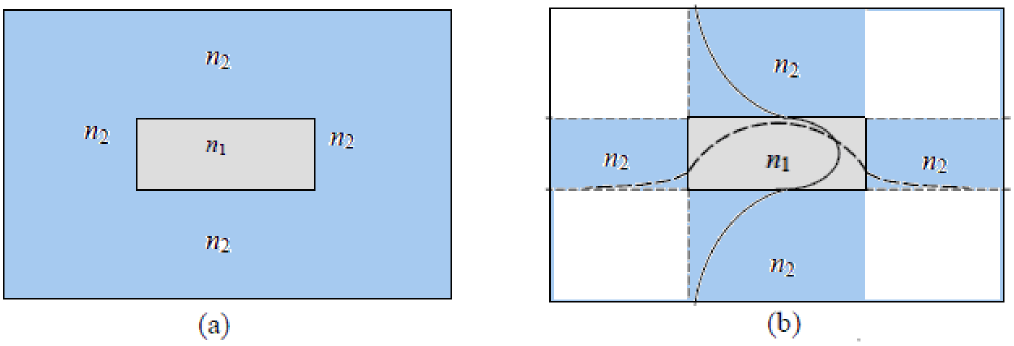

Figure 3.1: (a) the original structure, (b) the equivalent structure obtained by Marcatili’s Method

3.1.2 The Effective Index (EI) Method

Proposed by Knox and Toulios, the Effective Index (EI) Method is an improvement based on Marcatili’s Method [3]. The basic idea of this method is to analyse two-dimensional optical waveguide structure by simply repeating the slab optical waveguide analyses, and finally combining the results to get the effective refractive index of the original structure. A rib waveguide is taken as an example as shown in Fig. 3.2 to explain the effective index calculation procedure. Firstly, the original waveguide is vertically divided into three slabs as shown in Fig. 3.2(a), and then the effective indices of each single slab along the y-axis, n_{eff}^{outer} and n_{eff}^{inner}, are calculated as shown in Fig. 3.2 (b). Calculated effective indices are now combined to form an optical slab waveguide which is solved for the effective index of the rib waveguide, n_{eff}^{rib}, as shown in Fig. 3.2(c) [5].

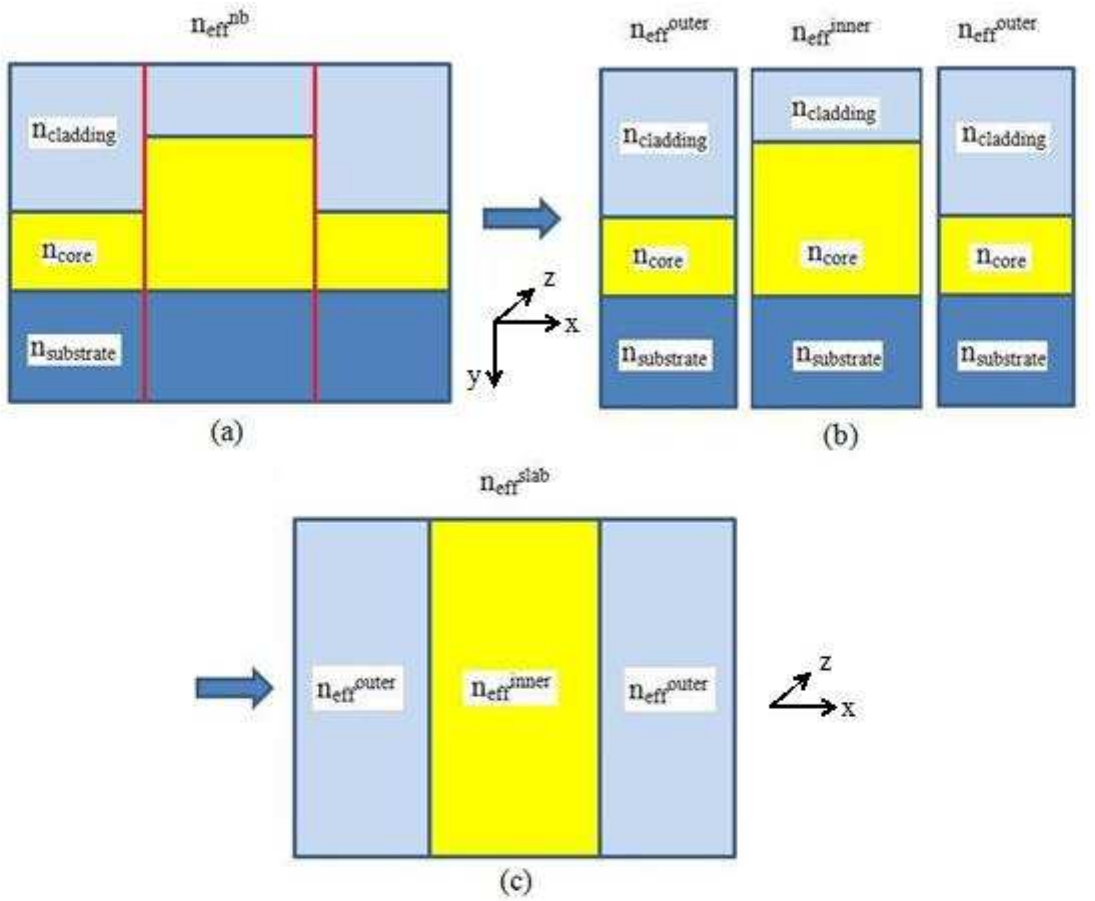

Figure 3.2: Illustration of the EI method for a rib waveguide. (a) The physical structure is vertically divided into three 2D slabs by the red lines. (b) Solving the vertical slab problem to define the slab effective indices. (c) Solving the equivalent horizontal slab problem to find the horizontal effective index.

The EI method gives a good approximation of the propagation constant of a target waveguide. Due to its simplicity and speed, this method has been used to analyse a wide variety of optical structures including graded-index channel waveguide [6]. However, it does not give good results when the structure operates near cut-off or when the outer slab of a rib guide is not a guiding slab [7].

3.1.3 The Spectral Index Method

The Spectral Index (SI) method is applied to air-clad rib waveguides that have high refractive index difference between the core and cladding, typically in ratio 3:1 [4, 8-12]. Fig. 3.3 illustrates the principle of the method. The physical semiconductor-air boundary in the transverse plane of the waveguide is replaced with a polarisation dependant evanescent boundary, upon which the field is set to zero. The effective structure illustrated in Fig. 3.3 (b) is divided into two regions, the rib region Ω_1 ($0<x<H'$) and the layered slab region Ω_2 ($x<0$), for analysing separately. The SI method proceeds by three steps: (1) finding a simple solution to the wave equation inside the rib, (2) finding a Fourier transform of the solution on the layered region below the rib, and (3) using a variational boundary condition to join the two together at the base of the rib [4].

For the cases when structures operate near cut-off, which are difficult to deal with the previously described methods, the SI method is more reliable and gives better results. Further extension of this method has allowed it to be applied to more complex structures such as rib coupler problems [13, 14], disk resonators [15], cases with loss and gain [16] and cases with leaky modes [17].

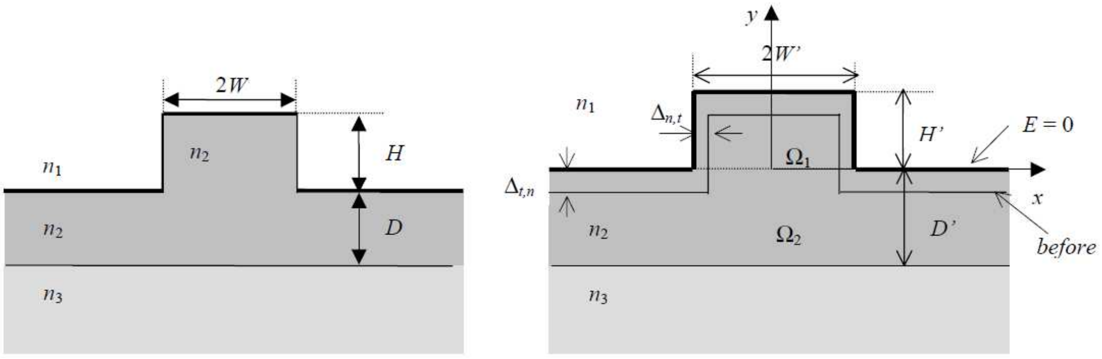

(a) (b)

Figure 3.3: (a) The dimensions and refractive index distribution of the rib waveguide’s lateral cross-section, (b) The effective structure for the SI method. The position of the rib is moved outwards to a new position on which the boundary condition becomes E = 0.

3.2 Numerical Methods

The numerical methods are versatile and robust analysis tools that are generally applicable to a wide variety of optical structures. They are often regarded as a benchmark when analysing the accuracy of other methods. Compared to the semi-analytical methods, the application of the numerical methods requires heavier computation, but little knowledge of the physical behaviour. Generally, the numerical methods fall into two classes as frequency domain methods and time domain methods. The former is utilised for the fixed frequency to obtain continuous wave (CW) response, and the latter can capture the behaviour of the target optical devices over a wide frequency range in a single simulation, but requires large computer memory and computational time.

3.2.1 The Finite Element (FE) Method

The Finite Element (FE) Method [18] is a numerical tool that discretises the modelling domain into non-overlapping polygons, which are a set of adjoining triangular or rectangular elements for 2D problems, as given in Fig. 3.4, or tetrahedral or hexahedral elements for 3D problems. Inside each element the field is expressed in terms of polynomial functions, which are usually low order and constrained by boundary conditions, and the total field over the whole modelling domain is obtained by a linear summation of the fields over each element [19, 20]. The FE method uses a variational expression formulated from Maxwell's equations and a matrix eigenvalue equation is produced mathematically.

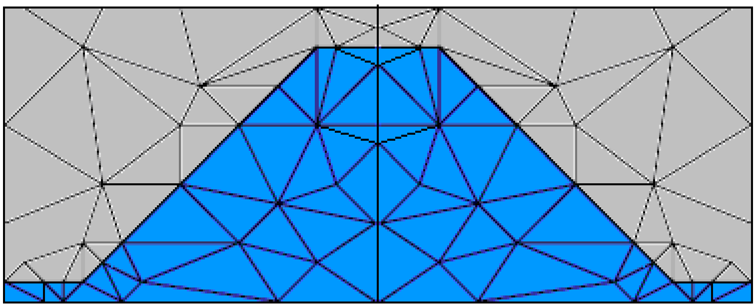

Figure 3.4: An example of FE representation of a waveguide using a triangular mesh.

FE discretisation approach allows an area with high interest to be densely meshed and the material boundaries of arbitrary structures to be faithfully modelled. However, the discretisation approach for complex system is not straightforward to implement, and if higher accuracy results are required, denser meshes are generally employed or higher order polynomials need to be solved, which leads to the increase of programming effort and computational overheads [21]. The application of the simple scalar and vectorial FE methods to commonly used optical waveguides are reported in [22, 23].

3.2.2 The Finite Difference (FD) Method

The Finite Difference (FD) Method is one of the frequently used numerical analysis techniques [19]. This method discretises the modelling domain into a rectangular mesh of points for 2D problems or cube mesh for 3D problems. The discretisation of the problem can be uniform with fixed width and height for each mesh cell, or can be non-uniform with variable size for different mesh cells, which improves the mesh accuracy by using denser mesh for the part with high interest, as shown in Fig.3.5.

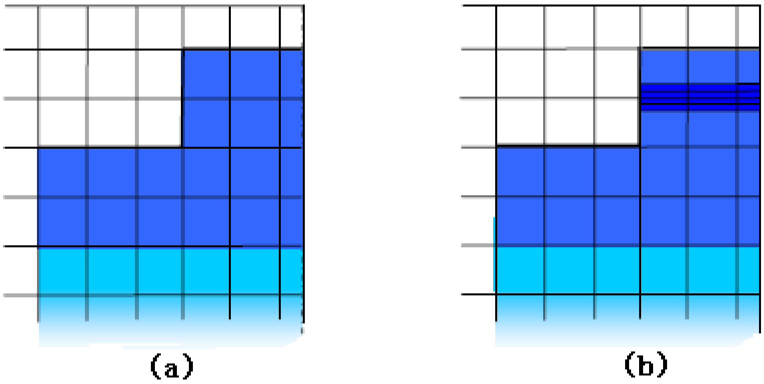

Figure 3.5: 2D Finite difference discretisation schemes: (a) Uniform orthogonal mesh (b) Non-uniform orthogonal mesh

Like most of other numerical methods, the FD method is a procedure for transforming the wave equations of a physical problem into a matrix eigenvalue equation containing a finite set of linear equations, where the modal propagation constant is the eigenvalue and the corresponding fields represent the eigenvector. In this method, the discrete electromagnetic field values are stored by the sampling points which could be chosen to either lie at the centre of each cell so that each sampling point is associated with a constant refractive index, or at the mesh points so that each sampling point is associated to up to four different refractive indices [24], as shown in Fig. 3.6.

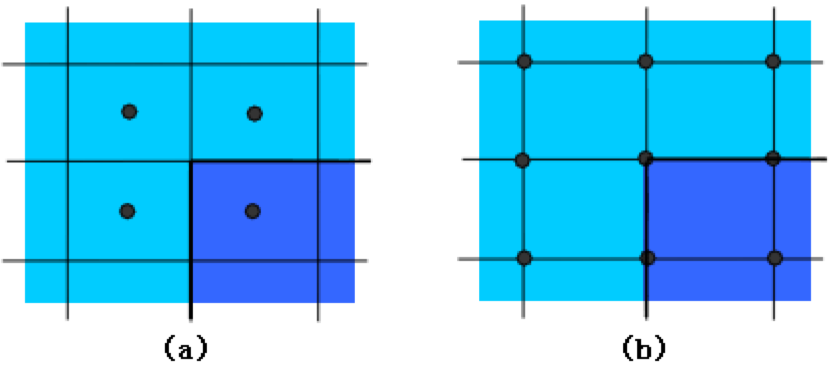

Figure 3.6: Finite difference discretisation schemes: (a) Sampling points at the centre of the cell, (b) Sampling points at the mesh points

Fig.3.7 illustrates an example of 2D FD mesh for the cross section of a rib waveguide. In the figure, a square mesh composed of lines parallel to coordinate axes is superimposed on the problem space. The indices i, j represent the coordinates of the mesh points. The distance between any two neighboring mesh points, Δx for x-direction and Δy for y-direction, is the same over the cross section. The discrete electromagnetic field values are stored by the mesh points lying at the intersection of the mesh lines. An approximate expression for the derivatives occurring in the wave equation is formed that involves the field value at sampling point (i, j), and at some of its surrounding points. Once this discretisation process has been performed for all derivatives in the wave equation, a complete set of linear matrix eigenvalue equations relating the field values at all points is formed. The solution of the resulting matrix equation can be solved by an iterative method or through the application of a sparse matrix routine [25].

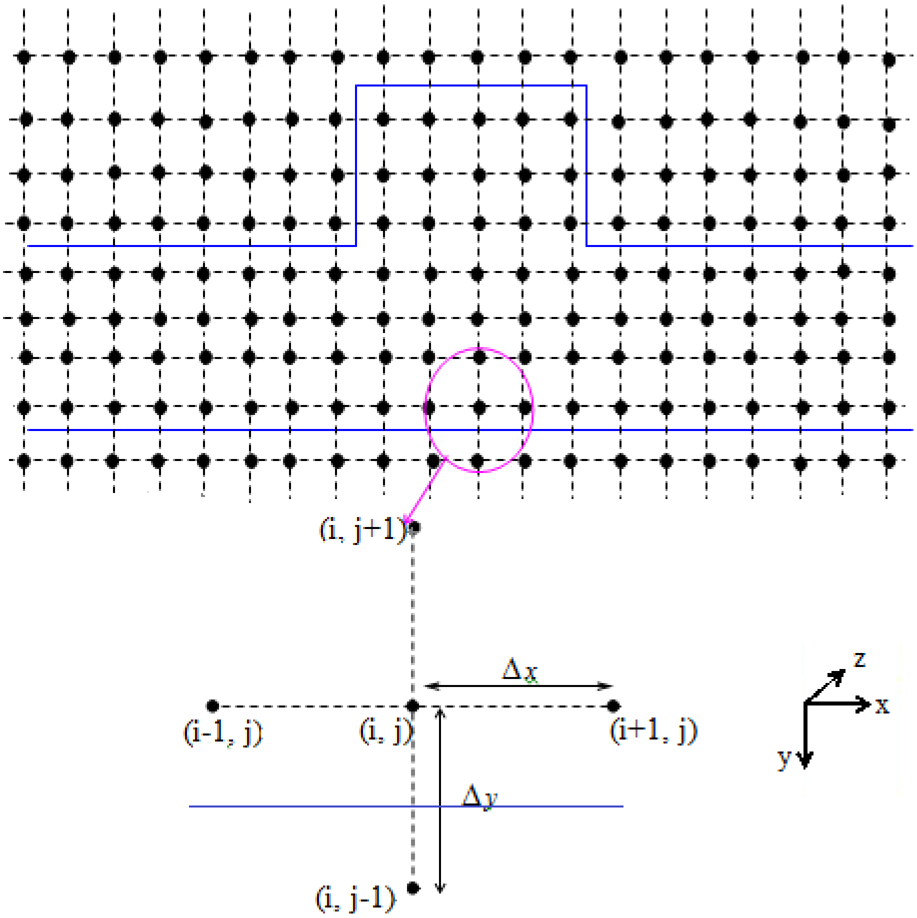

Figure 3.7: Illustration of five point finite difference scheme of the finite difference method

Generally, the finite difference discretisation of the first order and the second order derivative at any mesh point ϕ_m in Fig. 3.7 can be expressed in the following forms with the truncation errors $O(\Delta^2)$ in homogeneous region as:

$$\frac{\partial\phi_m}{\partial\alpha} = \frac{\phi_{m+1} - \phi_m}{\Delta\alpha} + O\left(\Delta^2\right) \tag{3.2.1}$$

$$\frac{\partial^2\phi_m}{\partial\alpha^2} = \frac{\phi_{m+1} - 2\phi_m + \phi_{m-1}}{\Delta\alpha^2} + O\left(\Delta^2\right) \tag{3.2.2}$$

in which α is the transverse direction x or y in orthogonal coordinate system and m is the corresponding subscript i or j. Eq. (3.2.1) and Eq. (3.2.2) can be substituted into the wave equations for the corresponding terms in order to replace the original PDEs by the equations in terms of the sampled field values in the homogeneous regions. This replacement is only valid if all the sampling points are located in the region of single material. Additional factors need to be taken into account if there is an interface of different materials between the sampling points.

The accuracy of the FD method depends on the mesh size, the assumed nature of the electromagnetic field (scalar, semi-vectorial or vectorial), and the order of the finite difference scheme used. One approach to improve the accuracy of the method is to reduce the mesh size in the regions where the field changes rapidly. Another effective approach is to apply a higher order finite difference scheme, such as generalised Douglas (GD) scheme [26].

Moreover, the successful application of the FD method also requires careful consideration of the problem domain boundaries to maintain a good accuracy. For instance, open structures must be boxed before the implementation of the method. Application of the correct boundary conditions at the edge of the simulation window can absorb the field reaching the boundaries and prevent unwanted reflection into the modelling space. Moreover, the structures lying obliquely to the orthogonal mesh require a staircase approximation, which introduces artificial corners. The staircase approximation results in a series of reflections along the staircase and affects the accuracy of the algorithm. This problem can be overcame by structure-related (SR) co-ordinate schemes which allow the physical boundaries to be modelled exactly [27].

Both the FE methods and the FD methods have their own features and should be chosen carefully to solve different practical problems. Generally, due to the great flexible feature of triangular elements, the FE method can deal with complex geometry structures and complex boundary problems such as waveguides with curved or slanting sections [7], which are not suitable for the FD method because of the possible negative effects like staircase effects and unphysical scattering.

In addition, the most attractive feature of the FD method is that it is much easier to implement and more efficient for simple geometry problems compared with the FE method [28]. Therefore, the FD method is usually taken as the basic discretisation technique of some other popular numerical techniques, such as the FDTD method [29] and the BPM method algorithm [30].

3.2.3 The Finite Difference Time Domain (FDTD) Method

FDTD is a widely used numerical method, which uses central difference approximations to the space and time partial derivatives to discretize the time dependent Maxwell's equation [31]. It solves the electric field components and magnetic field components alternately in a leapfrog pattern in time on the basis of Yee cell, as illustrated in Fig. 3.8. As a time domain method, it can cover a wide frequency range within a single simulation run, and treat dispersive and nonlinear material properties in a natural way [32].

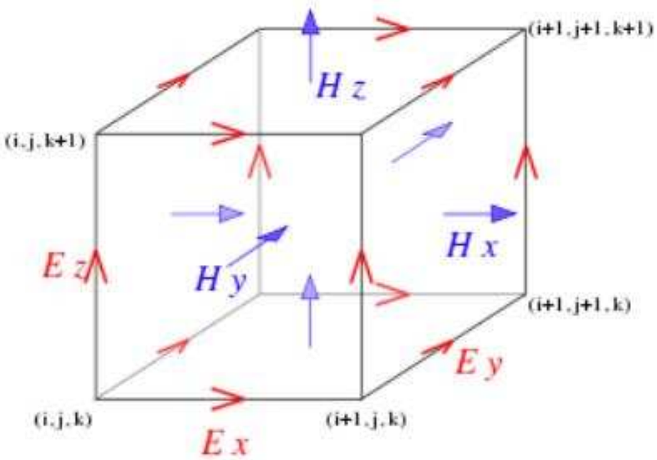

Figure 3.8: Illustration of a standard Cartesian Yee cell used for FDTD, about which electric and magnetic field vector components are distributed.

To achieve a good accuracy, the mesh size used in FDTD needs to be much smaller, typically 10-20 times, than the operating wavelength. Moreover, based on the Courant-Friedrichs-Lewy (CFL) stability condition, the time step must be less than a certain time in simulations to keep the algorithm stable. These preconditions lead to one of the major drawbacks of the FDTD method, which is the heavy computational demand on both execution time and memory. In order to reduce computational effort, various extensions for FDTD have been achieved such as the scalar FDTD [33] and the ADI FDTD, which makes it possible to use a larger time step for simulation and provides unconditional numerical stability [34].

3.3 Beam Propagation Method

A lot of practical optical waveguides have nonuniform structures such as bends, tapers and crosses in the propagation direction. One of the most commonly used methods to analyse such nonuniform structures is the Beam Propagation Method (BPM). The essence of the BPM method is the application of the slowly varying envelope approximation (SVEA), which means that the BPM method samples the envelope of the signal and not the fast varying carrier. Various kinds of BPMs have been developed including the Fast Fourier Transform BPM (FFT-BPM), the Finite Element BPM (FE-BPM), the Finite Difference Beam Propagation Method (FD-BPM) and Time Domain BPM (TD-BPM).

The original Beam Propagation Method (BPM) was first introduced into optoelectronics in 1980 by M.D.Fiet and J.A.Fleck [35, 36]. The BPM method was first developed with the Fast Fourier Transform (FFT) technique, known as FFT-BPM, for modelling weakly guiding structures. The limitations of the FFT-BPM method are: a requirement that lateral sampling is a power of 2 due to the use of FFT algorithm, small propagation step and long computational time. Moreover, it is not suitable for the application of artificial absorbing boundary condition [30, 37]. In order to avoid the application of FFT, the Finite Element Beam Propagation Method (FE-BPM) [23, 38, 39] and the Finite Difference Beam Propagation Method (FD-BPM) [38, 40, 41] have been developed.

FE-BPM uses unstructured meshes with flexible shape for the arbitrary cross-sectional boundaries. It also provides an adaptive discretisation method that can be renewed at every propagation step [42]. However, the discretisation in non-uniform elements still requires high computational cost and the quality of approximation highly affects the accuracy of the method [43]. Meanwhile, the implementation of 3D FE-BPM is less straightforward [44].

FD-BPM is another choice to replace traditional FFT-BPM for modern simulations. Compared to FFT-BPM, FD-BPM is a more efficient method as it can employ a larger propagation step to achieve comparable accuracy and the computational time is much shorter for each propagation step [30]. In fact, FD-BPM is one of the most popular and powerful tools for both 2D and 3D problems because it can discretise the structure easily and its implementation is straightforward. Generally, depending on the approximations applied, FD-BPM is divided into paraxial FD-BPM and Wide-Angle (WA) FD-BPM [45, 46]. Paraxial approximation assumes that the incident wave is inclined by a small angle with respect to the propagation axis, whilst WA-FD-BPM attempts to overcome this restriction.

WA-BPM uses the Padé approximation [45] to derive the PDE to be a tri-diagonal matrix problem, which can be solved by the Thomas algorithm [45]. For complex structures, higher order Padé approximation operators are applied to improve the accuracy of the scheme. In this situation, larger band matrix needs to be considered and computational cost increases. To resolve this problem, multistep method is introduced to split each propagation step to several sub-steps and repeat utilising simple tri-diagonal matrix solver for every sub-step [46]. The less intensive matrix solver results in an algorithm much faster than that of a large band matrix created by Padé approximation only.

An important significance of the WA scheme is that the application scope of FD-BPM is widely extended. The WA scheme provides a possibility for FD-BPM to deal with the propagation in both forward direction and backward direction, even to deal with multiple reflections existing. This powerful scheme is known as Bi-directional BPM

[47, 48].

TD-BPM is another choice for the analysis of the reflection problems [49]. It applies the SVEA in the propagation with respect to time, not to space [50]. The whole spatial space needs to be analysed and evaluated at each time propagation step. Compared to frequency domain methods, it introduces an additional time dimension to the modelling and increases computational demand. TD-BPM will not be considered during the work of this thesis.

To successfully employ FD-BPM, the edge of the simulation range needs to be considered carefully and a suitable boundary condition should be chosen for a specific problem. The commonly used boundary conditions include Absorbing Boundary Condition (ABC) [51], Transparent Boundary Condition [52], Perfectly Matched Layer (PML) boundary condition [53, 54] and Periodic Boundary Condition (PBC). An introduction of these common boundary conditions will be given in section 3.4.

In the following sections, SVEA approximation, discretisation schemes in the propagation direction and a paraxial FD-BPM are derived, followed by a description of different boundary conditions. The scalar case and TM-polarized case are considered, and the situation for TE-polarized case can be derived similarly.

3.3.1 SVEA Approximation

The slowly varying envelope approximation (SVEA) can be applied when the envelope of a forward-travelling wave varies slowly along direction of propagation. This requires the spectrum of the signal to be narrow-banded, hence it is also known as the narrow-band approximation, In longitudinally invariant structures, the time-harmonic field can be expressed as a product of the slowly varying envelope ψ and rapid oscillatory phase term $e^{-j\beta_0 z}$ as:

$$E(x, y, z) = \psi(x, y)e^{-j\beta_0 z}, \qquad (3.3.1)$$

where $\beta_0 = k_0 n_0$ is the propagation constant and n_0 is the reference refractive index, field can be either for x or y directed. For example for the x-directed field, $E_x(x, y, z) = \psi(x, y)e^{-j\beta_0 z}$. Replacing Eq. (3.3.1) in Eq. (2.3.25) and Eq. Eq. (2.3.26) leads to the semi-vectorial wave equations for x-directed component as:

$$2j\beta_0 \frac{\partial \psi}{\partial z} = \frac{\partial}{\partial x}\left[\frac{1}{n_r^2}\frac{\partial}{\partial x}(n_r^2\psi)\right] + \frac{\partial^2 \psi}{\partial y^2} + \frac{\partial^2 \psi}{\partial z^2} + (k_0^2 n_r^2 - \beta_0^2)\psi\,. \qquad (3.3.2)$$

If the envelope ψ varies slowly with respect to the propagation z-direction, the second order derivative along z-direction can be neglected:

$$2j\beta_0\left|\frac{\partial \psi}{\partial z}\right| \gg \left|\frac{\partial^2 \psi}{\partial z^2}\right| \approx 0\,, \qquad (3.3.3)$$

resulting in the paraxial approximation as:

$$2j\beta_0 \frac{\partial \psi}{\partial z} = \frac{\partial}{\partial x}\left[\frac{1}{n_r^2}\frac{\partial}{\partial x}(n_r^2\psi)\right] + \frac{\partial^2 \psi}{\partial y^2} + (k_0^2 n_r^2 - \beta_0^2)\psi \qquad (3.3.4)$$

If the structure is a weakly guiding structure with low refractive index contrast and the propagating field can be regarded as scalar wave, the equation can be further simplified by neglecting term $\frac{\partial}{\partial x}\left[\frac{1}{n_r^2}\frac{\partial}{\partial x}(n_r^2\psi)\right]$ and results in:

$$2j\beta_0\frac{\partial\psi}{\partial z}=\frac{\partial^2\psi}{\partial x^2}+\frac{\partial^2\psi}{\partial y^2}+(k_0^2n_r^2-\beta_0^2)\psi \qquad (3.3.5)$$

which is much easier to implement.

3.3.2 Discretisation Schemes in the Propagation Direction

The FD-BPM finds the field intensity iteratively in the propagation direction based on the field from the previous slice as shown in Fig. 3.9 (a). The wave equation (3.3.5) that needs to be solved in optoelectronics is essentially partial differential equation (PDE), which needs to be discretised for the purpose of numerical implementation. Therefore, to find an effective and stable algorithm for discretisation is vital for any numerical method, including the FD-BPM. This section will discuss various commonly utilised FD schemes in terms of matrix solver requirement and stability.

Eq.(3.3.5) and Eq.(3.3.4) can be rewritten in a more compact way as:

$$2j\beta_0\frac{\partial\psi}{\partial z}=L\psi \qquad (3.3.6)$$

where L is the operator. $L=\frac{\partial^2}{\partial x^2}+\frac{\partial^2}{\partial y^2}+k_0^2n_r^2-\beta_0^2$ for 3D scalar case or

$\mathrm{L}=\frac{\partial^2}{\partial x^2}+k_0^2 n_r^2-\beta_0^2$ for 2D scalar case, and $\mathrm{L}=\frac{\partial}{\partial x}\left[\frac{1}{n_r^2}\frac{\partial}{\partial x}(n_r^2)\right]+\frac{\partial^2}{\partial y^2}+k_0^2 n_r^2-\beta_0^2$ for 3D TM-polarized case and $\mathrm{L}=\frac{\partial}{\partial x}\left[\frac{1}{n_r^2}\frac{\partial}{\partial x}(n_r^2)\right]+k_0^2 n_r^2-\beta_0^2$ for 2D TM-polarized case. If the propagating step is set as *Δz*, the left hand side of Eq. (3.3.6) can be replaced through the first order FD discretisation. If a stability factor *α*, which determines the weighting of the halfway field point along the propagation direction, is introduced to the right hand side of Eq.(3.3.6), a general explicit-implicit scheme is given as:

$$2\,j\beta_0\frac{\psi_{(x,z+\Delta z)}-\psi_{(x,z)}}{\Delta z}=\alpha \mathrm{L}\psi_{(x,z+\Delta z)}+(1-\alpha)\mathrm{L}\psi_{(x,z)}\,, \tag{3.3.7}$$

in which the value of *α* is within the range $0\le\alpha\le1$.

Here three particular choices for parameter *α* are considered. When $\alpha=1$, Eq.(3.3.7) becomes:

$$2\,j\beta_0\frac{\psi_{(x,z+\Delta z)}-\psi_{(x,z)}}{\Delta z}=\mathrm{L}\psi_{(x,z+\Delta z)} \tag{3.3.8}$$

or

$$(2\,j\beta_0-\Delta z\cdot \mathrm{L})\cdot\psi_{(x,z+\Delta z)}=2\,j\beta_0\cdot\psi_{(x,z)}\,, \tag{3.3.9}$$

and corresponds to an implicit or backward-difference scheme. L is approximated in the unknown domain as shown in Fig. 3.9 (b). Operator L consists of second order derivatives of the transverse operator, which results in a tri-diagonal matrix for a 2D structure. Thomas algorithm [55] can be used to solve the matrix equation efficiently. However for a 3D structure, more computational intensive method has to be used for solving a large, but sparse matrix.

When $\alpha = 0$, Eq. (3.3.7) becomes

$$2\,\mathrm{j}\beta_0 \frac{\psi_{(x,z+\Delta z)} - \psi_{(x,z)}}{\Delta z} = \mathrm{L}\psi_{(x,z)} \tag{3.3.10}$$

or

$$2\,\mathrm{j}\beta_0 \cdot \psi_{(x,z+\Delta z)} = (2\,\mathrm{j}\beta_0 + \Delta z \cdot \mathrm{L}) \cdot \psi_{(x,z)}, \tag{3.3.11}$$

which results in an explicit or forward-difference scheme [56] as illustrated in Fig.3.9(c). The operator L is taken on the current propagation step where the field values are known and the value in the next step can be directly calculated without using matrix solver [57]. Explicit scheme is very suitable for parallel computing. The calculation processes can be divided into numerous threads for different processor nodes to solve the unknown values independently.

When $\alpha = 0.5$, the points of calculation are set exactly at half-way between sampling points along propagation direction and a central difference based scheme, named the Crank-Nicholson (CN) scheme is obtained. Eq. (3.3.7) becomes:

$$2\,\mathrm{j}\beta_0 \frac{\psi_{(x,z+\Delta z)} - \psi_{(x,z)}}{\Delta z} = \frac{\mathrm{L}}{2}(\psi_{(x,z+\Delta z)} + \psi_{(x,z)})\,. \tag{3.3.12}$$

or

$$(2\,\mathrm{j}\beta_0 - \frac{1}{2} \cdot \Delta z \cdot \mathrm{L}) \cdot \psi_{(x,z+\Delta z)} = (2\,\mathrm{j}\beta_0 + \frac{1}{2} \cdot \Delta z \cdot \mathrm{L}) \cdot \psi_{(x,z)} \tag{3.3.13}$$

Fig. 3.9 (d) shows the CN scheme. Similarly as in the implicit scheme, matrix solver is required for solving Eq.(3.3.12) because the transverse operator is discretised between the current slice and the next slice, and the solution depends on the transverse neighboring nodes on both slices.

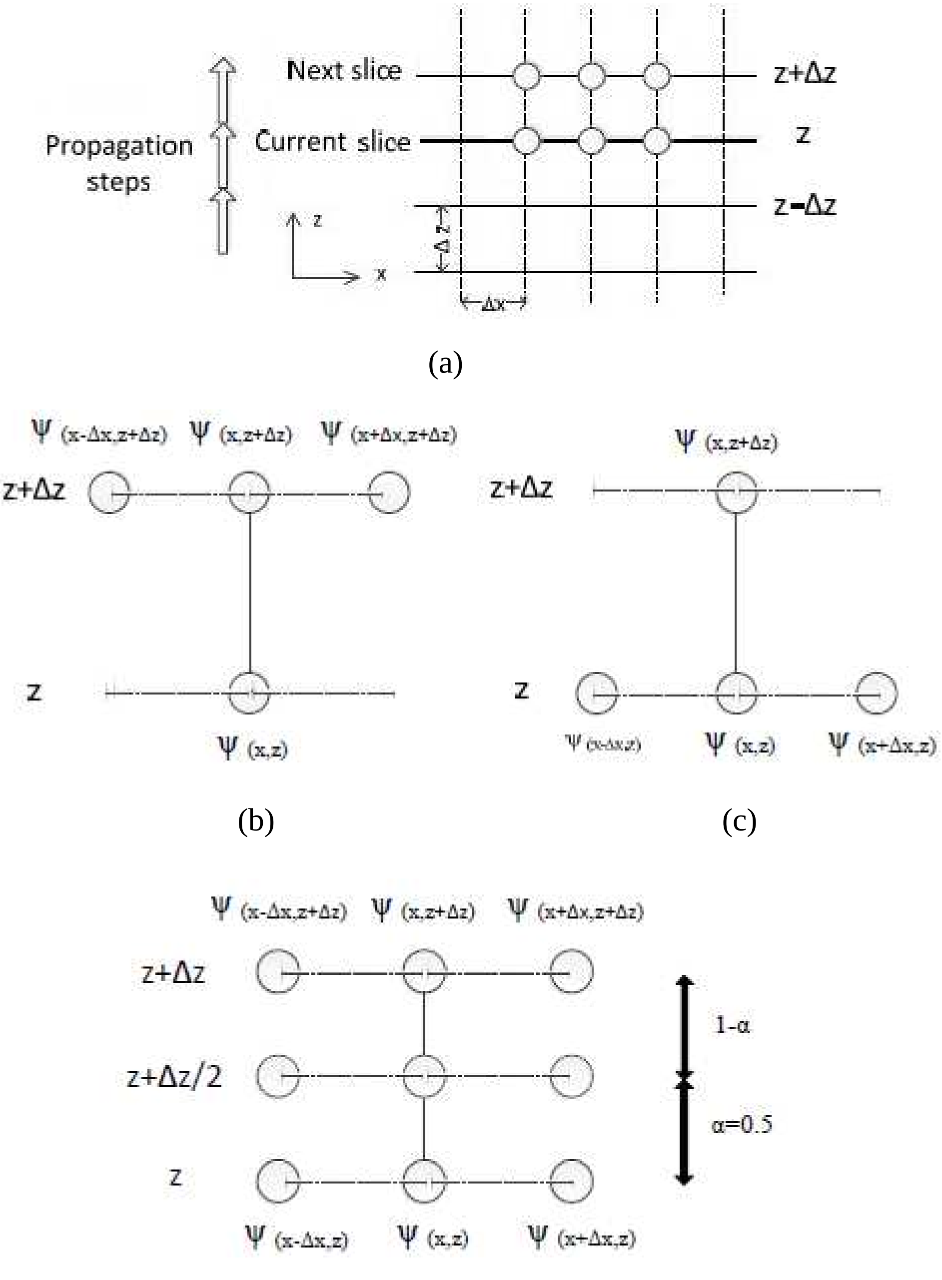

(a)

(b)

(c)

(d)

Figure 3.9: Illustration of (a) the FD-BPM arrangement in longitudinal direction, (b) Implicit scheme, (c) Explicit scheme, (d) Crank-Nicholson scheme.

In order to investigate the stability of different discretisation schemes mentioned above, the field gain per propagation step is introduced and defined as:

$$g = \frac{\psi_{(x,z+\Delta z)}}{\psi_{(x,z)}}. \qquad (3.3.14)$$

If $|g| > 1$, the fields in each propagation step continuously grow and accumulate step by step and non-physical power gain is generated. In this situation, the algorithm is unstable and the accuracy of the scheme cannot be trusted. If $|g| \le 1$, the fields decay with the propagation and the algorithm is stable but lossy. The ideal situation is when $|g| = 1$, which means that the scheme is not only stable but also non-dissipative [58].

Eq.(3.3.7) can be rearranged as:

$$\left(1 + \frac{j\Delta z \alpha L}{2\beta_0}\right)\psi_{(x,z+\Delta z)} = \left(1 - \frac{j\Delta z(1-\alpha)L}{2\beta_0}\right)\psi_{(x,z)}. \qquad (3.3.15)$$

If a 2D homogenous structure is considered, then the discretisation of the second order derivative in the transverse direction is expressed as:

$$\frac{\psi_{(x+\Delta x,z)} - 2\psi_{(x,z)} + \psi_{(x-\Delta x,z)}}{\Delta x^2} = \frac{\psi_{(x,z)}e^{-j(k_0^2 n_r^2 - \beta_0^2)\Delta x} - 2\psi_{(x,z)} + \psi_{(x,z)}e^{j(k_0^2 n_r^2 - \beta_0^2)\Delta x}}{\Delta x^2}. \qquad (3.3.16)$$

Based on Euler's formula, the phase term in Eq. (3.3.16) can be expressed as:

$$e^{j(k_0^2 n_r^2 - \beta_0^2)\Delta x} = \cos[(k_0^2 n_r^2 - \beta_0^2)\Delta x] + j\sin[(k_0^2 n_r^2 - \beta_0^2)\Delta x], \qquad (3.3.17)$$

$$e^{-j(k_0^2 n_r^2 - \beta_0^2)\Delta x} = \cos[(k_0^2 n_r^2 - \beta_0^2)\Delta x] - j\sin[(k_0^2 n_r^2 - \beta_0^2)\Delta x]. \qquad (3.3.18)$$

Therefore, the right hand side of Eq. (3.3.16) can be rewritten as:

$$\frac{\psi_{(x,z)}e^{-j(k_0^2n_r^2-\beta_0^2)\Delta x}-2\psi_{(x,z)}+\psi_{(x,z)}e^{j(k_0^2n_r^2-\beta_0^2)\Delta x}}{\Delta x^2}=2\psi_{(x,z)}\frac{\cos[(k_0^2n_r^2-\beta_0^2)\Delta x]-1}{\Delta x^2}. \tag{3.3.19}$$

Using this relationship to replace the corresponding term in operator L in Eq. (3.3.15) leads the gain to be [58]:

$$g=\frac{1-j\dfrac{\Delta z(1-\alpha)\left(2\dfrac{\cos[(k_0^2n_r^2-\beta_0^2)\Delta x]-1}{\Delta x^2}+k_0^2n_r^2-\beta_0^2\right)}{2\beta_0}}{1+j\dfrac{\Delta z\alpha\left(2\dfrac{\cos[(k_0^2n_r^2-\beta_0^2)\Delta x]-1}{\Delta x^2}+k_0^2n_r^2-\beta_0^2\right)}{2\beta_0}} \tag{3.3.20}$$

If $\alpha=0$, the gain for explicit scheme becomes:

$$g=1-j\frac{\Delta z\left(2\dfrac{\cos[(k_0^2n_r^2-\beta_0^2)\Delta x]-1}{\Delta x^2}+k_0^2n_r^2-\beta_0^2\right)}{2\beta_0}, \tag{3.3.21}$$

and the absolute value of gain $|g|>1$, resulting in explicit scheme being an unstable algorithm.

If $\alpha=1$, the gain for implicit scheme is obtained as:

$$g=\frac{1}{1+j\dfrac{\Delta z\left(2\dfrac{\cos[(k_0^2n_r^2-\beta_0^2)\Delta x]-1}{\Delta x^2}+k_0^2n_r^2-\beta_0^2\right)}{2\beta_0}}, \tag{3.3.22}$$

and the absolute value of gain $|g|<1$, resulting in implicit scheme being stable, but lossy. The non-physical power loss will limit its applications where prediction of power is essential.

If $\alpha = 0.5$, the gain for CN scheme is:

$$g = \frac{1 - j\dfrac{\Delta z\left(2\dfrac{\cos[(k_0^2 n_r^2 - \beta_0^2)\Delta x] - 1}{\Delta x^2} + k_0^2 n_r^2 - \beta_0^2\right)}{4\beta_0}}{1 + j\dfrac{\Delta z\left(2\dfrac{\cos[(k_0^2 n_r^2 - \beta_0^2)\Delta x] - 1}{\Delta x^2} + k_0^2 n_r^2 - \beta_0^2\right)}{4\beta_0}}, \qquad (3.3.23)$$

and the absolute value of gain $|g| = 1$, resulting in unconditionally stable and non-dissipative algorithm. CN scheme will be considered throughout in this thesis.

3.3.3 Paraxial FD-BPM

The 2D CN FD-BPM equation is derived from Eq. (3.3.13) and can be written as:

$$A_{m+1}\psi_{(p+1,m+1)} + B_{m+1}\psi_{(p-1,m+1)} + C_{m+1}\psi_{(p,m+1)} = A_m\psi_{(p+1,m)} + B_m\psi_{(p-1,m)} + C_m\psi_{(p,m)} \quad (3.3.24)$$

where subscripts p, and m denote the node position of the “current node” in transverse x and propagation direction z respectively. A, B and C are different coefficients according to the types of field approximation. For scalar case, coefficients are:

$$A_{m+1} = B_{m+1} = -\frac{1}{2\Delta x^2}$$

$$C_{m+1} = \frac{2j\beta_0}{\Delta z} + \frac{1}{\Delta x^2} - \frac{k_0^2 n_r^2 - \beta_0^2}{2}$$

$$A_m = B_m = \frac{1}{2\Delta x^2}$$

$$C_m = \frac{2j\beta_0}{\Delta z} - \frac{1}{\Delta x^2} + \frac{k_0^2 n_r^2 - \beta_0^2}{2},$$

For TM mode, the coefficients are:

$$A_{m+1} = -\frac{1}{\Delta x^2}\frac{n^2_{(p+1,q,m+1)}}{n^2_{(p+1,q,m+1)} + n^2_{(p,q,m+1)}}$$

$$A_{m} = \frac{1}{\Delta x^2}\frac{n^2_{(p+1,q,m)}}{n^2_{(p+1,q,m)} + n^2_{(p,q,m)}}$$

$$B_{m+1} = -\frac{1}{\Delta x^2}\frac{n^2_{(p-1,q,m+1)}}{n^2_{(p-1,q,m+1)} + n^2_{(p,q,m+1)}}$$

$$B_{m} = \frac{1}{\Delta x^2}\frac{n^2_{(p-1,q,m)}}{n^2_{(p-1,q,m)} + n^2_{(p,q,m)}}$$

$$C_{m+1} = \frac{2\,j\beta_0}{\Delta z} + \frac{1}{\Delta x^2}\left(\frac{n^2_{(p,q,m+1)}}{n^2_{(p+1,q,m+1)} + n^2_{(p,q,m+1)}} + \frac{n^2_{(p,q,m+1)}}{n^2_{(p-1,q,m+1)} + n^2_{(p,q,m+1)}}\right) - \frac{k_0^2 n_r^2 - \beta_0^2}{2}$$

$$C_{m} = \frac{2\,j\beta_0}{\Delta z} - \frac{1}{\Delta x^2}\left(\frac{n^2_{(p,q,m)}}{n^2_{(p+1,q,m)} + n^2_{(p,q,m)}} + \frac{n^2_{(p,q,m)}}{n^2_{(p-1,q,m)} + n^2_{(p,q,m)}}\right) + \frac{k_0^2 n_r^2 - \beta_0^2}{2}$$

Eq. (3.3.24) can be expressed by a three-band sparse diagonal matrix system respectively for further processing. The coefficients on the left hand side of the equations can populate a coefficient matrix $[M_{m+1}]$. The field values on the next slice, from $\psi_{(1,m+1)}$ to $\psi_{(p,m+1)}$, where p is the number of nodes sampled in the x direction, can be placed as a column vector $[\psi_{m+1}]$. The coefficient matrix and the column vector compose the left hand side of the matrix system. Likewise, the coefficients and the field values of current slice compose the right hand side of the matrix system. Because the field values and the coefficients of the current slice are all known for calculating the field values of next slice, the terms on the right hand side of the matrix system can be consolidated into a column vector $[[M_m]\cdot[\psi_m]]$. The matrix equation is in the form of $[M_{m+1}]\cdot[\psi_{m+1}] = [[M_m]\cdot[\psi_m]]$, and the relevant sparse diagonal matrix system is shown as follows:

$$\begin{pmatrix}
C_{1,m+1} & A_{1,m+1} & & & & & & & \\
B_{2,m+1} & C_{2,m+1} & A_{2,m+1} & & & & & & \\
 & \cdot & \cdot & \cdot & & & & & \\
 & & \cdot & \cdot & \cdot & & & & \\
 & & & B_{p,m+1} & C_{p,m+1} & A_{p,m+1} & & & \\
 & & & & \cdot & \cdot & \cdot & & \\
 & & & & & \cdot & \cdot & \cdot & \\
 & & & & & & B_{P-1,m+1} & C_{P-1,m+1} & A_{P-1,m+1} \\
 & & & & & & & B_{P,m+1} & C_{P,m+1}
\end{pmatrix} \times \begin{pmatrix}
\psi_{(1,m+1)} \\ \psi_{(2,m+1)} \\ \\ \\ \psi_{(p,m+1)} \\ \\ \\ \psi_{(P-1,m+1)} \\ \psi_{(P,m+1)}
\end{pmatrix}$$

$$= \begin{pmatrix}
C_{1,m} & A_{1,m} & & & & & & & \\
B_{2,m} & C_{2,m} & A_{2,m} & & & & & & \\
 & \cdot & \cdot & \cdot & & & & & \\
 & & \cdot & \cdot & \cdot & & & & \\
 & & & B_{p,m} & C_{p,m} & A_{p,m} & & & \\
 & & & & \cdot & \cdot & \cdot & & \\
 & & & & & \cdot & \cdot & \cdot & \\
 & & & & & & B_{P-1,m} & C_{P-1,m} & A_{P-1,m} \\
 & & & & & & & B_{P,m} & C_{P,m}
\end{pmatrix} \times \begin{pmatrix}
\psi_{(1,m)} \\ \psi_{(2,m)} \\ \\ \\ \psi_{(p,m)} \\ \\ \\ \psi_{(P-1,m)} \\ \psi_{(P,m)}
\end{pmatrix} = \begin{pmatrix}
R_{(1,m)} \\ R_{(2,m)} \\ \\ \\ R_{(p,m)} \\ \\ \\ R_{(P-1,m)} \\ R_{(P,m)}
\end{pmatrix} \tag{3.3.25}$$

It is clearly seen that the large but sparse matrix on the left hand side of the matrix systems in Eq. (3.3.25) has tri-diagonal property and its size is $P \times P$. This kind of sparse matrix can be easily reduced to be a memory efficient form with the size of $3 \times P$, which results in the whole equation to be simplified as:

$$\begin{pmatrix} C_{1,m+1} & A_{1,m+1} & 0 \\ B_{2,m+1} & C_{2,m+1} & A_{2,m+1} \\ \cdot & \cdot & \cdot \\ \cdot & \cdot & \cdot \\ B_{p,m+1} & C_{p,m+1} & A_{p,m+1} \\ \cdot & \cdot & \cdot \\ \cdot & \cdot & \cdot \\ B_{P-1,m+1} & C_{P-1,m+1} & A_{P-1,m+1} \\ 0 & B_{P,m+1} & C_{P,m+1} \end{pmatrix} \times \begin{pmatrix} \psi_{(1,m+1)} \\ \psi_{(2,m+1)} \\ \cdot \\ \cdot \\ \psi_{(p,m+1)} \\ \cdot \\ \cdot \\ \psi_{(P-1,m+1)} \\ \psi_{(P,m+1)} \end{pmatrix} = \begin{pmatrix} R_{(1,m)} \\ R_{(2,m)} \\ \cdot \\ \cdot \\ R_{(p,m)} \\ \cdot \\ \cdot \\ R_{(P-1,m)} \\ R_{(P,m)} \end{pmatrix} \qquad (3.3.26)$$

and solved by Thomas algorithm efficiently [59].

The 3D CN FD-BPM can be derived in the same way as:

$$\begin{aligned} &A_{m+1}\psi_{(p+1,q,m+1)} + B_{m+1}\psi_{(p-1,q,m+1)} + C_{m+1}\psi_{(p,q,m+1)} + D_{m+1}\psi_{(p,q+1,m+1)} + E_{m+1}\psi_{(p,q-1,m+1)} \\ &= A_m\psi_{(p+1,q,m)} + B_m\psi_{(p-1,q,m)} + C_m\psi_{(p,q,m)} + D_m\psi_{(p,q+1,m)} + E_m\psi_{(p,q-1,m)} \end{aligned} \qquad (3.3.27)$$

where subscripts p, q, and m denote the node position of the “current node” in transverse x, transverse y and propagation direction z respectively. For scalar case, the coefficients A, B, C, D and E are:

$$\begin{aligned} A_{m+1} &= B_{m+1} = -\frac{1}{2\Delta x^2} \\ C_{m+1} &= \frac{2j\beta_0}{\Delta z} + \frac{1}{\Delta x^2} + \frac{1}{\Delta y^2} - \frac{k_0^2 n_r^2 - \beta_0^2}{2} \\ D_{m+1} &= E_{m+1} = -\frac{1}{2\Delta y^2} \end{aligned}$$

$$\begin{aligned} A_m &= B_m = \frac{1}{2\Delta x^2} \\ C_m &= \frac{2j\beta_0}{\Delta z} - \frac{1}{\Delta x^2} - \frac{1}{\Delta y^2} + \frac{k_0^2 n_r^2 - \beta_0^2}{2} \\ D_m &= E_m = \frac{1}{2\Delta y^2} \end{aligned}$$

For TM mode, the coefficients are:

$$A_{m+1} = -\frac{1}{\Delta x^2}\frac{n^2_{(p+1,q,m+1)}}{n^2_{(p+1,q,m+1)} + n^2_{(p,q,m+1)}}$$

$$A_m = \frac{1}{\Delta x^2}\frac{n^2_{(p+1,q,m)}}{n^2_{(p+1,q,m)} + n^2_{(p,q,m)}}$$

$$B_{m+1} = -\frac{1}{\Delta x^2}\frac{n^2_{(p-1,q,m+1)}}{n^2_{(p-1,q,m+1)} + n^2_{(p,q,m+1)}}$$

$$B_m = \frac{1}{\Delta x^2}\frac{n^2_{(p-1,q,m)}}{n^2_{(p-1,q,m)} + n^2_{(p,q,m)}}$$

$$D_{m+1} = E_{m+1} = -D_m = -E_m = -\frac{1}{2\Delta y^2}$$

$$C_{m+1} = \frac{2j\beta_0}{\Delta z} + \frac{1}{\Delta x^2}\left(\frac{n^2_{(p,q,m+1)}}{n^2_{(p+1,q,m+1)} + n^2_{(p,q,m+1)}} + \frac{n^2_{(p,q,m+1)}}{n^2_{(p-1,q,m+1)} + n^2_{(p,q,m+1)}}\right) + \frac{1}{\Delta y^2} - \frac{k_0^2 n_r^2 - \beta_0^2}{2}$$

$$C_m = \frac{2j\beta_0}{\Delta z} - \frac{1}{\Delta x^2}\left(\frac{n^2_{(p,q,m)}}{n^2_{(p+1,q,m)} + n^2_{(p,q,m)}} + \frac{n^2_{(p,q,m)}}{n^2_{(p-1,q,m)} + n^2_{(p,q,m)}}\right) - \frac{1}{\Delta y^2} + \frac{k_0^2 n_r^2 - \beta_0^2}{2}$$

Eq. (3.3.27) could be expressed by a five-band sparse matrix system. The matrix system for 3D FD-BPM is not a simple tri-diagonal matrix system and cannot be solved by Thomas algorithm. Therefore, a popular scheme, the Alternating-Direction Implicit (ADI) method [60, 61], is developed to deal with the problem. The ADI method splits each propagation step in two halves, one for x-derivative taken implicitly and the other one for y-derivative taken implicitly, and then handles the derivative for x direction and y direction alternately.

If the 3D scalar FD-BPM equation in Eq. (3.3.5) is to be solved by the ADI scheme, it can be divided into two associated equations with the propagation step $\frac{\Delta z}{2}$ [60]. The first equation calculates x-derivative by full implicit scheme and calculates y-derivative by full explicit scheme, and the second equation is reversed. Then the original equation can be split as:

$$
\begin{aligned}
2\,j\beta_0 \frac{\psi_{(x,y,z+\Delta z/2)} - \psi_{(x,y,z)}}{\Delta z/2} &= \frac{\partial^2}{\partial x^2}\psi_{(x,y,z+\Delta z/2)} + \frac{\partial^2}{\partial y^2}\psi_{(x,y,z)} \\
&\quad + (k_0^2 n_r^2 - \beta_0^2)\frac{\psi_{(x,y,z+\Delta z/2)} + \psi_{(x,y,z)}}{2},
\end{aligned}
\tag{3.3.28}
$$

$$
\begin{aligned}
2\,j\beta_0 \frac{\psi_{(x,y,z+\Delta z)} - \psi_{(x,y,z+\Delta z/2)}}{\Delta z/2} &= \frac{\partial^2}{\partial x^2}\psi_{(x,y,z+\Delta z/2)} + \frac{\partial^2}{\partial y^2}\psi_{(x,y,z+\Delta z)} \\
&\quad + (k_0^2 n_r^2 - \beta_0^2)\frac{\psi_{(x,y,z+\Delta z)} + \psi_{(x,y,z+\Delta z/2)}}{2}.
\end{aligned}
\tag{3.3.29}
$$

These two equations can be expanded as:

$$
\begin{aligned}
\frac{4\,j\beta_0}{\Delta z}(\psi_{(x,y,z+\Delta z/2)} - \psi_{(x,y,z)}) &= \frac{\psi_{(x+1,y,z+\Delta z/2)} - 2\psi_{(x,y,z+\Delta z/2)} + \psi_{(x-1,y,z+\Delta z/2)}}{\Delta x^2} \\
&\quad + \frac{\psi_{(x,y+1,z)} - 2\psi_{(x,y,z)} + \psi_{(x,y-1,z)}}{\Delta y^2} + \frac{k_0^2 n_r^2 - \beta_0^2}{2}\psi_{(x,y,z+\Delta z/2)} + \frac{k_0^2 n_r^2 - \beta_0^2}{2}\psi_{(x,y,z)},
\end{aligned}
\tag{3.3.30}
$$

$$
\begin{aligned}
\frac{4\,j\beta_0}{\Delta z}(\psi_{(x,y,z+\Delta z)} - \psi_{(x,y,z+\Delta z/2)}) &= \frac{\psi_{(x+1,y,z+\Delta z/2)} - 2\psi_{(x,y,z+\Delta z/2)} + \psi_{(x-1,y,z+\Delta z/2)}}{\Delta x^2} \\
&\quad + \frac{\psi_{(x,y+1,z+\Delta z)} - 2\psi_{(x,y,z+\Delta z)} + \psi_{(x,y-1,z+\Delta z)}}{\Delta y^2} + \frac{k_0^2 n_r^2 - \beta_0^2}{2}\psi_{(x,y,z+\Delta z)} + \frac{k_0^2 n_r^2 - \beta_0^2}{2}\psi_{(x,y,z+\Delta z/2)}
\end{aligned}
\tag{3.3.31}
$$

To rearrange these two equations separately as Eq. (3.3.25) and combine the coefficients of the same field terms leads to equations as:

$$
\begin{aligned}
&Al_{m+1/2}\psi_{(p+1,q,m+1/2)} + Bl_{m+1/2}\psi_{(p-1,q,m+1/2)} + Cl_{m+1/2}\psi_{(p,q,m+1/2)} \\
&= Ar_m\psi_{(p,q+1,m)} + Br_m\psi_{(p,q-1,m)} + Cr_m\psi_{(p,q,m)},
\end{aligned}
\tag{3.3.32}
$$

in which

$$\begin{aligned}
\mathrm{Al}_{m+1/2} &= \mathrm{Bl}_{m+1/2} = -\frac{1}{\Delta x^2} \\
\mathrm{Cl}_{m+1/2} &= \frac{4j\beta_0}{\Delta z} + \frac{2}{\Delta x^2} - \frac{k_0^2 n_r^2 - \beta_0^2}{2} \\
\mathrm{Ar}_m &= \mathrm{Br}_m = \frac{1}{\Delta y^2} \\
\mathrm{Cr}_m &= \frac{4j\beta_0}{\Delta z} - \frac{2}{\Delta y^2} + \frac{k_0^2 n_r^2 - \beta_0^2}{2}
\end{aligned},$$

and

$$\begin{aligned}
&\mathrm{Al}_{m+1}\psi_{(p,q+1,m+1)} + \mathrm{Bl}_{m+1}\psi_{(p,q-1,m+1)} + \mathrm{Cl}_{m+1}\psi_{(p,q,m+1)} \\
&\quad = \mathrm{Ar}_{m+1/2}\psi_{(p+1,q,m+1/2)} + \mathrm{Br}_{m+1/2}\psi_{(p-1,q,m+1/2)} + \mathrm{Cr}_{m+1/2}\psi_{(p,q,m+1/2)}
\end{aligned}, \qquad (3.3.33)$$

in which

$$\begin{aligned}
\mathrm{Al}_{m+1} &= \mathrm{Bl}_{m+1} = -\frac{1}{\Delta y^2} \\
\mathrm{Cl}_{m+1} &= \frac{4j\beta_0}{\Delta z} + \frac{2}{\Delta y^2} - \frac{k_0^2 n_r^2 - \beta_0^2}{2} \\
\mathrm{Ar}_{m+1/2} &= \mathrm{Br}_{m+1/2} = \frac{1}{\Delta x^2} \\
\mathrm{Cr}_{m+1/2} &= \frac{4j\beta_0}{\Delta z} - \frac{2}{\Delta x^2} + \frac{k_0^2 n_r^2 - \beta_0^2}{2}
\end{aligned}.$$

It is obvious that the ADI method decomposes the five-band matrix problem into two three-band tri-diagonal matrices problem which can be solved by applying Thomas algorithm repeatedly.

Another choice for solving the sparse matrix systems mentioned in Eq. (3.3.27) is utilising a matrix solver such as Gaussian elimination method and iterative solver. Typical iterative solvers like Bi-Conjugate Stable (BI-CGSTAB) method [62] and Generalized Minimal Residual (GMRES) method [63] are widely applied because the solutions can converge in a reasonable time, which makes the method more reliable.

However, if a large number of iterations are used to achieve a better accuracy, the requirement for computational time and memory will be heavy for large matrices. Therefore, the application of an iterative solution normally needs to be supported by powerful modern computing tools.

3.4 Boundary Conditions for FD-BPM

Photonic devices are open structures but they need to be placed in a finite computational domain. Therefore, structure boundaries must be set at an appropriate distance from an optical waveguide. This section will overview various boundary conditions that have been developed for numerical simulation methods, include Neumann boundary condition, Dirichlet boundary condition, Transparent Boundary Condition (TBC), Perfectly Matched Layer (PML) boundary condition and Periodic Boundary Condition (PBC) [52, 53, 64].

3.4.1 Neumann and Dirichlet Boundary Condition

Consider a 2D structure with P sampling points on the transverse modelling space as shown in Fig. 3.10. Neumann boundary condition [64] defines the field gradient at the boundary to be zero which means the field values are equal on either side of the boundary (ie. $\psi_0 = \psi_1$ and $\psi_\mathrm{p} = \psi_{\mathrm{p+1}}$). According to Eq. (3.2.2), the second order derivative for the left boundary is:

and similarly for the right boundary.

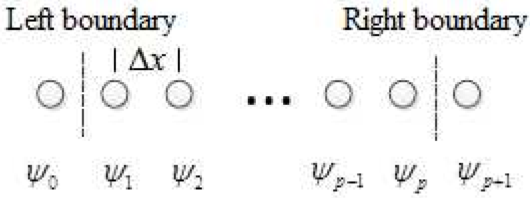

Figure 3.10: 2D structure with p sampling points on the transverse modelling space

As Neumann boundary condition mirrors field values of the sampling nodes on both sides of the boundary, it is also used to simplify the problem for structure that possesses symmetry. This is done by halving the structure along the line of symmetry and applying Neumann boundary condition on the symmetry plane, as shown in Fig.3.11, resulting in 50% computational saving.

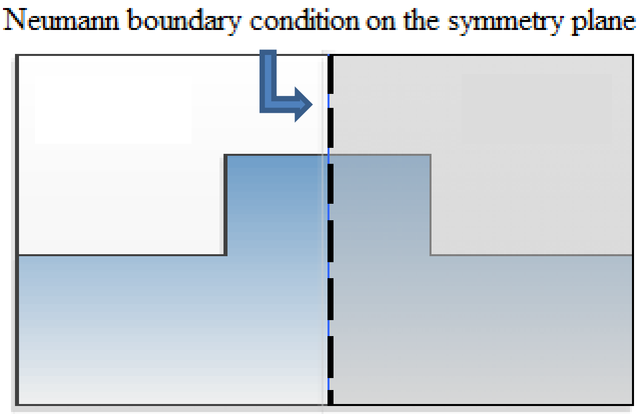

Figure 3.11: Neumann boundary condition is applied at the symmetry plane and computational domain is valued

The Dirichlet boundary condition specifies a value on the boundary as $\psi_{p+1} = -\psi_p$ on the right boundary. This is equivalent to placing a metal boundary which can cause reflection at the edge of the computational window. The second order derivative in transverse operator is written as

$$\frac{\partial^2 \psi_p}{\partial x^2} = \frac{-3\psi_p + \psi_{p-1}}{\Delta x^2} \tag{3.3.34}$$

for the right and similarly for the left boundary.

3.4.2 Transparent Boundary Condition (TBC)

TBC is an absorbing boundary condition proposed by Hadley for FD-BPM specifically [52]. It introduces an estimated complex transverse propagation constant k_x at the boundary based on the field values of the nodes close by the boundary. It also assumes that the outgoing radiation leaves the simulation space and is exponentially decreasing. With respect to Fig. 3.10, the field values of the nodes next to the right boundary follow the relationships:

$$\frac{\psi_P}{\psi_{P-1}} \approx \frac{\psi_{P+1}}{\psi_P} \approx \exp(-jk_x \Delta x) \tag{3.3.35}$$

and for the left boundary:

$$\frac{\psi_1}{\psi_2} \approx \frac{\psi_0}{\psi_1} \approx \exp(jk_x \Delta x)\ . \tag{3.3.36}$$

Based on the known values in these two equations, k_x can be obtained for the right boundary as

$$k_x = j\left(\ln\frac{\psi_P}{\psi_{P-1}}\right)/\Delta x, \tag{3.3.37}$$

and for the left boundary as

$$k_x = -j\left(\ln\frac{\psi_1}{\psi_2}\right)/\Delta x \tag{3.3.38}$$

It is worth noticing that the real part of the propagation constant k_x must be positive to make sure the radiation leaves and does not come into the simulation space. Therefore, the field values of the boundary nodes are obtained as:

$$\psi_{P+1} \approx \psi_P \exp(-jk_x\Delta x) \tag{3.3.39}$$

$$\psi_0 \approx \psi_1 \exp(jk_x\Delta x) \tag{3.3.40}$$

The TBC is a computationally efficient algorithm since no additional virtual absorbing layer needs to be introduced. However, the radiation angle entering the boundary cannot be arbitrary since the rules shown in Eq. (3.3.35) and Eq. (3.3.36) may be broken. The TBC is the most effective if the field approaches the boundary at near-normal incident angle, but is less effective for higher angles. Moreover, this algorithm is not simple to implement for 3D situations in which the field approaches the boundary at different angles.

3.4.3 Perfectly Matched Layers (PML)

Perfectly Matched Layers (PML) [53] is a powerful scheme to provide the boundary condition for 3D structure simulations. It is imposed by introducing an artificial material at the edges of the boundary, which is backed by perfect electric conductor walls. This additional layer acts as an absorber and allows plane waves of arbitrary incidence angles and frequencies to pass through with zero reflection. For a sufficiently thick layer, the plane waves will exponentially decay within the layer to a negligible level and any reflection from the metal boundary will be further attenuated.

Fig. 3.12 shows a 2D computational domain where the original simulation space is extended and the whole problem is divided into nine separate areas including the original simulation space, two extended regions along y direction, two extended regions along x direction and four corner areas. Thus, more computational effort is required since the computational window is enlarged, but it has been proved to be an effective approach to improve the accuracy of the numerical methods and widely applied in optical simulations [53].

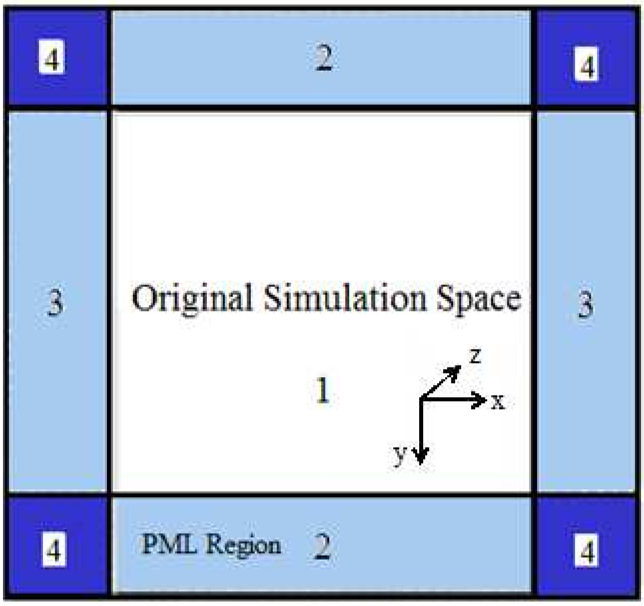

Figure 3.12: Cross-section of a 3D simulation space truncated by PML

Fig. 3.13 illustrates the configurations of the PML applied on the interface between the original simulation window and the region 3 in Fig.3.12, where x' is the distance between the boundary interface and the current node in the PML region. In region 3, the PML boundary condition is implemented by using complex variable transverse coordinate *x'* as [65]:

$$x' = x\left(1 - j\frac{\delta_x \dfrac{\eta'^2}{w^2}}{\omega\varepsilon_0 n_p^2}\right) \tag{3.3.41}$$

in which ω is the operational wavelength, ε_0 is the free space permittivity, δ_x is the attenuation strength, n_p is a reference refractive index which can be chosen to be equal to that of the material adjacent to the PML, η' is the distance into the PML, (starting at zero at the inside edge of the PML), and w is the thickness of the PML [66].

The second order transverse derivative $\frac{\partial^2 \psi_m}{\partial x'^2}$ inside the PML is expressed as:

$$\frac{\partial^2 \psi_m}{\partial x'^2} = \left(1 \Big/ 1 - j \frac{\delta_x \frac{\eta'^2}{w^2}}{\omega \varepsilon_0 n_p^2} \right) \frac{\partial}{\partial x'} \left[\left(1 \Big/ 1 - j \frac{\delta_x \frac{\eta'^2}{w^2}}{\omega \varepsilon_0 n_p^2} \right) \frac{\partial}{\partial x'} \right] \psi_m , \qquad (3.3.42)$$

or introducing an absorption strength factor A^2 to represent the term $\frac{\delta_x \frac{1}{w^2}}{\omega \varepsilon_0 n_p^2}$ so that

Eq.(3.3.42) is rewritten as:

$$\frac{\partial^2 \psi_m}{\partial x'^2} = \left(\frac{1}{1 - j(A\eta')^2} \right) \frac{\partial}{\partial x'} \left[\left(\frac{1}{1 - j(A\eta')^2} \right) \frac{\partial}{\partial x'} \right] \psi_m \qquad (3.3.43)$$

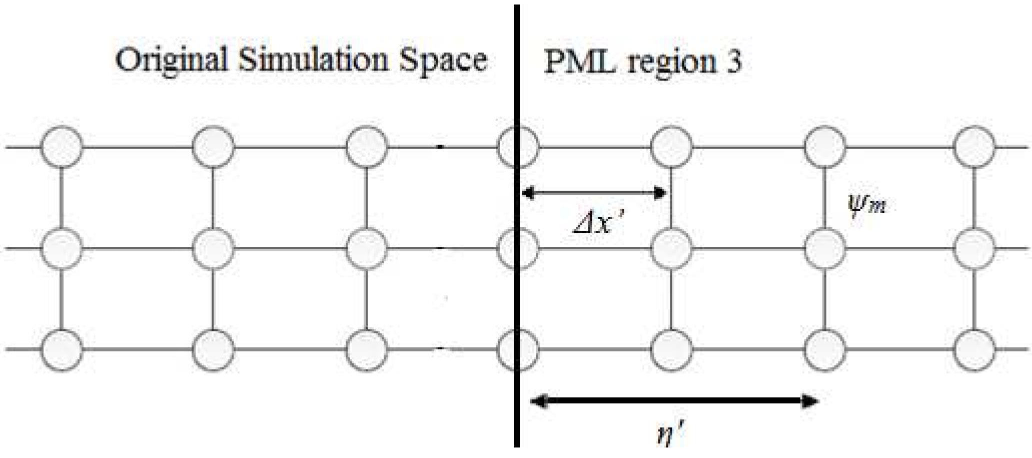

Figure 3.13: Configuration within PML region 3

If the absorption factor is set to be a small value, the PML region needs to be thick to sufficiently eliminate the radiation. In addition, if the absorption factor is set as a large value, the absorption is strong and the layer can be made thinner. However, if the gradient of absorbing material is set to change too rapidly, unwanted reflection may be introduced.

With reference to Eq.(3.3.43), the second derivative in transverse operator x for the PML region 3 is:

$$\frac{\partial^2\psi_m}{\partial x^2}\rightarrow\frac{1}{\Delta x^2}\frac{2}{2-jp_{+a}-jp_{-a}}\left(\frac{\psi_{m+1}-\psi_m}{1-jp_{+a}}-\frac{\psi_m-\psi_{m-1}}{1-jp_{-a}}\right), \qquad (3.3.44)$$

in which

$$P_{\pm a}=\left(A\times(\eta'\pm\frac{\Delta x'}{2})\right). \qquad (3.3.45)$$

Similarly, the second order derivative in transverse operator y can be transformed for absorption in the PML region 2. In the region 4, both the second order x-derivative and y-derivative need to be transformed.

3.4.4 Periodic Boundary Condition

Periodic Boundary Condition (PBC) [67] is a particularly suitable scheme for analysis of infinite periodic structures [68] such as PBG waveguides. Fig.3.14 illustrates the principle of the PBC, where one period of width w is modelled and suitable periodic boundary conditions are applied to the left and right boundary. The field values of the nodes outside the boundary ψ_0 and ψ_{p+1} could be deduced by the field values of the nodes ψ_p and ψ_1 inside the boundary by adding a phase change term as:

$$\psi_{p+1}=\psi_1\cdot\exp(-j\beta_0 w\sin\theta), \qquad (3.3.46)$$

$$\psi_0 = \psi_p \cdot \exp(+j\beta_0 w \sin\theta) \quad (3.3.47)$$
,

both of which can be used directly as known values in the three-band matrix system to calculate the field values on the next propagation step. Therefore, the value of transverse radiation coming out of the boundary on one side of the original space equals that coming in through the other boundary along the same transverse coordinate, and the total energy is unchanged.

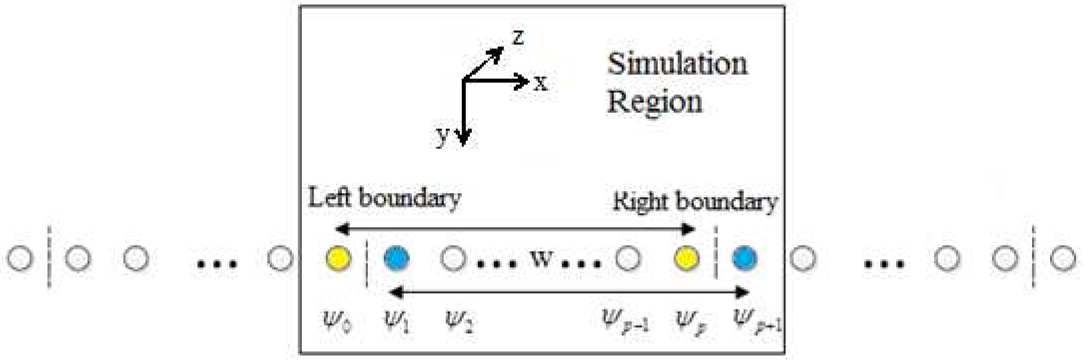

Figure 3.14: 2D simulation with periodic boundary condition along transverse direction x

3.5 Imaginary Distance BPM

In this section an approach for extracting effective refractive index of the modes using BPM method is presented. For a longitudinally invariant waveguide, if the radiation field is assumed to be negligible, the fields may be expressed as a summation of transverse guided waveguide modes multiplied by a phase term:

$$E(x, y, z) = \sum_n A_n E_n(x, y) e^{-j\beta_n z} \quad (3.5.1)$$

It is often necessary to characterize the behavior of these guided mode fields in a waveguide by calculating their propagation constant, β_n, using a mode solver. Frequently, the fundamental or the first-order mode is used as the initial excitation field. In order to efficiently calculate the fundamental mode, three techniques within BPM have been developed. The first one is to excite an arbitrary field and propagate until field tends to fundamental mode. It is slow, and inaccuracy if multi-mode is propagated. The second one is similar with the first one, but evaluates the overlap of a superposition of all the modes of field at each step by Fourier transform, and possesses peaks at all propagating constant corresponding to a mode. The third one is the Imaginary Distance (ID) BPM method, which is a faster mode solver derived from BPM algorithm. The ID procedure was firstly developed by Yevick [69] and extended by others [70, 71]. This section will describe the principle of the ID BPM. For simplicity, the ID BPM formulation will only be developed for the scalar case, which can be easily extended to the semi-vectorial formulas.

The scalar wave equation, Eq. (2.4.27), can be rearranged to get [72]:

$$\frac{\partial \psi}{\partial z} = \frac{-j}{2\beta_0}\left[\frac{\partial^2}{\partial x^2} + \frac{\partial^2}{\partial y^2} + (k_0^2 n_r^2 - \beta_0^2)\right]\psi \, . \tag{3.5.2}$$

For the waveguides which are uniform along the propagating direction, an arbitrary input field can be represented as a summation of the eigenmodes as:

$$\psi(x, y, z) = \sum_{m}^{\infty} a_m \psi_m(x, y) \tag{3.5.3}$$

in which a_m represents the amplitude of the m^th order mode.

On the other hand, the eigenvalue equation for the m^th order mode is:

$$\frac{\partial^2 \psi_m}{\partial x^2} + \frac{\partial^2 \psi_m}{\partial y^2} + (k_0^2 n_r^2 - \beta_m^2)\psi_m = 0\,, \tag{3.5.4}$$

which can be re-expressed in the form of:

$$\left(\frac{\partial^2}{\partial x^2} + \frac{\partial^2}{\partial y^2}\right)\psi_m = (\beta_m^2 - k_0^2 n_r^2)\psi_m\,, \tag{3.5.5}$$

in which β_m is the propagation constant of the m^th order mode.

Replacing Eq. (3.5.5) into Eq. (3.5.2) can obtain equation:

$$\frac{\partial \psi_m}{\partial z} = \frac{-j}{2\beta_0}\left[(\beta_m^2 - k_0^2 n_r^2) + (k_0^2 n_r^2 - \beta_0^2)\right]\psi_m = \frac{-j}{2\beta_0}(\beta_m^2 - \beta_0^2)\psi_m \tag{3.5.6}$$

Under the condition that $\beta_m \simeq \beta_0$, the coefficient on the right hand side of Eq. (3.5.6) can be approximated and defined as:

$$\frac{1}{2\beta_0}(\beta_m^2 - \beta_0^2) \approx \beta_m - \beta_0 \equiv \lambda_m \tag{3.5.7}$$

where λ_m is the eigenvalue.

Substituting λ_m into Eq.(3.5.6), the solution of the equation can be formally written as:

$$\psi_m(x, y, z) = \psi_m(x, y)e^{-j\lambda_m z} \tag{3.5.8}$$

which leads Eq.(3.5.3) to be:

$$\psi(x, y, z) = \sum_{m}^{\infty} a_m \psi_m(x, y) e^{-j\lambda_m z} \tag{3.5.9}$$

In the imaginary distance BPM, the propagation axis z is assumed to be imaginary i.e,

$$z = j\tau, \tag{3.5.10}$$

leading to

$$\psi(x, y, \tau) = \sum_{m}^{\infty} a_m \psi_m(x, y) e^{\lambda_m \tau} \ . \tag{3.5.11}$$

As seen from Eq.(3.5.11), a sinusoidal phase change of the field is replaced with its exponential amplitude change in the imaginary distance procedure [72]. The eigenvalues are arranged in this order:

$$\lambda_0 > \lambda_1 > \lambda_2 > \cdots > \lambda_m > \cdots \tag{3.5.12}$$

where λ_0 is the largest eigenvalue and corresponds to the fundamental mode.

Eq. (3.5.11) says that the field propagating with the largest eigenvalue λ_0 increases much faster than all the other fields. Therefore, the propagating field converges to the fundamental mode as:

$$\lim_{\tau \to \infty} \psi(x, y, \tau) = a_0 \psi_0(x, y) \tag{3.5.13}$$

From the viewpoint of power, the following relationship is deduced:

$$\iint (\psi_{(x,y,\tau)} e^{\lambda_0 \Delta\tau})^2 \, dxdy = \iint (\psi_{(x,y,\tau+\Delta\tau)})^2 \, dxdy \tag{3.5.14}$$

or rearranged as:

$$e^{2\lambda_0\Delta\tau} = \frac{\iint (\psi_{(x,y,\tau+\Delta\tau)})^2 \, dxdy}{\iint (\psi_{(x,y,\tau)})^2 \, dxdy} \tag{3.5.15}$$

Taking logarithm of both sides of Eq.(3.5.15) leads to:

$$2\lambda_0\Delta\tau = \ln\left(\frac{\iint (\psi_{(x,y,\tau+\Delta\tau)})^2 \, dxdy}{\iint (\psi_{(x,y,\tau)})^2 \, dxdy}\right) \tag{3.5.16}$$

Based on Eq.(3.5.7), the calculated effective refractive index of the fundamental mode which is essentially a function of τ, is obtained as:

$$n_{eff} = n_0 + \frac{1}{k_0\Delta\tau} \ln\left(\frac{\iint (\psi_{(x,y,\tau+\Delta\tau)}) dxdy}{\iint (\psi_{(x,y,\tau)}) dxdy}\right) \tag{3.5.17}$$

During the FD-BPM simulation, it is necessary to choose the reference refractive index n_0 close to the effective refractive index n_{eff} of the waveguide to obtain a good convergence. A popular technique, which is applied throughout this thesis, is to repeatedly substitute n_0 by $n_{eff}(\tau)$ of the immediately preceding numerical step for each step calculation to obtain a better convergence [73].

It is worth to noticing that once the fundamental mode is found by Eq.(3.5.13), the ID BPM mode solver can also be used to find other eigenmodes. Removing the fundamental mode from Eq. (3.5.11) results in:

$$\sum_{m}^{\infty} a_m\psi_m(x,y)e^{\lambda_m z} - a_0\psi_0(x,y)e^{\lambda_0 z} = a_1\psi_1(x,y)e^{\lambda_1 z} + a_2\psi_2(x,y)e^{\lambda_2 z}\cdots\cdots \tag{3.5.18}$$

Based on Eq.(3.5.18), the propagating field along the imaginary distance converges to the next eigenmode as

$$\lim_{\tau\to\infty}\psi(\mathrm{x},\mathrm{y},\tau)=\mathrm{a}_1\psi_1(\mathrm{x},\mathrm{y}) \tag{3.5.19}$$

Similarly, other eigenmodes can be obtained by repeating the same procedure.

3.5.1 Numerical Implementation of the Paraxial ID Procedure

This section will outline the numerical implementation of the ID BPM method. Starting from the 3D wave equation

$$\frac{\partial^2\mathrm{E}_{(x,y,z)}}{\partial x^2}+\frac{\partial^2\mathrm{E}_{(x,y,z)}}{\partial y^2}+\frac{\partial^2\mathrm{E}_{(x,y,z)}}{\partial z^2}+\mathrm{k}_0^2\mathrm{n}_\mathrm{r}^2\mathrm{E}_{(x,y,z)}=0 \tag{3.5.20}$$

and replacing the field term by $\mathrm{E}_{(x,y,z)}=\psi_{(x,y)}\mathrm{e}^{-\mathrm{j}\beta_0 z}$, previous equation is reduced to:

$$\frac{\partial^2\left(\psi_{(x,y)}\mathrm{e}^{-\mathrm{j}\beta_0 z}\right)}{\partial x^2}+\frac{\partial^2\left(\psi_{(x,y)}\mathrm{e}^{-\mathrm{j}\beta_0 z}\right)}{\partial y^2}+\frac{\partial^2\left(\psi_{(x,y)}\mathrm{e}^{-\mathrm{j}\beta_0 z}\right)}{\partial z^2}+\mathrm{k}_0^2\mathrm{n}_\mathrm{r}^2\psi_{(x,y)}\mathrm{e}^{-\mathrm{j}\beta_0 z}=0\,. \tag{3.5.21}$$

If $z=\mathrm{j}\tau$ is used to convert the real propagation axis into the imaginary axis, Eq.(3.5.21) can be rewritten as:

$$\frac{\partial^2\left(\psi_{(x,y)}\mathrm{e}^{\beta_0\tau}\right)}{\partial x^2}+\frac{\partial^2\left(\psi_{(x,y)}\mathrm{e}^{\beta_0\tau}\right)}{\partial y^2}-\frac{\partial^2\left(\psi_{(x,y)}\mathrm{e}^{\beta_0\tau}\right)}{\partial \tau^2}+\mathrm{k}_0^2\mathrm{n}_\mathrm{r}^2\left(\psi_{(x,y)}\mathrm{e}^{\beta_0\tau}\right)=0\,, \tag{3.5.22}$$

or expanding the field term as:

$$\frac{\partial^2\psi_{(x,y)}}{\partial x^2}+\frac{\partial^2\psi_{(x,y)}}{\partial y^2}+k_0^2n_r^2\psi_{(x,y)}-\left(\frac{\partial^2\psi_{(x,y)}}{\partial\tau^2}+2\beta_0\frac{\partial\psi_{(x,y)}}{\partial\tau}+\beta_0^2\psi_{(x,y)}\right)=0. \qquad (3.5.23)$$

Under SVEA $\frac{\partial^2\psi}{\partial z^2}\approx 0$ and Eq. (3.5.23) becomes:

$$2\beta_0\frac{\partial\psi_{(x,y)}}{\partial\tau}=\frac{\partial^2\psi_{(x,y)}}{\partial x^2}+\frac{\partial^2\psi_{(x,y)}}{\partial y^2}+k_0^2n_r^2\psi_{(x,y)}-\beta_0^2\psi_{(x,y)} \qquad (3.5.24)$$

which can be discretised by the CN scheme to obtain the numerical discretised form:

$$\begin{aligned}&A_{\tau+\Delta\tau}\psi_{(x+\Delta x,y,\tau+\Delta\tau)}+B_{\tau+\Delta\tau}\psi_{(x-\Delta x,y,\tau+\Delta\tau)}+C_{\tau+\Delta\tau}\psi_{(x,y,\tau+\Delta\tau)}+D_{\tau+\Delta\tau}\psi_{(x,y+\Delta y,\tau+\Delta\tau)}+E_{\tau+\Delta\tau}\psi_{(x,y-\Delta y,\tau+\Delta\tau)}\\&\quad=A_\tau\psi_{(x+\Delta x,y,\tau)}+B_\tau\psi_{(x-\Delta x,y,\tau)}+C_\tau\psi_{(x,y,\tau)}+D_\tau\psi_{(x,y+\Delta y,\tau)}+E_\tau\psi_{(x,y-\Delta y,\tau)}\end{aligned}$$

(3.5.25)

where the coefficients are:

$$\begin{aligned}A_{\tau+\Delta\tau}&=B_{\tau+\Delta\tau}=-\frac{1}{\Delta x^2}\\C_{\tau+\Delta\tau}&=\frac{4\beta_0}{\Delta\tau}+\frac{2}{\Delta x^2}+\frac{2}{\Delta y^2}-(k_0^2n_r^2-\beta_0^2)\\D_{\tau+\Delta\tau}&=E_{\tau+\Delta\tau}=-\frac{1}{\Delta y^2}\end{aligned}$$

$$\begin{aligned}A_\tau&=B_\tau=\frac{1}{\Delta x^2}\\C_\tau&=\frac{4\beta_0}{\Delta\tau}-\frac{2}{\Delta x^2}-\frac{2}{\Delta y^2}+(k_0^2n_r^2-\beta_0^2)\\D_\tau&=E_\tau=\frac{1}{\Delta y^2}\end{aligned}$$

For 2D problem, Eq. (3.5.25) becomes:

$$A_{\tau+\Delta\tau}\psi_{(x+\Delta x,\tau+\Delta\tau)}+B_{\tau+\Delta\tau}\psi_{(x-\Delta x,\tau+\Delta\tau)}+C_{\tau+\Delta\tau}\psi_{(x,\tau+\Delta\tau)}=A_\tau\psi_{(x+\Delta x,\tau)}+B_\tau\psi_{(x-\Delta x,\tau)}+C_\tau\psi_{(x,\tau)}$$

(3.5.26)

with the coefficients:

$$
\begin{aligned}
A_{\tau+\Delta\tau} &= B_{\tau+\Delta\tau} = -\frac{1}{\Delta x^2} \\
C_{\tau+\Delta\tau} &= \frac{4\beta_0}{\Delta\tau} + \frac{2}{\Delta x^2} - (k_0^2 n_r^2 - \beta_0^2) \\
A_\tau &= B_\tau = \frac{1}{\Delta x^2} \\
C_\tau &= \frac{4\beta_0}{\Delta\tau} - \frac{2}{\Delta x^2} + (k_0^2 n_r^2 - \beta_0^2)
\end{aligned}
$$

By using Eq.(3.5.17) and Eq.(3.5.24), a suitable propagation constant and the fundamental mode input field for BPM simulation can be obtained. An easy method to avoid the excessive growth of the field during ID BPM is to gradually rescale the field by:

$$\psi(x, y) \rightarrow \frac{\psi(x, y)}{\sqrt{\iint |\psi(x, y)|^2 \, dxdy}} \qquad (3.5.27)$$

The field rescaling can be repetitively employed when the field propagates a certain distance, for example after each propagation step, along the imaginary axis.

3.5.2 Results

In this section, the performance of the ID BPM mode solver is analysed in three aspects, including the accuracy for various sampling intervals in transverse and longitudinal direction, the reliability of the method for different initial values of the effective refractive index and different waveguide widths. The structure considered is a symmetrical slab waveguide as shown in Fig. 3.15. The refractive indices are 1.5 for the core and 1.45 for the cladding, respectively. The width of the simulation window along x-direction is set to 10μm. TBC is applied as the boundary condition. Input beam in the form of Gaussian function is launched at the wavelength $\lambda = 1.55$ μm and the peak value is located at -2μm on the x-axis.

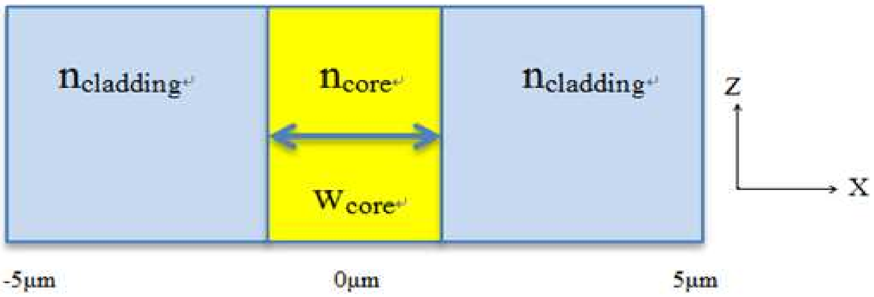

Figure 3.15: The cross section of the simulated slab waveguide

Firstly, the convergence of the calculated effective refractive index n_{eff} for the fundamental mode for different transverse mesh size Δx (Δx=0.002μm, 0.005μm, 0.01μm, 0.02μm, 0.05μm and 0.1μm, respectively) is tested for both TE and TM polarisation. The core width is set as W_{core} =3μm. The propagation step along z-direction is kept at a fixed value of Δz=0.01. A random start guess value of the effective refractive index is set as $n_{eff} = 2.25$, although the true value should be in the range between the value of n_{core} and $n_{cladding}$.

For every propagation step along the imaginary axis, the eigenvalue λ_0 is found and the effective refractive index is calculated and updated by Eq.(3.5.17). The simulation is stopped when

$$| n_{\mathrm{eff\,(new)}} - n_{\mathrm{eff\,(old)}} | < 1 \times 10^{-8} \tag{3.5.28}$$

where $n_{\mathrm{eff\,(old)}}$ and $n_{\mathrm{eff\,(new)}}$ denote the calculated n_{eff} of previous and current propagation step respectively. The propagation distances for which convergence is achieved are plotted in Fig. 3.16 (a) for the TE and TM polarisition. it can be seen that for a smaller transverse sampling interval, the simulation requires a longer propagation distance to achieve convergence.

In order to confirm the accuracy of simulation results, the exact solutions from an analytical slab waveguide mode solver are considered as the benchmark. The analytical value of the effective refractive index for the chosen slab waveguide is $n_{\mathrm{eff}} = 1.489311$ for TE mode and $n_{\mathrm{eff}} = 1.488941$ for TM mode. The errors of the calculated effective refractive index by the ID BPM mode solver of the fundamental TE and TM modes comparing to the analytical values are calculated as

$$\mathrm{Error} = 10 \cdot \log(| n_{\mathrm{eff}} - n_{\mathrm{exact}} |) \tag{3.5.29}$$

and shown in Fig. 3.16 (b). It shows that for both TE and TM mode, the calculated n_{eff} gradually converges to the analytical solution with the decrease of the transverse mesh size. When the transverse mesh size is less than 0.02μm, the errors between the calculated results and the analytical value are very small. However with a smaller mesh size, the calculated n_{eff} needs a longer propagation distance along the imaginary axis for converging, and the CPU time and memory required for the simulation will be increased. Therefore, how to choose a suitable transverse mesh size is determined by the accuracy requirement of the calculated n_{eff} and the consuming time and memory of CPU.

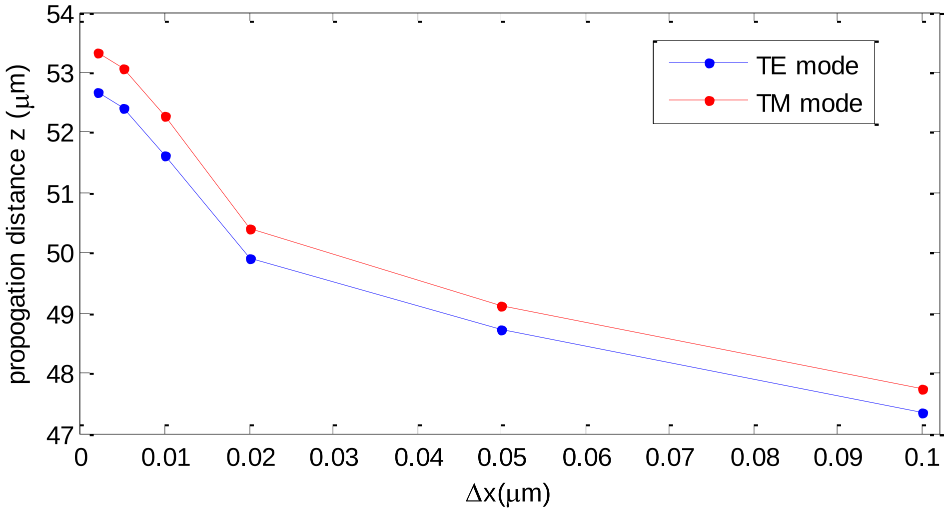

(a)

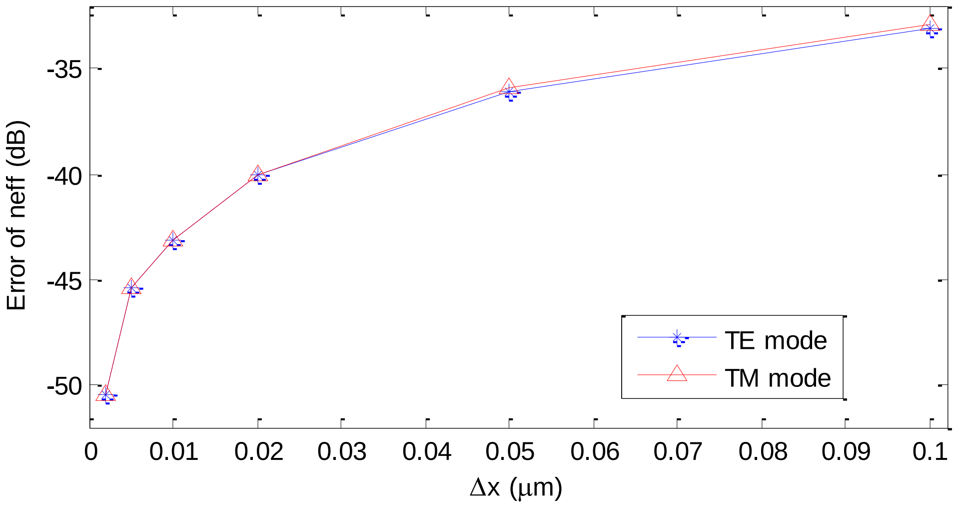

(b)

Figure 3.16: (a) The propagation distance along the imaginary axis as a function of the transverse mesh size Δx; (b) The error between the calculated value and the analytical solution of n_{eff} as a function of the transverse mesh size Δx.

Secondly, the transverse mesh size is set at a fixed value of $\Delta x = 0.01\mu m$, 0.02μm, and 0.05μm respectively and the propagation step along z-direction is set at $\Delta z =$ 0.002μm, 0.005μm, 0.01μm, 0.02μm, 0.05μm and 0.1μm for each certain value of Δx. The effective refractive index is calculated for each case and the errors compared to the analytical values are calculated by Eq.(3.5.29) and shown in Fig. 3.17 (a). It can be seen that for the same transverse mesh size and different propagation steps, the error of the calculated n_{eff} keeps the same value for both TE and TM mode. As the accuracy of the calculated n_{eff} is not affected by the change of the propagation step, a large propagation step can be used during the ID BPM simulation to reduce the time and memory consumption of CPU. Propagation distances for which n_{eff} is obtained for TE and TM mode when $\Delta x = 0.01\mu m$ are plotted in Fig. 3.17 (b). It shows that if the longitudinal propagation step is set as a larger value, the propagation distance to obtain accurate calculated result is longer.

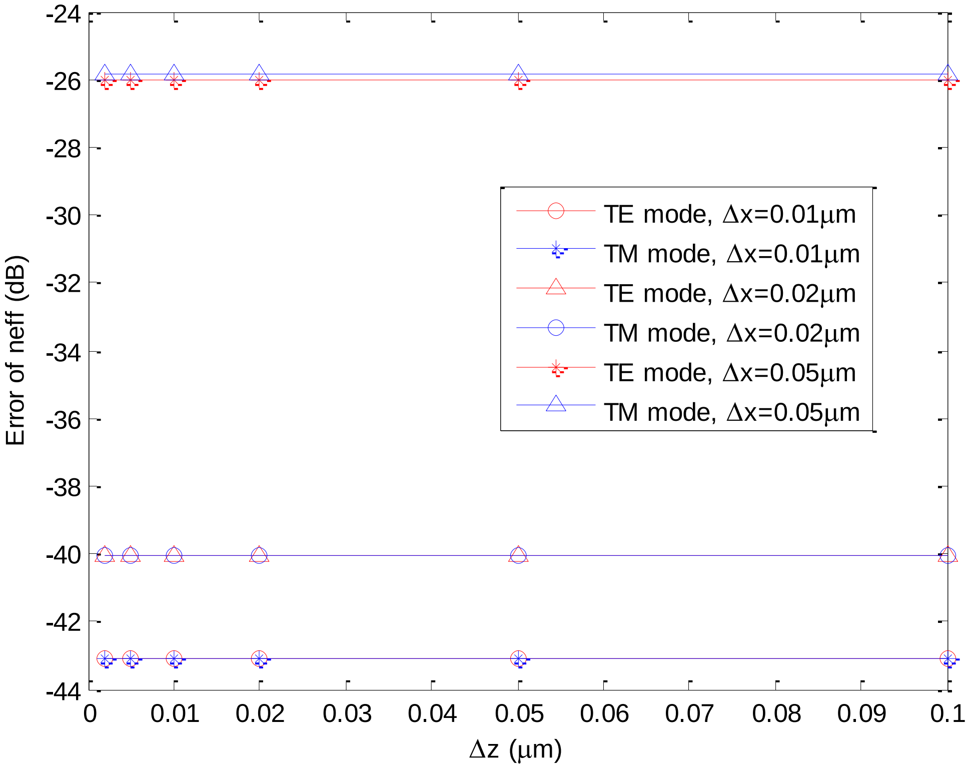

(a)

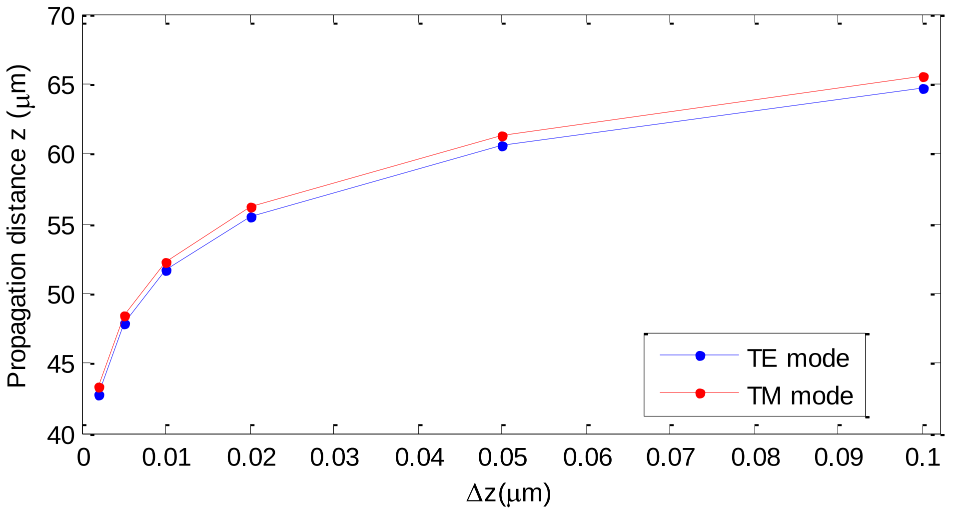

(b)

Figure 3.17: (a) The error between the calculated value and the analytical solution of n_{eff} as a function of the longitudinal propagation step; (b) The propagation distance along the imaginary axis where the calculated n_{eff} is obtained as a function of the longitudinal propagation step.

The effect of the choice of the starting effective refractive index is investigated next. Different initial guess values n_{eff} =1.25,2.25 and 5.45 are set for fixed transerve mesh size and propagation step as $\Delta x = \Delta z = 0.01$. The waveguide parameters are the same. For both TE and TM mode, when the starting value of n_{eff} is different, the differences between the calculated n_{eff} of two adjacent propagation steps are calculated by

$$Difference = 10 \cdot \log(| n_{eff\,(new)} - n_{eff\,(old)} |) \tag{3.5.30}$$

The convergence of n_{eff} is presented as a function of the propagation distance along the imaginary axis in Fig. 3.18. Fig. 3.18(a) and Fig. 3.18(b) illustrate the change rate in the first ten propagation steps (propagation distance from 0 to 0.1μm) for TE and TM polarisation, respectively. It can be seen that for both TE and TM mode, no matter what the starting value is, the effective refractive index converges very fast. The differences between the calculated values of n_{eff} obtained by different starting values are particularly evident at the first few steps. After a short propagation distance, n_{eff} converges to the same value regardless of the starting value. It can also be seen that a starting value which is closer to the analytical value leads to faster convergence. Fig. 3.18(c) illustrates how the calculated n_{eff} converges along the propagation direction over a long distance (propagation distance from 0.1μm to 80μm) when the starting value is different. It can be seen that different starting values result in the similar convergence curve for both TE and TM polarisation. With the increasing of the propagation distance, the change of n_{eff} becomes inconspicuous. The simulation results prove that the ID BPM mode solver is reliable for any random initial guess value of the effective refractive index.

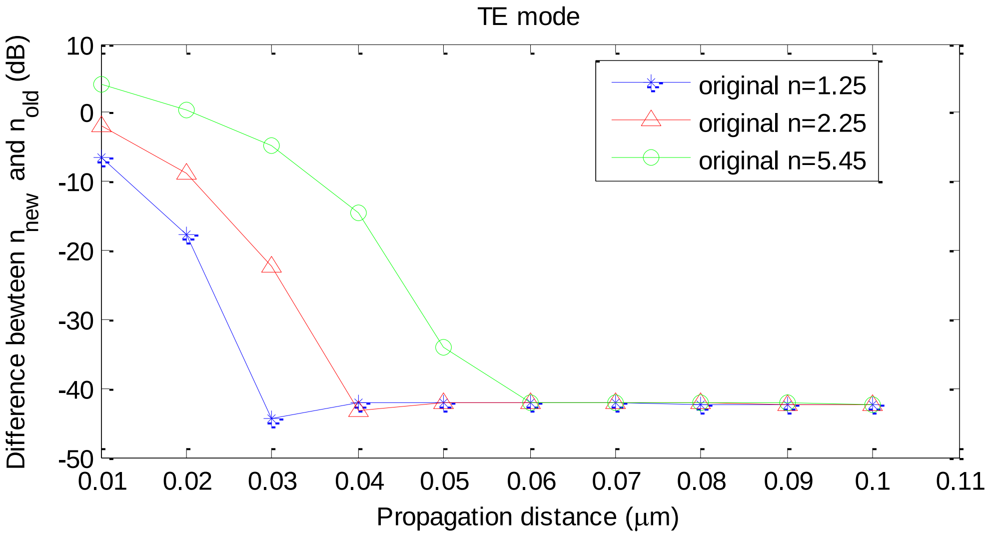

(a)

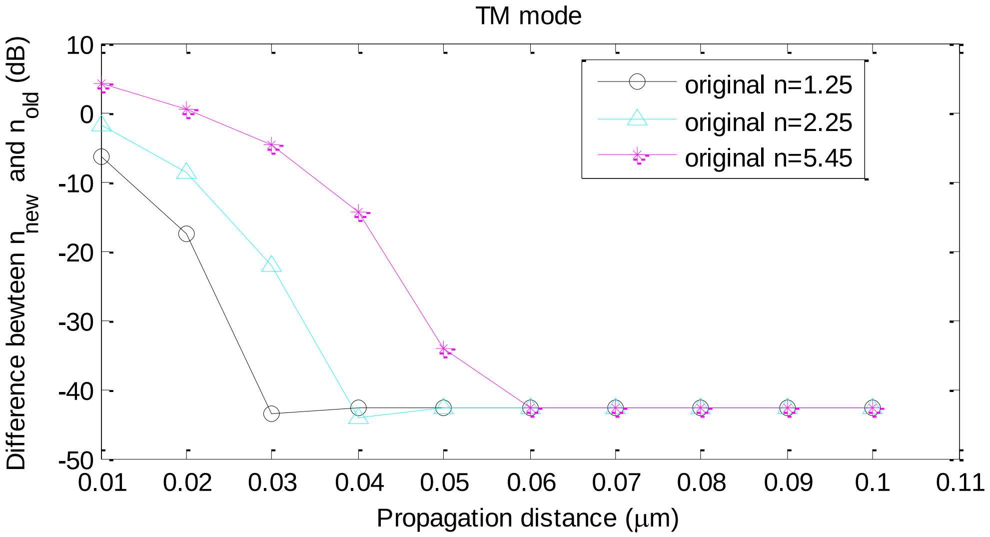

(b)

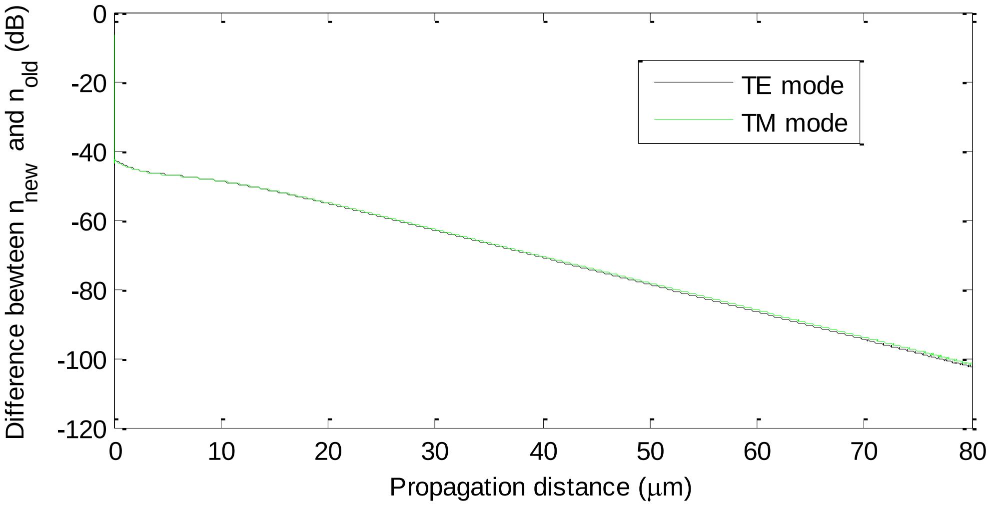

(c)

Figure 3.18: The differences between the calculated n_{eff} of two adjacent propagation steps are presented as a function of the propagation distance along the imaginary axis for three different initial values. (a) First ten propagation steps for TE mode; (b) First ten propagation steps for TM mode; (c) The change rate of n_{eff} over a distance of 80μm.

In order to further verify the effectiveness and reliability of the ID BPM as a mode solver, more test simulations have been done for different core widths of a slab waveguide, W_{core} =0.1μm, 0.5μm, 1μm, 2μm, and 3μm. The transverse mesh size and the propagation step are $\Delta x = \Delta z = 0.01$, and the initial guess value of n_{eff} is 2.25. For a chosen value of the core width, when the convergence of n_{eff} is achieved according to Eq.(3.5.28), simulation is terminated, and the error compared with the analytical value is calculated by Eq.(3.5.29). Table 3.1 displays the analytical values and the calculated values of n_{eff} for different core widths. It also lists the differences between the analytical values and the calculated values.

The comparison is presented more intuitively as a function of the core width in Fig.3.19. Fig. 3.19(a) illustrates the values of n_{eff} for different core widths and Fig.3.19(b) illustrates the errors. It can be seen that for both TE and TM mode, the calculated values are very close to the analytical values. The errors are small regardless of the slab core width.

Core Width (µm)		TE mode				TM mode		
		Analytical value	Calculated value	Difference		Analytical value	Calculated value	Difference
0.1		1.450311	1.45037	5.9x10^{-5}		1.450271	1.45027	- 10^{-6}
0.5		1.456421	1.45664	2.19x10^{-4}		1.455781	1.45591	1.29 x10^{-4}
1		1.467511	1.46772	2.09 x10^{-4}		1.466461	1.46665	1.89 x10^{-4}
2		1.482341	1.48244	9.9 x10^{-5}		1.481651	1.48175	9.9 x10^{-5}
3		1.489311	1.48936	4.9 x10^{-5}		1.488941	1.48899	4.9 x10^{-5}

Table 3.1: The comparison between the analytical values and the calculated values of n_{eff} for different core width of a slab waveguide.

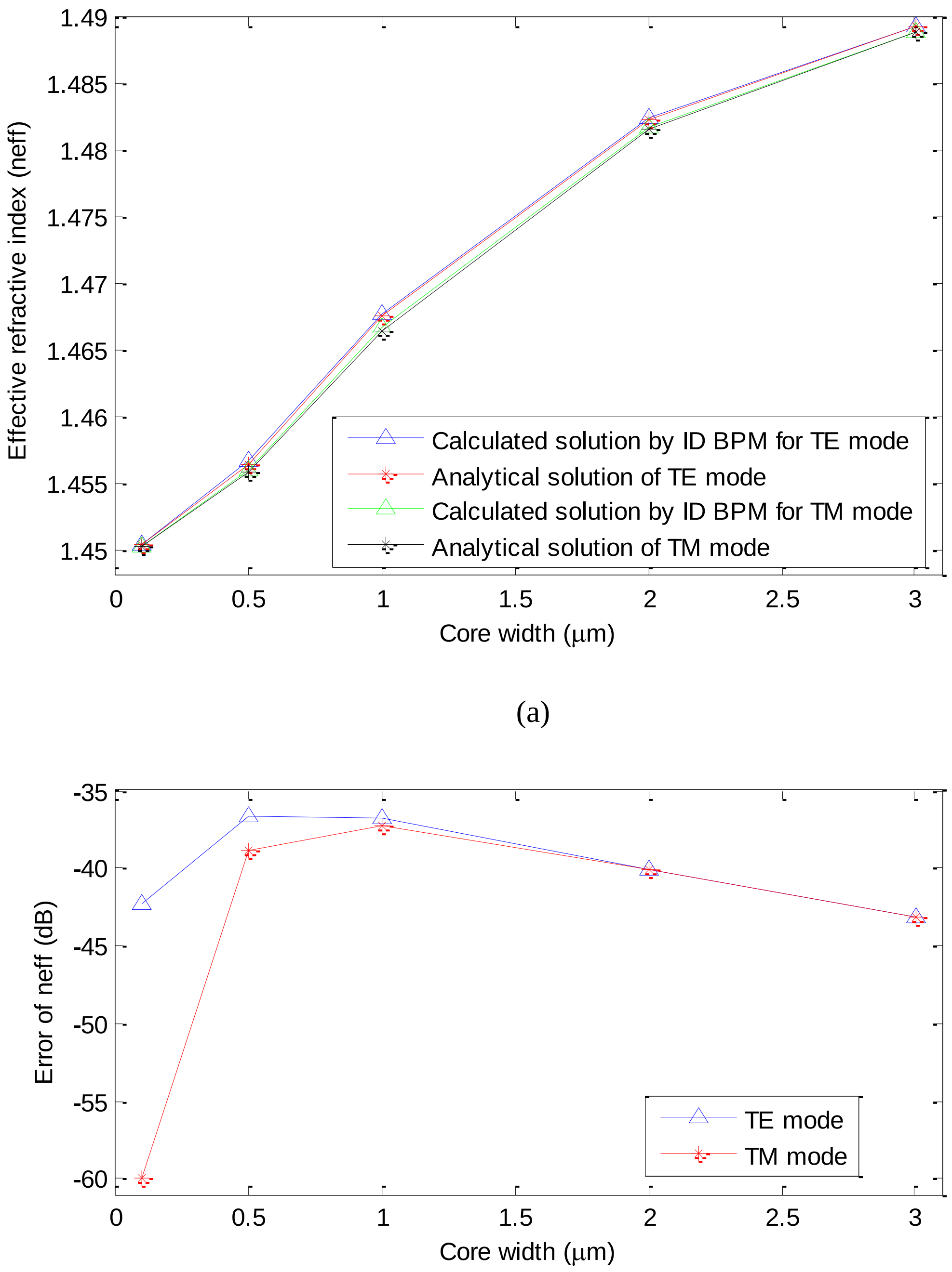

(a)

(b)

Figure 3.19: The comparison between the analytical values and the calculated values of n_{eff} for different core width of a slab waveguide: (a) the value n_{eff} is presented as a function of the core width; (b) the error of n_{eff} is presented as a function of the core width.

Fig. 3.20 illustrates the beam profiles obtained for the TE mode for the transverse mesh size and the propagation step as $\Delta x = \Delta z = 0.01$, the initial guess value of n_{eff} is 2.25, and the slab core width is W_{core} =3μm. The incident field is launched into the structure at a random position. It can be seen that the field profiles changes fast at the beginning of the propagation, and then resumes the field profile of the dominant mode in the slab waveguide.

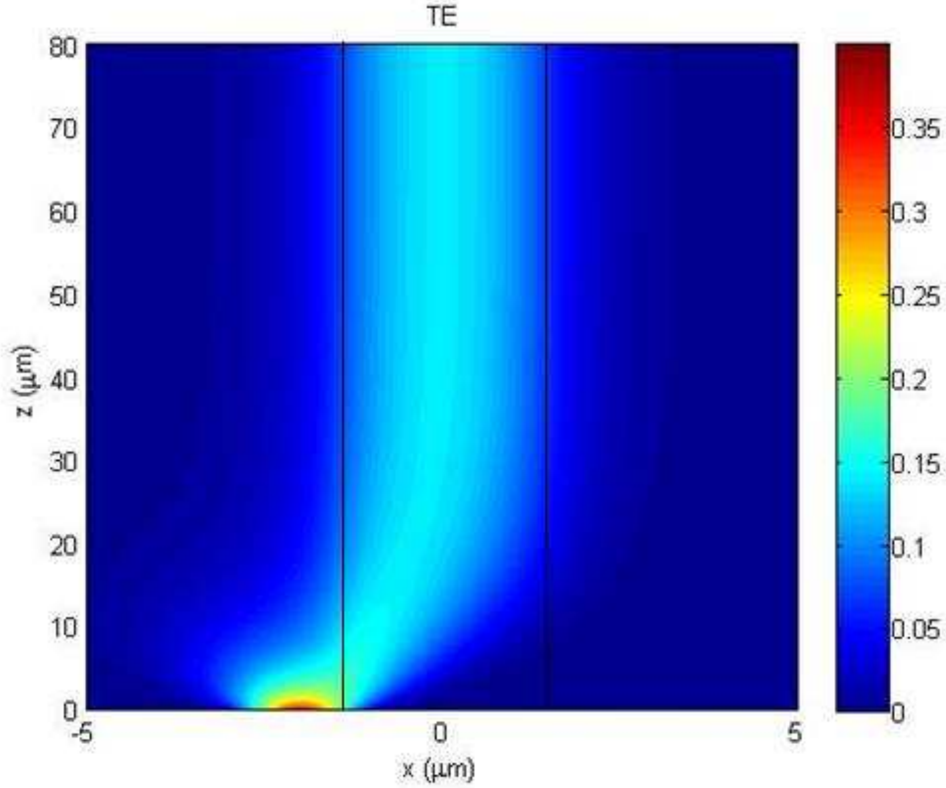

Figure 3.20: The TE mode beam profile along the imaginary axis.

3.6 Conclusions

This chapter introduced the most commonly applied analysis tools for optical devices. Typical semi-analytical methods such as the Marcatili’s method, the Effective Index (EI) method and the Spectral Index (SI) method are fast and efficient schemes that can provide accurate results. However, they are not suitable to solve complex photonic structures since these schemes are specifically developed for particular types of waveguides. In addition, the numerical methods such as the Finite Element (FE) Method and the Finite Difference (FD) Method have general applicability. They are highly accurate schemes and suitable for complex geometries, but large computational memory and time are often required as the carrier is sampled during the application of these methods.

As a numerical method, FD-BPM is widely applied in optical simulations recently because of its flexibility and efficiency. It samples the envelope of the fields rather than the carrier so that it is more efficient than the conventional FE and FD methods. This chapter overviewed the theory and numerical implementation of the paraxial FD-BPM method. It considered the related concepts including discretisation schemes and different boundary conditions. The FD-BPM transforms the wave equation to be a matrix system problem which can be solved by the tri-diagonal algorithm. TBC and PML are two effective boundary conditions for FD-BPM simulation. They can eliminate the unwanted reflections from the edges of the simulation window.

The ID BPM scheme is overviewed and tested as a mode solver. The simulation results demonstrated that the ID BPM mode solver is accurate and reliable when solving for the effective refractive index of the fundamental mode of a waveguide, regardless of the initial guess value. The accuracy of the method can be improved by using smaller transverse mesh size. In following chapters, ID BPM will be used as the mode solver to calculate the fundamental mode of the input for simulations and the refractive index of the waveguides. A restriction of the application of the paraxial FD-BPM in optical simulation is that the input beam cannot propagate at large angles with respect to the longitudinal direction. A WA BPM removes this restriction and is overviewed in the next chapter.

3.7 Reference

1. H. Nishihara, T. Suhara, Optical Integrated Circuit. 1989.
2. E.A.J. Marcatili, Dielectric rectangular waveguide and directional coupler for integrated optics. Bell Syst. Tech, 1969. **J., 48,**: p. 2071-2102.
3. R. M. Knox, Integrated circuits for the millimeter through optical frequency range. 1970: p. 479-516.
4. P.C. Kendall, P.W.A. McIlroy, and M.S. Stern, Spectral index method for rib waveguide analysis. Electronics Letters, 1989. **25**(2): p. 107-108.

5. Kenji Kawano, Introduction to optical waveguide analysis. 2001.

6. G. Lifante, Integrated Photonics Fundamentals. 2003.

7. K.S. Chiang, Review of numerical and approximate methods fort the analysis of general optical dielectric waveguides. Optical and Quantum Electronics, 1994. **26**: p. S113-S134.

8. P. McIlroy, *Spectral Index method: single rib waveguide, Chapter 5 of "Rib* Waveguide Theory by the Spectral Index Method". 1990.

9. P. McIlroy, M.S. Stern, and P.C. Kendall, Fast and accurate method for calculation of polarised modes in semiconductor rib waveguides. Electronics Letters, 1989. **25**(23): p. 1586-1587.

10. P. McIlroy, M.S. Stern, and P.C. Kendall, Spectral index method for polarized modes in semiconductor rib waveguides. Lightwave Technology, Journal of, 1990. **8**(1): p. 113-117.

11. M.S. Stern, P.C. Kendall, and P.W.A. McIlroy, Analysis of the spectral index method for vector modes of rib waveguides. Optoelectronics, IEE Proceedings J, 1990. **137**(1): p. 21-26.

12. M.S. Stern, *"Discrete Spectral Index method for rib waveguides", Chapter 6 of "Rib Waveguide Theory by the Spectral Index Method".* 1990.

13. S.V. Burke, Spectral index method applied to coupled rib waveguides. Electronics Letters, 1989. **25**(9): p. 605-606.

14. S.V. Burke, Spectral index method applied to two nonidentical closely separated rib waveguides. Optoelectronics, IEE Proceedings J, 1990. **137**(5):

p. 289-292.

15. S. Greedy, P. Swell., T.M. Benson, Spextral index method applied to the analysis of whispering callery modes in semiconductor disk resonator. MMET proceeding, 2000.

16. S.V. Burke, Planar waveguide analysis by the spectral index method: II: Multiple layers, optical gain and loss. 1994: p. 63-77.

17. G. M. Berry, J. M. Heaton, and D. R. Wight, Leaky mode analysis of semiconductor optical rib waveguides. Integrated Photonics Research Technical Digest, 1994: p. 81-83.

18. A.J. Davies, The Finite Element Method. 1980.

19. M.N.O. Sadiku, Numerical techniques in electromagnetics. 1992.

20. F. Fernandez, Microwave and optical waveguide analysis by the Finite Element mathod. 1996.

21. J.M. Jin, The Finite Element Mehod in Electromagnetics,2nd ed. Wiley, 2002.

22. M. Koshiba, Simple scalar finite element approach to optical rib waveguides. Optoelectronics, IEE Proceedings J, 1992. **139**(2): p. 166-171.

23. S.S.A. Obayya, B.M.A. Rahman, and H.A. El-Mikati, New full-vectorial numerically efficient propagation algorithm based on the finite element method. Lightwave Technology, Journal of, 2000. **18**(3): p. 409-415.

24. K. Bierwirth, N. Schulz, and F. Arndt, Finite-Difference Analysis of Rectangular Dielectric Waveguide Structures. Microwave Theory and Techniques, IEEE Transactions on, 1986. **34**(11): p. 1104-1114.

25. S. Greedy, *"Advances in the Spectral Index Method for Optoelectronic Design,"* PhD Thesis, University of Nottingham. 2002.

26. J.Yamauchi, and H. Nakano, Application of the generalized Douglas scheme to optical waveguide analysis. Opt. Quantum Electron, 1999. **31**: p. 675-687.

27. D.Z. Djurdjevic, P. Sewell, T.M. Benson and A. Vukovic, highly efficient finite-difference schemes for structures of non-rectangular cross section. Microwave and Optical Technology Letters, 2002. **33**: p. 401-407.

28. S.S. Patrick, and K.J. Webb, A variational vector finite difference analysis for dielectric waveguides. Microwave Theory and Techniques, IEEE Transactions on, 1992. **40**(4): p. 692-698.

29. A. Taflove, Computational Electrodynamics: the Finite-Difference Time Domain Method. 1998.

30. Y. Chung, N. Dagli, An assessment of finite difference beam propagation method. Quantum Electronics, IEEE Journal of, 1990. **26**(8): p. 1335-1339.

31. Y. Kane, Numerical solution of initial boundary value problems involving maxwell's equations in isotropic media. Antennas and Propagation, IEEE Transactions on, 1966. **14**(3): p. 302-307.

32. R. Luebbers, A frequency-dependent finite-difference time-domain formulation for dispersive materials. Electromagnetic Compatibility, IEEE Transactions on, 1990. **32**(3): p. 222-227.

33. W.P. Huang, A scalar finite-difference time-domain approach to guided-wave optics. Photonics Technology Letters, IEEE, 1991. **3**(6): p. 524-526.

34. F. Zheng, and C. Zhizhang, Numerical dispersion analysis of the unconditionally stable 3-D ADI-FDTD method. Microwave Theory and Techniques, IEEE Transactions on, 2001. **49**(5): p. 1006-1009.

35. M. D. Fiet, *"Computation of mode eigenfunctions in gradedindex optical fibres by the beam propagation method".* Appl. Optics, 1980. **19**: p. 2240-2246.

36. J.A. Fleck, Light propagation in graded-index optical fibers. 1978. **17**(24): p. 2990-3998.

37. R. Osgood, Comparison of finite-difference and Fourier-transform solutions of the parabolic wave equation with emphasis on integrated-optics applications. Journal of the Optical Society of America, 1991. **18**: p. 724-731.

38. T.B. Koch, and D. Wickramasinghe, Finite Element Finite Difference Propagation Algorithm for Integrated Optical Device. Electronics Letters, 1989. **28**: p. 514-516.

39. Y. Tsuji, M. Koshiba, and T. Shiraishi, Finite element beam propagation method for three-dimensional optical waveguide structures. Lightwave Technology, Journal of, 1997. **15**(9): p. 1728-1734.

40. Y. Chung, , N. Dagli, and L. Thylen, Explicit finite difference vectorial beam propagation method. Electronics Letters, 1991. **27**(23): p. 2119-2121.

41. Y. Chung, and N. Dagli, An assessment of finite difference beam propagation method. Quantum Electronics, IEEE Journal of, 1990. **26**(8): p. 1335-1339.

42. F. Schmidt, "An adaptive approach to the numerical solution of Fresnel's wave

equation". Journal of Lightwave Technology, 1993. **11**: p. 1425-1434.

43. D. Braess, and R.H.W Hoppe, "Error Reduction in Adaptive Finite Element Approximations of Elliptic Obstacle Problems". Journal of Computational Mathematics, 2009. **27**: p. 148-169.

44. Y. Tsuji, and T. Shiraishi, Finite Element Beam Propagation Method for Three-Dimensional Optical Waveguide Structures. Journal of Lightwave Technology, 1997. **15**: p. 1728-1734.

45. G.R.Hadley,"Wide-Angle Beam Propagation Using Padé approximant operators". Optics Letters, 1992. **17**: p. 1426-1428.

46. G.R.Hadley,"Multistep Method for Wide-Angle Beam Propagation". OpticsLetters, 1992. **17**(1743-1745).

47. H. Scarmozzino, "A Bidirectional Beam Propagation Method for Multiple Dielectric Interfaces". Photonics Technology Letters, 1999. **11**: p. 830-832.

48. L. Yuan and Y.Y. Lu, "An Efficient Bidirectional Propagation Method Based on Dirichlet-to-Neumann Maps". Photonics Technology Letters, 2006. **18**: p. 1967-1969.

49. M. Koshiba, Y. Tsuji, and M. Hikari, Time-domain beam propagation method and its application to photonic crystal circuits. Lightwave Technology, Journal of, 2000. **18**(1): p. 102-110.

50. L. Pao-Lo, Z. Qida, and C. Fow-Sen, Slow-wave finite-difference beam propagation method. Photonics Technology Letters, IEEE, 1995. **7**(8): p. 890-892.

51. A. Boag, and R. Mittra. A numerical absorbing boundary condition for finite element analysis. in Electrical and Electronics Engineers in Israel, 1995., Eighteenth Convention of. 1995.

52. G.R. Hadley, Transparent boundary condition for the beam propagation method. Quantum Electronics, IEEE Journal of, 1992. **28**(1): p. 363-370.

53. W.P. Huang, The perfectly matched layer (PML) boundary condition for the beam propagation method. Photonics Technology Letters, IEEE, 1996. **8**(5): p. 649-651.

54. Akleman, F. and L. Sevgi, A novel implementation of Berenger's PML for FDTD applications. Microwave and Guided Wave Letters, IEEE, 1998. **8**(10): p. 324-326.

55. I. Mansour, A.D. Capobianco, and C. Rosa, Noniterative vectorial beam propagation method with a smoothing digital filter. Lightwave Technology, Journal of, 1996. **14**(5): p. 908-913.

56. H.M. Masoudi, and J.M. Arnold, Parallel beam propagation methods. Photonics Technology Letters, IEEE, 1994. **6**(7): p. 848-850.

57. Y. Chung, and N. Dagli, Explicit finite difference beam propagation method: application to semiconductor rib waveguide Y-junction analysis. Electronics Letters, 1990. **26**(11): p. 711-713.

58. W. Huang, The finite-difference vector beam propagation method: analysis and assessment. Lightwave Technology, Journal of, 1992. **10**(3): p. 295-305.

59. W. Press, W.T. Vetterling, and B.P. Flannery, Numerical Recipes in C, 2nd ed.

1997.

60. H. Yu-Li, Y. Ming-Chuan, and C. Hung-Chun, Three-dimensional noniterative full-vectorial beam propagation method based on the alternating direction implicit method. Lightwave Technology, Journal of, 1999. **17**(11): p. 2389-2397.

61. D. W. Peaceman and H. H. Rachford, The numerical solution of parabolic and elliptic differential equations. J. Soc. Industrial Appl. Math, 1955. **3**: p. 28-41.

62. H. Vorst, *“Bi*-CGSTAB: A fast and smoothly converging variant of Bi-CG for *the solution of nonsymmetric linear systems”.* SIAM J. Sci. Statist. Comput, 1992. **13**: p. 631–644.

63. Y. Saad, "GMRES: A generalized minimal residual algorithm for solving nonsymmetric linear systems". SIAM Journal on Scientific and Statistical Computing, 1986. **7**: p. 856-869.

64. A. Cheng, Heritage and early history of the boundary element method. Engineering Analysis with Boundary Elements, 2000. **29**: p. 268-302.

65. C.M. Rappaport, Perfectly matched absorbing boundary conditions based on anisotropic lossy mapping of space. Microwave and Guided Wave Letters, IEEE, 1995. **5**(3): p. 90-92.

66. J.J. Lim,*“Investigation of Factors Influencing the Brightness of High*-Power, High-*Brightness Laser Diodes”,PhD Thesis, University of Nottingham.* 2003.

67. D.T. McGrath, and V.P. Pyati. Periodic boundary conditions for finite element analysis of infinite phased array antennas. in Antennas and Propagation

Society International Symposium, 1994. AP-S. Digest. 1994.

68. M. Lai-Ching, R. Mittra. Parallel implementation of the periodic boundary condition (PBC) in the FDTD for the investigation of spatial filters. in Antennas and Propagation Society International Symposium, 2008. AP-S 2008. IEEE. 2008.

69. D. Yevick, and B. Hermansson, New formulations of the matrix beam propagation method: application to rib waveguides. Quantum Electronics, IEEE Journal of, 1989. **25**(2): p. 221-229.

70. C.L. Xu, W.P. Huang, and S.K. Chaudhuri, Efficient and accurate vector mode calculations by beam propagation method. Lightwave Technology, Journal of, 1993. **11**(7): p. 1209-1215.

71. S. Jungling, and J.C. Chen, A study and optimization of eigenmode calculations using the imaginary-distance beam-propagation method. Quantum Electronics, IEEE Journal of, 1994. **30**(9): p. 2098-2105.

72. J. Yamauchi, Propagation Beam Analysis of Optical Waveguides. 2003.

73. Y.Z. He, Finite-difference imaginary-distance beam propagation method for modeling of the fundamental mode of photonic crystal fibers. 2003.

Chapter 4: Wide Angle FD-BPM

The previous chapter derived the paraxial FD-BPM method that can only be used to simulate propagation under a slowly varying envelope approximation (SVEA), for which $\frac{\partial^2}{\partial z^2}\psi \approx 0$ is true. This also means that only beams that propagate at small angles with respect to the propagation direction can be described accurately. Moreover, the reference refractive index needs to be appropriately chosen for the paraxial scheme [1]. In order to relax the paraxial requirement and weaken the dependence on the choice of reference refractive index, a more robust scheme, the Wide Angle (WA) FD-BPM has been developed [2, 3].

The WA-BPM scheme was first proposed by Hadley [2]. He introduced recurrence Padé method, which iteratively applies a Padé approximation process to re-introduce the $\frac{\partial^2}{\partial z^2}$ derivative in the BPM wave equation so that the SVEA approximation is removed. The recurrence Padé method can achieve good accuracy by using a high order Padé approximation operator. However, the treatment of a high order Padé approximation operator can be a challenge. To avoid the complex mathematical process, he presented the Multistep Method [3] in which a propagation step is split into several substeps and the Padé approximant operator is factored into a series of simpler Padé (1, 1) operators. Later on, rational square root approximation is combined with WA scheme [4, 5], which allows the wave equation to be written in the form that contains square root operators. The rewritten wave equation can be expressed as a rational polynomial and solved though factorization for the application of the Multistep Method. A drawback of the standard Padé approximation is that propagation of evanescent modes is incorrectly modelled, which may cause instability during the simulations. Therefore, a modification scheme, known as the rotated branch cut approximation or the rotated Padé approximation is introduced to give the evanescent modes the desired damping [4]. This chapter will introduce the WA FD-BPM issues such as the recurrence Padé approximation, the multistep method and the rotated Padé approximation, and apply the method to analyse slab and rib waveguides

4.1 Recurrence Padé Approximation

Consider the 3D scalar wave equation:

$$\frac{\partial^2\psi}{\partial x^2}+\frac{\partial^2\psi}{\partial y^2}+\frac{\partial^2\psi}{\partial z^2}-2\,j\beta_0\frac{\partial\psi}{\partial z}+(k_0^2n_r^2-\beta_0^2)\psi=0 \qquad (4.1.1)$$

which can be rearranged as:

$$\frac{\partial}{\partial z}(2\,j\beta_0-\frac{\partial}{\partial z})\psi=(\frac{\partial^2}{\partial x^2}+\frac{\partial^2}{\partial y^2}+k_0^2n_r^2-\beta_0^2)\psi \qquad (4.1.2)$$

or written as:

$$\frac{\partial}{\partial z}\psi=\frac{(\frac{\partial^2}{\partial x^2}+\frac{\partial^2}{\partial y^2}+k_0^2n_r^2-\beta_0^2)}{(2\,j\beta_0-\frac{\partial}{\partial z})}\psi \qquad (4.1.3)$$

From Eq. (4.1.3), the recurrence relation for Padé approximation is obtained as [2]:

$$\left.\frac{\partial}{\partial z}\right|_{j+1} = \frac{M}{L - \left.\frac{\partial}{\partial z}\right|_{j}} \tag{4.1.4}$$

where the subscript $j+1$ and j represent the order of the Padé approximation, and M and L are the operators, $M = \frac{\partial^2}{\partial x^2} + \frac{\partial^2}{\partial y^2} + k_0{}^2 n_r^2 - \beta_0^2$ and $L = 2j\beta_0$. Different orders of the Padé approximation can be obtained iteratively from this equation.

If Padé (1,0) is adopted, then the paraxial approximation with SVEA discussed in Chapter 3 is obtained as:

$$\frac{\partial}{\partial z} = \frac{M}{L} \tag{4.1.5}$$

By substituting Eq. (4.1.5) into Eq. (4.1.4), Padé (1,1) is obtained as:

$$\frac{\partial}{\partial z} = \frac{M}{L - \frac{M}{L}} = \frac{LM}{L^2 - M} \tag{4.1.6}$$

Similarly, this new operator could be used to obtain a higher order Padé approximation for better accuracy. Details of the recursive process are given in [2]. However, when the high order Padé approximant operator is applied, the numerator and denominator in Eq. (4.1.4) become much more complex because the number of terms for the second derivative terms $\frac{\partial^2}{\partial x^2}$ and $\frac{\partial^2}{\partial y^2}$ included in the equation increase with the recursive process. This results in large and complicated matrix problems. To avoid solving this problem, the Multistep Method for wide angle approximation is introduced, and explained in the next section.

4.2 Multistep Method

The Multistep Method [3] is a more computationally efficient algorithm compared with the recurrence Padé method. The idea is to employ an alternative propagation equation which splits each propagation step into multiple steps so that the high order Padé approximant operator is factored into a series of simpler Padé (1,1) operators. To deal with the second derivative terms in the Padé approximation operator, the Rational Square-Root Approximations [5, 6] is often applied with the Multistep Method. The scalar scheme of the Multistep Method with Rational Square-Root Approximation starts from Eq.(4.1.1), and the wave equation can be rewritten as:

$$\left(\frac{\partial}{\partial z} - j\beta_0 + j\beta_0\sqrt{1+Q}\right)\left(\frac{\partial}{\partial z} - j\beta_0 - j\beta_0\sqrt{1+Q}\right)\psi = 0\,, \qquad (4.1.7)$$

where the operator Q is set as:

$$Q = \frac{\frac{\partial^2}{\partial x^2} + \frac{\partial^2}{\partial y^2} + k_0^2 n_r^2 - \beta_0^2}{\beta_0^2}\,, \qquad (4.1.8)$$

for the scalar wave equation.

The term in the first bracket of Eq. (4.1.7) represents the forward wave propagating in the positive z-direction, and the term in the second bracket represents the backward wave propagating in the negative z-direction. If only forward propagation is assumed, then the wave equation is written as:

$$\left(\frac{\partial}{\partial \mathrm{z}} - \mathrm{j}\beta_0 + \mathrm{j}\beta_0\sqrt{1+\mathrm{Q}}\right)\psi = 0\,, \tag{4.1.9}$$

or

$$\frac{\partial \psi}{\partial \mathrm{z}} = \mathrm{j}\beta_0(1-\sqrt{1+\mathrm{Q}})\psi\,. \tag{4.1.10}$$

The discretization of Eq. (4.1.10) is:

$$\frac{\psi_{(\mathrm{x,y,z+\Delta z})} - \psi_{(\mathrm{x,y,z})}}{\Delta \mathrm{z}} = \mathrm{j}\beta_0(1-\sqrt{1+\mathrm{Q}})\frac{\psi_{(\mathrm{x,y,z+\Delta z})} + \psi_{(\mathrm{x,y,z})}}{2} \tag{4.1.11}$$

or rearranged as:

$$[1-\frac{\Delta \mathrm{z}}{2}\,\mathrm{j}\beta_0(1-\sqrt{1+\mathrm{Q}})]\psi_{(\mathrm{x,y,z+\Delta z})} = [1+\frac{\Delta \mathrm{z}}{2}\,\mathrm{j}\beta_0(1-\sqrt{1+\mathrm{Q}})]\psi_{(\mathrm{x,y,z})} \tag{4.1.12}$$

It is known that the Padé (n, n) approximation of $\sqrt{1+\mathrm{Q}}$ can be written as [7]:

$$\sqrt{1+\mathrm{Q}} = 1 + \sum_{\mathrm{j}=1}^{\mathrm{n}} \frac{\mathrm{a}_\mathrm{j}^{(\mathrm{n})}\mathrm{Q}}{1+\mathrm{b}_\mathrm{j}^{(\mathrm{n})}\mathrm{Q}} = \prod_{\mathrm{j}=1}^{\mathrm{n}} \frac{1+\mathrm{c}_\mathrm{j}^{(\mathrm{n})}\mathrm{Q}}{1+\mathrm{b}_\mathrm{j}^{(\mathrm{n})}\mathrm{Q}} \tag{4.1.13}$$

where $\mathrm{b}_\mathrm{j}^{(\mathrm{n})} = \cos^2\left(\frac{\mathrm{j}\pi}{2\mathrm{n}+1}\right)$, $\mathrm{c}_\mathrm{j}^{(\mathrm{n})} = \sin^2\left(\frac{\mathrm{j}\pi}{2\mathrm{n}+1}\right)$ and $\mathrm{a}_\mathrm{j}^{(\mathrm{n})} = \frac{2\mathrm{c}_\mathrm{j}^{(\mathrm{n})}}{2\mathrm{n}+1}$. In order to avoid the treatment of the trigonometric function in Eq.(4.1.13), an alternative approach to apply the Padé approximant is introduced in the following part.

A commonly used approximation method for the square root operator $\sqrt{1+Q}$ is to apply the Taylor series and the operator is approximated as:

$$\sqrt{1+Q}=\sum_{n=0}^{\infty}\frac{(-1)^n(2n)!}{(1-2n)n!^2\,4^n}Q^n \approx 1+\frac{1}{2}Q-\frac{1}{8}Q^2+\frac{1}{16}Q^3-\frac{5}{128}Q^4\cdots \tag{4.1.14}$$

where n represents the n^{th} order of the series. The larger the n value is, the more accurate the approximation is.

Therefore, the whole expression in the bracket can be approximated as:

$$1-\sqrt{1+Q}=1-\sum_{n=0}^{\infty}\frac{(-1)^n(2n)!}{(1-2n)n!^2\,4^n}Q^n \approx -\frac{1}{2}Q+\frac{1}{8}Q^2-\frac{1}{16}Q^3+\frac{5}{128}Q^4\cdots \tag{4.1.15}$$

By applying Padé approximation to the square root operator, a rational function is obtained as:

$$1-\sqrt{1+Q}=\frac{\sum_{i=0}^{k}a_iQ^i}{\sum_{i=0}^{k}b_iQ^i} \tag{4.1.16}$$

where k represents the k^{th} order of Padé approximation.

Therefore, Eq. (4.1.12) can be written as:

$$[1-\frac{\Delta z}{2}\,j\beta_0\frac{\sum_{i=0}^{k}a_iQ^i}{\sum_{i=0}^{k}b_iQ^i}]\cdot\psi_{(x,y,z+\Delta z)}=[1+\frac{\Delta z}{2}\,j\beta_0\frac{\sum_{i=0}^{k}a_iQ^i}{\sum_{i=0}^{k}b_iQ^i}]\cdot\psi_{(x,y,z)} \tag{4.1.17}$$

or rearranged as:

$$[\sum_{i=0}^{k} b_i Q^i - \frac{\Delta z}{2} j\beta_0 \sum_{i=0}^{k} a_i Q^i] \cdot \psi_{(x,y,z+\Delta z)} = [\sum_{i=0}^{k} b_i Q^i + \frac{\Delta z}{2} j\beta_0 \sum_{i=0}^{k} a_i Q^i] \cdot \psi_{(x,y,z)} \quad (4.1.18)$$

In Eq.(4.1.18), the coefficients b_i and a_i can be combined as a complex coefficient of a specific order operator Q^i as:

$$\begin{aligned}&[(b_0 - \frac{\Delta z}{2} j\beta_0 a_0)Q^0 + (b_1 - \frac{\Delta z}{2} j\beta_0 a_1)Q^1 + \cdots (b_k - \frac{\Delta z}{2} j\beta_0 a_k)Q^k] \cdot \psi_{(x,y,z+\Delta z)} \\ &= [(b_0 + \frac{\Delta z}{2} j\beta_0 a_0)Q^0 + (b_1 + \frac{\Delta z}{2} j\beta_0 a_1)Q^1 + \cdots (b_k + \frac{\Delta z}{2} j\beta_0 a_k)Q^k] \cdot \psi_{(x,y,z)}\end{aligned} \quad (4.1.19)$$

Eq. (4.1.19) shows clearly that the coefficients on the right hand side are the conjugate of those on the left hand side for the same order operator Q. If it is set that $c_i = b_i - \frac{\Delta z}{2} j\beta a_i$ and $c_i^* = b_i + \frac{\Delta z}{2} j\beta a_i$, then the equation can be rewritten in simpler polynomial form as:

$$[\sum_{i=0}^{k} c_i Q^i] \cdot \psi_{(x,y,z+\Delta z)} = [\sum_{i=0}^{k} c_i^* Q^i] \cdot \psi_{(x,y,z)} \quad (4.1.20)$$

Eq.(4.1.20) can be rewritten in terms of:

$$A \cdot \prod_{i=1}^{k} (Q - d_i) \cdot \psi_{(x,y,z+\Delta z)} = A^* \cdot \prod_{i=1}^{k} (Q - d_i^*) \cdot \psi_{(x,y,z)} \quad (4.1.21)$$

where A and A^* are conjugate constants, d_i and d_i^* are conjugate roots of the i^{th} order operator Q.

By adopting the Multistep Method, each propagation step is split into k steps with the space interval $\frac{1}{k}\Delta z$ and Eq. (4.1.21) is broken into k equations as:

$$\begin{aligned}
\sqrt[k]{A}\cdot(Q-d_1)\cdot\psi_{(x,y,z+\frac{1}{k}\Delta z)} &= \sqrt[k]{A^*}\cdot(Q-d_1^*)\cdot\psi_{(x,y,z)} \\
&\vdots \\
\sqrt[k]{A}\cdot(Q-d_j)\cdot\psi_{(x,y,z+\frac{j}{k}\Delta z)} &= \sqrt[k]{A^*}\cdot(Q-d_j^*)\cdot\psi_{(x,y,z+\frac{j-1}{k}\Delta z)} \\
&\vdots \\
\sqrt[k]{A}\cdot(Q-d_k)\cdot\psi_{(x,y,z+\Delta z)} &= \sqrt[k]{A^*}\cdot(Q-d_k^*)\cdot\psi_{(x,y,z+\frac{k-1}{k}\Delta z)}
\end{aligned} \tag{4.1.22}$$

Extending the operator Q and applying the CN scheme to the j$^{\text{th}}$ equation of Eq.(4.1.22) gives:

$$\begin{aligned}
&\frac{\sqrt[k]{A}}{\beta_0^2}\cdot\Bigg[\frac{\psi_{(x+\Delta x,y,z+\frac{j}{k}\Delta z)}-2\psi_{(x,y,z+\frac{j}{k}\Delta z)}+\psi_{(x-\Delta x,y,z+\frac{j}{k}\Delta z)}}{\Delta x^2}+\frac{\psi_{(x,y+\Delta y,z+\frac{j}{k}\Delta z)}-2\psi_{(x,y,z+\frac{j}{k}\Delta z)}+\psi_{(x,y-\Delta y,z+\frac{j}{k}\Delta z)}}{\Delta y^2} \\
&\qquad +(k_0^2n_r^2-\beta_0^2)\cdot\psi_{(x,y,z+\frac{j}{k}\Delta z)}\Bigg]-\sqrt[k]{A}\cdot d_j\cdot\psi_{(x,y,z+\frac{j}{k}\Delta z)} \\
&=\frac{\sqrt[k]{A^*}}{\beta_0^2}\cdot\Bigg[\frac{\psi_{(x+\Delta x,y,z+\frac{j-1}{k}\Delta z)}-2\psi_{(x,y,z+\frac{j-1}{k}\Delta z)}+\psi_{(x-\Delta x,y,z+\frac{j-1}{k}\Delta z)}}{\Delta x^2}+\frac{\psi_{(x,y+\Delta y,z+\frac{j-1}{k}\Delta z)}-2\psi_{(x,y,z+\frac{j-1}{k}\Delta z)}+\psi_{(x,y-\Delta y,z+\frac{j-1}{k}\Delta z)}}{\Delta y^2} \\
&\qquad +(k_0^2n_r^2-\beta_0^2)\cdot\psi_{(x,y,z+\frac{j-1}{k}\Delta z)}\Bigg]-\sqrt[k]{A^*}\cdot d_j^*\cdot\psi_{(x,y,z+\frac{j-1}{k}\Delta z)}
\end{aligned} \tag{4.1.23}$$

Eq. (4.1.23) can be rearranged in the form of:

$$\begin{aligned}
&A_{z+\frac{j}{k}\Delta z}\psi_{(x+\Delta x,y,z+\frac{j}{k}\Delta z)}+B_{z+\frac{j}{k}\Delta z}\psi_{(x-\Delta x,y,z+\frac{j}{k}\Delta z)}+C_{z+\frac{j}{k}\Delta z}\psi_{(x,y,z+\frac{j}{k}\Delta z)} \\
&\qquad +D_{z+\frac{j}{k}\Delta z}\psi_{(x,y+\Delta y,z+\frac{j}{k}\Delta z)}+E_{z+\frac{j}{k}\Delta z}\psi_{(x,y-\Delta y,z+\frac{j}{k}\Delta z)} \\
&=A_{z+\frac{j-1}{k}\Delta z}\psi_{(x+\Delta x,y,z+\frac{j-1}{k}\Delta z)}+B_{z+\frac{j-1}{k}\Delta z}\psi_{(x-\Delta x,y,z+\frac{j-1}{k}\Delta z)}+C_{z+\frac{j-1}{k}\Delta z}\psi_{(x,y,z+\frac{j-1}{k}\Delta z)} \\
&\qquad +D_{z+\frac{j-1}{k}\Delta z}\psi_{(x,y+\Delta y,z+\frac{j-1}{k}\Delta z)}+E_{z+\frac{j-1}{k}\Delta z}\psi_{(x,y-\Delta y,z+\frac{j-1}{k}\Delta z)}
\end{aligned} \tag{4.1.24}$$

where the coefficients are:

$$
\begin{aligned}
&A_{z+\frac{j}{k}\Delta z} = B_{z+\frac{j}{k}\Delta z} = \frac{\sqrt[k]{A}}{\beta_0^2 \Delta x^2} \\
&D_{z+\frac{j}{k}\Delta z} = E_{z+\frac{j}{k}\Delta z} = \frac{\sqrt[k]{A}}{\beta_0^2 \Delta y^2} \\
&C_{z+\frac{j}{k}\Delta z} = \frac{\sqrt[k]{A}}{\beta_0^2}[\frac{-2}{\Delta x^2} + \frac{-2}{\Delta y^2} + (k_0^2 n_r^2 - \beta_0^2)] - \sqrt[k]{A} \cdot d_j \\
&A_{z+\frac{j-1}{k}\Delta z} = B_{z+\frac{j-1}{k}\Delta z} = \frac{\sqrt[k]{A^*}}{\beta_0^2 \Delta x^2} \\
&D_{z+\frac{j-1}{k}\Delta z} = E_{z+\frac{j-1}{k}\Delta z} = \frac{\sqrt[k]{A^*}}{\beta_0^2 \Delta y^2} \\
&C_{z+\frac{j-1}{k}\Delta z} = \frac{\sqrt[k]{A^*}}{\beta_0^2}[\frac{-2}{\Delta x^2} + \frac{-2}{\Delta y^2} + (k_0^2 n_r^2 - \beta_0^2)] - \sqrt[k]{A^*} \cdot d_j^*
\end{aligned}
,
$$

For 2D problem, the term $\frac{\partial^2}{\partial y^2}$ in Eq. (4.1.8) is removed and Eq. (4.1.24) reduces to:

$$
\begin{aligned}
&A_{z+\frac{j}{k}\Delta z}\psi_{(x+\Delta x, z+\frac{j}{k}\Delta z)} + B_{z+\frac{j}{k}\Delta z}\psi_{(x-\Delta x, z+\frac{j}{k}\Delta z)} + C_{z+\frac{j}{k}\Delta z}\psi_{(x, z+\frac{j}{k}\Delta z)} \\
&= A_{z+\frac{j-1}{k}\Delta z}\psi_{(x+\Delta x, z+\frac{j-1}{k}\Delta z)} + B_{z+\frac{j-1}{k}\Delta z}\psi_{(x-\Delta x, z+\frac{j-1}{k}\Delta z)} + C_{z+\frac{j-1}{k}\Delta z}\psi_{(x, z+\frac{j-1}{k}\Delta z)}
\end{aligned}
\qquad (4.1.25)
$$

where the coefficients are:

$$
\begin{aligned}
&A_{z+\frac{j}{k}\Delta z} = B_{z+\frac{j}{k}\Delta z} = \frac{\sqrt[k]{A}}{\beta_0^2 \Delta x^2} \\
&C_{z+\frac{j}{k}\Delta z} = \frac{\sqrt[k]{A}}{\beta_0^2}[\frac{-2}{\Delta x^2} + (k_0^2 n_r^2 - \beta_0^2)] - \sqrt[k]{A} \cdot d_j \\
&A_{z+\frac{j-1}{k}\Delta z} = B_{z+\frac{j-1}{k}\Delta z} = \frac{\sqrt[k]{A^*}}{\beta_0^2 \Delta x^2} \\
&C_{z+\frac{j-1}{k}\Delta z} = \frac{\sqrt[k]{A^*}}{\beta_0^2}[\frac{-2}{\Delta x^2} + (k_0^2 n_r^2 - \beta_0^2)] - \sqrt[k]{A^*} \cdot d_j^*
\end{aligned}
$$

Eq.(4.1.24) or Eq. (4.1.25) can be treated as a sparse diagonal matrix system and solved by the matrix solvers as the paraxial FD-BPM problem discussed in Chapter 3.

For the 3D TM polarisation semi-vectorial wave equation, the operator in Eq. (4.1.7) is:

$$Q = \frac{\frac{\partial}{\partial x}\left[\frac{1}{n_r^2}\frac{\partial}{\partial x}(n_r^2)\right] + \frac{\partial^2}{\partial y^2} + k_0^2 n_r^2 - \beta_0^2}{\beta_0^2}. \tag{4.1.26}$$

For the 3D TE polarisation semi-vectorial wave equation, the operator in Eq. (4.1.7) is:

$$Q = \frac{\frac{\partial^2}{\partial x^2} + \frac{\partial}{\partial y}\left[\frac{1}{n_r^2}\frac{\partial}{\partial y}(n_r^2)\right] + k_0^2 n_r^2 - \beta_0^2}{\beta_0^2}. \tag{4.1.27}$$

The coefficients for both semi-vectorial cases are derived similarly and summarised in the **Appendix 1**.

Theoretically, good accuracy of the simulation results can be achieved if a high order Padé approximation is applied. However, the drawback of this scheme is the presence of unphysical poles along the negative real axis when the square root operator is evaluated by the Padé approximation. The square roots d_j and d_j^* in Eq.(4.1.21) may have negative solutions less than -1 if high order Padé approximation operator is applied. From the viewpoint of a control system, these solutions result in the instability of the system and produce large errors. One of the methods to solve this problem is to rotate the original real axis branch [4, 8]. This will be discussed in the next section.

4.3 Rotated Branch Cut Approximation

The poles on the real axis that cause instability can be rotated using the rotated branch cut approximation [4]. This method rotates the poles by a specific angle θ so that the poles are off the real axis. Typically, the angle is set as $\theta = \pm 90^{\circ}$, which moves the poles to the imaginary axis and makes the Padé approximation stable.

If axis rotation by an angle $\boldsymbol{\theta}$ is used, the square root operator in Eq.(4.1.7) can be written as:

$$\sqrt{1+\mathrm{Q}} = \mathrm{e}^{\mathrm{j}\theta/2}\sqrt{1+\left\{\left(1+\mathrm{Q}\right)\mathrm{e}^{-\mathrm{j}\theta}-1\right\}}\ . \tag{4.2.1}$$

A new operator $\mathrm{R} = \left(1+\mathrm{Q}\right)\mathrm{e}^{-\mathrm{j}\theta} - 1$ can be introduced where

$$1-\sqrt{1+\mathrm{Q}} = 1-\mathrm{e}^{\mathrm{j}\theta/2}\sqrt{1+\mathrm{R}}\ . \tag{4.2.2}$$

If $\theta = -90^{\circ}$,

$$1-\sqrt{1+\mathrm{Q}} = 1-\mathrm{e}^{\mathrm{j}\theta/2}\sqrt{1+\mathrm{R}} = 1-\left(\frac{\sqrt{2}}{2}-\mathrm{j}\,\frac{\sqrt{2}}{2}\right)\cdot\sqrt{1+\mathrm{R}}\,, \tag{4.2.3}$$

and the Taylor series of Eq.(4.2.3) is:

$$1-\left(\frac{\sqrt{2}}{2}-\mathrm{j}\,\frac{\sqrt{2}}{2}\right)\cdot\sqrt{1+\mathrm{R}} = 1-\left(\frac{\sqrt{2}}{2}-\mathrm{j}\,\frac{\sqrt{2}}{2}\right)\cdot\sum_{\mathrm{n}=0}^{\infty}\frac{(-1)^{\mathrm{n}}(2\mathrm{n})!}{(1-2\mathrm{n})\mathrm{n}!^{2}\,4^{\mathrm{n}}}\mathrm{R}^{\mathrm{n}} \tag{4.2.4}$$

Padé approximation of Eq.(4.2.4) gives the factor in the form of k roots to obtain equation:

$$B\cdot\prod_{i=0}^{k}(R-f_i)\cdot\psi_{(x,y,z+\Delta z)} = B^*\cdot\prod_{i=0}^{k}(R-f_i^*)\cdot\psi_{(x,y,z)} \qquad (4.2.5)$$

If the operator R is replaced by $-1+j\cdot(1+Q)$, this results in a new form as:

$$\sqrt[k]{B}\cdot(-1+j\cdot(1+Q)-f_j)\cdot\psi_{(x,y,z+\frac{j}{k}\Delta z)} = \sqrt[k]{B^*}\cdot(-1+j\cdot(1+Q)-f_j^*)\cdot\psi_{(x,y,z+\frac{j-1}{k}\Delta z)}$$

$$(4.2.6)$$

Extending the operator Q and applying the CN scheme results in an equation in the form of Eq. (4.1.24). For 3D scalar situation, the coefficients are:

$$A_{z+\frac{j}{k}\Delta z} = B_{z+\frac{j}{k}\Delta z} = j\frac{\sqrt[k]{B}}{\beta_0^2\Delta x^2}$$

$$D_{z+\frac{j}{k}\Delta z} = E_{z+\frac{j}{k}\Delta z} = j\frac{\sqrt[k]{B}}{\beta_0^2\Delta y^2}$$

$$C_{z+\frac{j}{k}\Delta z} = \sqrt[k]{B}\left(-1-f_j+j\frac{k_0^2n_r^2}{\beta_0^2}\right)-j\frac{2\sqrt[k]{B}}{\beta_0^2\Delta x^2}-j\frac{2\sqrt[k]{B}}{\beta_0^2\Delta y^2}$$

$$A_{z+\frac{j-1}{k}\Delta z} = B_{z+\frac{j-1}{k}\Delta z} = j\frac{\sqrt[k]{B^*}}{\beta_0^2\Delta x^2}$$

$$D_{z+\frac{j-1}{k}\Delta z} = E_{z+\frac{j-1}{k}\Delta z} = j\frac{\sqrt[k]{B^*}}{\beta_0^2\Delta y^2}$$

$$C_{z+\frac{j-1}{k}\Delta z} = \sqrt[k]{B^*}\left(-1-f_j^*+j\frac{k_0^2n_r^2}{\beta_0^2}\right)-j\frac{2\sqrt[k]{B^*}}{\beta_0^2\Delta x^2}-j\frac{2\sqrt[k]{B^*}}{\beta_0^2\Delta y^2}$$

The coefficients for the semi-vectorial cases are summarised in the **Appendix 2**.

For 2D problems, the wave equation is reduced to the form of Eq. (4.1.25) with the coefficients that are only with respect to one transverse direction.

It should be noticed that this method requires the Padé approximation operator to be a high order for good accuracy [8]. In [8], an alternative rotated branch cut approach is provided. A complex coefficient rational approximation for the square root operator is developed and an efficient numerical algorithm for computing the prime fraction expansion of the modified Padé approximation is presented. By this method, the rotated square root operator is expanded using a Padé approximation denoted by Padé(n,n) as

$$\sqrt{1+R} = \prod_{i=1}^{n} \frac{1+c_i^{(n)}R}{1+b_i^{(n)}R} \tag{4.2.7}$$

where $c_i^{(n)}$ and $b_i^{(n)}$ are the zeros of the following functions F and G [8], respectively:

$$F(z) = \sum_{i=1}^{n} \frac{\sin^2(2i\theta)}{z-\cos^2(i\theta)} + (2n+1)(1-\frac{2j}{\beta}) \tag{4.2.8}$$

$$G(z) = \sum_{i=1}^{n} \frac{\sin^2(2i\theta)}{z-\sin^2(i\theta)} + (2n+1)(1-\frac{2j}{\beta}) \tag{4.2.9}$$

in which $\theta = \pi/(2n+1)$ and $\boldsymbol{\beta}$ is taken to be unity in the present analysis.

4.4 Results

This part will test the feasibility and the effectiveness of the WA-BPM scheme. The simulation results are obtained for slab waveguide and rib waveguide, respectively. For each case, the field profiles obtained by the paraxial BPM and the WA-BPM with different order Padé approximations will be compared firstly to give an intuitive concept that how the WA scheme improves the simulations for a tilted waveguide compared to the paraxial scheme, and then the simulation accuracy of the WA scheme will be investigated. The running time of the WA scheme will also be discussed for the case of slab waveguide.

4.4.1 Results for Slab Waveguide

To verify the implementation of the wide angle scheme, a slab waveguide is chosen for the test simulation in this section. The core width of the waveguide is w_{core}=1μm. The waveguide core and the cladding refractive indices are n_{core}=3.6 and $n_{cladding}$=3.42 respectively. The high refractive index contrast is deliberate to show the effect of changing refractive index in the propagation direction. The operating wavelength is λ= 0.86μm. The initial input is the fundamental mode of the waveguide, obtained by the ID BPM mode solver. The transverse mesh size is set as Δx=0.01μm and the longitudinal calculation step Δz is adjusted according to the need of different test simulations.

The waveguide is tilted by an angle δ with respect to the z-axis, as shown in Fig. 4.1. The projected core width, w^*, and transverse mesh size, Δx^*, onto the x-axis is $w^* = w/\cos\delta$ and $\Delta x^* = \Delta x/\cos\delta$, where w and Δx represent the waveguide width and the transverse mesh size used in normal incident case. The width of the simulation window is set as $W^* = W/\cos\delta$, where W is 100µm. The broad width of the simulation window is to mitigate the effect of reflection from the boundaries. PML is applied at the edges of the simulation window. The thickness of the PML layer is 5µm and the absorption strength factor in Eq. (3.4.11) is set as A=4. To excite the tilted waveguide, the fundamental modal field is adjusted by taking the inclination of the wavefront into account:

$$\psi(x^*) = E_0(x)\exp(-j\beta_{eff}\,x^*\sin\delta) \tag{4.2.10}$$

in which $E_0(x)$ and β_{eff} represent the field profile and propagation constant of the fundamental mode obtained by the ID BPM solver, respectively [9].

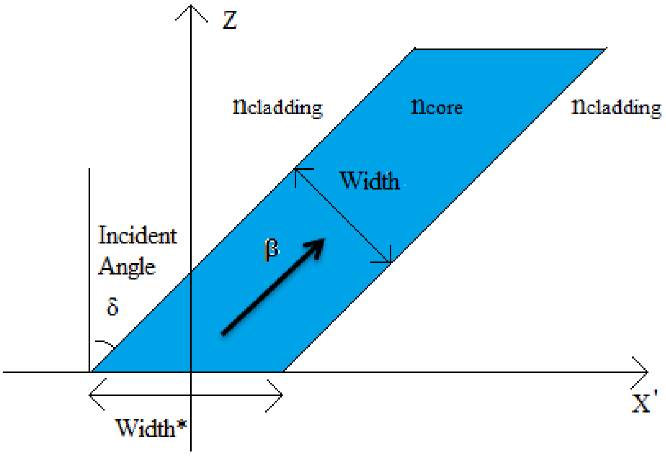

Figure 4.1: fundamental modal field launched into a tilted waveguide

Firstly, the performances of the Paraxial scheme and the WA scheme applying multistep method for simulating the beam propagation in a slab waveguide with different tilted angles are tested. The tilted angles of the waveguide are in step of every 5 degrees, form 0 degrees to 45 degrees. The length of the simulation window is 20µm along z-direction and the longitudinal calculation step is 0.1 µm. Fig. 4-2 to Fig. 4-4 illustrate the field profiles obtained by the paraxial, Padé (1,1) and Padé (2,2) schemes respectively. They clearly show how the field profiles change with the tilted angle when different approximation schemes are applied.

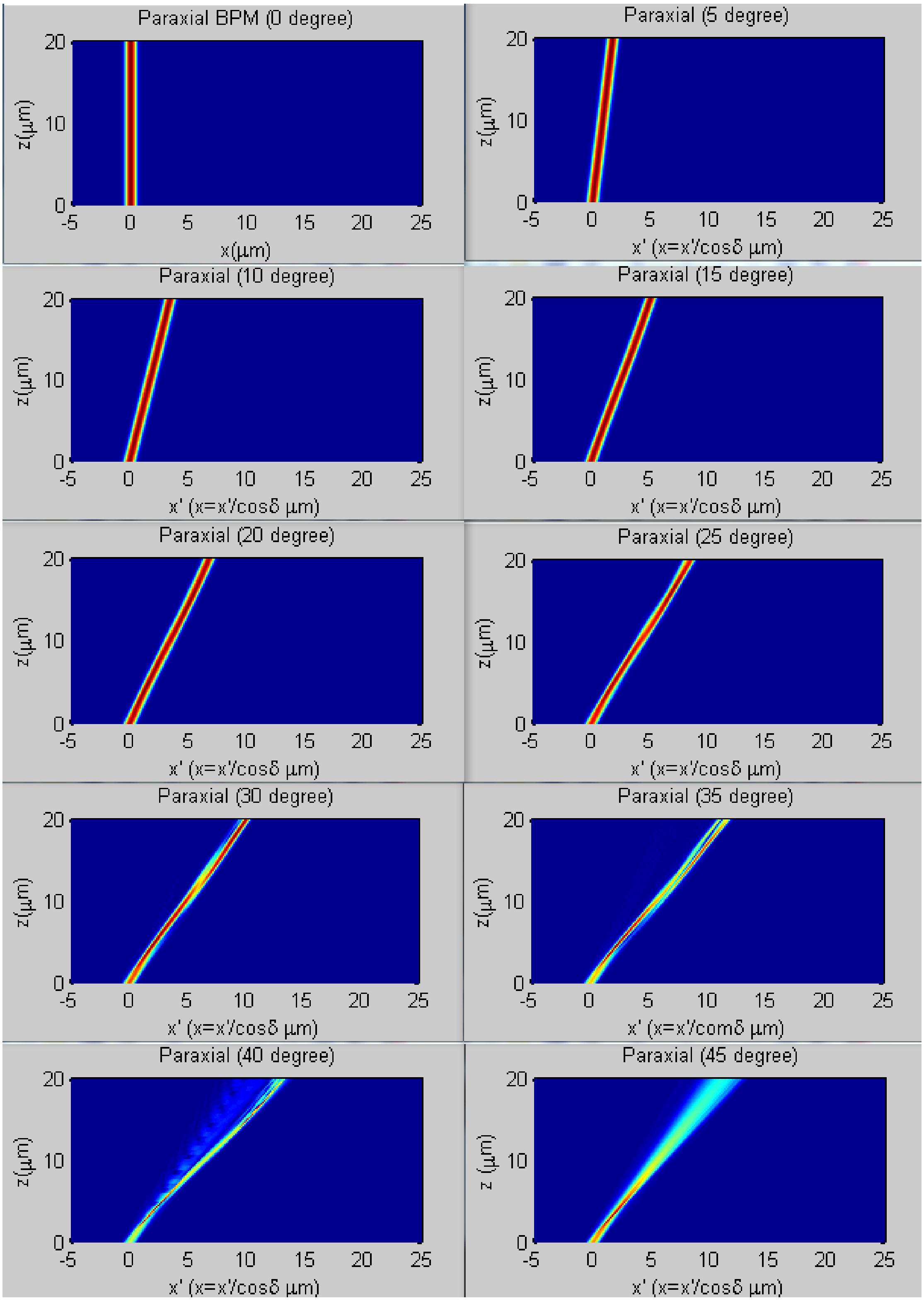

Figure 4.2: Field profiles of fundamental mode being launched into a tilted slab waveguide using the paraxial BPM scheme for different tilted angles

from 0^o to 45^o.

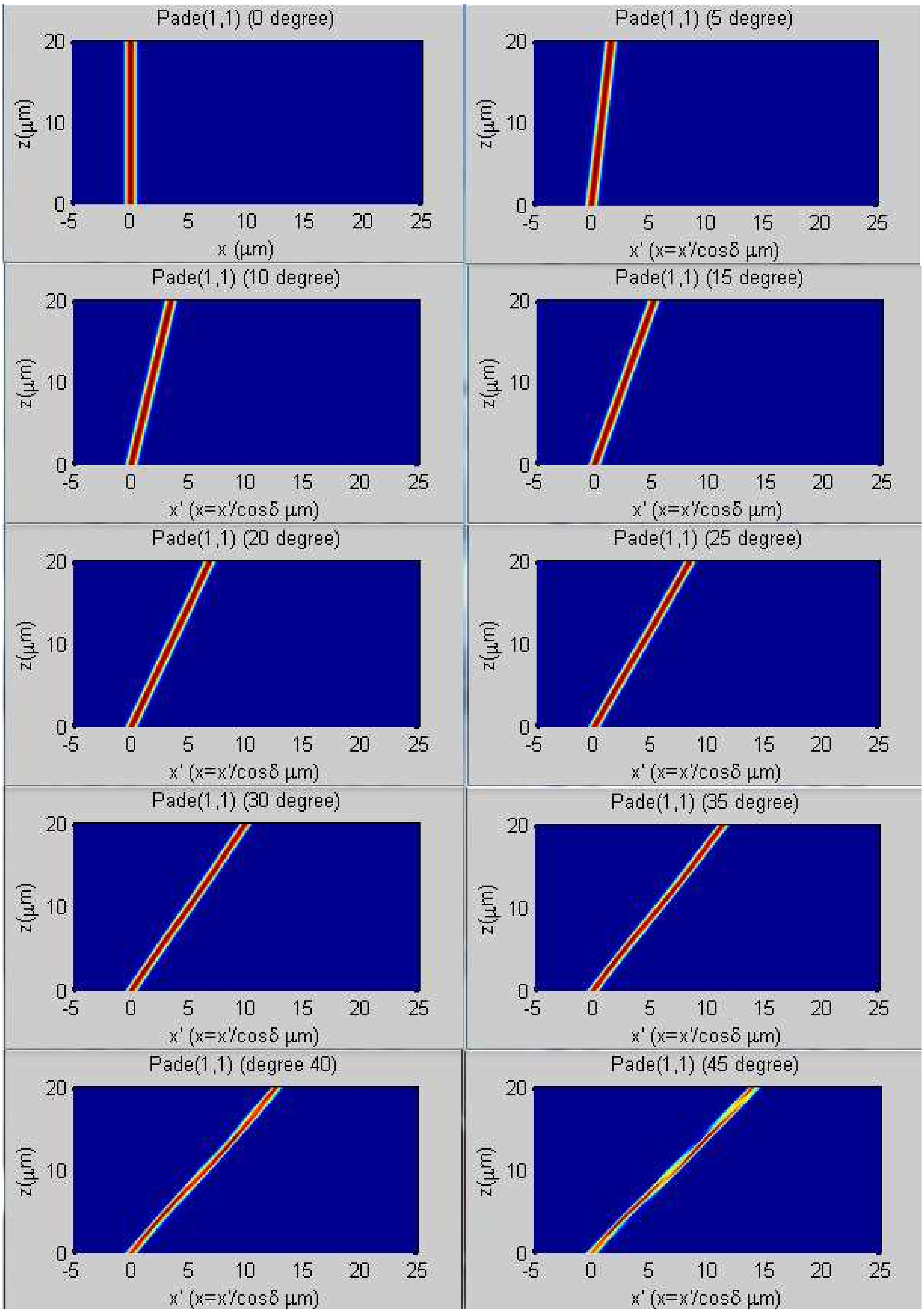

Figure 4.3: Field profiles of fundamental mode being launched into a tilted slab waveguide using the WA scheme with Padé (1,1) for different tilted

angles from 0^o to 45^o.

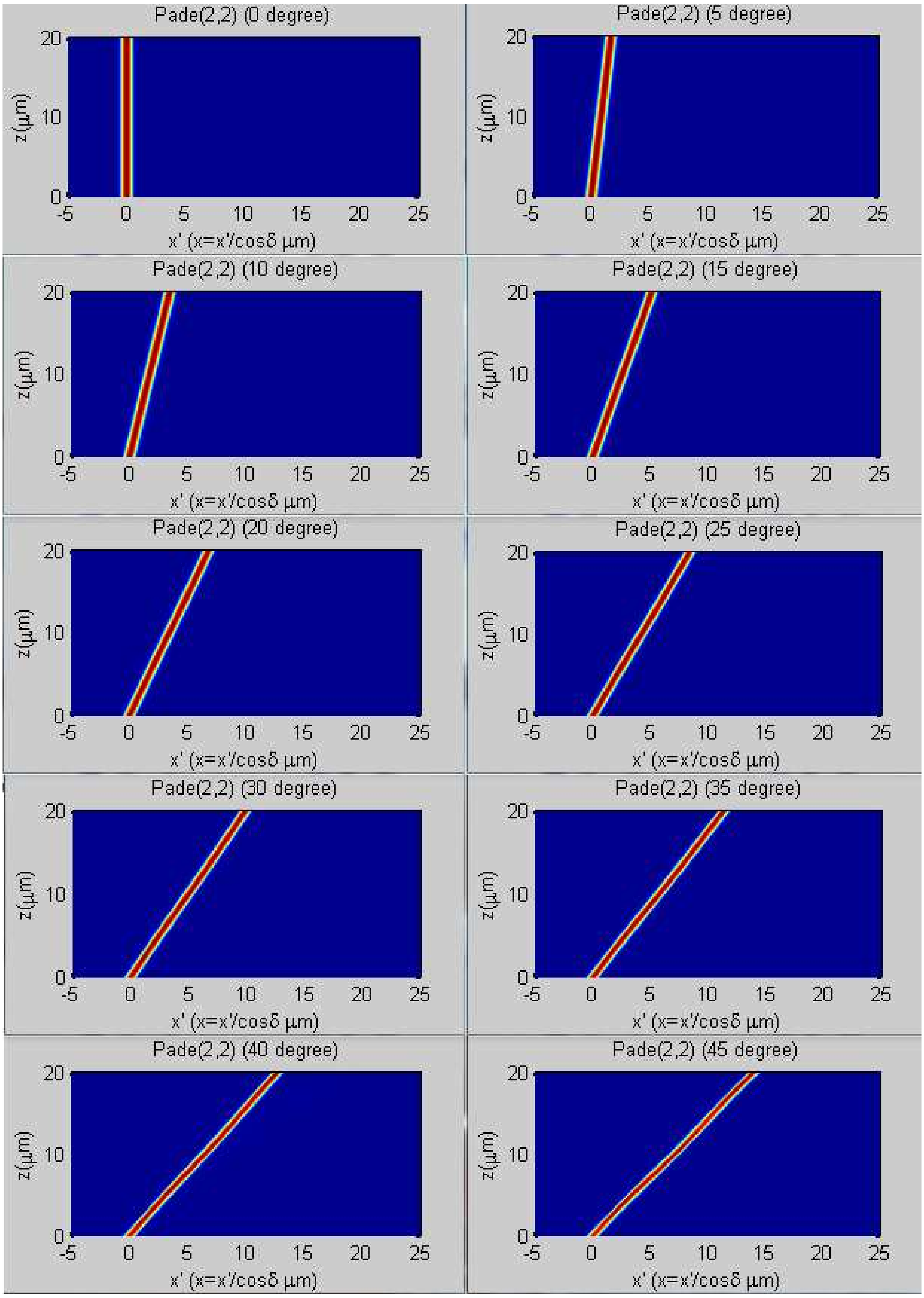

Figure 4.4: Field profiles of fundamental mode being launched into a tilted slab waveguide using the WA scheme with Padé (2,2) for different tilted

angles from 0^o to 45^o.

Ideally, the profile pattern of the beam should be that of the fundamental waveguide mode. However, from Fig.4.2-Fig.4.4, it can be seen that different Padé schemes provided different simulation results with the changes of the tilted angle. When the tilted angle of the waveguide is small ($\delta \le 20$ degree), the wave is well confined in the waveguide, regardless of what approximation scheme is applied. With increasing of the tilted angle, the paraxial approximation is no longer suitable. Fringes of wave can be seen and the mode is not confined in the waveguide. The results are improved by using the WA approximation. The wave is confined in the waveguide even when the tilted angle is large. Moreover, the WA scheme with a higher order Padé operator allows better representation of the waveguide with a large tilted angle.

In order to further analyze the field profiles, Fig. 4.5 presents the field distributions obtained by different approximation schemes after 50μm propagation along z-direction when the waveguide is tilted 30 degree. The longitudinal calculation step is 0.1 μm. The obtained FD-BPM results are compared against the analytical result. It can be seen that the field distribution obtained from the paraxial scheme is seriously distorted. Comparatively, the WA scheme provided much better results where increased Padé order increases the accuracy of the result.

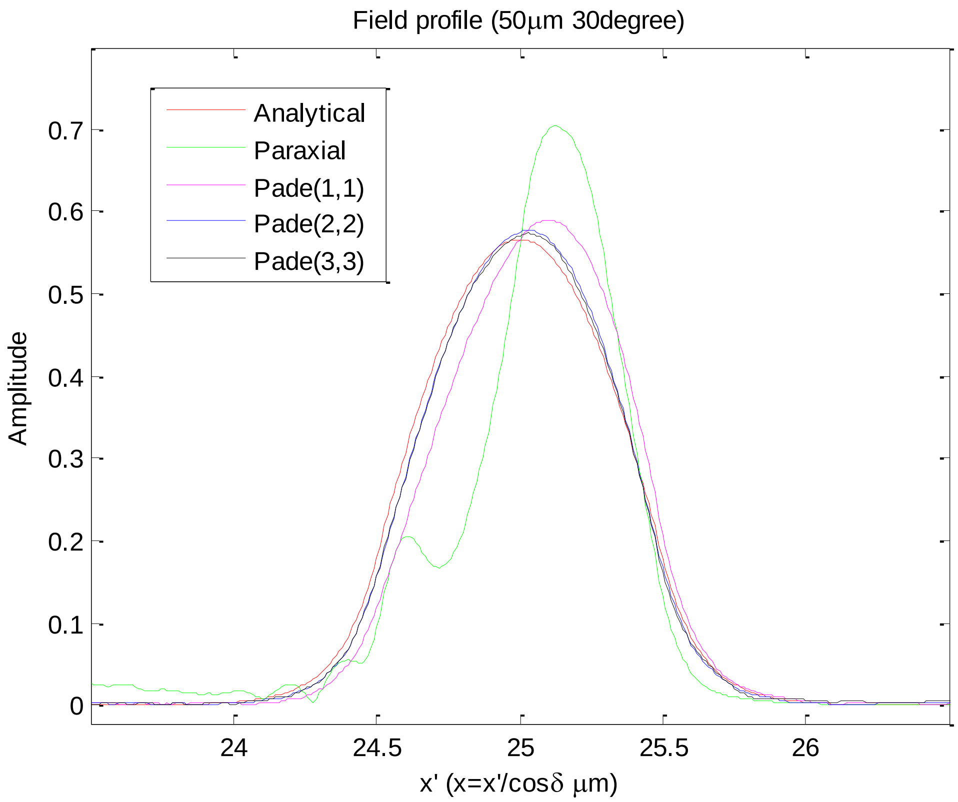

Figure 4.5: Field distribution of a 30 degree tilted Gaussian profile wave launched in a slab waveguide after 50μm using different simulation schemes

The accuracy is improved by using a higher order Padé approximation. However, higher order WA approximation requires higher computational cost and longer simulation time. Typically, Padé(n,n) wide angle scheme should take n/m times longer than Padé(m,m), where n>m . Fig.4.6 illustrates the simulation time of Padé(5,5), Padé(10,10) and Padé(20,20) with different longitudinal calculation steps Δz when the slab waveguide is tilted by an angle of 45 degree. The simulation window is 50μm wide along x-direction and 5μm long along z-direction.

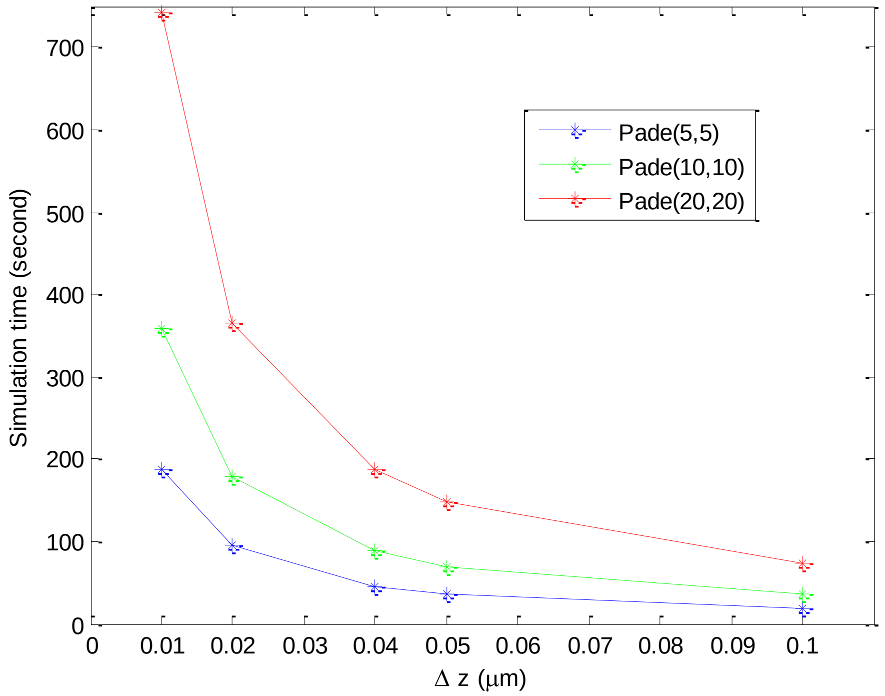

Figure 4.6: Simulation run-time for different order Padé approximations versus changed longitudinal sampling step. The transverse mesh size is Δx=0.01μm.

It can be seen that a lower order Padé approximation or a larger calculation step consumes shorter simulation time, but a higher order Padé approximation or a smaller calculation step consumes longer simulation time. In practice, the simulation time is dependent on the cycling times of the application of the tri-diagonal matrix solver. It can be evaluated by the relationship:

$$t = Z / \Delta z \cdot n \cdot T_0 \tag{4.2.11}$$

where t is the simulation time, Z is the propagation distance along z-direction, n is the order of Padé approximation, and T_0 is the running time of the matrix solver for a single operation. This equation is also efficient to estimate the run-time of the

WA-BPM for modelling other waveguides.

Subsequently, it is investigating how the simulation accuracy of the WA scheme is affected by the change of the longitudinal sampling step Δz and the Padé order. Power error between the incident field and the output field is taken into account to assess the simulation accuracy.

The simulations are based on the slab waveguide with a tilted angle of 45 degree excited by the fundamental mode. Over a distance of 30 μm along the propagation direction, the output power is calculated and compared with the incident power. The power error is calculated by the equation:

$$\mathrm{Error} = 10 \cdot \log \left| \frac{\int \left|\psi_{\mathrm{output}}\right|^2 dx}{\int \left|\psi_{\mathrm{incident}}\right|^2 dx} - 1 \right| \tag{4.2.12}$$

Firstly, simulation is implemented under the condition that the Padé order is fixed but the longitudinal calculation step Δz is changed. Three different order Padé approximations, Padé(1,1), Padé(2,2) and Padé(3,3), are applied respectively for various Δz, which is set as 10 different values between 0.01μm to 0.2μm. The errors for different Δz are plotted in Fig. 4.7.

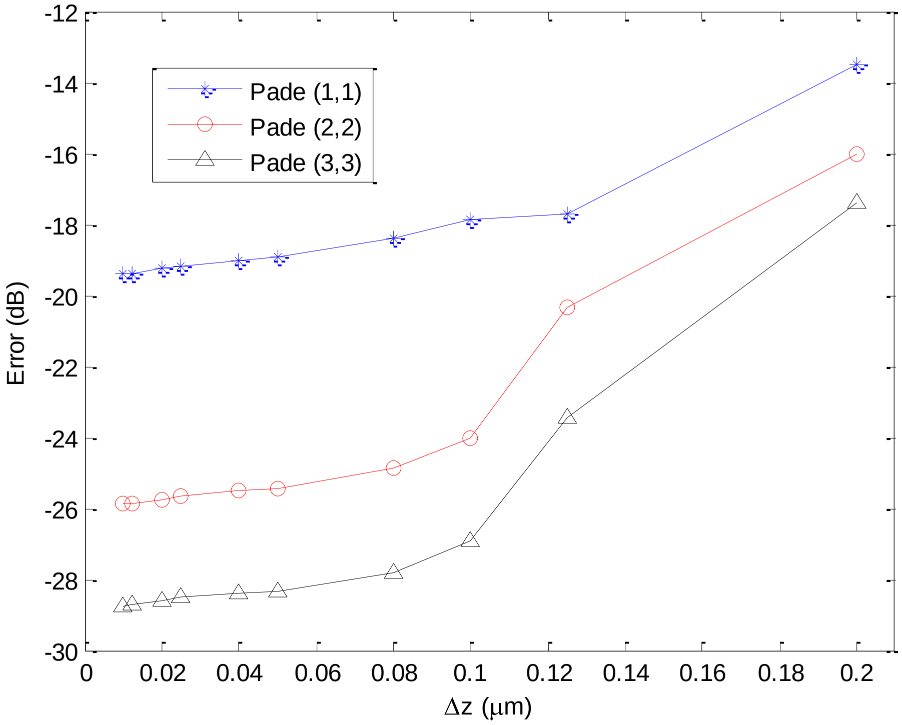

Figure 4.7: Calculation errors obtained by Padé(1,1), Padé(2,2) and Padé(3,3) approximations for the slab waveguide are presented as a function of the longitudinal calculation step Δz. The transverse mesh size is Δx=0.01µm.

Fig.4.7 indicates that the simulation accuracy can be improved by reducing the longitudinal calculation step. Comparing the power errors obtained when Δz=0.01µm and Δz=0.2µm, a significant improvement is achieved. However, smaller Δz requires longer simulation time for a fixed Padé order.

Secondly, simulation is implemented under the condition that the longitudinal calculation step Δz is fixed but the Padé order is changed. Different order Padé approximations are applied for the situation that Δz is set 0.125µm. To avoid the instability, the rotated scheme discussed in section 4.3 is applied for high order Padé approximation. The power errors obtained by Padé (1,1), Padé(2,2), Padé(3,3), Padé(5,5) and rotated Padé(10,10) approximations are plotted in Fig. 4.8. It can be seen that the simulation accuracy is improved with the increasing of the Padé order.

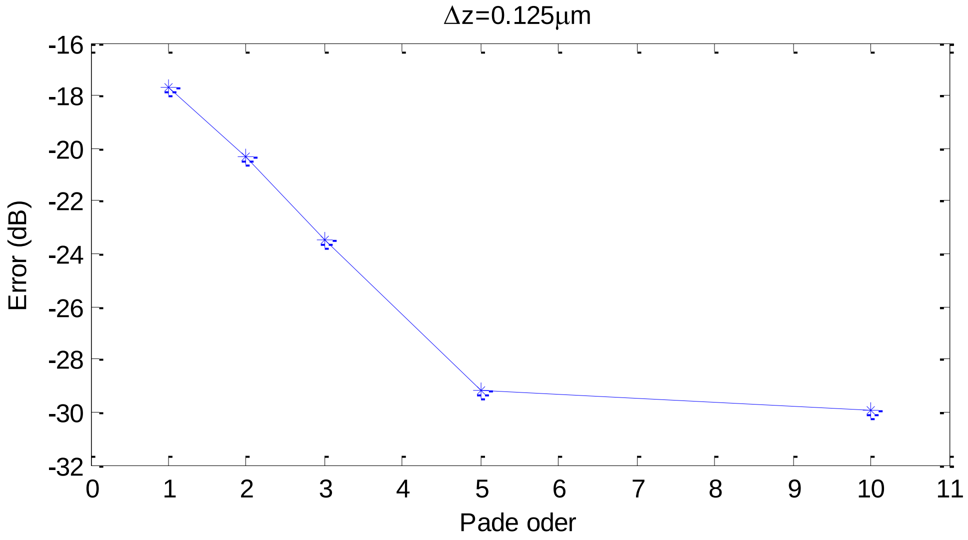

Figure 4.8: Calculation errors obtained by different order Padé approximations for the slab waveguide when the longitudinal calculation step is Δz=0.125μm. The transverse mesh size is Δx=0.01μm.

It is noted that increasing the Padé order is more effective than reducing the longitudinal sampling step Δz in order to improve the simulation accuracy of the WA scheme. To obtain good simulation accuracy within acceptable running time, simulation can be implemented by a relatively higher Padé order approximation with a larger longitudinal calculation step Δz.

Fig.4.9 plots the error as a function of the Padé order when the tilted angle of waveguide is 15^{o}, 30^{o} and 45^{o}, respectively. The transverse mesh size and the longitudinal sampling step are $\Delta x = 0.01\,\mu m$ and $\Delta z = 0.125\,\mu m$. The wavelength is 0.86μm. Padé(1,1) to Padé(5,5) are used for the simulations. It can be seen that for a certain angle, increasing the Padé order reduces the error. For a larger incident angle, a higher Padé order is required to provide a more accurate result.

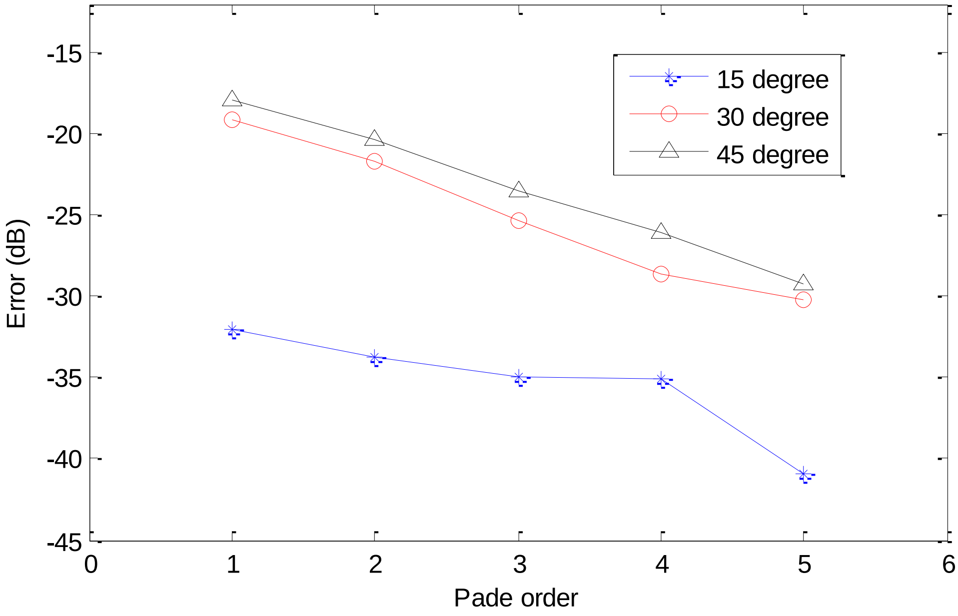

Figure 4.9: Calculation errors obtained by different order Padé approximations for slab waveguides with different tilted angle. The transverse mesh size is Δx=0.01μm and the longitudinal sampling step is $\Delta z = 0.125\,\mu m$.

The investigation of how the simulation accuracy of the WA scheme is affected by the change of the transverse sampling interval Δx is presented in Fig.4.10. The tilted angle of a slab waveguide with 1μm core width is 45^{o}. The longitudinal sampling step is $\Delta z = 0.125\,\mu m$ and the operating wavelength is 0.86μm. The propagating distance is 30μm and the width of simulation window is 100μm. PML is applied at the edges of the simulation window. Padé(1,1) to Padé(4,4) are applied for the WA-BPM for different value of Δx. The power errors are calculated respectively, and plotted as a function of Δx in Fig.4.10.

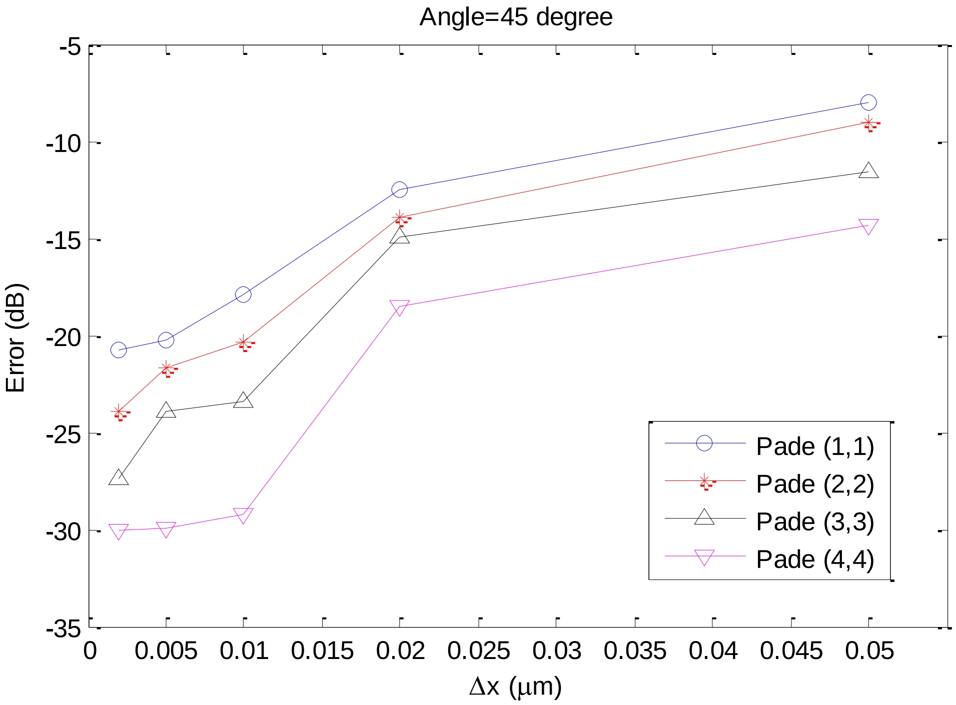

Figure 4.10: Calculation errors obtained by Padé(1,1) - Padé(4,4) approximations for the slab waveguide are presented as a function of the transverse sampling interval Δx. Longitudinal sampling step is $\Delta z = 0.125\,\mu\text{m}$

It shows that regardless which order of Padé approximation is used, the smaller transverse sampling interval results in smaller error. These results prove that the accuracy of the WA-BPM can be improved by reducing the transverse sampling interval.

4.4.2 Results for Rib Waveguide

In this section, the WA-BPM scheme is used to model forward propagation in a classical rib waveguide. The dimensions of the cross section of the rib waveguide are shown in Fig. 4.11 (a). The refractive indices of the cladding, the guiding region and the substrate are $n_1=1$ (air), $n_2=3.44$ (GaAs) and $n_3=3.4$ ($Ga_{0.9}Al_{0.1}As$). The width and the height of the outer slab is w=3 μm and H= 0.5 μm. The depth of the core is D = 0.5 μm. The ID BPM method is applied to obtain the fundamental mode for both TE and TM mode. The operating wavelength is λ = 1.15 μm. The transverse sampling intervals are $\Delta x = \Delta y = 0.05$ μm.

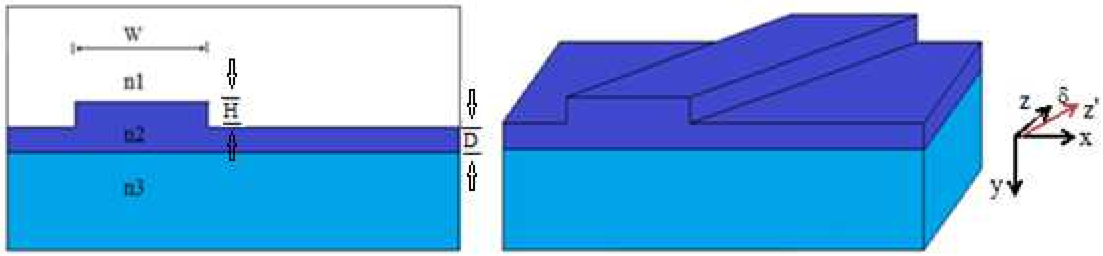

(a) (b)

Figure 4.11: 3D rib waveguide for WA-BPM modelling. (a) The cross section of the waveguide (b) Configuration of the tilted outer slab

In Fig. 4.11 (b), the top layer of the rib waveguide is tilted by 30 degree with respect to the z-direction. The tilted waveguide is excited by the obtained fundamental mode and the propagation in the waveguide is modelled by the BPM method with different approximation schemes. The width and height of the simulation window are set as $W^* = 20\mu m / \cos 30^\circ$ and $H^* = 5\mu m$. The transverse sampling interval along x-axis are adjusted with respect to the tilted angle as $\Delta x^* = \Delta x / \cos\delta = 0.05\mu m / \cos 30^\circ$. The transverse sampling interval along y-axis is kept as $\Delta y =$ 0.05 μm. The longitudinal calculation step is set as $\Delta z = 0.25$ μm. A PML boundary condition with a width W_{PML}=1μm and an absorption strength factor A=2 is applied at the end of the simulation window. Similarly to Eq.(4.2.10), the fundamental field is multiplied by a phase term $\exp(-j\beta_{eff} x^* \sin\delta)$ and used as the input excitation for the tilted waveguide.

Firstly, the field profiles obtained by different Padé schemes are compared. The results presented in this section are based on the TE polarisation, and the results of the TM polarisation are presented in **Appendix 3**. Fig. 4.12 shows the input field profile that is launched into the waveguide. The paraxial, Padé(1,1) and Padé(2,2) approximations are applied respectively to obtain the field profiles after 10 μm propagation.

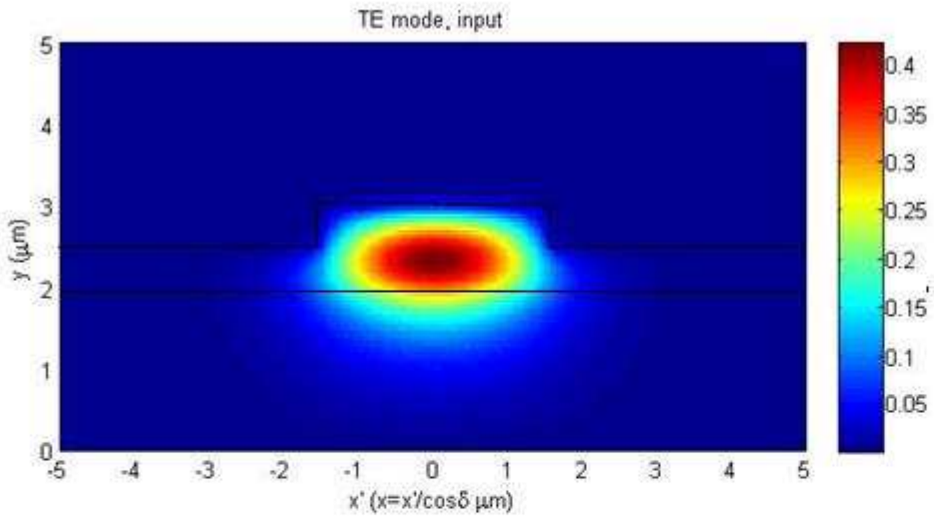

Figure 4.12: The input field profile launched into the 30 degree tilted rib waveguide.

The field profile obtained by the paraxial BPM is illustrated in Fig. 4.13.

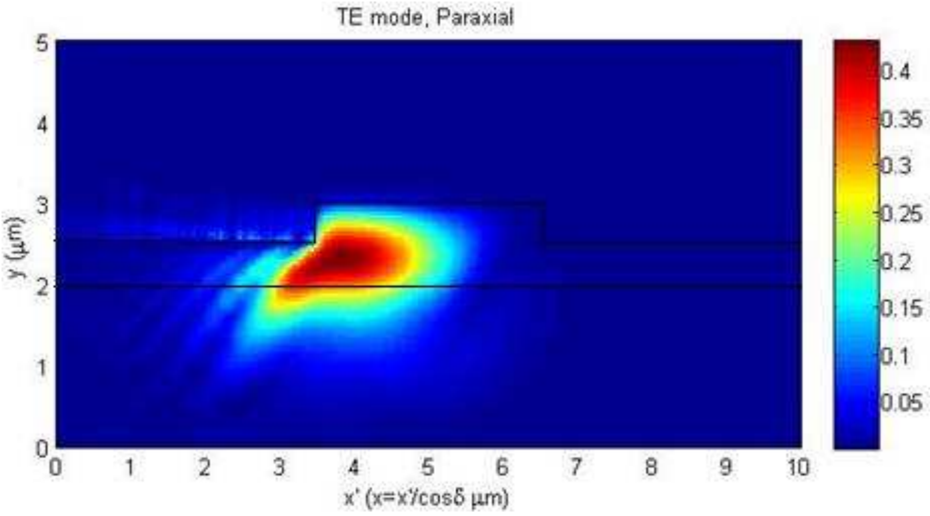

Figure 4.13: The field profile obtained by the paraxial BPM after 10µm propagation distance in a 30 degree tilted rib waveguide

It illustrates that the paraxial scheme cannot provide an acceptable simulation results. The field profile is seriously distorted and field is not positioned around the centre of the rib. This leads to a big loss of the power of the field propagating in the waveguide. This result strongly suggests that the paraxial BPM is not effective for the tilted rib waveguide.

For the same propagation distance, the field profiles obtained by the WA-BPM using Padé(1,1) approximation and Padé(2,2) approximation are illustrated in Fig. 4.14(a) and (b) respectively. It can be seen that the field profiles obtained by Padé(1,1) approximation still present a ripple in the left part of the simulation window, but the ripple is smaller comparing with the one caused by the paraxial method. Correspondingly, Padé(2,2) approximation eliminates most of the ripple and provides better simulation results. Obviously, the simulation results have been significantly improved when the WA-BPM is applied. The centre of the output field is located nearby the centre of the rib and the field profile is very close to the original input.

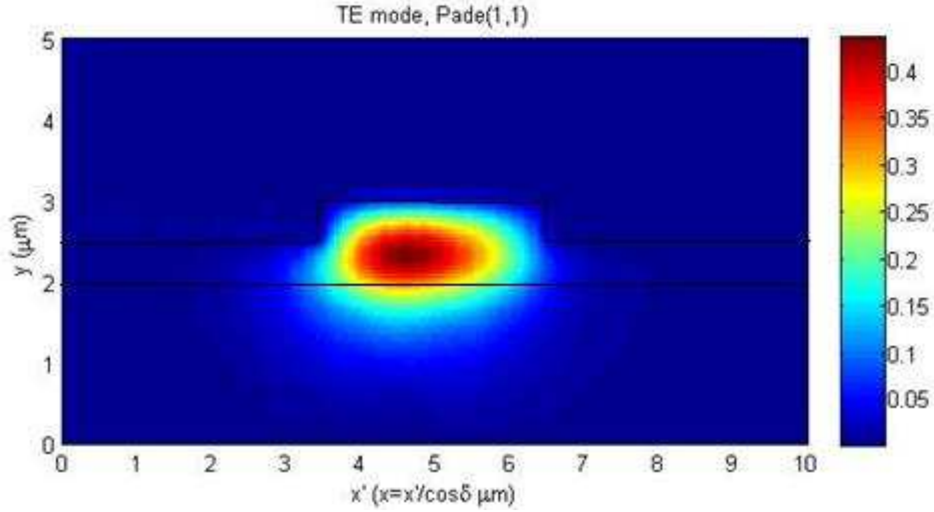

(a)

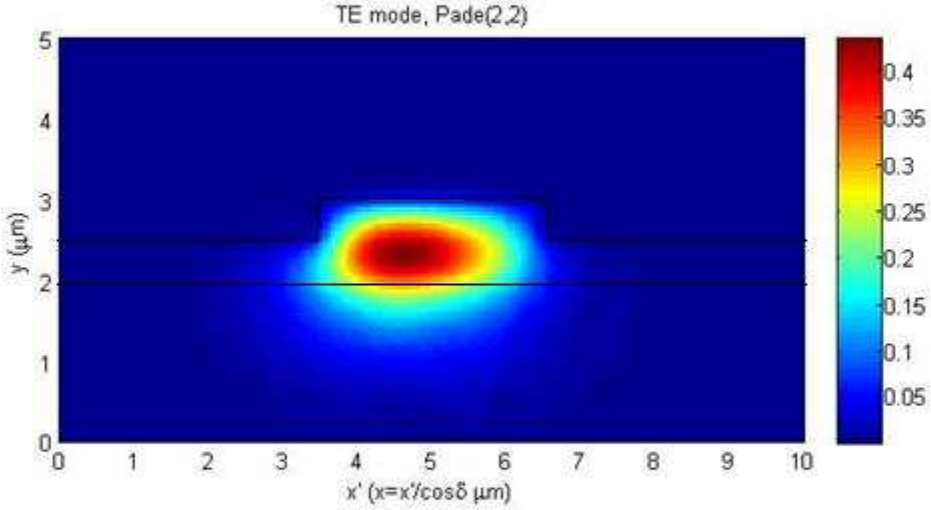

(b)

Figure 4.14: The field profiles obtained by the WA-BPM after 10μm propagation distance in the 30 degree tilted rib waveguide with (a) Padé(1,1) and (b) Padé(2,2).

Moreover, Fig. 4.15 illustrated the simulation result of rotated Padé(10,10) approximation after the same distance propagation. The result has been further improved and the field profile is much smoother comparing with the results obtained by the low order standard Padé approximation. This phenomenon proves that higher order Padé approximation is effective in improving the simulation accuracy of the 3D off-axis propagation problems.

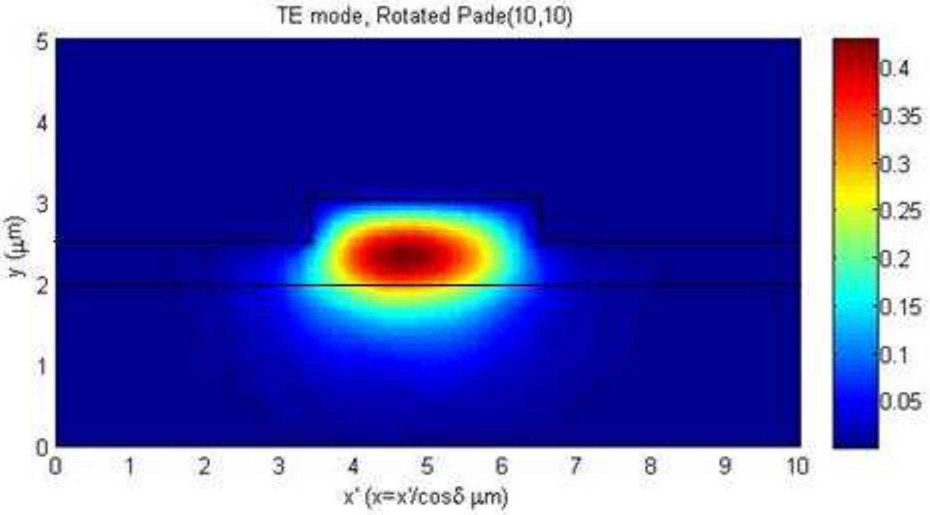

Figure 4.15: The field profile obtained by the WA-BPM with rotated Padé(10,10) approximation after 10μm propagation distance in the 30 degree tilted rib waveguide.

The following part is investigating the simulation accuracy of the WA scheme when applying to 30 degree tilted rib waveguide. The simulations are implemented with various longitudinal calculation step Δz, which is set as 6 different values between 0.1μm to 0.5μm. Padé(1,1), Padé(2,2) and Padé(3,3) approximations are applied respectively to calculate the results after 10μm propagating distance. The power errors are calculated by Eq.(4.2.12) and plotted in Fig. 4.16 according to different values of Δz.

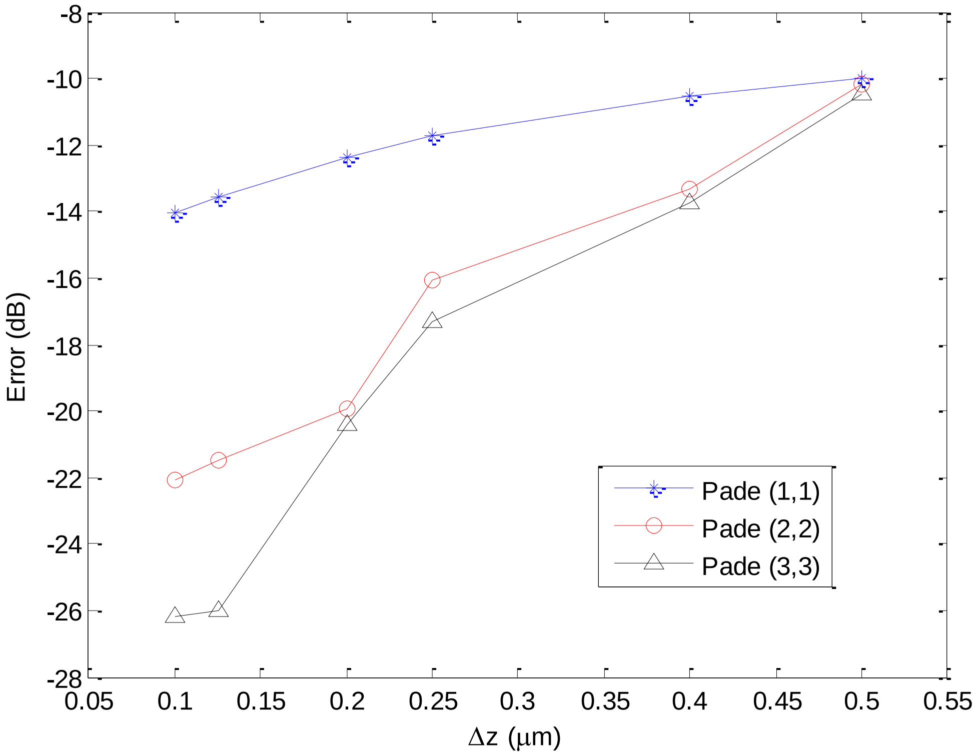

Figure 4.16: Calculation errors obtained by Padé(1,1), Padé(2,2) and Padé(3,3) approximations for the rib waveguide are presented as a function of the longitudinal calculation step Δz

It can be seen that the higher Padé order approximation with smaller longitudinal calculation step generates smaller errors comparing to the lower Padé order approximation with larger longitudinal calculation step. This conclusion is in agreement with that obtained for the slab waveguide.

Fig.4.17 plots the power errors obtained by various order Padé approximations when longitudinal calculation step is Δz=0.2μm.

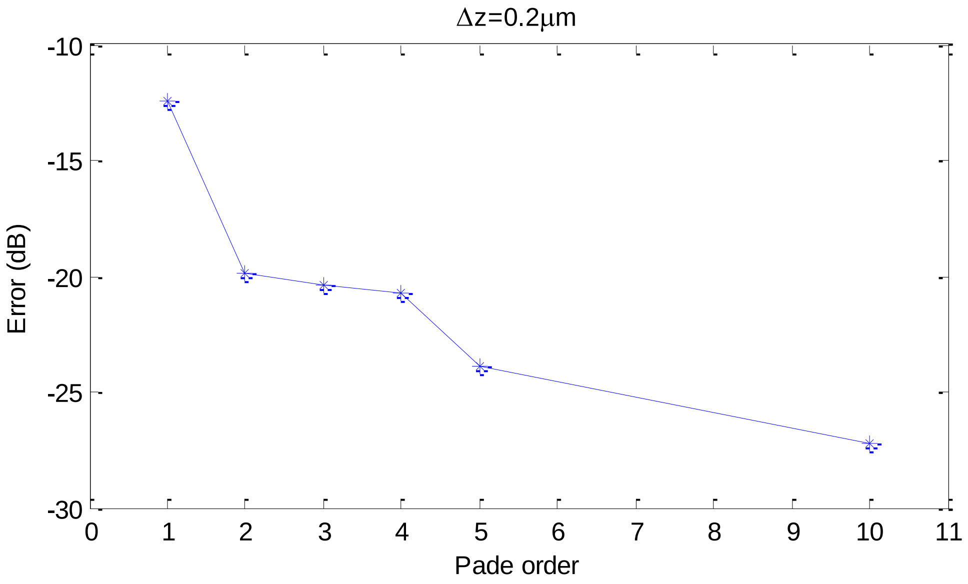

Figure 4.17: Calculation errors obtained by different order Padé approximations for the rib waveguide when the longitudinal calculation step is Δz=0.2μm.

It shows that the errors become smaller with the increasing order of the Padé approximations. The results further proved that the WA-BPM can achieve good accuracy if high order Padé approximation is applied.

4.5 Conclusions

This chapter introduced the wide angle BPM scheme for forward wave propagation simulation. Two common wide angle approximations, the recurrence Padé approximation and the multistep method with rational square root approximation have been presented, followed by the introduction of the branch cut rotation method which improves the stability of the simulation.

The paraxial approximation scheme and the wide angle approximation scheme with different order Padé operators are tested in the simulation for both slab and rib tilted waveguides. By comparing all the results obtained by different approximation schemes, a firm conclusion is achieved that the wide angle scheme is much more effective than the paraxial scheme to deal with the off-axis forward propagation situation. Moreover, it also has proved that the WA-BPM with a higher order Padé approximation can provide better simulation results with good accuracy than a lower order Padé approximation, at the cost of more computational time. The accuracy of the WA-BPM method can also be improved by reducing the longitudinal calculation step or the transverse sampling interval. Simulation also shows that a larger incident angle requires a higher order Padé approximation to provide a better accuracy. In the next chapter, the application of the WA scheme will be extended to the analysis of bi-directional propagation, which cannot be solved by the paraxial scheme.

4.7 Reference

1. W. Huang, The finite-difference vector beam propagation method: analysis and assessment Journal ofLightwave Technology, 1992. **10**: p. 295 - 305
2. G.R. Hadley, Wide-Angle Beam Propagation Using Padé approximant operators. Optics Letters, 1992. **17**: p. 1426-1428.
3. G.R. Hadley, Multistep Method for Wide-Angle Beam Propagation. Optics

Letters, 1992. **17**: p. 1743-1745.

4. F.A. Milinazzo, and G.H. Brooke, Rational square-root approximations for parabolic equation algorithms. Journal of the Acoustical Society of America, 1997. **101**: p. 760-766.
5. Q.L. Khai, Complex Padé approximant operators for wide-angle beam propagation. Optics Communications, 2009. **282**: p. 1252-1254.
6. F.A. Milinazzo, and G.H. Brooke, Rational square-root approximations for parabolic equation algorithms. Journal of the Acoustical Society of America, 1997. **101**: p. 760-766.
7. G.Q. Zhang, High Order Approximate One-way Wave Equation. Journal of Computational Mathematics, 1985: p. 90-97.
8. Y.Y. Lu, a complex coefficient rational approximation of root1+x. Applied Numerical Mathematics, 1998. **27**: p. 141-154.
9. J. Yamauchi, Propagation Beam Analysis of Optical Waveguide. 2003.

Chapter 5 Bidirectional Propagation Wide Angle FD-BPM

As discussed in Chapter 4, the WA FD-BPM is required when dealing with problems where the incident beam is propagating at an angle with respect to the propagation axis. Another important application of the WA FD-BPM is when considering bidirectional propagation problems where there are discontinuities in the waveguide and where reflections need to be taken into account. This chapter will discuss the performance of the Bidirectional Beam Propagation Method (Bi-BPM) in details.

Waveguide discontinuities are frequently encountered in many practical photonic components such as laser facets, grating structures, multiple dielectric layers, waveguide ends and junctions between different waveguides. Discontinuities that result in a change of a cross section of the waveguide or change in the refractive index along the propagation direction cause reflections.

Consequently, reflections lead to negative effects such as loss of power, noise, power fluctuations and dispersion, which limit the performance of integrated devices. For example, minimising reflections from the waveguide facet is important in order to avoid resonances building up within a semiconductor optical amplifier (SOA). Typically facet reflection of SOAs is required to be less than -40dB [1]. There are several different approaches that can reduce facet reflectivity. One of them is to use angled facets to redirect reflected light away from the waveguides, therefore reducing coupling back into the guided mode [2, 3]. Furthermore, the use of optical antireflection (AR) coatings further reduces the reflections and enhances the transmissions [4, 5]. In practice, facets with a combination of both tilting and coating are frequently employed [6-8].

A variety of numerical approaches have been developed for the purpose of accurately calculating facet reflectivity and reflections from discontinuities. One of these techniques is the Free Space Radiation Mode (FSRM) method [9]. The FSRM method takes the guided modes to be exact, but assumes the radiation modes supported by the waveguide to propagate in a region of uniform refractive index. This approximation holds true whenever the variation of refractive index in the transverse direction is small so that the effective index method could be applied to reduce the dimensionality of a general three-dimensional device [10]. There is no restriction on the variation of refractive index in the propagation direction, so the FSRM method can be applied where reflected waves are significant. So far, FSRM method has been developed for analysis of 2D and 3D angled and coated facet reflections and propagation along tapers [11, 12]. It has yielded useful results, allowing full 3D effects to be modelled, including the case of angled and coated facets [10, 13, 14]. The method is fast and efficient. It provides accurate results comparable to the benchmark results which obtained by Vassallo who used an integral equation approach [15-17], Smartt who used Fourier operator methods [18, 19] and Ikegami's variational formula [20]. However, the limitation of FSRM is that it is not suitable for structures with high refractive index contrasts. The index difference in transverse direction is typically restricted to be less than 10%.

Another efficient approach successfully employed to simulate bidirectional wave propagation is the Transfer Matrix Method (TMM), and is based on mode matching for distributed-feedback structures [21]. However, the TMM does not account for radiation modes and thus is not appropriate for a wide range of problems. As a general-purpose algorithm, the Finite Difference Time Domain (FDTD) method developed by Yee [22] provides another possible choice. The FDTD method is an approach that directly solves Maxwell's equations by a proper discretisation of both the time and space domains. It is accurate and straightforward but very expensive in time and memory resources [23]. With increases in computational power, the FDTD method has been applied not only to optical guiding structures [24], but also the optical waveguides with anti-reflection and high-reflection coatings [25, 26].

As a widely used technique for simulation integrated optical components, BPM is naturally to be investigated for the analysis of bidirectional propagation problems. So far, various Bi-BPM algorithms have been proposed for handing the reflection problems for single [27-29] or multiple interfaces [30-33]. In Bi-BPMs, the incident, reflected and transmitted waves that occur at discontinuities, can be expressed in terms of propagation matrix that contains square root operators. Depending on how the matrix systems are solved computationally, the Bi-BPM algorithms can be classified into two categories including iterative schemes [27-31] and non-iterative schemes [32, 33]. The iterative schemes propagate the field back and forth until a convergence is reached. Meanwhile, the non-iterative schemes involve direct manipulations of propagation operators which are approximated by matrices. Compared to the FDTD method, the Bi-BPMs is much more efficient and yet offers a good accuracy for simulation of the reflection, transmission and scatting loss.

Properly modelling the evanescent modes excited at reflecting interfaces is a major challenge for the Bi-BPM. Incorrect treatment of evanescent modes leads to numerical instability and results in degradation of accuracy. This problem becomes even more serious when modelling strongly reflecting structures with high refractive index contrast [34]. To overcome this problem, rational approximants to the square root operators are frequently applied to facilitate the calculation. The Bi-BPMs are based upon the WA scheme and hence the Padé approximation of the square root operators can be implemented. It should be noted that the standard Padé approximation fails to treat the evanescent modes correctly. Two approaches have been developed to improve the Padé approximation to deal with the evanescent modes for the bidirectional propagation problems, named rotated branch cut approximation [35] and complex coefficient Padé approximation [36]. The former obtains complex valued approximation by rotating the real axis branch cut by a rotation angle and then applies the standard Padé approximation to the rotated variable, as shown in Chapter 4.

The latter solves nonlinear equations by Newton's method to obtain the complex coefficients. Different Padé approximations for the square root operator in Bi-BPM have been assessed in [37]. The comparison of four types of rational approximations (real Padé, complex coefficient Padé, rotated branch cut Padé and complex coefficient Padé with rotated branch cut) demonstrates that under the same simulation conditions, the real Padé exhibits the worst performance because it treats the evanescent modes which are supposed to decay exponentially as the propagating modes. In contrast, the complex coefficient Padé avoids this problem and exhibits better performance. The rotated branch cut Padé achieves higher accuracy than the complex coefficient Padé. Both the rotated branch cut Padé and the complex coefficient Padé with rotated branch cut exhibit very close performance [37]. Therefore, in this thesis, the rotated branch cut Padé approximation will be adopted to evaluate the square root operator as it offers good accuracy and avoids the computational load for calculating the complex coefficients [37].

In the following sections a detailed theory for the Bi-BPM method will be presented. The study will start with the overview of the single interface reflective BPM [27-29], followed by the introduction of the Bi-BPM for modelling multiple-interface reflection problems [30-33].

5.1 Single Interface Reflective BPM Scheme

This section overviews the BPM scheme for single interface reflection problems. A typical single interface reflection problem is shown in Fig. 5.1, in which two different media A and B joined at interface. The left half space z<0 is a slab waveguide with a refractive index n_{rA}, incident on a lossless homogeneous dielectric with a refractive index n_{rB} (z>0). At the interface the incident signal is part transmitted into region z>0 and part reflected into region z<0.

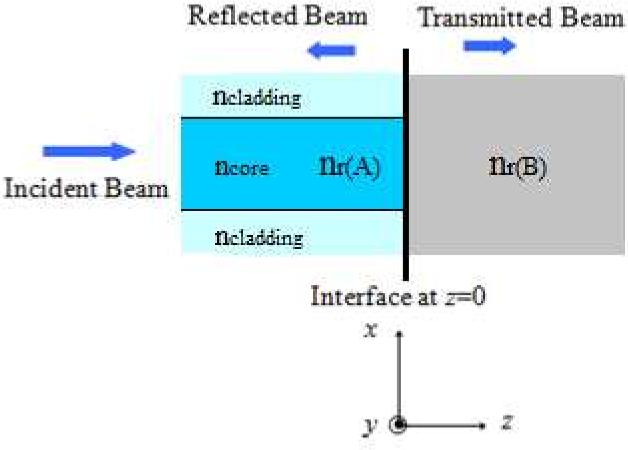

Figure 5.1: Two different media A and B joined at interface

This single interface reflective problem can be solved by establishing the connection between the incident beam, the reflective beam and the transmitted beam via the boundary condition for the tangential fields at the media interfaces. Once the reflected field and transmitted field equations at the interface are derived, they can be solved by the multistep method in the similar way as the one wave propagation equation represented using the WA-BPM.

First, a two-dimensional reflective problem is considered to derive the connection equations at the interface. Assume the refractive index of the medium is uniform in the y-direction and z-direction, the y-polarized electric field satisfies the equation

$$\frac{\partial^2 E_y}{\partial x^2}+\frac{\partial^2 E_y}{\partial z^2}+k_0^2 n_r^2 E_y=0 \tag{5.1.1}$$

for the TE mode, and the y-polarized magnetic field satisfies the equation

$$n_r^2\left[\frac{\partial}{\partial x}\left(\frac{1}{n_r^2}\frac{\partial H_y}{\partial x}\right)\right]+\frac{\partial^2 H_y}{\partial z^2}+k_0^2 n_r^2 H_y=0 \tag{5.1.2}$$

for the TM mode [38]. In the following part, equations will be derived from Eq. (5.1.1) for the TE mode, and the TM case can be derived similarly.

Eq. (5.1.1) can be factorized into:

$$\left(\frac{\partial}{\partial z}+j\beta L\right)\left(\frac{\partial}{\partial z}-j\beta L\right)E_y=0, \tag{5.1.3}$$

L is the square root operator and is defined as

$$L=\sqrt{1+\frac{\frac{\partial^2}{\partial x^2}+k_0^2 n_r^2-\beta^2}{\beta^2}}=\sqrt{1+X} \tag{5.1.4}$$

[28], where n_r and β are the refractive index and the propagation constant of the respective regions. The X is the transverse operator as:

$$X=\frac{\frac{\partial^2}{\partial x^2}+k_0^2 n_r^2-\beta^2}{\beta^2}. \tag{5.1.5}$$

The propagating fields can be decomposed into forward and backward propagating fields as $E_y = E_y^+ + E_y^-$,where E_y^+ and E_y^- are identified by the solutions of the terms in the first and the second bracket of Eq.(5.1.3), $\left(\frac{\partial}{\partial z} + j\beta L\right)E_y^+ = 0$ and $\left(\frac{\partial}{\partial z} - j\beta L\right)E_y^- = 0$, respectively. Therefore, in Fig. 5.1, forward and backward propagating fields in different medium can be presented as $E_{yA}^+ \cdot e^{-j\beta z}$, $E_{yA}^- \cdot e^{+j\beta z}$ for media A, and $E_{yB}^+ \cdot e^{-j\beta z}$, $E_{yB}^- \cdot e^{+j\beta z}$ for media B. At the interface, z=0, hence the phase terms, $e^{-j\beta z}$ and $e^{-j\beta z}$, are equal to one.

In the case that an incident field is launched onto the interface from media A, $E_{yB}^- = 0$. Applying the boundary conditions as:

$$E_{yA}^+ + E_{yA}^- = E_{yB}^+,$$

$$\frac{\partial E_{yA}^+}{\partial z} + \frac{\partial E_{yA}^-}{\partial z} = \frac{\partial E_{yB}^+}{\partial z}.$$

The expressions for the reflected field and transmitted field can be obtained in terms of the incident field as [27]:

$$(\beta_A\sqrt{1+X_A} + \beta_B\sqrt{1+X_B})E_{yr} = (\beta_A\sqrt{1+X_A} - \beta_B\sqrt{1+X_B})E_{yi}, \quad (5.1.6)$$

$$(\beta_A\sqrt{1+X_A} + \beta_B\sqrt{1+X_B})E_{yt} = 2\beta_A\sqrt{1+X_A}E_{yi}, \quad (5.1.7)$$

X_A and X_B are the relevant operators in different media which have different refractive index n_r as from Eq.(5.1.4).

The key to solve Eq. (5.1.6) and Eq. (5.1.7) is to evaluate the square root operators.

This can be achieved by the rotated Padé approximation as discussed in Chapter 4. However, employing the rotated Padé approximation to the equations directly is not advisable because each equation involves two different square root operators in terms of both X_A and X_B. Therefore, alternative formulations amenable to the straightforward application of the rotated Padé approximation are necessary. Considering Eq. (5.1.6) as an example, the equation can be expressed in the form of:

$$\left(\beta_A + \beta_B\sqrt{\frac{1+X_B}{1+X_A}}\right)E_{yr} = \left(\beta_A - \beta_B\sqrt{\frac{1+X_B}{1+X_A}}\right)E_{yi} \quad (5.1.8)$$
,

or

$$\left(\beta_A + \beta_B\sqrt{1+\frac{X_B - X_A}{1+X_A}}\right)E_{yr} = \left(\beta_A - \beta_B\sqrt{1+\frac{X_B - X_A}{1+X_A}}\right)E_{yi} \quad (5.1.9)$$
.

Applying the axis rotation method to the square root operator by $e^{-j\theta}$ [29, 35] results in:

$$\sqrt{1+\frac{X_B - X_A}{1+X_A}} = e^{j\theta/2}\sqrt{1+\left[\left(1+\frac{X_B - X_A}{1+X_A}\right)e^{-j\theta} - 1\right]},$$

If $\theta = -90^o$, Eq. (5.1.9) is transformed as:

$$\left(\beta_A + \beta_B\left(\frac{\sqrt{2}}{2} - j\frac{\sqrt{2}}{2}\right)\sqrt{1+\left[j\left(1+\frac{X_B - X_A}{1+X_A}\right) - 1\right]}\right)E_{yr}$$
$$= \left(\beta_A - \beta_B\left(\frac{\sqrt{2}}{2} - j\frac{\sqrt{2}}{2}\right)\sqrt{1+\left[j\left(1+\frac{X_B - X_A}{1+X_A}\right) - 1\right]}\right)E_{yi} \quad (5.1.10)$$
.

Expanding the square root operators in the same way as that for the forward WA-BPM in section 4.2 and 4.3 leads to:

$$A\cdot\prod_{i=1}^{k}(j + j\frac{X_B - X_A}{1+X_A} - 1 - d_i)\cdot E_{yr} = A^*\cdot\prod_{i=1}^{k}(j + j\frac{X_B - X_A}{1+X_A} - 1 - n_i)\cdot E_{yi} \qquad (5.1.11)$$

or:

$$A\cdot\prod_{i=1}^{k}(j - 1 - d_i + jX_B - X_A - d_i X_A)\cdot E_{yr} = A^*\cdot\prod_{i=1}^{k}(j - 1 - n_i + jX_B - X_A - n_i X_A)\cdot E_{yi} \quad (5.1.12)$$
,

where A and A^* are conjugate constants, d_i and n_i are conjugate roots of the i^{th} order operator $\left[j(1+\frac{X_B - X_A}{1+X_A}) - 1\right]$.

By using Multistep Method, the calculation is split into k steps and Eq. (5.1.12) is broken into k equations as:

$$\begin{gathered}
\sqrt[k]{A}\cdot(j - 1 - d_1 + jX_B - X_A - d_1 X_A)\cdot E_{yr}^{i=1} = \sqrt[k]{A^*}\cdot(j - 1 - n_1 + jX_B - X_A - n_1 X_A)\cdot E_{yi} \\
\vdots \\
\sqrt[k]{A}\cdot(j - 1 - d_j + jX_B - X_A - d_j X_A)\cdot E_{yr}^{i=j} = \sqrt[k]{A^*}\cdot(j - 1 - n_j + jX_B - X_A - n_j X_A)\cdot E_{yr}^{i=j-1} \\
\vdots \\
\sqrt[k]{A}\cdot(j - 1 - d_k + jX_B - X_A - d_k X_A)\cdot E_{yr} = \sqrt[k]{A^*}\cdot(j - 1 - n_k + jX_B - X_A - n_k X_A)\cdot E_{yr}^{i=k-1}
\end{gathered} \qquad (5.1.13)$$

Substituting $X_{(A/B)} = \dfrac{\frac{\partial^2}{\partial x^2} + k_0^2 n_{r(A/B)}^2 - \beta_{(A/B)}^2}{\beta_{(A/B)}^2}$ and applying the CN scheme to the j^{th} equation of Eq.(4.1.22), the equation becomes:

$$\sqrt[k]{A}\left[A_r E_{yr(x+\Delta x)}^{i=j} + B_r E_{yr(x-\Delta x)}^{i=j} + C_r E_{yr(x)}^{i=j}\right] = \sqrt[k]{A^*}\left[A_i E_{yr(x+\Delta x)}^{i=j-1} + B_i E_{yr(x-\Delta x)}^{i=j-1} + C_i E_{yr(x)}^{i=j-1}\right] \quad (5.1.14)$$

with the coefficients:

$$A_r = \frac{1}{\Delta x^2}(\,j\beta_A^2 - \beta_B^2 - d_i\beta_B^2)$$

$$B_r = \frac{1}{\Delta x^2}(\,j\beta_A^2 - \beta_B^2 - d_i\beta_B^2)$$

$$C_r = (\,j\beta_A^2 k_0^2 n_{rB}^2 - \beta_B^2 k_0^2 n_{rA}^2 - d_i\beta_B^2 k_0^2 n_{rA}^2) - \frac{2}{\Delta x^2}(\,j\beta_A^2 - \beta_B^2 - d_i\beta_B^2)$$

$$A_i = \frac{1}{\Delta x^2}(\,j\beta_A^2 - \beta_B^2 - n_i\beta_B^2)$$

$$B_i = \frac{1}{\Delta x^2}(\,j\beta_A^2 - \beta_B^2 - n_i\beta_B^2)$$

$$C_i = (\,j\beta_A^2 k_0^2 n_{rB}^2 - \beta_B^2 k_0^2 n_{rA}^2 - n_i\beta_B^2 k_0^2 n_{rA}^2) - \frac{2}{\Delta x^2}(\,j\beta_A^2 - \beta_B^2 - n_i\beta_B^2)$$

Once the reflected field is obtained by the above procedure, the transmitted field will be easily calculated using the boundary conditions. Alternatively, the transmitted field can also be calculated individually by a similar process starting from Eq. (5.1.7). The wave equation can be rewritten as:

$$\left(\beta_A + \beta_B\sqrt{1 + \frac{X_B - X_A}{1 + X_A}}\right)E_{yt} = 2\beta_A E_{yi} \quad , \qquad (5.1.15)$$

or in the form of axis rotated by -90^o:

$$\left(\beta_A + \beta_B\left(\frac{\sqrt{2}}{2} - j\frac{\sqrt{2}}{2}\right)\sqrt{1 + \left[\;j\left(1 + \frac{X_B - X_A}{1 + X_A}\right) - 1\right]}\right)E_{yt} = 2\beta_A E_{yi} \quad . \qquad (5.1.16)$$

Using the same procedure, Eq. (5.1.16) can be solved in the same way as Eq. (5.1.10), and reflected field can be obtained from boundary conditions.

For the TM mode, Eq. (5.1.2) can be derived into the similar form of Eq. (5.1.14) to solve the reflected field, as:

$$\sqrt[k]{A}\left[A_r H^{i=j}_{yr(x+\Delta x)} + B_r H^{i=j}_{yr(x-\Delta x)} + C_r H^{i=j}_{yr(x)}\right] = \sqrt[k]{A^*}\left[A_i H^{i=j-1}_{yr(x+\Delta x)} + B_i H^{i=j-1}_{yr(x-\Delta x)} + C_i H^{i=j-1}_{yr(x)}\right] \quad (5.1.17)$$

with the coefficients:

$$A_r = \frac{1}{\Delta x^2}\left[j\beta_A^2 \frac{2n^2_{rB(x)}}{n^2_{rB(x+\Delta x)} + n^2_{rB(x)}} - \beta_B^2(1+d_i)\frac{2n^2_{rA(x)}}{n^2_{rA(x+\Delta x)} + n^2_{rA(x)}}\right]$$

$$B_r = \frac{1}{\Delta x^2}\left[j\beta_A^2 \frac{2n^2_{rB(x)}}{n^2_{rB(x-\Delta x)} + n^2_{rB(x)}} - \beta_B^2(1+d_i)\frac{2n^2_{rA(x)}}{n^2_{rA(x-\Delta x)} + n^2_{rA(x)}}\right]$$

$$\begin{aligned} C_r &= (j\beta_A^2 k_0^2 n_{rB}^2 - \beta_B^2 k_0^2 n_{rA}^2 - d_i \beta_B^2 k_0^2 n_{rA}^2) \\ &\quad - \frac{2}{\Delta x^2}\left[\begin{aligned} & j\beta_A^2\left(\frac{n^2_{rB(x)}}{n^2_{rB(x+\Delta x)} + n^2_{rB(x)}} + \frac{n^2_{rB(x)}}{n^2_{rB(x-\Delta x)} + n^2_{rB(x)}}\right) \\ & -\beta_B^2(1+d_i)\left(\frac{n^2_{rA(x)}}{n^2_{rA(x+\Delta x)} + n^2_{rA(x)}} + \frac{n^2_{rA(x)}}{n^2_{rA(x-\Delta x)} + n^2_{rA(x)}}\right)\end{aligned}\right]\end{aligned}$$

$$A_i = \frac{1}{\Delta x^2}\left[j\beta_A^2 \frac{2n^2_{rB(x)}}{n^2_{rB(x+\Delta x)} + n^2_{rB(x)}} - \beta_B^2(1+n_i)\frac{2n^2_{rA(x)}}{n^2_{rA(x+\Delta x)} + n^2_{rA(x)}}\right]$$

$$B_i = \frac{1}{\Delta x^2}\left[j\beta_A^2 \frac{2n^2_{rB(x)}}{n^2_{rB(x-\Delta x)} + n^2_{rB(x)}} - \beta_B^2(1+n_i)\frac{2n^2_{rA(x)}}{n^2_{rA(x-\Delta x)} + n^2_{rA(x)}}\right]$$

$$\begin{aligned} C_i &= (j\beta_A^2 k_0^2 n_{rB}^2 - \beta_B^2 k_0^2 n_{rA}^2 - n_i \beta_B^2 k_0^2 n_{rA}^2) \\ &\quad - \frac{2}{\Delta x^2}\left[\begin{aligned} & j\beta_A^2\left(\frac{n^2_{rB(x)}}{n^2_{rB(x+\Delta x)} + n^2_{rB(x)}} + \frac{n^2_{rB(x)}}{n^2_{rB(x-\Delta x)} + n^2_{rB(x)}}\right) \\ & -\beta_B^2(1+n_i)\left(\frac{n^2_{rA(x)}}{n^2_{rA(x+\Delta x)} + n^2_{rA(x)}} + \frac{n^2_{rA(x)}}{n^2_{rA(x-\Delta x)} + n^2_{rA(x)}}\right)\end{aligned}\right]\end{aligned}$$

The transmitted field can be obtained by using the relationship $H_{yi} + H_{yr} = H_{yt}$.

5.2 Multiple-Interface Bi-directional BPM

This section presents a way of dealing with multiple discontinuities in the BPM method. Optical structures containing multiple interfaces, such as Bragg gratings, multilayer antireflection coatings and high-reflection coatings, lead to a more complicated situation for modelling. The difficulty to model this kind of problem is that the multiple interfaces will cause multiple reflections among different material layers. The typical multiple-interface bi-directional propagation problem is illustrated in Fig. 5.2. The incident field excites a series of reflected and transmitted waves in the longitudinally varying integrated optical structure. In order to solve this problem, the waveguide can be discretized into a number of longitudinally–invariant waveguide sections separated by interfaces. The modelling of electromagnetic field propagation through this structure focus on two steps: [30]:

(1) Solving for the total propagating fields in each waveguide section.

(2) Applying boundary conditions at the interfaces connecting two adjacent waveguide sections and solving for the reflected and the transmitted fields.

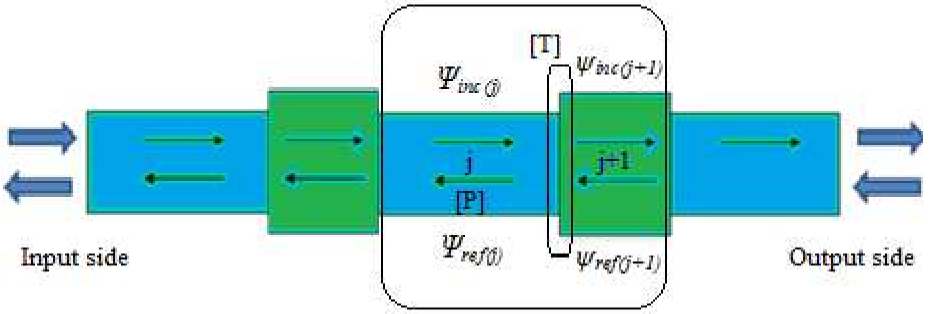

Figure 5.2: A longitudinally varying integrated optical structure is discretized into a series of longitudinally–invariant sections separated by interfaces

These two steps can be achieved via two kinds of matrices: the propagation matrices

[P] for step 1 and the interface matrices [T] for step 2, as shown in the highlight part in Fig.5.2. The propagation matrices propagate the forward and backward fields to the next junction by using the single directional BPM. The interface matrices can be written by analogy with the single reflective BPM scheme. Once the matrix operators of these two processes are found for each section, they can be applied alternatively to yield the overall transfer matrix [G] for the whole structure and obtain the reflected and transmitted fields at the input and the output of the structure, as [32]:

$$\psi_{\mathrm{output}} = [\mathrm{G}] \cdot \psi_{\mathrm{input}} \tag{5.2.1}$$

where

$$[\mathrm{G}] = [\mathrm{T}_\mathrm{n}][\mathrm{P}_\mathrm{n}][\mathrm{T}_{\mathrm{n}-1}][\mathrm{P}_{\mathrm{n}-1}]...[\mathrm{T}_2][\mathrm{P}_2][\mathrm{T}_1][\mathrm{P}_1] \tag{5.2.2}$$

is the transfer matrix, and [Tj] and $[P_j]$ represent the interface matrix and propagation matrix for the j^{th} section.

Firstly, the reflection and the transmission at the interface are taken into account, and the interface matrix is derived. Fig.5.2 shows incident and reflected fields in two adjacent waveguide sections, namely $(j)^{th}$ and $(j+1)^{th}$. $\psi_{\mathrm{inc}(j)}$, $\psi_{\mathrm{ref}(j)}$, $\psi_{\mathrm{inc}(j+1)}$ and $\psi_{\mathrm{ref}(j+1)}$ represent the electric fields for the TE polarization and the magnetic fields for the TM polarization. Here the TE polarization is considered and the TM case can be derived similarly. The boundary conditions require that the total electric fields are continues at the interface as:

$$\mathrm{E}_{\mathrm{inc}(j)} + \mathrm{E}_{\mathrm{ref}(j)} = \mathrm{E}_{\mathrm{inc}(j+1)} + \mathrm{E}_{\mathrm{ref}(j+1)}, \tag{5.2.3}$$

and the derivations of the fields have the relationship that:

$$\beta_j\sqrt{1+X_j}E_{inc(j)}-\beta_j\sqrt{1+X_j}E_{ref(j)} = \beta_{j+1}\sqrt{1+X_{j+1}}E_{ref(j+1)}-\beta_{j+1}\sqrt{1+X_{j+1}}E_{inc(j+1)}, \tag{5.2.4}$$

where the transverse operator X_j and X_{j+1} for the two sides of the interface are in the similar form of that in Eq.(5.1.5), β_j and β_{j+1} are the propagation constants in region j and j+1, respectively.

Solving Eq. (5.2.3) and Eq. (5.2.4) for the fields on the right hand side of the interface gives:

$$E_{ref(j+1)} = \frac{1}{2}(1+\frac{\beta_j\sqrt{1+X_j}}{\beta_{j+1}\sqrt{1+X_{j+1}}})E_{inc(j)}+\frac{1}{2}(1-\frac{\beta_j\sqrt{1+X_j}}{\beta_{j+1}\sqrt{1+X_{j+1}}})E_{ref(j)}, \tag{5.2.5}$$

$$E_{inc(j+1)} = \frac{1}{2}(1-\frac{\beta_j\sqrt{1+X_j}}{\beta_{j+1}\sqrt{1+X_{j+1}}})E_{inc(j)}+\frac{1}{2}(1+\frac{\beta_j\sqrt{1+X_j}}{\beta_{j+1}\sqrt{1+X_{j+1}}})E_{ref(j)}. \tag{5.2.6}$$

Eq.(5.2.5) and Eq.(5.2.6) can be expressed in the form of a matrix system [32]:

$$\begin{pmatrix} E_{ref(j+1)} \\ E_{inc(j+1)} \end{pmatrix} = [T_j]\cdot\begin{pmatrix} E_{inc(j)} \\ E_{ref(j)} \end{pmatrix}, \tag{5.2.7}$$

where $[T_j]$ is the interface matrix as:

$$[T_j] = \frac{1}{2}\begin{pmatrix} 1+\frac{\beta_j\sqrt{1+X_j}}{\beta_{j+1}\sqrt{1+X_{j+1}}} & 1-\frac{\beta_j\sqrt{1+X_j}}{\beta_{j+1}\sqrt{1+X_{j+1}}} \\ 1-\frac{\beta_j\sqrt{1+X_j}}{\beta_{j+1}\sqrt{1+X_{j+1}}} & 1+\frac{\beta_j\sqrt{1+X_j}}{\beta_{j+1}\sqrt{1+X_{j+1}}} \end{pmatrix} \tag{5.2.8}$$

Secondly, the forward and backward propagations in a single region are considered, and the propagation matrix is derived. Based on the formula which is calculating the field propagation in single direction discussed in section 4.2, the propagation equation of the jth section can be written as:

$$E_j^+(z+\Delta z)=\frac{(1+\frac{1}{2}\,j\beta\left(1-\sqrt{1+X}\right)\Delta z)}{(1-\frac{1}{2}\,j\beta\left(1-\sqrt{1+X}\right)\Delta z)}E_j^+(z) \qquad (5.2.9)$$

for the forward propagation, and,

$$E_j^-(z-\Delta z)=\frac{(1-\frac{1}{2}\,j\beta\left(1-\sqrt{1+X}\right)\Delta z)}{(1+\frac{1}{2}\,j\beta\left(1-\sqrt{1+X}\right)\Delta z)}E_j^-(z) \qquad (5.2.10)$$

for backward propagation.

Eq. (5.2.9) and Eq. (5.2.10) can be written in the form of a matrix system as:

$$\begin{pmatrix} E_j^+(z+\Delta z) \\ E_j^-(z-\Delta z) \end{pmatrix}=[P_j]\cdot\begin{pmatrix} E_j^+(z) \\ E_j^-(z) \end{pmatrix}, \qquad (5.2.11)$$

where [P_j] is the propagation matrix as:

$$[P_j]=\begin{pmatrix} P_j^+ & 0 \\ 0 & P_j^- \end{pmatrix} \qquad (5.2.12)$$

with $P_j^{\pm}=\dfrac{(1\pm\frac{1}{2}\,j\beta\left(1-\sqrt{1+X}\right)\Delta z)}{(1\mp\frac{1}{2}\,j\beta\left(1-\sqrt{1+X}\right)\Delta z)}$.

The final field yielded at the output side of the structure can be calculated by alternately applying the above two matrix equations as [32]:

$$\begin{pmatrix} E_{out}^+ \\ E_{out}^- \end{pmatrix}=[G]\cdot\begin{pmatrix} E_{in}^+ \\ E_{in}^- \end{pmatrix}, \qquad (5.2.13)$$

where E_{in}^+ and E_{in}^- denote the forward and backward field components at the input side, E_{out}^{+} and E_{out}^{-} denote the forward and backward field components at the output side. [G] is the overall transfer matrix as given in Eq.(5.2.2). It can be represented in another form as:

$$[G]=\begin{pmatrix} g_{11} & g_{12} \\ g_{21} & g_{22} \end{pmatrix}. \tag{5.2.14}$$

The square root operators in the characteristic matrices $[T_j]$ and $[P_j]$ can be evaluated by the well- known Padé approximation. It is important to note that the branch cut rotation method needs to be used in order to treat the evanescent modes correctly, as discussed in section 5.1.

Physically, $E_{out}^{-}=0$ because the output side of the structure only contains forward travelling fields. Therefore, the total reflected fields at the input end of the structure can be presented as [32]:

$$E_{in}^{-}=-g_{22}^{-1}g_{21}E_{in}^{+}, \tag{5.2.15}$$

and the total transmitted fields at the output end of the structure can be presented by:

$$E_{out}^{+}=(g_{11}-g_{12}g_{21}g_{22}^{-1})E_{in}^{+}. \tag{5.2.16}$$

Eq. (5.2.15) and Eq. (5.2.16) can be solved by applying a standard iterative algorithm, such as the Bi-conjugate gradient or the quasi-minimal residual methods [39-41].

Because the matrix operators involve complicated matrix multiplications, the successful application of the multiple-interface Bi-BPM frequently requires preconditioning for the matrix operators. Unfortunately, the presence of the inverse matrices increases the difficulty of preconditioning. Therefore, an alternative formulation, amenable to algebraic preconditioning is necessary. For the special case of a single coating structure which contains only two reflective points, a simplified variant of this approach is possible. This will be discussed in the next chapter.

5.3 Conclusions

This chapter recalled the commonly used Bi-BPM methods for solving the facet reflectivity of discontinuous waveguides. The Bi-BPM methods based on the WA approximation are efficient schemes that can provide good accuracy when dealing with reflection problems. In the next chapter, based on the conventional Bi-BPM theories, a transmission matrix based Bi-BPM, T-Bi-BPM, will be proposed for solving single coating layer or uncoated facet reflection problems. The performance of the T-Bi-BPM scheme will be assessed on a waveguide normal incident or at an angle to the facet plane.

5.4 References

1. M. Mahony, Semiconductor laser optical amplifiers for use in future fiber

systems. Lightwave Technology, Journal of, 1988. **6**(4): p. 531-544.

2. C.E. Zah, Fabrication and performance of 1.5μm GaInAsP travelling-wave laser amplifiers with angled facets. Electronics Letters, 1987. **23**(19): p. 990-992.

3. W. Rideout, Ultra-low-reflectivity semiconductor optical amplifiers without antireflection coatings. Electronics Letters, 1990. **26**(1): p. 36-38.

4. T. Saitoh, T. Mukai, and O. Mikami, Theoretical analysis and fabrication of antireflection coatings on laser-diode facets. Lightwave Technology, Journal of, 1985. **3**(2): p. 288-293.

5. N.A. Olsson, Ultra-low reflectivity 1.5 μm semiconductor laser preamplifier. Electronics Letters, 1988. **24**(9): p. 569-570.

6. J. Buus, M.C. Farries, and D.J. Robbins, Reflectivity of coated and tilted semiconductor facets. Quantum Electronics, IEEE Journal of, 1991. **27**(6): p. 1837-1842.

7. C.E. Zah, 1.3 μm GaInAsP near-travelling-wave laser amplifiers made by combination of angled facets and antireflection coatings. Electronics Letters, 1988. **24**(20): p. 1275-1276.

8. P.E. Barnsley, J.J. Isaac, and D.J. Elton, Ultra-low reflectivity broadband 1.5 μm GaInAsP semiconductor optical amplifiers. Electronics Letters, 1990. **26**(12): p. 825-827.

9. C. J. Smartt, T.M. Benson, and P. C. Kendall, 'Free space radiation mode' method for the analysis of propagation in optical waveguide devices. IEE

PROCEEDINGS-J, 1993. **140**: p. 56-61.

10. M. Reed, Antireflection-coated angled facet design. Optoelectronics, IEE Proceedings, 1996. **143**(4): p. 214-220.

11. P.C. Kendall, New formula for semiconductor laser facet reflectivity. Photonics Technology Letters, IEEE, 1993. **5**(2): p. 148-150.

12. P.C. Kendall, Semiconductor laser facet reflectivities using free-space radiation modes. Optoelectronics, IEE Proceedings J, 1993. **140**(1): p. 49-55.

13. M. Reed, Efficient propagation algorithm for 3D optical waveguides. Optoelectronics, IEE Proceedings, 1998. **145**(1): p. 53-58.

14. P. Sewell, Full vector analysis of two-dimensional angled and coated optical waveguide facets. Quantum Electronics, IEEE Journal of, 1997. **33**(12): p. 2311-2318.

15. C. Vassallo, Reflectivity of multidielectric coatings deposited on the end of a weakly guiding dielectric slab waveguide. J. Opt. Soc. Amer. A, 1988. **5**: p. 1918-1928.

16. C. Vassallo, Theory and practical calculation of antireflection coatings on semiconductor laser diode optical amplifiers. IEE Proc. J, 1990. **137**: p. 133-137.

17. C.Vassallo,Polarization-independant antireflection coatings for semiconductor optical amplifiers. Electron. Lett., 1988. **24**: p. 61-62.

18. C. SMARTT, T.M. BENSON, and P.C. KENDALL, Exact analysis of waveguide discontinuities: Junctions and laser facets. Electron. Lett., 1993. **29**:

p. 1352-1352.

19. C. SMARTT, T.M. BENSON, and P.C. KENDALL, Exact operator method for the analysis of dielectric waveguides with application to integrated optics devices and laser facets. Proceedings of 2nd international conference on Computation in electromagnetics, 1994: p. 335-338.

20. T. IKEGAMI, Reflectivity of mode of facet and oscillation mode in double heterostructure injection lasers. IEEE J. Quantum Electron, 1972: p. 470-476.

21. J. Hong, W. Huang, and T. Makino, On the transfer matrix method for distributed-feedback waveguide devices. Lightwave Technology, Journal of, 1992. **10**(12): p. 1860-1868.

22. Y. Kane, Numerical solution of initial boundary value problems involving maxwell's equations in isotropic media. Antennas and Propagation, IEEE Transactions on, 1966. **14**(3): p. 302-307.

23. J. Yamauchi, Propagation Beam Analysis of Optical Waveguides. 2003.

24. S.T. Chu, and S.K. Chaudhuri, A finite-difference time-domain method for the design and analysis of guided-wave optical structures. Lightwave Technology, Journal of, 1989. **7**(12): p. 2033-2038.

25. J. Yamauchi, and H. Nakano, Analysis of optical waveguides with high-reflection coatings using the FD-TD method. IEEE Photon. Technol. Lett, 1998. **10**: p. 111-113.

26. J. Yamauchi, Analysis of antireflection coatings using the FD-TD method with the PML absorbing boundary condition. Photonics Technology Letters, IEEE,

1996. **8**(2): p. 239-241.

27. C. Yih-Peng, and C. Hung-Chun, Analysis of optical waveguide discontinuities using the Pade approximants. Photonics Technology Letters, IEEE, 1997. **9**(7): p. 964-966.

28. C. Yevick, application of the bidirectional parabolic equation method to optical waveguide facets J. Opt. Soc. Amer. A, 1997. **14**: p. 1448–1450.

29. H. El-Refaei, I. Betty, and D. Yevick, The application of complex Pade approximants to reflection at optical waveguide facets. Photonics Technology Letters, IEEE, 2000. **12**(2): p. 158-160.

30. R. Hongling, R. Scarmozzino, and R.M. Osgood, A bidirectional beam propagation method for multiple dielectric interfaces. Photonics Technology Letters, IEEE, 1999. **11**(7): p. 830-832.

31. L. Ya Yan, and W. Su Hua, A new iterative bidirectional beam propagation method. Photonics Technology Letters, IEEE, 2002. **14**(11): p. 1533-1535.

32. H. El-Refaei, D. Yevick, and I. Betty, Stable and noniterative bidirectional beam propagation method. Photonics Technology Letters, IEEE, 2000. **12**(4): p. 389-391.

33. H. Pui Lin, and L. Ya Yan, A stable bidirectional propagation method based on scattering operators. Photonics Technology Letters, IEEE, 2001. **13**(12): p. 1316-1318.

34. H. Rao, Complex propagators for evanescent waves in bidirectional beam propagation method. in Lasers and Electro-Optics, 2000. (CLEO 2000).

Conference on. 2000.

35. F.A. Milinazzo, and G.H. Brooke, Rational square-root approximations for parabolic equation algorithms. Journal of the Acoustical Society of America, 1997. **101**: p. 760-766.

36. Y.Y. Lu, a complex coefficient rational approximation of root1+x. Applied Numerical Mathematics, 1998. **27**: p. 141-154.

37. Z. Hua, , M. Jianwei, and H. Wei-Ping, Assessment of Rational Approximations for Square Root Operator in Bidirectional Beam Propagation Method. Lightwave Technology, Journal of, 2008. **26**(5): p. 600-607.

38. Kenji Kawano, Introduction to optical waveguide analysis: Solving Maxwell's quations and the Schrodinger Equation. 2001.

39. R.W. Freund, Conjugate gradient-tpye methods for linear systems with complex symmetric coefficient matrices. SLAM J.Sci.Statist.Comptat, 1992. **13**: p. 425-448.

40. Roland W. Freund, QMR: a quasi-minimal residual method for non-Hermitian linear systems. Numerische Mathematik, 1991. **60**: p. 315-339.

41. D. W. Peaceman and H. H. Rachford, The numerical solution of parabolic and elliptic differential equations. J. Soc. Industrial Appl. Math, 1955. **3**: p. 28-41.

Chapter 6 Transmission Matrix Based Bi-BPM (T-Bi-BPM) for Modelling Single Layer Coating Structures

In this chapter, a novel method, the T-Bi-BPM method, to solve the single coating structure reflection problems is proposed. This method takes the incident and the reflected fields from either side of the coating layer as a whole, and tries to solve the whole field based on the input of the structure. Based on the transmission line theory approach, the new method derives a matrix equation, which establishes the connection between the total fields on either side of the coating layer and the incident field at the input side of the structure. The matrix equation can be solved by sparse matrix multiplications once the incident field is given. Section 6.1 will present the derivation of the matrix equation in details by two steps. In the first step, the total field at the input side of the coating layer is connected with the total field at the output side by a transfer matrix. Different from the Bi-BPM discussed in section 5.2, the transfer matrix used in this method is derived on the basis of a transmission matrix used in the transmission line theory. In the second step, the matrix equation obtained in step one is rearranged to remove the unknown of the total field on the output, leaving only the field terms on the input. Therefore, the total field at the input side can be calculated on the basis of the incident field and from where the reflected field at the input can be obtained. Section 6.2 presents numerical implementation of the method. Simulation results will be presented in section 6.3 to test the accuracy and the effectiveness of the

T-Bi-BPM method. The results obtained by FSRM will be considered as the benchmark for comparison purpose. The limitation of FSRM is that it is only suitable for structures with low refractive index contrast because it makes use of the effective index method during mode analysis. The main advantage of the T-Bi-BPM method over FSRM is that the low refractive index contrast limitation is removed. Therefore, the method has the potential to handle a wider range of problems.

6.1 Matrix Formulation

Fig. 6.1 illustrates a two-port network. According to the transmission line theory, the voltage V_1 and the current I_1 at the left hand side port and the voltage V_2 and the current I_2 at the right hand side are connected via a transmission (ABCD) matrix as [1]:

$$\begin{pmatrix} V_1 \\ I_1 \end{pmatrix} = \begin{pmatrix} A & B \\ C & D \end{pmatrix} \cdot \begin{pmatrix} V_2 \\ I_2 \end{pmatrix} . \qquad (6.1.1)$$

The parameters in the transmission matrix are:

$$\begin{aligned} A &= D = \cos \beta l, \\ B &= jZ_0 \sin \beta l, \\ C &= jY_0 \sin \beta l. \end{aligned}$$

where Z_0 is the characteristic impedance and Y_0 is the characteristic admittance, β is the propagation constant and l is the physical length of the transmission line.

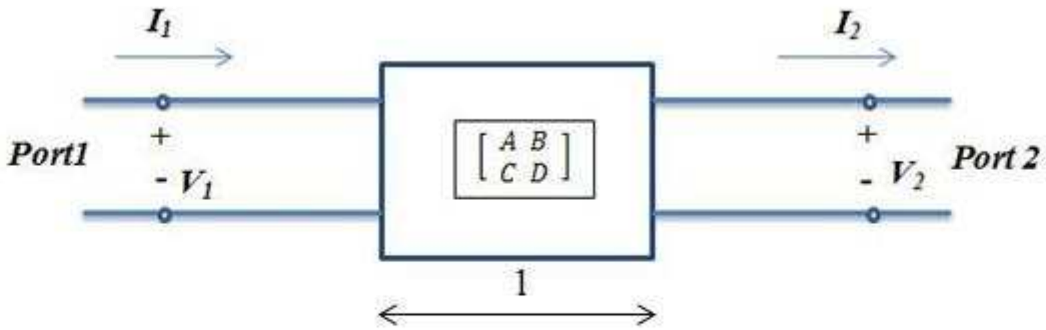

Figure 6.1: A two-port network

A single coating optical structure can be considered in the similar form as a transmission line, as illustrated in Fig. 6.2. The incident and reflected electric fields on the input side of the coating layer are set as $E_{inc(1)}$ and $E_{ref(1)}$, and on the output side of the coating layer are set as $E_{inc(2)}$ and $E_{ref(2)}$. where d denotes the thickness of the coating.

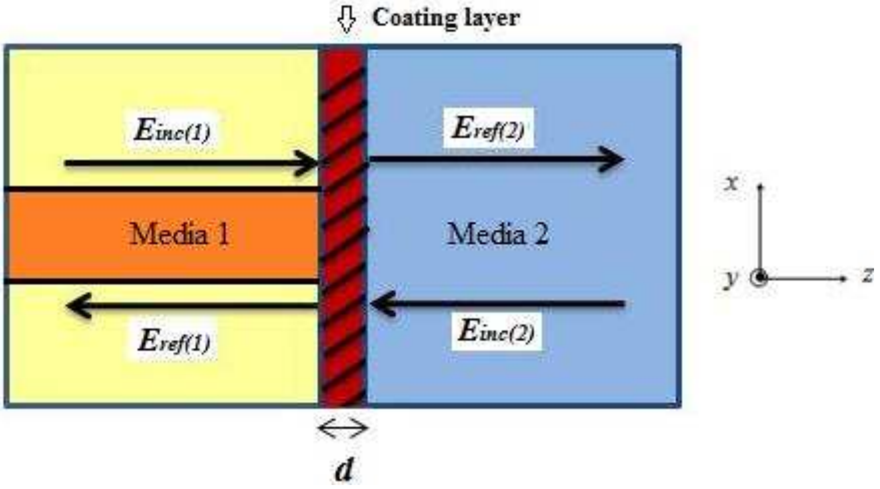

Figure 6.2: A single layer coating structure

Physically, the total electric field is proportional to the voltage as $E_{total} = E_{inc} + E_{ref}$, and the derivative of the total electric field along the propagation direction is

$G_{total} = \left.\frac{dE_{total}}{dz}\right|_{z=0}$. According to Eq.(6.1.1), the physical quantities at the start and end junctions of the coating are connected via a new transmission matrix as:

$$\begin{pmatrix} E_{total(2)} \\ G_{total(2)} \end{pmatrix} = \begin{pmatrix} A' & B' \\ C' & D' \end{pmatrix} \cdot \begin{pmatrix} E_{total(1)} \\ G_{total(1)} \end{pmatrix}, \tag{6.1.2}$$

where the matrix parameters are:

$$\begin{aligned} A' = D' &= \cos(\beta_c \sqrt{1+X_c} \cdot d), \\ B' &= -j \frac{\sin(\beta_c \sqrt{1+X_c} \cdot d)}{\beta_c \sqrt{1+X_c}}, \\ C' &= -j \cdot \beta_c \sqrt{1+X_c} \cdot \sin(\beta_c \sqrt{1+X_c} \cdot d), \end{aligned} \tag{6.1.3}$$

with X_c and β_c being the transverse operator and the propagation constant of the coating layer, respectively.

In order to avoid the manipulation of the trigonometric functions with square root operators, which are difficult to deal with during the computer processing, the trigonometric functions are approximated by polynomials as:

$$\begin{aligned} \sin x &= x \cdot \prod_{m=1}^{\infty} \left(1 - \frac{x^2}{m^2 \cdot \pi^2} \right), \\ \cos x &= \prod_{m=1}^{\infty} \left(1 - \frac{4 \cdot x^2}{(2m-1)^2 \cdot \pi^2} \right). \end{aligned} \tag{6.1.4}$$

In practice, the first M terms of the polynomials can be adopted to approximate the trigonometric functions, and a large value of M leads to good accuracy. Therefore, the operators *A'*, *B'*, *C'* and *D'* can be expressed via

$$A' = D' \approx \prod_{m=1}^{M}\left(1-\frac{4\cdot(\beta_c\sqrt{1+X_c}\cdot d)^2}{(2\cdot m-1)^2\cdot\pi^2}\right)$$
$$B' \approx -j\cdot d\cdot\prod_{m=1}^{M}\left(1-\frac{(\beta_c\sqrt{1+X_c}\cdot d)^2}{m^2\cdot\pi^2}\right) \qquad (6.1.5)$$
$$C' \approx -j\cdot d\cdot(\beta_c\sqrt{1+X_c})^2\cdot\prod_{m=1}^{M}\left(1-\frac{(\beta_c\sqrt{1+X_c}\cdot d)^2}{m^2\cdot\pi^2}\right)$$

Though Eq. (6.1.2) successfully established the connection between the total fields $E_{total(1)}$ and $E_{total(2)}$, it cannot be utilized directly to solve the reflected fields $E_{ref(1)}$ and $E_{ref(2)}$ at the same time. Therefore, Eq. (6.1.2) is transformed in order to eliminate $E_{ref(2)}$ and leave only $E_{ref(1)}$ for solving, as discussed in the following part.

In Fig. 6.1, total voltage on the port 1, $V_{total(1)}$, can be expressed as a sum of incident and reflected voltages as:

$$V_{total(1)} = V_{inc(1)} + V_{ref(1)}, \qquad (6.1.6)$$

and total current, $I_{total(1)}$, is:

$$I_{total(1)} = \frac{1}{Z_1}(V_{inc(1)} - V_{ref(1)}). \qquad (6.1.7)$$

where Z_1 is the characteristic impedance of port 1.

Eq.(6.1.6) and Eq.(6.1.7) lead to the following equation:

$$V_{total(1)} + Z_1 I_{total(1)} = (V_{inc(1)} + V_{ref(1)}) + Z_1\cdot\left(\frac{1}{Z_1}(V_{inc(1)} - V_{ref(1)})\right) = 2V_{inc(1)}. \qquad (6.1.8)$$

Replacing the physical quantities in Eq. (6.1.8) from a viewpoint of fields and expressing the characteristic impedance by $Z_1 = \frac{1}{\beta_1 \cdot \sqrt{1+X_1}}$ leads to the equation:

$$E_{total(1)} + \frac{1}{\beta_1 \cdot \sqrt{1+X_1}} G_{total(1)} = (E_{inc(1)} + E_{ref(1)}) + (E_{inc(1)} - E_{ref(1)}) = 2E_{inc(1)}, \quad (6.1.9)$$

where X_1 is the transverse operator of the left side of the coating layer and is in the same form of that in Eq.(5.1.5). The square root operators can be approximated by $\beta_1 \cdot \sqrt{1+X_1} \approx \frac{N(X_1)}{D(X_1)}$, where $N(X_1)$ and $D(X_1)$ are polynomials in X_1. This leads to:

$$N(X_1)E_{total(1)} + D(X_1)G_{total(1)} = 2N(X_1) \cdot E_{inc(1)}. \quad (6.1.10)$$

The incident and reflected fields at the other side of the coating layer, $E_{inc(2)}$ and $E_{ref(2)}$, propagate at a reverse direction to $E_{inc(1)}$ and $E_{ref(1)}$, as shown in Fig. 6.2, hence an equation similar to Eq.(6.1.9) is obtained as:

$$E_{total(2)} + \frac{1}{\beta_2 \cdot \sqrt{1+X_2}} G_{total(2)} = -(E_{inc(2)} + E_{ref(2)}) + (E_{ref(2)} - E_{inc(2)}) = -2E_{inc(2)} \quad (6.1.11)$$

Represent $\beta_2 \cdot \sqrt{1+X_2}$ by $\beta_2 \cdot \sqrt{1+X_2} \approx \frac{N(X_2)}{D(X_2)}$, Eq. (6.1.11) can be rewritten as:

$$N(X_2)E_{total(2)} - D(X_2)G_{total(2)} = 2N(X_2) \cdot E_{inc(2)}. \quad (6.1.12)$$

By solving Eq. (6.1.2) for $E_{total(2)}$ and $G_{total(2)}$ and taking the obtained expression of $E_{total(2)}$ and $G_{total(2)}$ into Eq. (6.1.12), a new expression is obtained as:

$$N(X_2)(A'E_{total(1)} + B'G_{total(1)}) - D(X_2)(C'E_{total(1)} + D'G_{total(1)}) = 2N(X_2) \cdot E_{inc(2)}, \quad (6.1.13)$$

which combines Eq.(6.1.10) to be a new matrix equation as:

$$\begin{pmatrix} N(X_1) & D(X_1) \\ N(X_2)\cdot A' - D(X_2)\cdot C' & N(X_2)\cdot B' - D(X_2)\cdot D' \end{pmatrix} \cdot \begin{pmatrix} E_{total(1)} \\ G_{total(1)} \end{pmatrix} = 2\cdot \begin{pmatrix} N(X_1)\cdot E_{inc(1)} \\ N(X_2)\cdot E_{inc(2)} \end{pmatrix} . \quad (6.1.14)$$

In Eq.(6.1.14), the terms $E_{total(2)}$ and $G_{total(2)}$ have been removed and the unknown values $E_{total(1)}$ and $G_{total(1)}$ can be solved by matrix multiplication if the incident fields $E_{inc(1)}$ and $E_{inc(2)}$ are known. Once the value $E_{total(1)}$ is obtained, the reflected field on the left hand side of the coating layer can be solved according to $E_{total(1)} = E_{inc(1)} + E_{ref(1)}$.

6.2 Numerical Implementation

The matrix equation, Eq.(6.1.14), is not suitable for computer processing. Two issues need to be resolved: the first one is that the square root operators are approximated by $\beta_i \cdot \sqrt{1+X_i} \approx \frac{N(X_i)}{D(X_i)}$ so that suitable expressions of $N(X_1)$ and $D(X_1)$ are required; the second one is that the second order derivative $\frac{\partial^2}{\partial x^2}$ contained in the transverse operators X_i need to be approximated before computer processing. This section is going to present how to deal with these issues.

For the first problem, the Padé approximation can be applied to approximate the square root operators. However, the standard Padé approximation may cause the instability as discussed in Chapter 4. In order to improve the stability of the algorithm, the branch cut of square root operator can be rotated by an angle θ. For the left hand side of the coating layer, the square root operator can be rewritten as:

$$\beta_1 \cdot \sqrt{1+X_1} = \beta_1 \cdot e^{j\theta/2}\sqrt{1+\left[\left(1+X_1\right)e^{-j\theta}-1\right]} = \beta_1 \cdot e^{j\theta/2}\sqrt{1+R_1} \approx \frac{N(R_1)}{D(R_1)} \qquad (6.2.1)$$

where $N(R_1)$ and $D(R_1)$ are polynomials in R₁. Similarly, $N(R_2)$ and $D(R_2)$ are introduced for the right side of the coating layer.

Physically, $E_{inc(2)} = 0$ is satisfied since no backward field is present at the right hand side of the coating layer. Replacing $N(X_i)$ and $D(X_i)$ by $N(R_i)$ and $D(R_i)$ in the matrix, respectively (i equals to 1 for the left side and 2 for the right side of the coating layer), the problem thus requires the solution of:

$$\begin{pmatrix} N(R_1) & D(R_1) \\ N(R_2)\cdot A' - D(R_2)\cdot C' & N(R_2)\cdot B' - D(R_2)\cdot D' \end{pmatrix} \cdot \begin{pmatrix} E_{total(1)} \\ G_{total(1)} \end{pmatrix} = 2\cdot \begin{pmatrix} N(R_1)\cdot E_{inc(1)} \\ 0 \end{pmatrix}. \qquad (6.2.2)$$

Eq.(6.2.1) can be expressed by the well-known Padé approximation as:

$$\beta_i \cdot e^{j\theta/2}\sqrt{1+R_i} \approx \beta_i \cdot e^{j\theta/2}\prod_{r=1}^{s}\frac{1+c_r^{(s)}R_i}{1+b_r^{(s)}R_i}, \qquad (6.2.3)$$

where the Padé coefficients are given by [2]

$$b_r^{(s)} = \cos^2\left(\frac{r\pi}{2s+1}\right) \text{ and } c_r^{(s)} = \sin^2\left(\frac{r\pi}{2s+1}\right) \qquad (6.2.4)$$

If the rotated angle is $\theta = -90^{o}$, N(R_i) and D(R_i) are expressed as:

$$
\begin{aligned}
\mathrm{N}(\mathrm{R}_i) &= \beta_i \cdot \left(\frac{\sqrt{2}}{2} - j\,\frac{\sqrt{2}}{2} \right) \prod_{r=1}^{s} \left(1 + \sin^2\left(\frac{r\pi}{2s+1} \right) \mathrm{R}_i \right) \\
&= \beta_i \cdot \left(\frac{\sqrt{2}}{2} - j\,\frac{\sqrt{2}}{2} \right) \prod_{r=1}^{s} \left(1 + \sin^2\left(\frac{r\pi}{2s+1} \right) \left(j\left(1 + \mathrm{X}_i\right) - 1 \right) \right)
\end{aligned} \qquad (6.2.5)
$$

$$
\mathrm{D}(\mathrm{R}_i) = \prod_{r=1}^{s} \left(1 + \cos^2\left(\frac{r\pi}{2s+1} \right) \mathrm{R}_i \right) = \prod_{r=1}^{s} \left(1 + \cos^2\left(\frac{r\pi}{2s+1} \right) \left(j\left(1 + \mathrm{X}_i\right) - 1 \right) \right) \qquad (6.2.6)
$$

So far the first problem has been solved. The square root operators are removed from the equation and the polynomials $\mathrm{N}(\mathrm{X}_i)$ and $\mathrm{D}(\mathrm{X}_i)$ are obtained.

Eq.(6.2.5) and Eq.(6.2.6) can be further extended by replacing the operator X_i with its original form, $\mathrm{X}_i = \dfrac{\dfrac{\partial^2}{\partial x^2} + k_0^2 n_{ri}^2 - \beta_i^2}{\beta_i^2}$. If the second order derivative $\dfrac{\partial^2}{\partial x^2}$ is considered as an unknown term, the expressions of $\mathrm{N}(\mathrm{R}_i)$ and $\mathrm{D}(\mathrm{R}_i)$ can be reorganized in the form of product or summation as:

$$
\begin{aligned}
\mathrm{N}(\mathrm{R}_i) &= \beta_i \cdot \left(\frac{\sqrt{2}}{2} - j\,\frac{\sqrt{2}}{2} \right) \prod_{r=1}^{s} \left(\underbrace{1 + \sin^2\left(\frac{r\pi}{2s+1} \right)\left(j\,\frac{k_0^2 n_{ri}^2}{\beta_i^2} - 1 \right)}_{p_0^{(r)}} + \underbrace{j \sin^2\left(\frac{r\pi}{2s+1} \right) \frac{1}{\beta_i^2}}_{p_1^{(r)}} \frac{\partial^2}{\partial x^2} \right) \\
&= \beta_i \cdot \left(\frac{\sqrt{2}}{2} - j\,\frac{\sqrt{2}}{2} \right) \sum_{r=0}^{s} \left(\tilde{p}_r \cdot \left(\frac{\partial^2}{\partial x^2} \right)^r \right)
\end{aligned} \qquad (6.2.7)
$$

$$
\mathrm{D}(\mathrm{R}_i) = \prod_{r=1}^{s} \left(\underbrace{1 + \cos^2\left(\frac{r\pi}{2s+1} \right)\left(j\,\frac{k_0^2 n_{ri}^2}{\beta_i^2} - 1 \right)}_{q_0^{(r)}} + \underbrace{j \cos^2\left(\frac{r\pi}{2s+1} \right) \frac{1}{\beta_i^2}}_{q_1^{(r)}} \frac{\partial^2}{\partial x^2} \right) = \sum_{r=0}^{s} \left(\tilde{q}_r \cdot \left(\frac{\partial^2}{\partial x^2} \right)^r \right) \quad (6.2.8)
$$

where $p_0^{(r)}$ and $q_0^{(r)}$ denote the coefficients of the constant terms (the order of $\dfrac{\partial^2}{\partial x^2}$

is 0), $p_1^{(r)}$ and $q_1^{(r)}$ denote the coefficients of the unknown terms (the order of $\frac{\partial^2}{\partial x^2}$ is 1), for the product, respectively. $\tilde{p}_r$ and $\tilde{q}_r$ denote the coefficients of different order unknown terms for the summation. The highest order of the second derivate operator $\frac{\partial^2}{\partial x^2}$ in these two equations equals to the value of the Padé order, s.

Similarly, replacing $X_c = \frac{\frac{\partial^2}{\partial x^2} + k_0^2 n_{rc}^2 - \beta_c^2}{\beta_c^2}$ into *A', B' C'* and *D'* gives:

$$A' = D' = \prod_{m=1}^{M} \left(1 - \underbrace{\frac{4\cdot d^2 \cdot k_0^2 n_{rc}^2}{(2\cdot m-1)^2 \cdot \pi^2}}_{a_0^{(m)}} - \underbrace{\frac{4\cdot d^2}{(2\cdot m-1)^2 \cdot \pi^2}}_{a_1^{(m)}} \cdot \frac{\partial^2}{\partial x^2} \right) = \sum_{r=0}^{M} \left(\tilde{a}_r \cdot \left(\frac{\partial^2}{\partial x^2}\right)^r \right) \quad (6.2.9)$$

$$B' = -j \cdot d \cdot \prod_{m=1}^{M} \left(1 - \underbrace{\frac{d^2 \cdot k_0^2 n_{rc}^2}{m^2 \cdot \pi^2}}_{b_0^{(m)}} - \underbrace{\frac{d^2}{m^2 \cdot \pi^2}}_{b_1^{(m)}} \frac{\partial^2}{\partial x^2} \right) = -j \cdot d \sum_{r=0}^{M} \left(\tilde{b}_r \cdot \left(\frac{\partial^2}{\partial x^2}\right)^r \right) \quad (6.2.10)$$

$$C' = \left(\underbrace{-j \cdot d \cdot k_0^2 n_{rc}^2}_{c_0} \underset{c_1}{- j \cdot d} \frac{\partial^2}{\partial x^2} \right) \cdot \prod_{m=1}^{M} \left(1 - \underbrace{\frac{d^2 \cdot k_0^2 n_{rc}^2}{m^2 \cdot \pi^2}}_{c_0^{(m)}} - \underbrace{\frac{d^2}{m^2 \cdot \pi^2}}_{c_1^{(m)}} \frac{\partial^2}{\partial x^2} \right) = \sum_{r=0}^{M+1} \left(\tilde{c}_r \cdot \left(\frac{\partial^2}{\partial x^2}\right)^r \right) (6.2.11)$$

where $\tilde{a}_r$, $\tilde{b}_r$ and $\tilde{c}_r$ denote the coefficients of different order unknown terms for the summation. The highest order of the second derivate operator $\frac{\partial^2}{\partial x^2}$ in Eq.(6.2.9) and Eq.(6.2.10) equals to the value of the parameter M, and the highest order in Eq.(6.2.11) equals to M+1. According to Eq.(6.2.7) - Eq.(6.2.11), the combined operators, $N(R_2)\cdot A' - D(R_2)\cdot C'$ and $N(R_2)\cdot B' - D(R_2)\cdot D'$, can also be expressed by polynomials in term of $\frac{\partial^2}{\partial x^2}$. In $N(R_2)\cdot A' - D(R_2)\cdot C'$, the highest order of the second derivate operator equals to $s+M+1$, and in $N(R_2)\cdot B'-D(R_2)\cdot D'$, equals to $s+M$.

Mathematically, the derivate of a term $C_n\left(\frac{\partial^2}{\partial x^2}\right)^n\varphi$, where C_n is a constant coefficient, can be expressed as a polynomial containing $(2n+1)$ terms as:

$$C_n\left(\frac{\partial^2}{\partial x^2}\right)^n\varphi=\sum_{i=0}^{2n}\left(C_{x+(i-n)\Delta x}\cdot\varphi_{x+(i-n)\Delta x}\right), \qquad (6.2.12)$$

where $C_{x+(i-n)\Delta x}$ is the coefficient of the term $\varphi_{x+(i-n)\Delta x}$ and equals to:

$$C_{x+(i-n)\Delta x}=C_n\cdot\left(\frac{(-1)^i\cdot(2n)!}{(2n-i)!\cdot i!}\cdot\Delta x^{-2n}\right). \qquad (6.2.13)$$

Using Eq.(6.2.12) to derive all the terms with respect to $\frac{\partial^2}{\partial x^2}$ in the polynomials of $N(R_1)$, $D(R_1)$, $N(R_2)\cdot A'-D(R_2)\cdot C'$ and $N(R_2)\cdot B'-D(R_2)\cdot D'$, and adding up all the coefficients for the same term $\varphi_{x+(i-n)\Delta x}$ in each polynomial, the combined coefficients for each term $\varphi_{x+(i-n)\Delta x}$, $\tilde{C}_{x+(i-n)\Delta x}$, can be generated. According to the order of Padé, s, and the parameter M of the approximations of trigonometric function, the number of terms in polynomials $N(R_1)$ and $D(R_1)$ is $2s+1$, the number of terms in polynomial $N(R_2)\cdot A'-D(R_2)\cdot C'$ is $2(s+M+1)+1$, and the number of terms in polynomial $N(R_2)\cdot B'-D(R_2)\cdot D'$ is $2(s+M)+1$. These obtained coefficients are the final non-zero elements in the matrices. If the number of the sampling points along the transverse direction is n ($n>>s$ & $n>>M$), Eq.(6.2.2) can be expressed in a new form with size 2n as:

$$\left(\begin{array}{ccccc|ccccc}
\ddots & & & & 0 & \ddots & & & & 0\\
& \ddots & & & & & \ddots & & & \\
{}^1\tilde{C}_{j-s} & \cdots & {}^1\tilde{C}_{j} & \cdots & {}^1\tilde{C}_{j+s} & {}^2\tilde{C}_{j-s} & \cdots & {}^2\tilde{C}_{j} & \cdots & {}^2\tilde{C}_{j+s}\\
& & & \ddots & & & & & \ddots & \\
0 & & & & \ddots & 0 & & & & \ddots\\
\hline
\ddots & & & & 0 & \ddots & & & & 0\\
& \ddots & & & & & \ddots & & & \\
{}^3\tilde{C}_{j-(s+M+1)} & \cdots & {}^3\tilde{C}_{j} & \cdots & {}^3\tilde{C}_{j+(s+M+1)} & {}^4\tilde{C}_{j-(s+M)} & \cdots & {}^4\tilde{C}_{j} & \cdots & {}^4\tilde{C}_{j+(s+M)}\\
& & & \ddots & & & & & \ddots & \\
0 & & & & \ddots & 0 & & & & \ddots
\end{array}\right)
\bullet
\left(\begin{array}{c}
E_0^{total(1)}\\
\vdots\\
E_j^{total(1)}\\
\vdots\\
E_n^{total(1)}\\
\hline
G_0^{total(1)}\\
\vdots\\
G_j^{total(1)}\\
\vdots\\
G_n^{total(1)}
\end{array}\right)
= 2
\left(\begin{array}{c}
\left(\begin{array}{ccccc}
\ddots & & & & 0\\
& \ddots & & & \\
{}^1\tilde{C}_{j-s} & \cdots & {}^1\tilde{C}_{j} & \cdots & {}^1\tilde{C}_{j+s}\\
& & & \ddots & \\
0 & & & & \ddots
\end{array}\right)
\left(\begin{array}{c}
E_0^{inc(1)}\\
\vdots\\
E_j^{inc(1)}\\
\vdots\\
E_n^{inc(1)}
\end{array}\right)\\
\hline
\\
0\\
\\
\end{array}\right)
\tag{6.2.14}$$

where, ${}^1\tilde{C}$, ${}^2\tilde{C}$, ${}^3\tilde{C}$ and ${}^4\tilde{C}$ represent the coefficients of polynomial $N(R_1)$, $D(R_1)$, $N(R_2)\cdot A' - D(R_2)\cdot C'$ and $N(R_2)\cdot B' - D(R_2)\cdot D'$, respectively. Eq.(6.2.14) can be explicitly evaluated by using sparse matrix multiplications. It also can be algebraically preconditioned. The attraction of Eq.(6.2.14) over the normal iterative approach is its potential for more rapid evaluation, especially when the coating is resonant and many iterations are required for convergence. Moreover, if the refractive index of the coating layer is set to be the same value as the refractive index of media 2, or if the thickness of the coating layer is set to be zero, the situation is equivalent to solving the uncoated facet reflection problem. In other words, the scheme proposed in this section has the potential to solve both single layer coated and uncoated facet reflection problems. This will be analysed in the following result section.

6.3 Simulation Results

This section presents the test of the formulation derived above. The simulation results for the facet reflectivity of a slab uncoated and coated waveguide facet are presented. In each case, the waveguide is incident normally and at an angle to the facet. WA-BPM propagation is used for a short distance on either side of the facet to permit extraction of the transmitted and reflected guided modes. All simulations are obtained for the TE polarisation.

6.3.1 Uncoated Facet

In this part, the uncoated waveguide facet reflection problem shown in Fig. 5.1 is tested. The single interface reflective BPM discussed in section 5.1 and the T-Bi-BPM for single coating layer structures proposed in this chapter are applied as the simulation tools respectively, for both the normally incident and tilted waveguide. The waveguide has core refractive index $n_{core}=3.6$ and the cladding refractive index is given by $n_{cladding}=n_{core}(1-p)$, where p is the percentage difference from n_{core}. In the following simulations, p has been chosen as 3%, 5% and10%. The core width of the slab is allowed to vary from 0 to 1μm. The material on the right side of the facet is air. The operating wavelength is λ=0.86μm. Simulations have been carried out using mesh size Δx=0.01μm and Δz=0.0125μm. The ID BPM is applied as the mode solver to obtain the fundamental mode profiles and effective refractive indices for different slab waveguides. The mesh size in transverse direction is $\Delta x / \cos\delta$, where δ is the angle of incidence. The simulation window is set as 20μm/ $\cos\delta$ wide and terminated by the TBC. In order to achieve good calculation accuracy, rotated Padé approximation with order (10, 10) is used for all the simulations in this section.

6.3.1.1 Simulation by conventional reflective BPM

Firstly, the single interface reflective BPM is applied to the uncoated facet reflection problems with normally incident waveguide, and BPM simulations are given in Fig. 6.3 and Fig.6.4. In Fig. 6.3 power reflectivities for the TE polarisation are plotted versus slab thicknesses. Three different cases of index contrast are considered, including p=3%, 5% and 10%. The results obtained by the BPM scheme are compared with those obtained by the Free Space Radiation Mode Method (FSRM) [3], which are presented by the solid line in the figure.

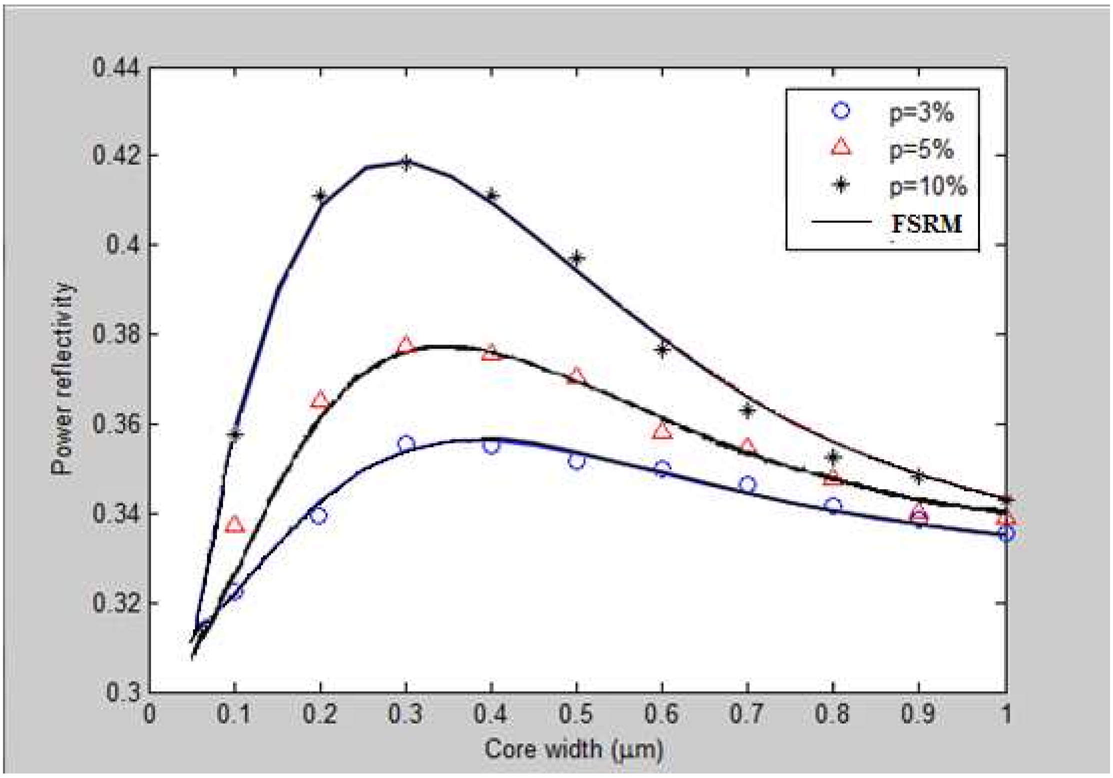

Figure 6.3: The TE power reflectivities obtained by the single interface reflective BPM versus slab width for the normally incident situation. The waveguide has core refractive index n_{core}=3.6 and the index contrast is p=3%, 5% and 10%. The operating wavelength is 0.86μm.

It can be seen that the results of the two methods have good agreement. In the beginning, the power reflectivity increases with the increasing of the core width regardless of what the value of the index contrast is. It reaches the maximum value when the core width is around 0.3μm, and then reduces with the increasing of the core width. Overall, for fixed waveguide width, larger index contrast, p, leads to larger power reflectivity.

Fig. 6.4 provides an example of the field profile when a waveguide normally incidents on an uncoated facet. The field profile is obtained in the case that the waveguide width is 0.4μm, n_{core}=3.6 and p=5%. The operating wavelength is 0.86μm.

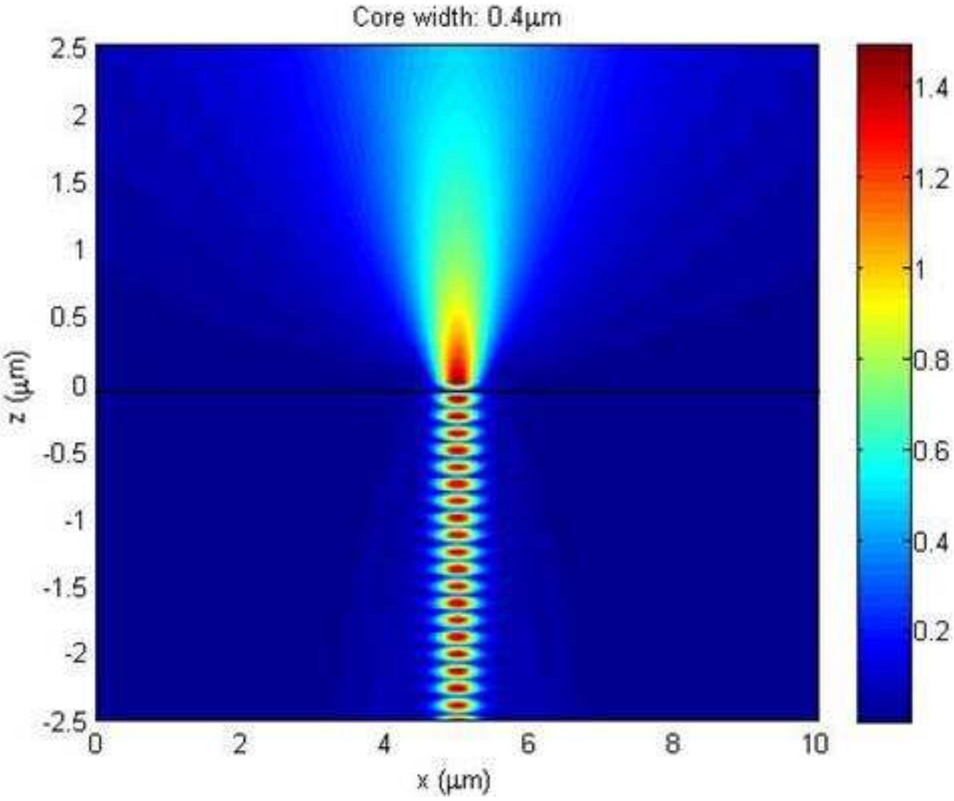

Figure 6.4: The obtained field profile of fundamental TE mode by the BPM for the normally incident situation when the core width is 0.4 μm. The refractive indices of the core and the cladding are n_{core}=3.6 and $n_{cladding}$=3.42, respectively. The operating wavelength is 0.86μm.

It shows in Fig.6.4 that a standing wave pattern is generated in the waveguide and specially obvious in the core because the reflected field interferes with the incident field. Beyond the facet, the transmitted field disperses in the free space along the propagation direction as expected.

The single interface reflective BPM scheme is also applied for waveguide incident at an angle onto the facet, and BPM simulations are given in Fig. 6.5 and Fig.6.6. Waveguides incident at an angle of 5^{o}, 10^{o} and 15^{o} to the facet are considered, respectively. In Fig. 6.5 (a, b, c), power reflectivities for the TE polarisation are plotted versus slab width for p=3%, p=5% and p=10%, respectively. The BPM and the FSRM [3] are compared and the results are in good agreement. For the fixed value of the index contrast, the larger the incident angle is, the smaller the facet reflectivity is. Moreover, for fixed waveguide width and fixed incident angle, larger index contrast results in larger power reflectivity.

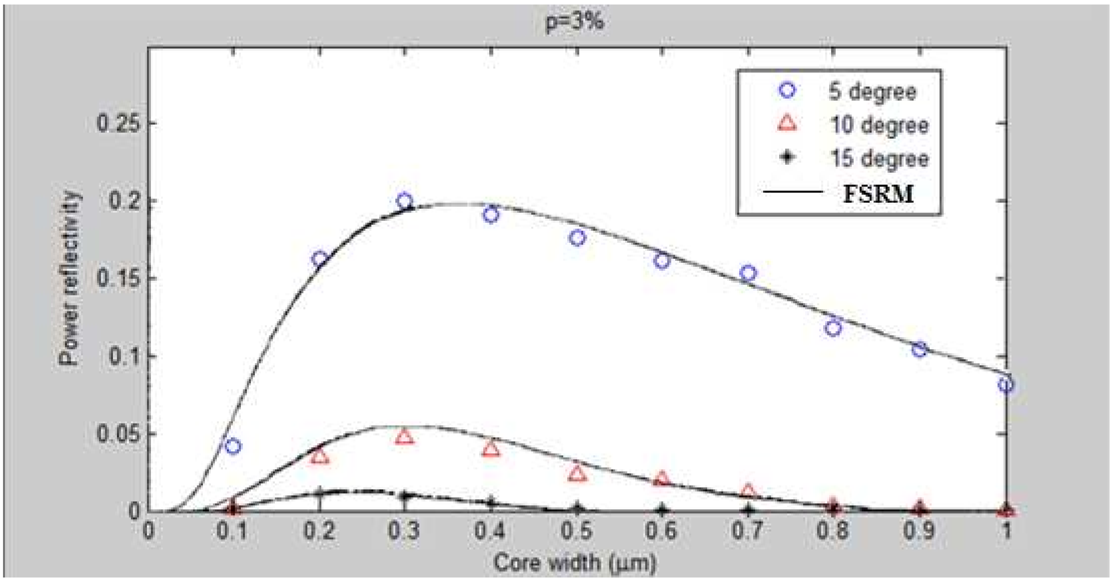

(a)

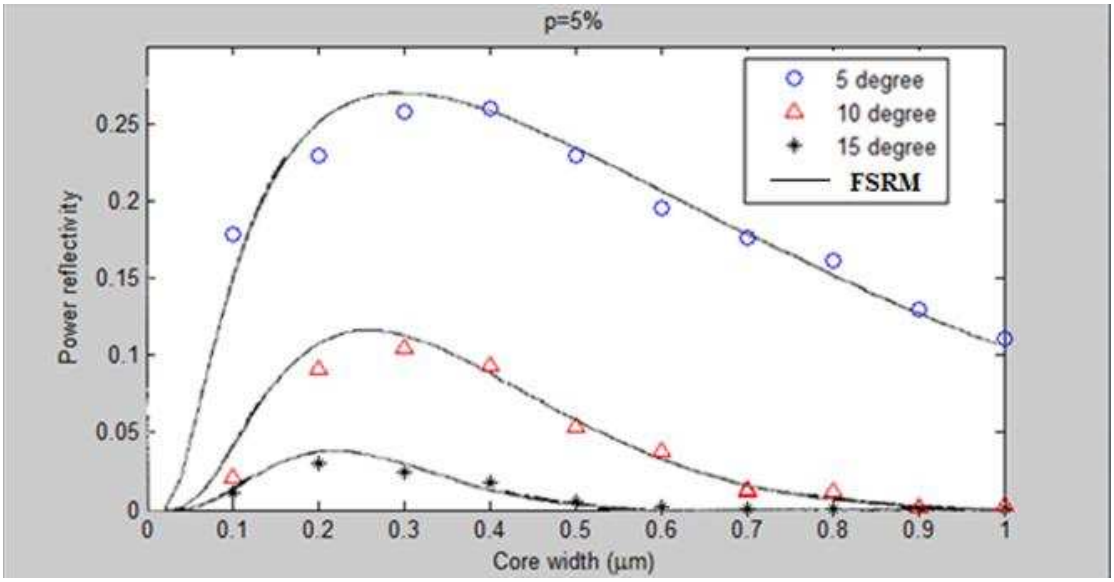

(b)

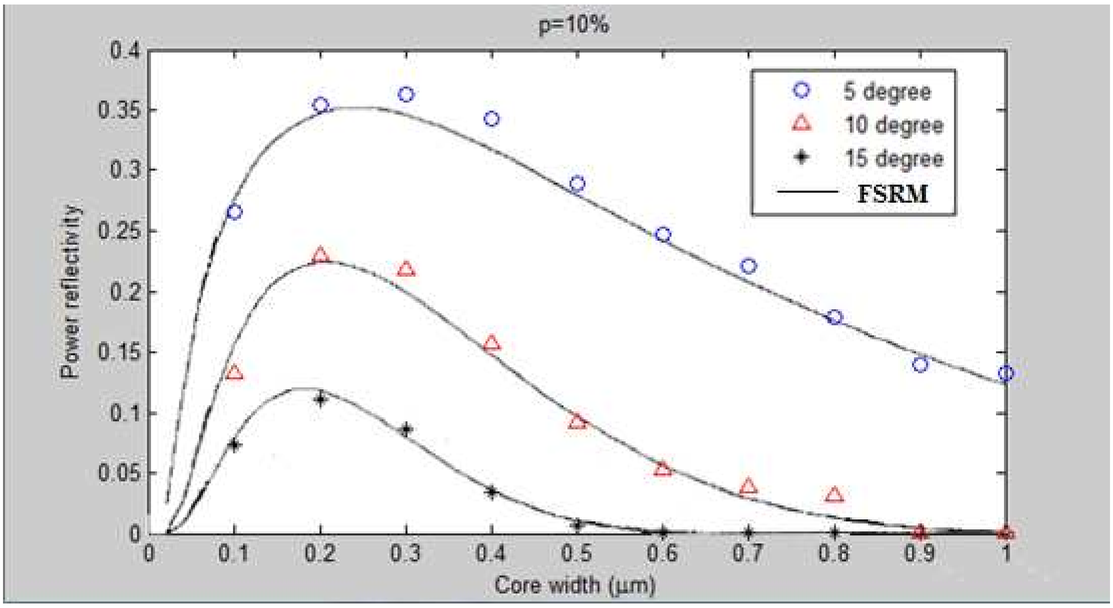

(c)

Figure 6.5: The TE power reflectivities as a function of waveguide width for waveguides tilted at an angle onto a facet. The tilted angle is 5°, 10° and 15°. The waveguide has core refractive index $n_{core}=3.6$ and the index contrast is (a) p=3%, (b) p=5% and (c) p=10%. The operating wavelength is 0.86µm.

Fig. 6.6 shows the reflection of the field from the facet for different incident angle (5°, 10°, 15° and 20°).

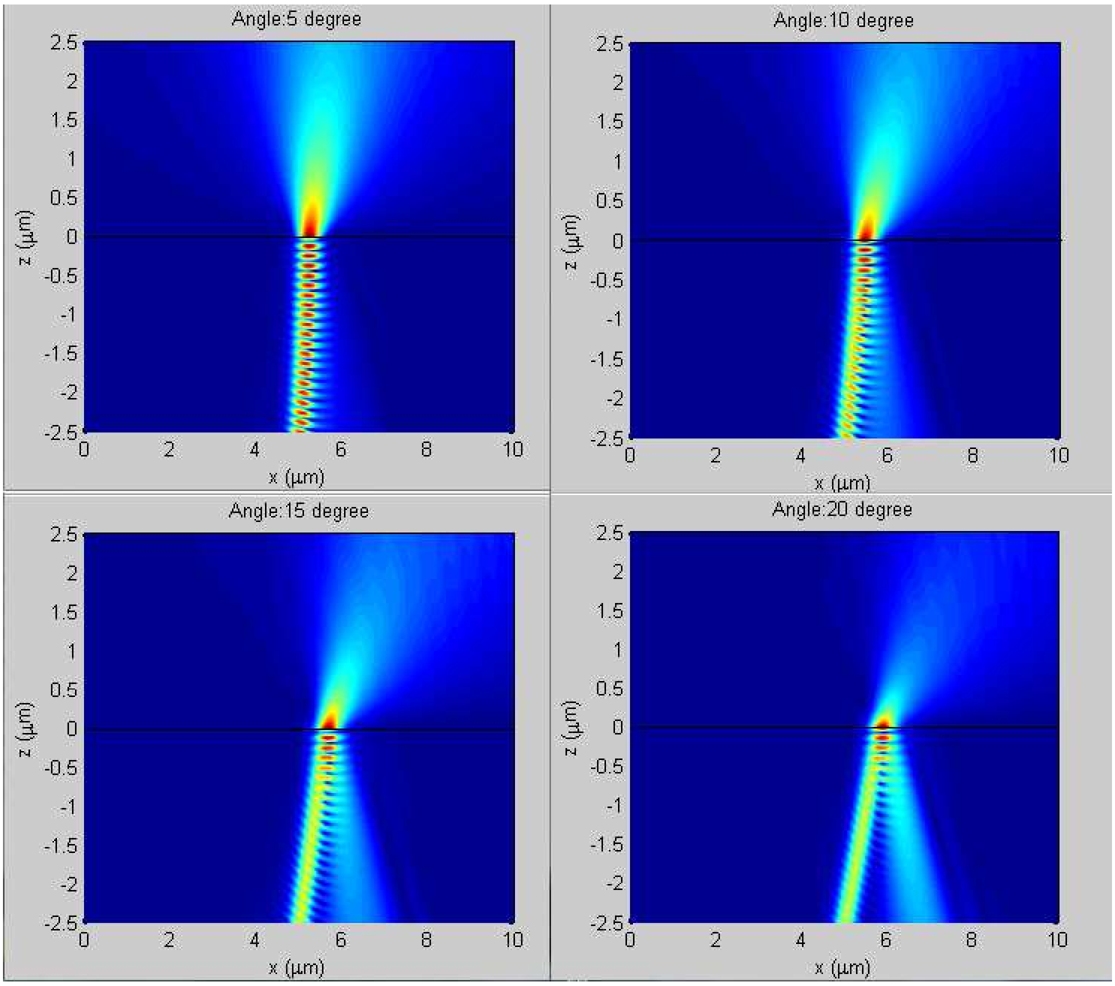

Figure 6.6: The obtained field profiles of fundamental TE mode for the waveguide tilted by 5°, 10°, 15° and 20°, respectively. The core width of the waveguide is 0.4μm. The refractive indices of the core and the cladding are n_{core}=3.6 and $n_{cladding}$=3.42. The operating wavelength is 0.86μm.

Similar to the normally incident simulations, the standing wave pattern is generated in the waveguide. However, the standing wave pattern is not as strong as in the case of normally incident waveguides due to the fact that large part of the reflected field is directed away from the core and into the cladding. As can be seen from the figures, with the increase of the titled angle, the reflectivity into guided mode reduces. This is why in many practical situations the waveguide is tilted to a facet.

6.3.1.2 Simulations by the T-Bi-BPM

The simulation results shown in Fig. 6.3 to Fig. 6.6 proved that the single interface reflection BPM is effective to solve the uncoated facet reflective problems, for both normally and angularly incident waveguides. In the following part, the T-Bi-BPM is applied to repeat all simulations which have been done by the single interface reflection BPM above. There are two ways to apply the new proposed method for the uncoated facet reflective problems: (a) setting the refractive index of the coating layer to be the same value as the refractive index of air, or (b) setting the thickness of the coating layer to be zero in the matrix equation. Here the latter one is used for the following simulations. This means in Eq.(6.1.5), the parameter d is zero, and hence the operator *A'*, and *D'* are equal to one, the operator *B'*, *C'* are equal to zero. The parameter M will not affect the simulation accuracy for this case.

Fig 6.7 illustrates the power reflectivities of the fundamental TE mode which are obtained by the T-Bi-BPM for the normally incident waveguides. Similarly as in the previous simulations, the core refractive index of 3.6 and the index contrast, p=3%, p=5% and p=10%, are considered. The operating wavelength is 0.86μm. All the results are plotted as a function of waveguide width which varies from 0 to 1μm. Results are compared with the results obtained by the FSRM method [3] and show good agreement.

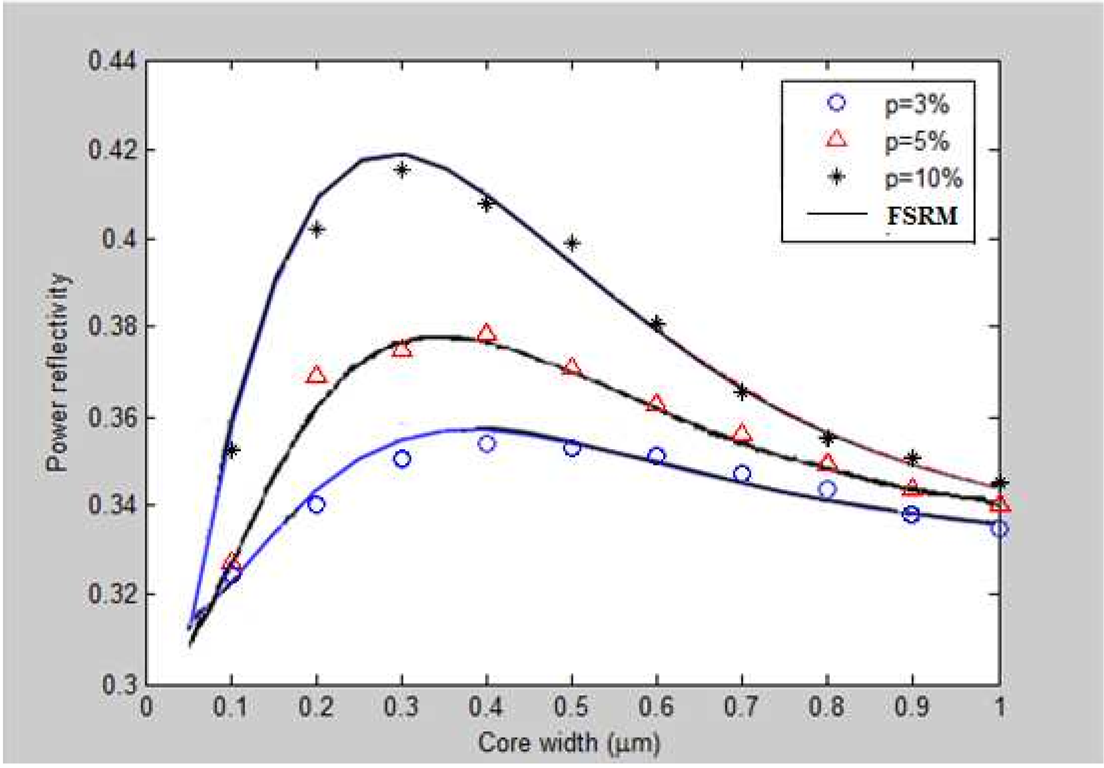

Figure 6.7: TE power reflectivities obtained by the transmission matrix based Bi-BPM versus slab width for the normally incident waveguides. The waveguide has core refractive index n_{core}=3.6 and the index contrast is p=3%, p=5% and p=10%. The operating wavelength is 0.86μm.

Fig. 6.8 (a, b, c) illustrates the power reflectivities of the fundamental TE mode which are obtained by the T-Bi-BPM for the tilted waveguides. The incident angles, δ= 5^o, 10^o, and 15^o, are tested. The operating wavelength is 0.86μm. All the results are plotted as a function of waveguide width which varies from 0 to 1μm. It can be seen that the results of T-Bi-BPM match those obtained by the FSRM method [3].

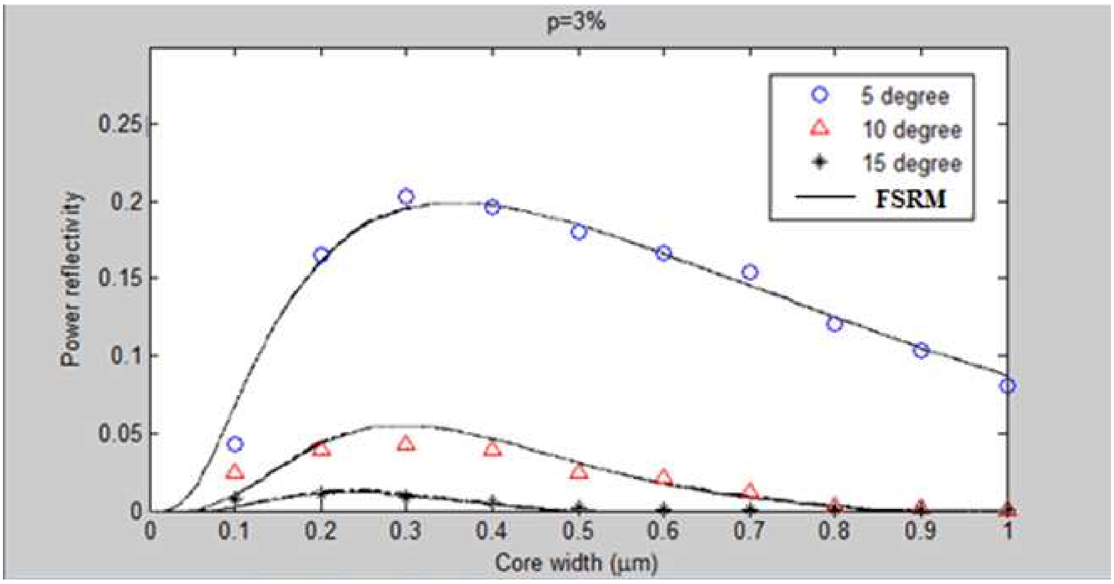

(a)

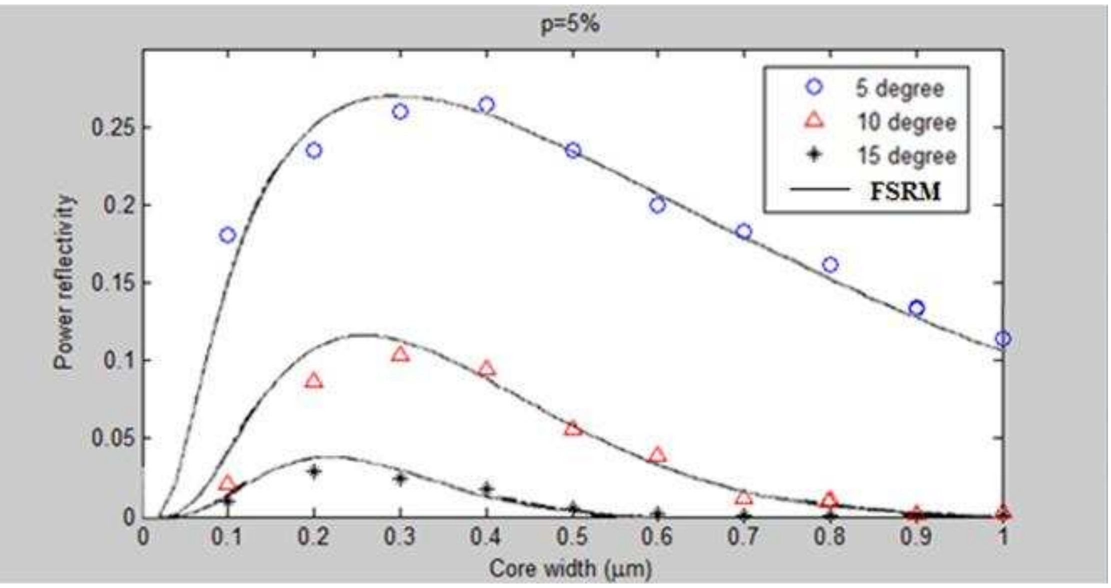

(b)

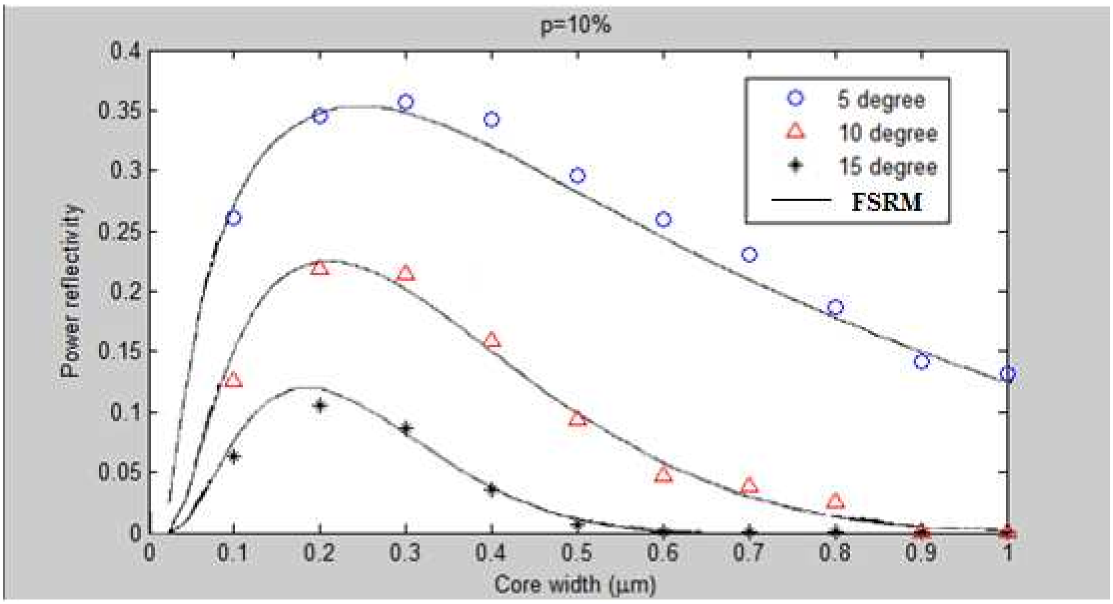

(c)

Figure 6.8: TE power reflectivities obtained by the transmission matrix based Bi-BPM versus slab width for the tilted waveguide. The tilted angle is 5°, 10°, and 15°. The waveguide has core refractive index n_{core}=3.6 and the index contrast is (a) p=3%, (b) p=5% and (c) p=10%. The operating wavelength is 0.86μm.

6.1.1.3 The comparison of the two BPM schemes

Fig. 6.9 illustrates the reflected power obtained by the two methods when the core width is 0.3μm, 0.4μm and 0.5μm, respectively. For each core width, the reflected power is given in dB and plotted versus the waveguide tilted angle. In the legend, S-BPM represents the Single interface reflective BPM and T-BPM represents the T-Bi-BPM. Results are obtained for the condition that the index contrast is p=3%, p=5% and p=10%, and the incident angle is 0°, 5°, 10°, 15° and 20°, respectively.

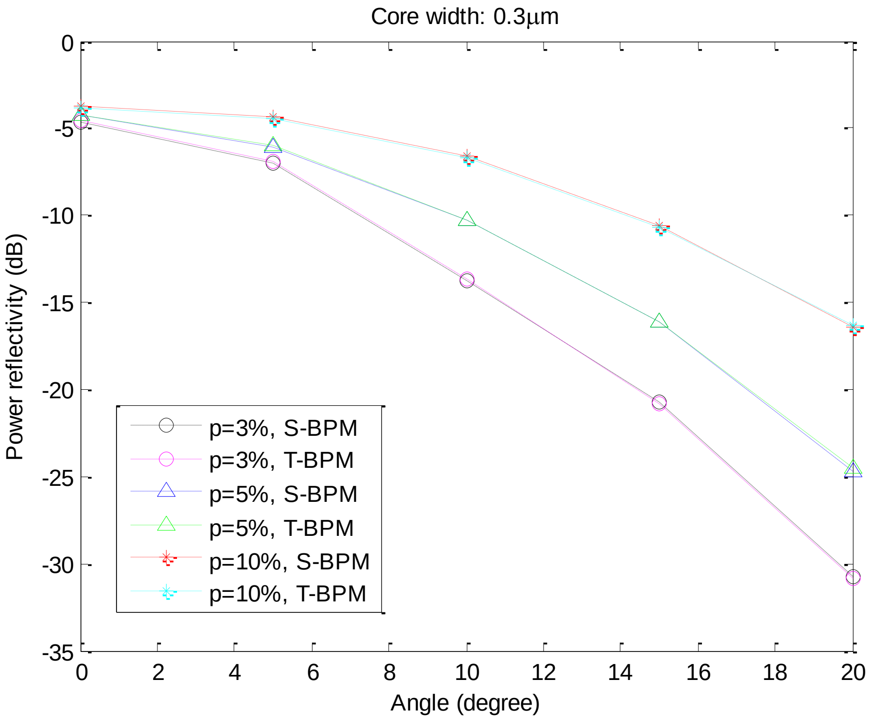
Core width: 0.3µm
Power reflectivity (dB)
Angle (degree)
0
-5
-10
-15
-20
-25
-30
-35
0
2
4
6
8
10
12
14
16
18
20
p=3%, S-BPM
p=3%, T-BPM
p=5%, S-BPM
p=5%, T-BPM
p=10%, S-BPM
p=10%, T-BPM

(a)

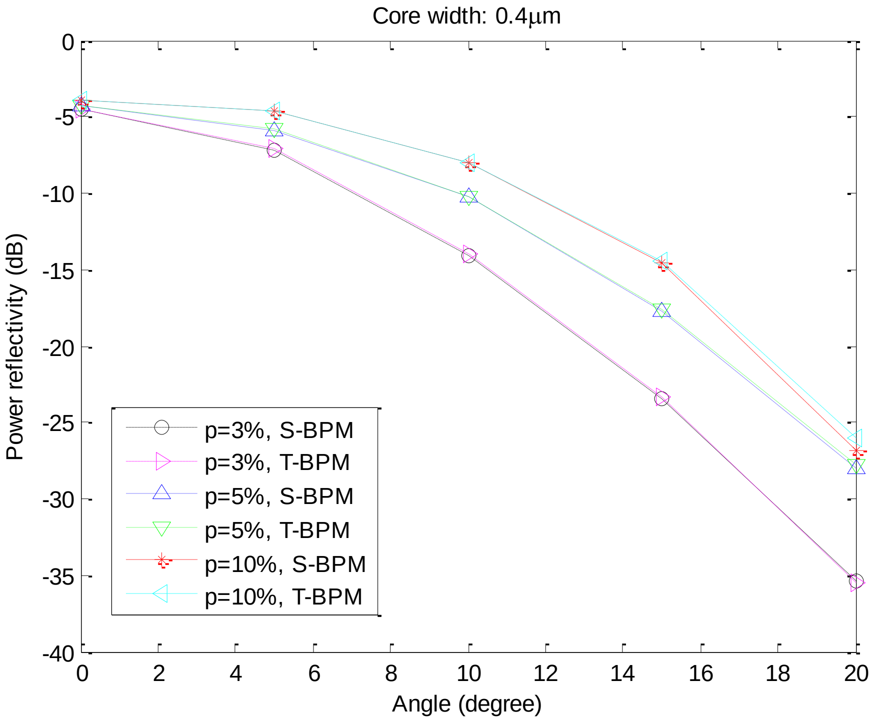
Core width: 0.4µm
Power reflectivity (dB)
Angle (degree)
0
-5
-10
-15
-20
-25
-30
-35
-40
0
2
4
6
8
10
12
14
16
18
20
p=3%, S-BPM
p=3%, T-BPM
p=5%, S-BPM
p=5%, T-BPM
p=10%, S-BPM
p=10%, T-BPM

(b)

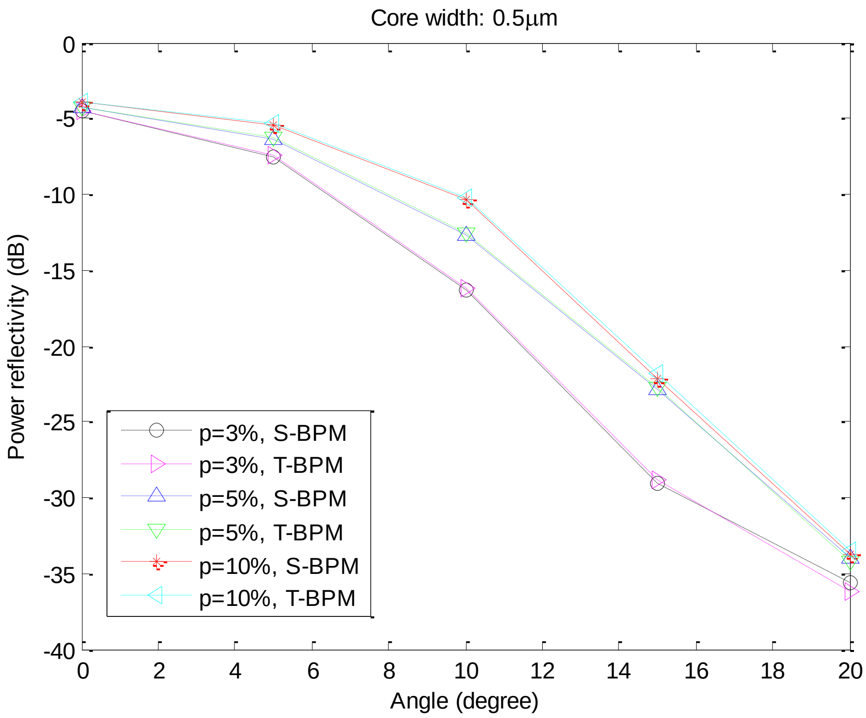

(c)

Figure 6.9: Comparison of power reflectivities obtained by the single interface reflective BPM and T-Bi-BPM versus tilted angle when waveguide core width is (a) 0.3μm, (b) 0.4μm and (c) 0.5μm.

As expected, the results show that the reflected guided power decreases as the tilted angle is increased. For fixed tilted angle, the large index contrast leads to large power reflectivity. It indicates that the results obtained by the two methods have good agreement. It also proves that when the same order of Padé approximation and the same transverse sampling interval are used, T-Bi-BPM and the single interface reflective BPM provide similar accuracy for the same simulation. The T-Bi-BPM scheme is reliable for solving the uncoated facet reflection problems.

6.1.1.4 Error analysis

It can be noticed that when the waveguide has a titled incident angle to the facet, the differences of the calculated results between the T-Bi-BPM method and the FSRM method are more obvious than the normal incident situation. One of the possible reasons is the staircase errors. All the simulations reported above have been carried out using uniform rectangular meshing. In the case of angle facets, the facet is aligned with the mesh and the waveguides are staircased. For all the simulations, the incident field is launched into the waveguide and propagates a short distance before reaching the facet. Though the WA BPM scheme is applied during this process, the effect of the staircase cannot be completely eliminated. Moreover, because the waveguide is titled, the width of the core of the waveguide connecting to the facet is adjusted according to the titled angle for the simulations. This process may also introduce calculation errors. A possible approach to eliminate the errors is to use a smaller mesh size along the transverse direction. This has been proved effective for BPM schemes for the single direction propagation problems, with a cost of longer simulation time.

6.3.2 Coated Facet for T-Bi-BPM

In this section, further simulation results will be provided in order to test and verify the effectiveness of the T-Bi-BPM scheme for the single layer coated structure reflection problems. As mentioned in section 6.1, the parameter M in Eq.(6.1.5), which is the order of polynomials representing the trigonometric functions, affects the accuracy of the T-Bi-BPM. Larger value of M leads to better simulation accuracy but it also means heavier computational cost because it results in the increase of the number of the non-zero coefficients in the matrix operators of Eq.(6.2.14). Therefore, it is necessary to investigate what value of M is suitable for simulations. A mathematical test has been done to find the value of M which can provide good accuracy with relatively low computational cost. The test is based on Eq. (6.1.4). Different order polynomials (M=1, 3, 5, 10, 15, 20, 30, 40, respectively) are used to approximate the trigonometric functions for various angle δ, and the errors compared to the exact values are shown in Fig.6.10 (a) and (b) for sine and cosine function as a function of angle.

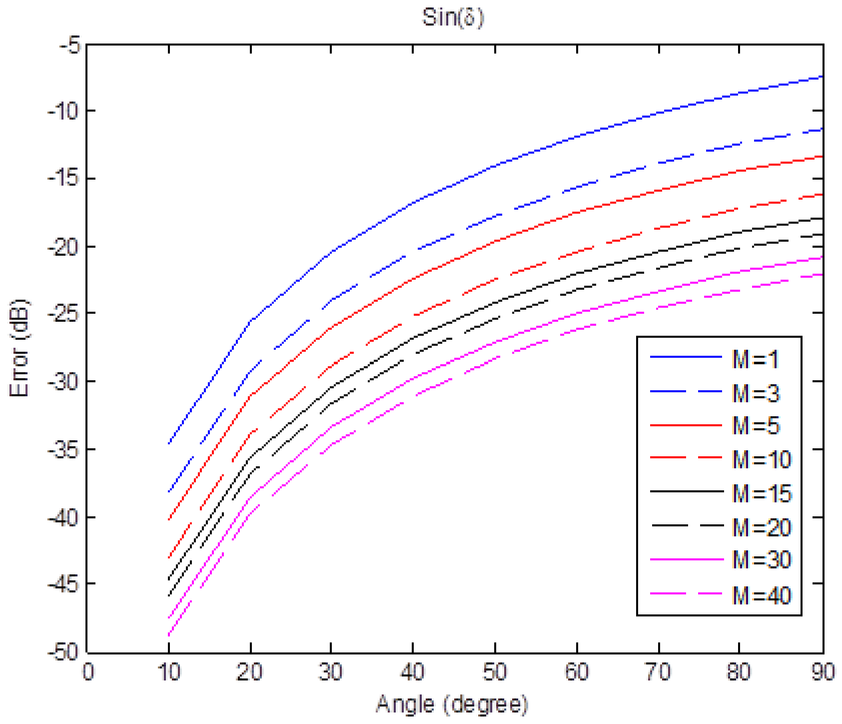

(a)

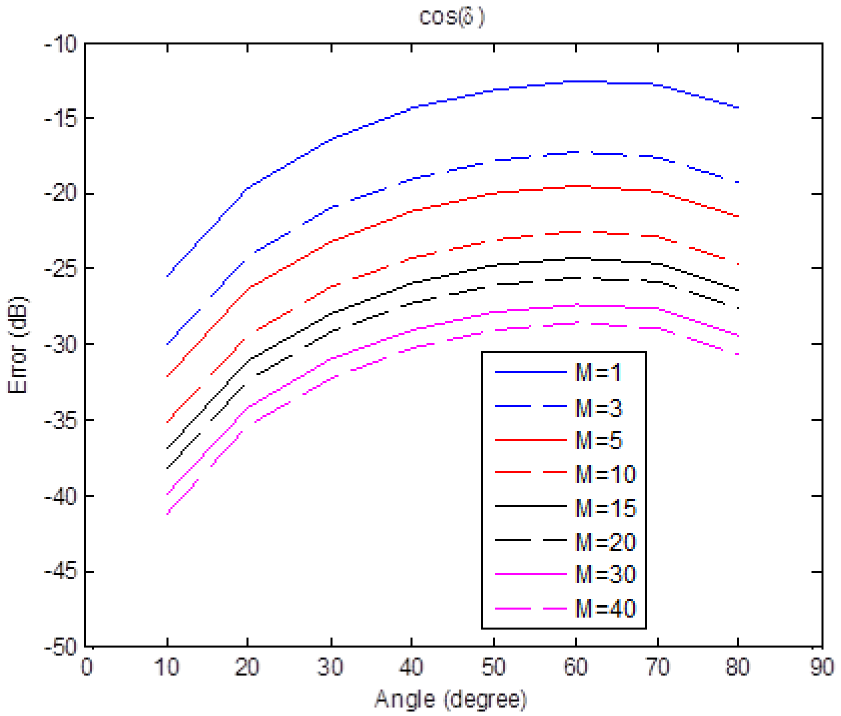

(b)

Figure 6.10: The errors between the real values and the approximate values by different parameter M of (a) sine function and (b) cosine function.

It can be seen that for both sine function and cosine function, the approximate values show better agreement with the real values when the angle is smaller. Moreover, the error reduces with the increase of the parameter M for a certain angle. This indicates that using larger parameter M to improve the method accuracy is effective. It also should be noted that, the effect of the improvement of the approximation accuracy by using a large value of M becomes weaker with the increase of M. For example, comparing the errors obtained by M=10 and M=1, the improvement is significant. However, comparing the errors obtained by M=20 and M=10, the improvement is not as obvious as the former case. Therefore, depending on the accuracy requirement of a practical problem, M should be chosen as a value that provides an acceptable accuracy and requires relatively low computational cost.

In the following part, the testing simulations include three aspects. Firstly, simulation is implemented for a waveguide with one AR coating excited by different operating wavelength. Different transverse sampling intervals are used to investigate if the method accuracy is affected by the transverse sampling interval. Secondly, the waveguides with different core widths normally incident on the facet with one AR coating are considered. Different values of parameter M for the approximations of the trigonometric functions are tested to investigate how the accuracy is affected by parameter M. Finally, the angularly incident situation is tested for a waveguide with various thickness of the AR coating. Different order Padé approximations are applied to investigate how the accuracy changes with different Padé orders. For the case of tilted waveguide the mesh size in transverse direction is changed to $\Delta x / \cos\delta$, where δ is the angle of incident. For each case, published results obtained by the FSRM method are referenced for comparison purpose.

6.3.2.1 Simulation for a single layer coated waveguide excited by variant wavelength

Fig.6.11 shows power reflectivity as a function of wavelength for the waveguide with core refractive index n_{core}=3.512 and cladding refractive index $n_{cladding}$=3.17, and core width of 0.1μm. Waveguide is normally incident on the AR coating with the refractive index $n_{coating}$=1.7936 and the thickness t=0.22256μm. The operating wavelength varies from 1.45μm to 1.65μm. Rotated Padé approximation with order (10, 10) is used to obtained the polynomials $N(R_i)$ and $D(R_i)$, and the parameter M=15 are used for the T-Bi-BPM scheme. The simulations are implemented with transverse sampling interval Δx=0.025μm and Δx=0.01μm, respectively. For each wavelength, the ID BPM method is applied as the mode solver to obtain the fundamental mode. The simulation results obtained by the T-Bi-BPM are compared with the ones obtained by the FSRM method [4].

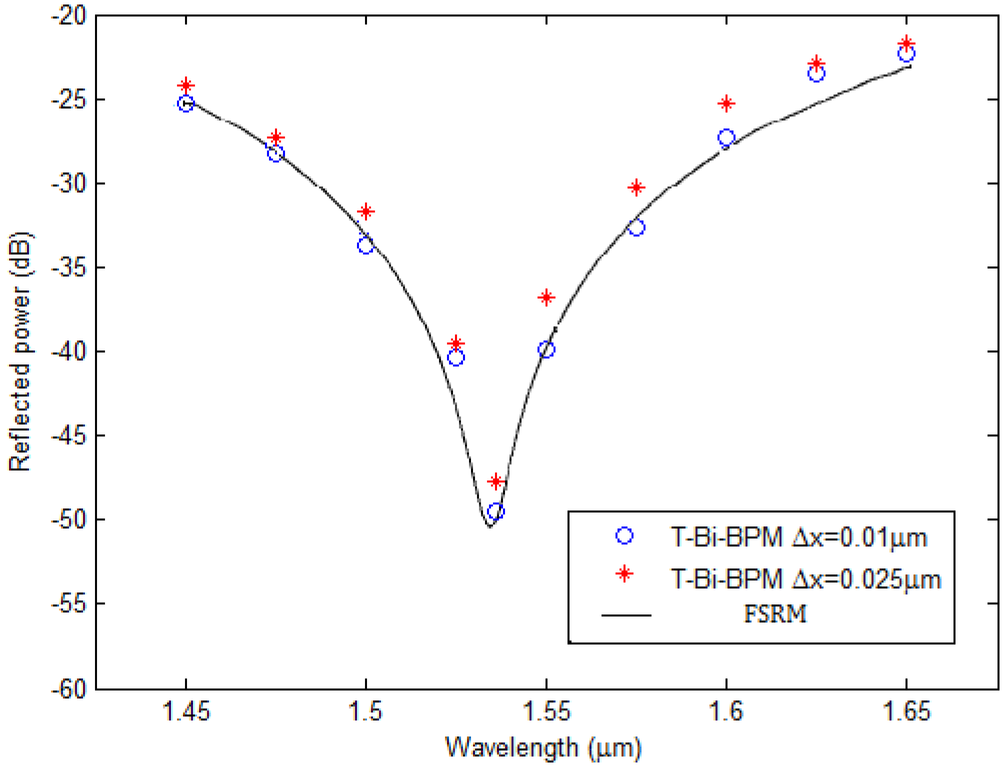

Figure 6.11: Wavelength dependence of TE power reflectivities. Waveguide refractive indices are n_{core}=3.512 and $n_{cladding}$=3.17. The core width is 0.1μm. The thickness of the coating layer is 0.22256μm and the refractive index is $n_{coating}$=1.7936.

It can be seen that the results of these two methods compare favourably for the case that Δx=0.01μm. For the case that Δx=0.025μm, the results agree less well because the transvers sampling interval is too big relative to the waveguide core width. Overall, the power reflectivity reduced with the increasing of the wavelength in the beginning, and then increased in the ascending order of the wavelength. The smallest reflectivity exists when the wavelength is between 1.525μm-1.55μm.

6.3.2.2 Simulation for single layer coated waveguides with different core width

The structures analysed for the normally incident situation have core refractive index n_{core}=3.6 and cladding refractive index is given by $n_{cladding}=n_{core}(1-p)$, where p is the percentage difference from n_{core}. In the following simulations, the percentage difference has been chosen as p=3 and p=10 separately, which means that $n_{cladding}$ equals to 3.492 and 3.24 correspondingly. The core width of the slab is allowed to vary from 0 to 1μm. The material on the right side of the coating layer is air. The operating wavelength is λ=0.86μm. The fundamental mode and the corresponding effective refractive indices obtained by the ID BPM mode solver for different cases are the same as those employed in the uncoated facet reflective simulations. The refractive index and thickness of a single AR coating are $n_{coating}=\sqrt{n_{eff}}$ and $d_{coating}=\frac{\lambda}{4n_{coating}}$, where n_{eff} is the effective refractive index of the tested waveguide.

T-Bi-BPM is implemented with rotated Padé (10, 10) approximation and transverse sampling interval *Δx*=0.01μm. The parameter M=5, 10 and 15 are tested respectively.

Fig. 6.12 illustrates the power reflectivities for the TE polarisation versus slab thickness when the waveguide normally incident on the facet, for (a) p=3% (Fig. 6.12(a)) and (b) p=10% (Fig. 6.12(b)). The results are presented in the form of dB and compared with the results obtained by the FSRM method [5].

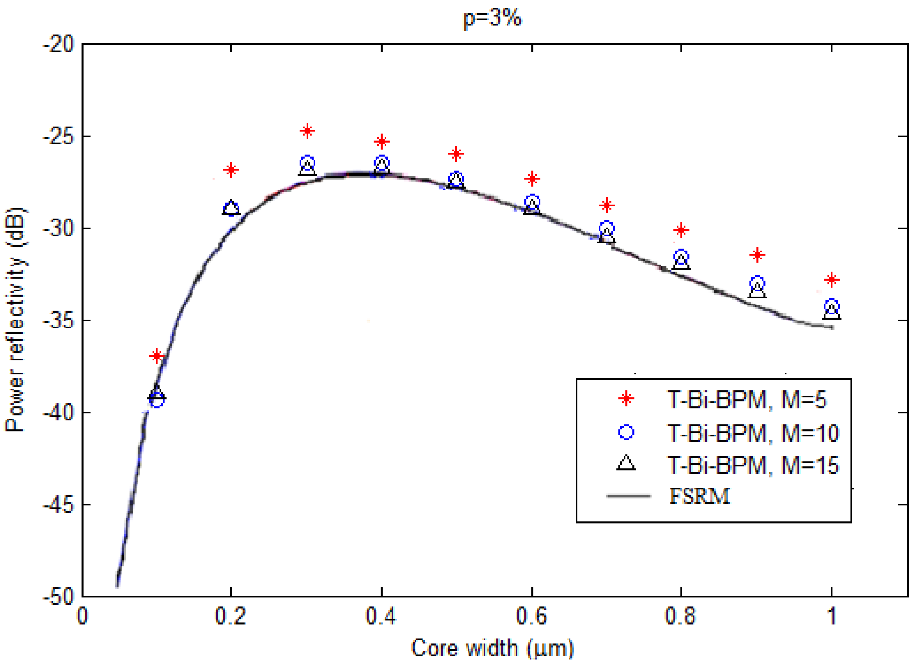

(a)

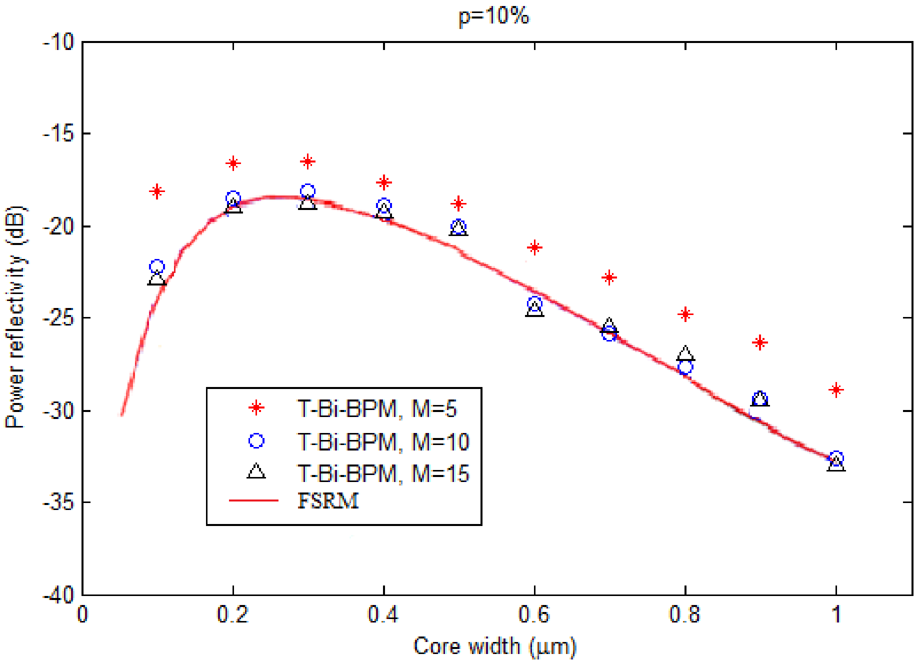

(b)

Figure 6.12: The TE power reflectivities of the coated facet versus slab width for the normally incident situation. The waveguide has core refractive index n_{core}=3.6 and the index contrast is (a) p=3% and (b) p=10%.

It can be noticed that the simulation results obtained when M=10 is in good agreement with the reference results. However, the simulation results obtained when M=5 show less agreement. Further simulation results with M=15 present similar agreement to the reference results as M=10.

It should be noticed that though increasing the parameter M can provide a better accuracy, it also means high computational overhead for the matrix solver because the number of non-zero elements of the matrix system in Eq.(6.2.14) is increased. The number of non-zero elements, $N_{element}$ can be calculated by

$$N_{element} = \left([2s+1] + [2s+1] + [2(s+M+1)+1] + [2(s+M)+1] \right) \bullet n \qquad (6.3.1)$$

in which s is the Padé order and n is the number of sampling points in transverse direction. Consider a waveguide with the percentage difference of the refractive index is p=3 and the core width is 1μm, when rotated Padé (10, 10) approximation is used and the operating wavelength is 0.86μm, the power reflectivities calculated by the T-Bi-BPM with different values of M are listed in Table.6.1. The number of non-zero elements of the matrix system according to different values of M is also presented. It can be seen that the accuracy of the T-Bi-BPM method is sensitive to the parameter M when M is a relative small value. When M is a large value the improvement of the accuracy is not remarkable but the number of non-zero element increases obviously.

	Power Reflectivity	Non-zero Elements
M=5	-32.5dB	106n
M=10	-34.11dB	126n
M=15	-34.49dB	146n
M=20	-34.74dB	166n
M=40	-34.98dB	246n
FSRM	-35.21dB	

Table.6.1: the calculated power reflectivity and the number of the non-zero element of the matrix system according to different values of the parameter M.

Comparing the results in Fig. 6.12 with the results for uncoated facet (Fig. 6.3 & Fig.

6.7), it shows that the reflectivity of a coated facet changes much more. For both situations (p=3% and p=10%), the power reflectivity reduced very obviously for the same core width. The results prove that adding an AR coating onto the facet of a waveguide is an efficient way to reduce the facet reflection. It also can be noticed that for the same core width, the smaller index contrast leads to smaller power reflectivity than the larger index contrast. Moreover, regardless of what the value of the index contrast is, the power reflectivity increases with the increasing of the core width at first. It reaches the maximum value when the core width is around 0.3-0.4μm for p=3% and when the core width is around 0.2-0.3μm for p=10%, and then reduces with the increasing of the core width.

6.3.2.3 Simulation for single layer coated waveguides with different thickness of the AR coating

In this part, the application of the T-Bi-BPM method for a one-layer AR coating structure is extended to the case of the angled facet and the dependence of reflectivity on coating thickness and angle for TE polarisation is investigated. The results obtained by the FSRM method are taken as the reference to test the accuracy of the proposed method [4]. In order to ensure a fair comparison, the same simulation conditions used by the FSRM method in [4] are applied for the T-Bi-BPM method. For a waveguide with core refractive index n_{core}=3.512, cladding refractive index $n_{cladding}$=3.17 and core width 0.1μm, the wavelength is fixed at λ=1.55μm and the coating layer has refractive index $n_{coating}$=1.7936. T-Bi-BPM is implemented with transverse sampling interval Δx=0.01μm and parameter M=15. Rotated Padé(6, 6) and rotated Padé(10, 10) have been used to show how the accuracy is effected by different Padé orders. The incident angle and the corresponding reflectivity versus the coating thickness are illustrated in Fig. 6.13 for (a) 0^o, (b) 10^o, (c) 15^o and (d) 20^o, respectively.

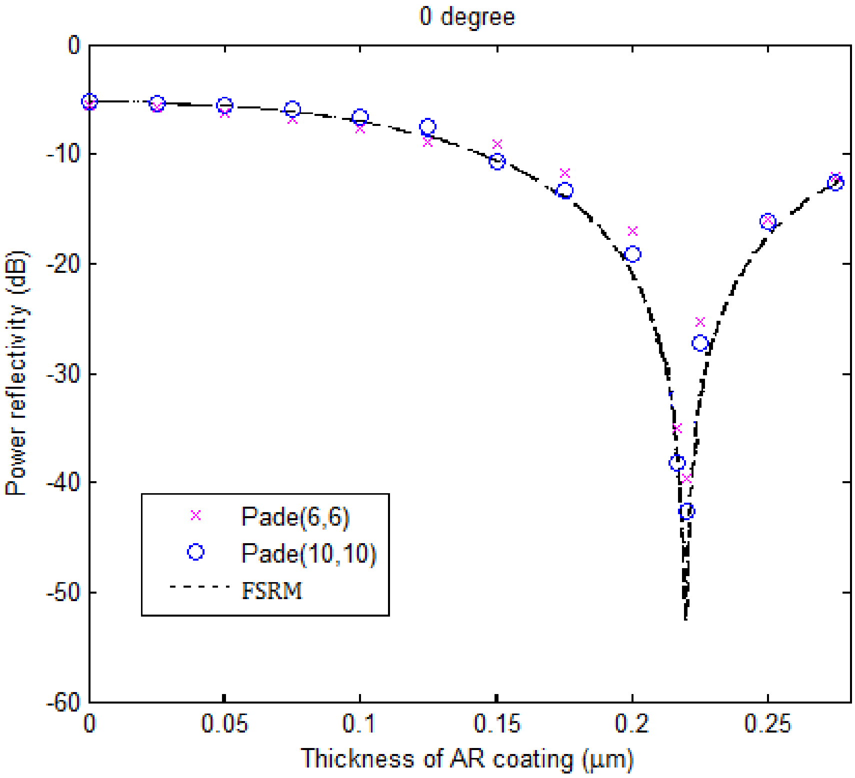

(a)

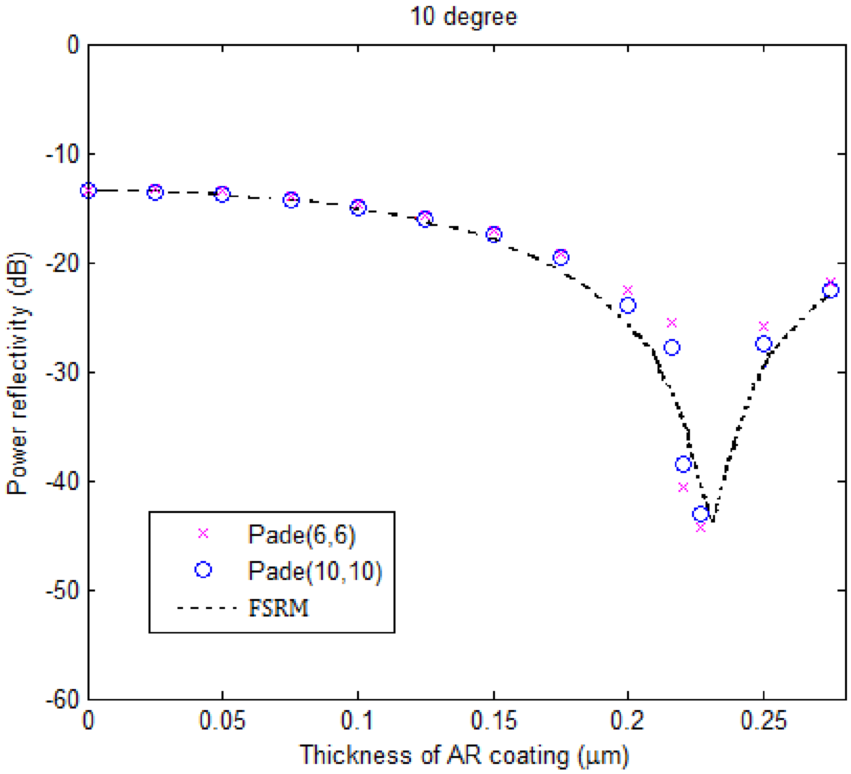
10 degree
0
-10
-20
-30
-40
-50
-60
Power reflectivity (dB)
0
0.05
0.1
0.15
0.2
0.25
Thickness of AR coating (µm)
Pade(6,6)
Pade(10,10)
FSRM

(b)

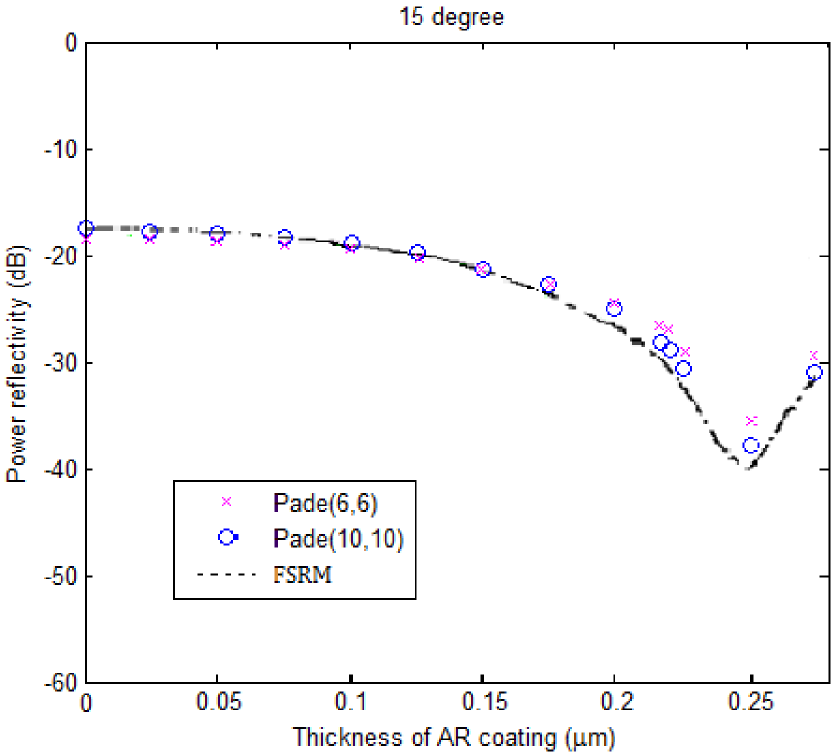
15 degree
0
-10
-20
-30
-40
-50
-60
Power reflectivity (dB)
0
0.05
0.1
0.15
0.2
0.25
Thickness of AR coating (µm)
Pade(6,6)
Pade(10,10)
FSRM

(c)

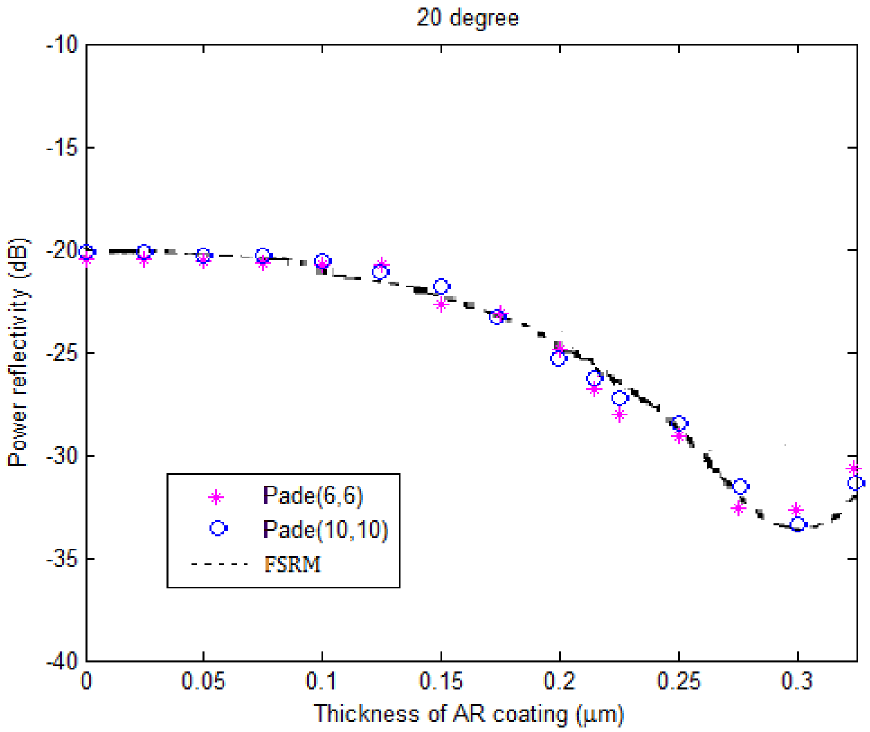

(d)

Figure 6.13: Dependence of TE power reflectivities on coating thickness for tilting angle of: (a) 0^o, (b) 10^o, (c) 15^o and (d) 20^o. The refractive indices are n_{core}=3.512, cladding $n_{cladding}$=3.17 and $n_{coating}$=1.7936. The core width of the waveguide is 0.1µm and the operating wavelength is λ=1.55µm.

In Fig. 6.13(a), which presents the normally incident results, the results obtained by the proposed method is in agreement with the results obtained by the FSRM method. The power reflectivity reduced with the increasing of the coating thickness at the beginning until it reaches the lowest value when the thickness is around 0.22µm, and then it increased in the ascending order of the thickness. In Fig. 6.13(b), (c), (d), which presents the angularly incident results, the two methods agreed less well. For each angle, there is an optimum coating thickness providing the smallest reflection.

The presenting results are not for optimising any structure in particular but merely to confirm that the proposed method may be used as a successful tool for optimisation purposes. Comparing Fig. 6.13(b), (c), (d) it can be noticed that the variation range of the reflectivity versus the thickness becomes smaller with the increasing of the incident angle. For different incident angles (0^{o}-20^{o}), the lowest reflectivity occurs when the thickness of the coating layer is larger than 0.2μm. For a larger incident angle, the coating layer needs to be thicker to provide the lowest reflectivity.

Moreover, it can be seen that the results obtained by Padé(10, 10) are just a little better agreement with the reference results than those obtained by Padé(6, 6) for all the tested incident angles. For each incident angle, Padé(10, 10) and Padé(6, 6) provided quite similar results when the thickness of the AR coating is relatively thin. The differences between the results obtained by the two different approximation schemes become obvious as the increase of the AR coating thickness.

6.4 Conclusions

In this chapter, a novel Bi-directional BPM scheme, the T-Bi-BPM, has been proposed for the uncoated and the single coating layer structures. The new scheme refers to the well-known transmission matrix in the transmission line theory. Based on the wave propagation features, this method sets a connection between the total fields at both sides of the facet by a matrix equation. Through matrix rearrangement, the method removes the field terms of the output side of the structure, leaving only the terms on the waveguide side. By a mathematical process through which the coefficients in the matrix operators are extracted, the rearranged matrix equation can be filled in with solvable elements, and then be solved by a matrix solver. Therefore, the total field and the reflected field on the waveguide side can be calculated according to the incident field. The advantages of the new method are that it can be explicitly evaluated by using sparse matrix multiplications and also can be algebraically preconditioned.

The Bi-BPM methods have been tested for calculating the facet reflectivity for uncoated and single coating layer waveguides. For the former case, both the conventional reflective BPM and the T-Bi-BPM have been applied for both normal and angled incidence situations. Comparing to the reference data obtained by the FSRM method, the BPM schemes provided reliable results. The comparison of the simulation results between the two BPM schemes show that the T-Bi-BPM method has a good capacity to handle the uncoated facet reflection problems. For the single coated facet reflection problems, the T-Bi-BPM BPM method has been tested for different situations including normal and angled incidence. Comparisons show that using higher order rotated Padé approximation and smaller transverse sampling interval can give better agreement with the FSRM method. The polynomial order M for approximating the trigonometric functions is another factor that affects the accuracy of the method. In the simulations presented in this part, M=15 provides acceptable accuracy with relative low computational cost.

6.5 Reference

1. M.Pozar, Microwave Engineering. 2005.
2. A. BAMBERGER, L. HALPERN AND P. JOLY, HIGHER ORDER PARAXIAL WAVE EQUATION APPROXIMATIONS IN HETEROGENEOUS MEDIA. SIAM J. APPL. MATH. **48**: p. 129-154.
3. P.C. Kendall, Robson,M.J. Adam, M.J. Robertson, Semiconductor laser facet reflectivities using free-space radiation modes. IEE PROCEEDINGS-J, 1993. **140**: p. 49-55.
4. M. Reed, Antireflection-coated angled facet design. Optoelectronics, IEE Proceedings , 1996. **143**(4): p. 214-220.
5. A. Vukovic, Fourier Transformation Analysis of Optoelectronic Components and Circuits. Thesis submitted to the University of Nottingham for the degree of Doctor of Philosophy, 2000.

Chapter 7: Conclusion

This chapter outlines the main conclusions of the work presented in this thesis and gives some suggestions for possible future work.

7.1 Review of the Work Presented in This Thesis

Photonic structures such as junctions between optical fibers and rib waveguides, grating structures and coating layers require accurate characterization of the reflection and transmission that occurs at the discontinuities in these structures. This work proposed a transmission matrix based Bi-BPM (T-Bi-BPM) method and provided a new choice of modelling method to solve the bi-directional propagation problems. The T-Bi-BPM is applied on the uncoated facet and the single coating layer reflection problems, including both normal and angled incident situations.

This thesis starts from an overview of basic electromagnetic theories in Chapter 2, including typical waveguides and materials used in optics, Maxwell's equations, boundary conditions at material interfaces and the derivation of the full-vectorial, semi-vectorial and scalar wave equations.

In Chapter 3, a review has been given for different popular modelling methods, including semi-analytical methods such as Marcatili’s method, the effective index method and the spectral index method, and numerical methods such as the FE method, the FD method and the FDTD method. FD-BPM is overviewed as one of the most popular techniques due to its numerical efficiency. The primary concept of its simplest form, the paraxial BPM, is provided. Different boundary conditions frequently used during the simulation process are introduced, including Neumann and Dirichlet boundary condition, TBC, PML and periodic boundary condition. The ID BPM is presented and proved as an effective mode solver and is applied throughout the work of this thesis to find the fundamental mode of the incident field and the effective refractive index of structures before further simulations. It is shown that three factors may affect the performance of ID-BPM, including the choice of the transverse sampling interval, the longitudinal propagation step and the initial value of the refractive index. Simulation results show that the accuracy of the mode solver can be improved by reducing the transverse sampling interval. Changing the longitudinal propagation step does not affect the accuracy, but changes the convergence speed of the method. When a smaller longitudinal propagation step is used, the method shows a better convergence in a short propagating distance. The simulation results also prove that different initial values of the refractive index will not change the accuracy of the mode solver.

Chapter 4 focuses on the introduction and application of the WA-BPM scheme for single direction propagation problems. A comparison between the paraxial BPM and WA-BPM for dealing with forward direction propagation problems has been given. The simulation results based on slab and rib waveguides show that the paraxial FDBPM is suitable for modelling the wave propagation in longitudinal invariant waveguides with no or little tilted incident angle due to its simplicity of implementation, whereas, the WA scheme is a more suitable choice for modelling propagation with a large tilted angle. Rotated Padé approximation with multistep method can be applied to enhance the stability of the WA-BPM. Increasing the order of the Padé approximation or deducing the longitudinal propagation step can improve the accuracy of the WA method, with heavier computational cost and longer simulation time. When the incident angle is lager, a higher order Padé approximation is required for better accuracy.

Bi-BPM schemes are overviewed in Chapter 5. The T-Bi-BPM method is proposed in Chapter 6 after a review of the exiting Bi-BPM schemes. The T-Bi-BPM is applied to uncoated and single layer coated facet reflectivity analysis. For the uncoated facet case, it shows simulation results for different percentage differences between the refractive indices of the core and the cladding of a slab waveguide when the tilted angle of the waveguide changes from 0^o to 15^o. The results obtained by the T-Bi-BPM method have a good agreement with the reference data obtained by the reflection BPM method and the FSRM method. For the single coating layer case, T-Bi-BPM presents a great potential to overcome the coating layer reflection problems. Simulation results show that increasing the order of Padé approximation and reducing the transverse sampling interval can improve the accuracy. Moreover, the matrix system of the T-Bi-BPM method includes the trigonometric functions, which can be mathematically approximated by polynomials. The order of the polynomials, M in Eq.(5.3.5), is another factor that affects the method accuracy. Larger value of M leads to better accuracy. However it also increases the non-zero elements in the matrix system and therefore results in heavier computational cost.

7.2 Suggestions for Future Work

There are several aspects of improvement worth attempting in order to optimize the T-Bi-BPM method. The first aspect of the possible future work is to improve the accuracy of the proposed method. Errors can be noticed when the simulation results obtained by the T-Bi-BPM method are compared with the reference results obtained by the FSRM method, though using higher order rotated Padé approximation and smaller transverse sampling interval can provide better agreement. It is believed that a significant reason can be in using the second-order accurate discretization scheme in transverse direction. Accuracy can be improved by applying the higher order schemes for transverse discretisation. A fourth-order scheme, the generalized Douglas scheme [1-3], is a possible choice. It maintains the same bandwidth of matrices as the original

BPM scheme and imposes no significant additional computation time [4]. Moreover, an improved 3-point finite difference scheme presented in [5] can deal correctly with all second-order terms regardless of the existence of multiple dielectric interfaces between sample points. These highly accurate schemes are worth implementing for the improvement of the new proposed method.

Another interesting future research area is to extend the application of the method to 3D propagation problems. However, it is always a big challenge to apply the WA scheme to 3D problems. The difficulty is to expand the high order derivatives for both transverse directions at the same time. A robust matrix solver based on BI-CGSTAB or GMRES is a possible choice to provide a possibility to deal with 3D problems.

Most of the existing reflective methods are based on the scalar wave equations. It is a formidable task for all the frequency domain reflective methods to model reflection problems for semi-vectorial and full-vectorial wave equations. Especially for the full-vector wave equation, the boundary conditions at the interfaces become much more complicated. Therefore, for the T-Bi-BPM method, solving the semi-vectorial and full-vectorial problems is a challenge. This will be a potential interesting area for future research.

The simulation results shown in Chapter 6 have proved that the T-Bi-BPM method has a good accuracy in solving the single coating reflection problems. Frequently, an optical waveguide may have a discontinuous coating layer, such as the periodic grating structures. A typical example is the SPP waveguide [6]. Fig. 7.1 illustrates a situation of the periodic grating structures. The dielectric substrate is covered by a discontinuous coating layer. If the coating of the structure is metal displaying a negative real part of the propagation constant, the waveguide will have the capacity to support and guide SP waves at the interface between the dielectric substrate and the metal coating. This structure can be considered as a periodic one. If one period is modelled, the fields of the neighbour subsections can be deduced by utilising the periodic boundary condition. The difficulty of the application of the T-Bi-BPM method to analyse this structure is that the parameters obtained by the expansion of the power of the second derivation of x in Eq.(6.2.12), C_n, contains different coating reflective indices, n_r. Therefore, the values of the elements in the operator matrix need to be modulated depending on the positions of the sampling points.

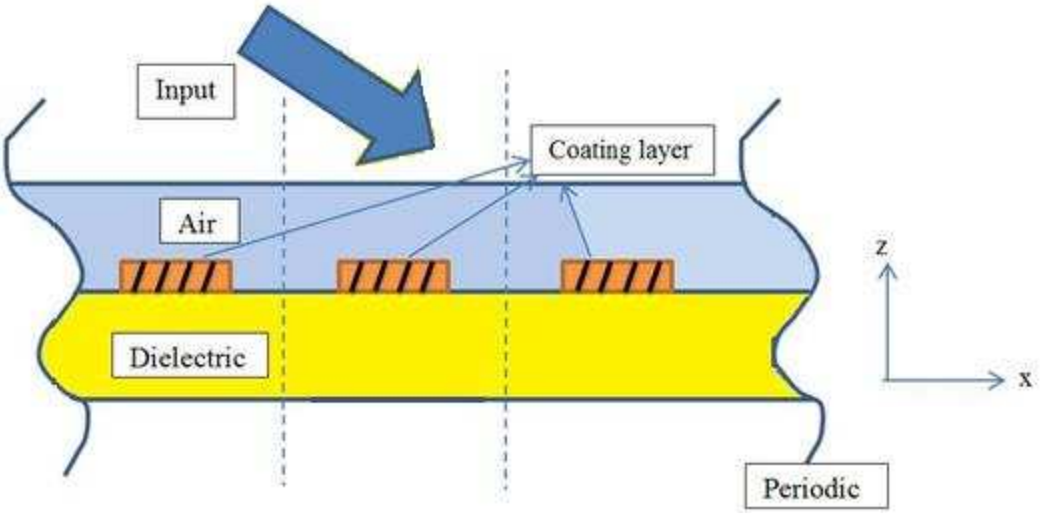

Figure 7.1: The optical structures with a discontinuous coating layer

Moreover, it is known that in order to excite the SP waves, the waveguide must be excited by E field perpendicular to the interface ie. TM polarised field. However, the T-Bi-BPM method presented in this thesis is divided from a scalar wave equation. Therefore, further development of T-Bi-BPM needs to deal with the polarization problem as mentioned earlier which will also extend its range of applications.

7.3 Reference

1. J.Yamauchi, Modified finite-difference beam propagation method based on the generalized Douglas scheme for variable coefficients. IEEE Photon. Technol Lett, 1995. **18**: p. 1229-1231.
2. J.Yamauchi, O.Saito, O. Uchiyama and H.Nakano, Improved finite-difference beam-propagation method based on the generalized Douglas shceme and its application to semivectorial analysis. Lightwave Technol, 1996. **14**: p. 2401-2406.
3. J.Yamauchi, and H.Nakano, Application of the generalized Douglas scheme to optical waveguide analysis. Opt. Quantum Electron, 1999. **31**: p. 675-687.
4. J. Yamauchi, Propagation Beam Analysis of Optical Waveguides. 2003.
5. J.G. Wykes, A. Vukovic, and T.M. Benson, Sub-sampling of fine features in finite-difference frequency-domain simulations. Microwave Opt Technol Lett, 2005. **44**: p. 95-101.

6. O.T.A. Janssen, G.W.Hooft, On the phase of plasmons excited by slits in a metal film. Optics Express, 2006. **14**: p. 11824-11832.

Appendices

Appendix 1

The coefficients of 3D semi-vectorial wave equations after Padé Approximation:

TM polarisation:

$$A_{z+\frac{j}{k}\Delta z} = \frac{\sqrt[k]{A}}{\beta_0^2 \Delta x^2} \left(\frac{2n^2_{(x+\Delta x,y,z+\frac{j}{k}\Delta z)}}{n^2_{(x+\Delta x,y,z+\frac{j}{k}\Delta z)} + n^2_{(x,y,z+\frac{j}{k}\Delta z)}} \right)$$

$$B_{z+\frac{j}{k}\Delta z} = \frac{\sqrt[k]{A}}{\beta_0^2 \Delta x^2} \left(\frac{2n^2_{(x-\Delta x,y,z+\frac{j}{k}\Delta z)}}{n^2_{(x-\Delta x,y,z+\frac{j}{k}\Delta z)} + n^2_{(x,y,z+\frac{j}{k}\Delta z)}} \right)$$

$$D_{z+\frac{j}{k}\Delta z} = E_{z+\frac{j}{k}\Delta z} = \frac{\sqrt[k]{A}}{\beta_0^2 \Delta y^2}$$

$$C_{z+\frac{j}{k}\Delta z} = \frac{\sqrt[k]{A}}{\beta_0^2} [\frac{-2}{\Delta x^2} \left(\frac{n^2_{(x,y,z+\frac{j}{k}\Delta z)}}{n^2_{(x+\Delta x,y,z+\frac{j}{k}\Delta z)} + n^2_{(x,y,z+\frac{j}{k}\Delta z)}} + \frac{n^2_{(x,y,z+\frac{j}{k}\Delta z)}}{n^2_{(x-\Delta x,y,z+\frac{j}{k}\Delta z)} + n^2_{(x,y,z+\frac{j}{k}\Delta z)}} \right)$$

$$+ \frac{-2}{\Delta y^2} + (k_0^2 n^2_{(x,y,z+\frac{j}{k}\Delta z)} - \beta_0^2)] - \sqrt[k]{A} \cdot d_j$$

$$A_{z+\frac{j-1}{k}\Delta z} = \frac{\sqrt[k]{A^*}}{\beta_0^2 \Delta x^2} \left(\frac{2n^2_{(x+\Delta x,y,z+\frac{j-1}{k}\Delta z)}}{n^2_{(x+\Delta x,y,z+\frac{j-1}{k}\Delta z)} + n^2_{(x,y,z+\frac{j-1}{k}\Delta z)}} \right)$$

$$B_{z+\frac{j-1}{k}\Delta z} = \frac{\sqrt[k]{A^*}}{\beta_0^2 \Delta x^2} \left(\frac{2n^2_{(x-\Delta x,y,z+\frac{j-1}{k}\Delta z)}}{n^2_{(x-\Delta x,y,z+\frac{j-1}{k}\Delta z)} + n^2_{(x,y,z+\frac{j-1}{k}\Delta z)}} \right)$$

$$D_{z+\frac{j-1}{k}\Delta z} = E_{z+\frac{j-1}{k}\Delta z} = \frac{\sqrt[k]{A^*}}{\beta_0^2 \Delta y^2}$$

$$C_{z+\frac{j-1}{k}\Delta z} = \frac{\sqrt[k]{A^*}}{\beta_0^2} [\frac{-2}{\Delta x^2} \left(\frac{n^2_{(x,y,z+\frac{j-1}{k}\Delta z)}}{n^2_{(x+\Delta x,y,z+\frac{j-1}{k}\Delta z)} + n^2_{(x,y,z+\frac{j-1}{k}\Delta z)}} + \frac{n^2_{(x,y,z+\frac{j-1}{k}\Delta z)}}{n^2_{(x-\Delta x,y,z+\frac{j-1}{k}\Delta z)} + n^2_{(x,y,z+\frac{j-1}{k}\Delta z)}} \right)$$

$$+ \frac{-2}{\Delta y^2} + (k_0^2 n^2_{(x,y,z+\frac{j-1}{k}\Delta z)} - \beta_0^2)] - \sqrt[k]{A^*} \cdot d_j^*$$

TE polarisation:

$$A_{z+\frac{j}{k}\Delta z} = B_{z+\frac{j}{k}\Delta z} = \frac{\sqrt[k]{A}}{\beta_0^2 \Delta x^2}$$

$$D_{z+\frac{j}{k}\Delta z} = \frac{\sqrt[k]{A}}{\beta_0^2 \Delta y^2}\left(\frac{2n^2_{(x,y+\Delta y,z+\frac{j}{k}\Delta z)}}{n^2_{(x,y+\Delta y,z+\frac{j}{k}\Delta z)} + n^2_{(x,y,z+\frac{j}{k}\Delta z)}}\right)$$

$$E_{z+\frac{j}{k}\Delta z} = \frac{\sqrt[k]{A}}{\beta_0^2 \Delta y^2}\left(\frac{2n^2_{(x,y-\Delta y,z+\frac{j}{k}\Delta z)}}{n^2_{(x,y-\Delta y,z+\frac{j}{k}\Delta z)} + n^2_{(x,y,z+\frac{j}{k}\Delta z)}}\right)$$

$$C_{z+\frac{j}{k}\Delta z} = \frac{\sqrt[k]{A}}{\beta_0^2}[\frac{-2}{\Delta x^2} + \frac{-2}{\Delta y^2}\left(\frac{n^2_{(x,y,z+\frac{j}{k}\Delta z)}}{n^2_{(x,y+\Delta y,z+\frac{j}{k}\Delta z)} + n^2_{(x,y,z+\frac{j}{k}\Delta z)}} + \frac{n^2_{(x,y,z+\frac{j}{k}\Delta z)}}{n^2_{(x,y-\Delta y,z+\frac{j}{k}\Delta z)} + n^2_{(x,y,z+\frac{j}{k}\Delta z)}}\right)]$$

$$+\sqrt[k]{A}(\frac{k_0^2 n^2_{(x,y,z+\frac{j}{k}\Delta z)}}{\beta_0^2} - 1 - d_j)$$

$$A_{z+\frac{j-1}{k}\Delta z} = B_{z+\frac{j-1}{k}\Delta z} = \frac{\sqrt[k]{A^*}}{\beta_0^2 \Delta x^2}$$

$$D_{z+\frac{j-1}{k}\Delta z} = \frac{\sqrt[k]{A^*}}{\beta_0^2 \Delta y^2}\left(\frac{2n^2_{(x,y+\Delta y,z+\frac{j-1}{k}\Delta z)}}{n^2_{(x,y+\Delta y,z+\frac{j-1}{k}\Delta z)} + n^2_{(x,y,z+\frac{j-1}{k}\Delta z)}}\right)$$

$$E_{z+\frac{j-1}{k}\Delta z} = \frac{\sqrt[k]{A^*}}{\beta_0^2 \Delta y^2}\left(\frac{2n^2_{(x,y-\Delta y,z+\frac{j-1}{k}\Delta z)}}{n^2_{(x,y-\Delta y,z+\frac{j-1}{k}\Delta z)} + n^2_{(x,y,z+\frac{j-1}{k}\Delta z)}}\right)$$

$$C_{z+\frac{j-1}{k}\Delta z} = \frac{\sqrt[k]{A^*}}{\beta_0^2}[\frac{-2}{\Delta x^2} + \frac{-2}{\Delta y^2}\left(\frac{n^2_{(x,y,z+\frac{j-1}{k}\Delta z)}}{n^2_{(x,y+\Delta y,z+\frac{j-1}{k}\Delta z)} + n^2_{(x,y,z+\frac{j-1}{k}\Delta z)}} + \frac{n^2_{(x,y,z+\frac{j-1}{k}\Delta z)}}{n^2_{(x,y-\Delta y,z+\frac{j-1}{k}\Delta z)} + n^2_{(x,y,z+\frac{j-1}{k}\Delta z)}}\right)]$$

$$+\sqrt[k]{A^*}(\frac{k_0^2 n^2_{(x,y,z+\frac{j-1}{k}\Delta z)}}{\beta_0^2} - 1 - d_j^*)$$

Appendix 2

The coefficients of 3D semi-vectorial wave equations after Rotated Branch Cut Approximation:

TM polarisation:

$$A_{z+\frac{j}{k}\Delta z} = j\,\frac{\sqrt[k]{B}}{\beta_0^2\Delta x^2}\left(\frac{2n^2_{(x+\Delta x,y,z+\frac{j}{k}\Delta z)}}{n^2_{(x+\Delta x,y,z+\frac{j}{k}\Delta z)}+n^2_{(x,y,z+\frac{j}{k}\Delta z)}}\right)$$

$$B_{z+\frac{j}{k}\Delta z} = j\,\frac{\sqrt[k]{B}}{\beta_0^2\Delta x^2}\left(\frac{2n^2_{(x-\Delta x,y,z+\frac{j}{k}\Delta z)}}{n^2_{(x-\Delta x,y,z+\frac{j}{k}\Delta z)}+n^2_{(x,y,z+\frac{j}{k}\Delta z)}}\right)$$

$$D_{z+\frac{j}{k}\Delta z} = E_{z+\frac{j}{k}\Delta z} = j\,\frac{\sqrt[k]{B}}{\beta_0^2\Delta y^2}$$

$$C_{z+\frac{j}{k}\Delta z} = -j\,\frac{2\sqrt[k]{B}}{\beta_0^2\Delta x^2}\left(\frac{n^2_{(x,y,z+\frac{j}{k}\Delta z)}}{n^2_{(x+\Delta x,y,z+\frac{j}{k}\Delta z)}+n^2_{(x,y,z+\frac{j}{k}\Delta z)}}+\frac{n^2_{(x,y,z+\frac{j}{k}\Delta z)}}{n^2_{(x-\Delta x,y,z+\frac{j}{k}\Delta z)}+n^2_{(x,y,z+\frac{j}{k}\Delta z)}}\right)$$

$$-\,j\,\frac{2\sqrt[k]{B}}{\beta_0^2\Delta y^2}+\sqrt[k]{B}\left(-1-\,f_j\,+\,j\,\frac{k_0^2 n^2_{(x,y,z+\frac{j}{k}\Delta z)}}{\beta_0^2}\right)$$

$$A_{z+\frac{j-1}{k}\Delta z} = j\,\frac{\sqrt[k]{B^*}}{\beta_0^2\Delta x^2}\left(\frac{2n^2_{(x+\Delta x,y,z+\frac{j-1}{k}\Delta z)}}{n^2_{(x+\Delta x,y,z+\frac{j-1}{k}\Delta z)}+n^2_{(x,y,z+\frac{j-1}{k}\Delta z)}}\right)$$

$$B_{z+\frac{j-1}{k}\Delta z} = j\,\frac{\sqrt[k]{B^*}}{\beta_0^2\Delta x^2}\left(\frac{2n^2_{(x-\Delta x,y,z+\frac{j-1}{k}\Delta z)}}{n^2_{(x-\Delta x,y,z+\frac{j-1}{k}\Delta z)}+n^2_{(x,y,z+\frac{j-1}{k}\Delta z)}}\right)$$

$$D_{z+\frac{j-1}{k}\Delta z} = E_{z+\frac{j-1}{k}\Delta z} = j\,\frac{\sqrt[k]{B^*}}{\beta_0^2\Delta y^2}$$

$$C_{z+\frac{j-1}{k}\Delta z} = -j\,\frac{2\sqrt[k]{B^*}}{\beta_0^2\Delta x^2}\left(\frac{n^2_{(x,y,z+\frac{j-1}{k}\Delta z)}}{n^2_{(x+\Delta x,y,z+\frac{j-1}{k}\Delta z)}+n^2_{(x,y,z+\frac{j-1}{k}\Delta z)}}+\frac{n^2_{(x,y,z+\frac{j-1}{k}\Delta z)}}{n^2_{(x-\Delta x,y,z+\frac{j-1}{k}\Delta z)}+n^2_{(x,y,z+\frac{j-1}{k}\Delta z)}}\right)$$

$$-\,j\,\frac{2\sqrt[k]{B^*}}{\beta_0^2\Delta y^2}+\sqrt[k]{B^*}\left(-1-\,f_j^*\,+\,j\,\frac{k_0^2 n^2_{(x,y,z+\frac{j-1}{k}\Delta z)}}{\beta_0^2}\right)$$

TE polarisation:

$$A_{z+\frac{j}{k}\Delta z} = B_{z+\frac{j}{k}\Delta z} = j\,\frac{\sqrt[k]{B}}{\beta_0^2\Delta x^2}$$

$$D_{z+\frac{j}{k}\Delta z} = j\,\frac{\sqrt[k]{B}}{\beta_0^2\Delta y^2}\left(\frac{2n^2_{(x,y+\Delta y,z+\frac{j}{k}\Delta z)}}{n^2_{(x,y+\Delta y,z+\frac{j}{k}\Delta z)}+n^2_{(x,y,z+\frac{j}{k}\Delta z)}}\right)$$

$$E_{z+\frac{j}{k}\Delta z} = j\,\frac{\sqrt[k]{B}}{\beta_0^2\Delta y^2}\left(\frac{2n^2_{(x,y-\Delta y,z+\frac{j}{k}\Delta z)}}{n^2_{(x,y-\Delta y,z+\frac{j}{k}\Delta z)}+n^2_{(x,y,z+\frac{j}{k}\Delta z)}}\right)$$

$$C_{z+\frac{j}{k}\Delta z} = -j\,\frac{2\sqrt[k]{B}}{\beta_0^2\Delta y^2}\left(\frac{n^2_{(x,y,z+\frac{j}{k}\Delta z)}}{n^2_{(x,y+\Delta y,z+\frac{j}{k}\Delta z)}+n^2_{(x,y,z+\frac{j}{k}\Delta z)}}+\frac{n^2_{(x,y,z+\frac{j}{k}\Delta z)}}{n^2_{(x,y-\Delta y,z+\frac{j}{k}\Delta z)}+n^2_{(x,y,z+\frac{j}{k}\Delta z)}}\right)$$
$$-\,j\,\frac{2\sqrt[k]{B}}{\beta_0^2\Delta x^2}+\sqrt[k]{B}\left(-1-f_j+j\,\frac{k_0^2n^2_{(x,y,z+\frac{j}{k}\Delta z)}}{\beta_0^2}\right)$$

$$A_{z+\frac{j-1}{k}\Delta z} = B_{z+\frac{j-1}{k}\Delta z} = j\,\frac{\sqrt[k]{B^*}}{\beta_0^2\Delta x^2}$$

$$D_{z+\frac{j-1}{k}\Delta z} = j\,\frac{\sqrt[k]{B^*}}{\beta_0^2\Delta y^2}\left(\frac{2n^2_{(x,y+\Delta y,z+\frac{j-1}{k}\Delta z)}}{n^2_{(x,y+\Delta y,z+\frac{j-1}{k}\Delta z)}+n^2_{(x,y,z+\frac{j-1}{k}\Delta z)}}\right)$$

$$E_{z+\frac{j-1}{k}\Delta z} = j\,\frac{\sqrt[k]{B^*}}{\beta_0^2\Delta y^2}\left(\frac{2n^2_{(x,y-\Delta y,z+\frac{j-1}{k}\Delta z)}}{n^2_{(x,y-\Delta y,z+\frac{j-1}{k}\Delta z)}+n^2_{(x,y,z+\frac{j-1}{k}\Delta z)}}\right)$$

$$C_{z+\frac{j-1}{k}\Delta z} = -j\,\frac{2\sqrt[k]{B^*}}{\beta_0^2\Delta y^2}\left(\frac{n^2_{(x,y,z+\frac{j-1}{k}\Delta z)}}{n^2_{(x,y+\Delta y,z+\frac{j-1}{k}\Delta z)}+n^2_{(x,y,z+\frac{j-1}{k}\Delta z)}}+\frac{n^2_{(x,y,z+\frac{j-1}{k}\Delta z)}}{n^2_{(x,y-\Delta y,z+\frac{j-1}{k}\Delta z)}+n^2_{(x,y,z+\frac{j-1}{k}\Delta z)}}\right)$$
$$-\,j\,\frac{2\sqrt[k]{B^*}}{\beta_0^2\Delta x^2}+\sqrt[k]{B^*}\left(-1-f_j^*+j\,\frac{k_0^2n^2_{(x,y,z+\frac{j-1}{k}\Delta z)}}{\beta_0^2}\right)$$

Appendix 3

The field profiles comparison for the TM polarisation when different approximation schemes are used.

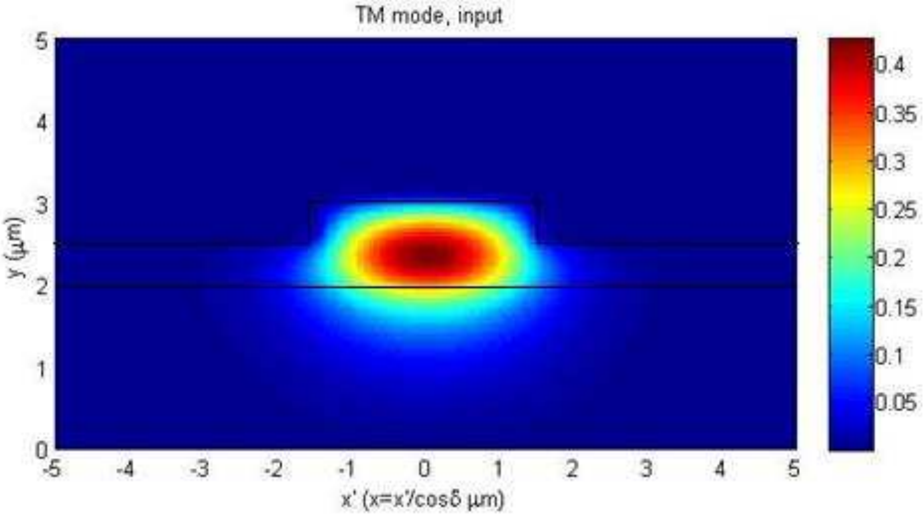

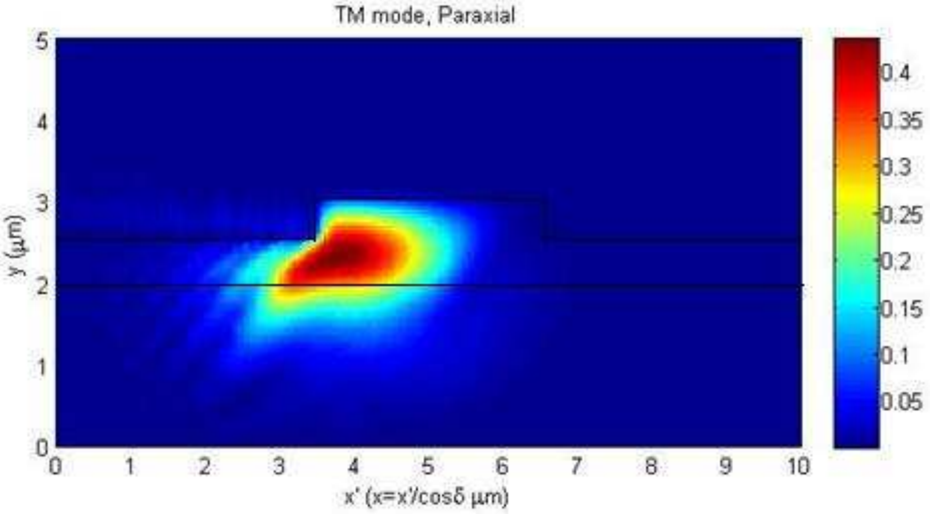

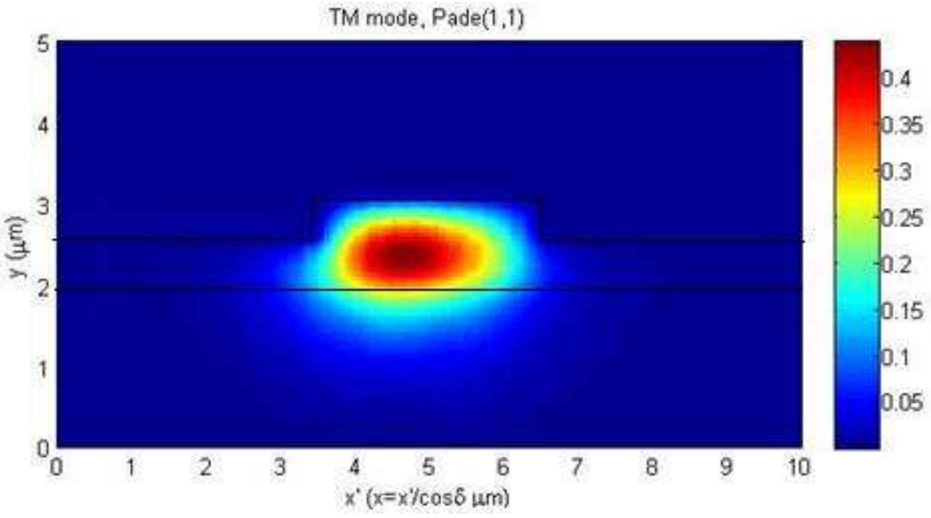
TM mode, Pade(1,1)
y (μm)
x' (x=x'/cosδ μm)
0
1
2
3
4
5
6
7
8
9
10
0.4
0.35
0.3
0.25
0.2
0.15
0.1
0.05

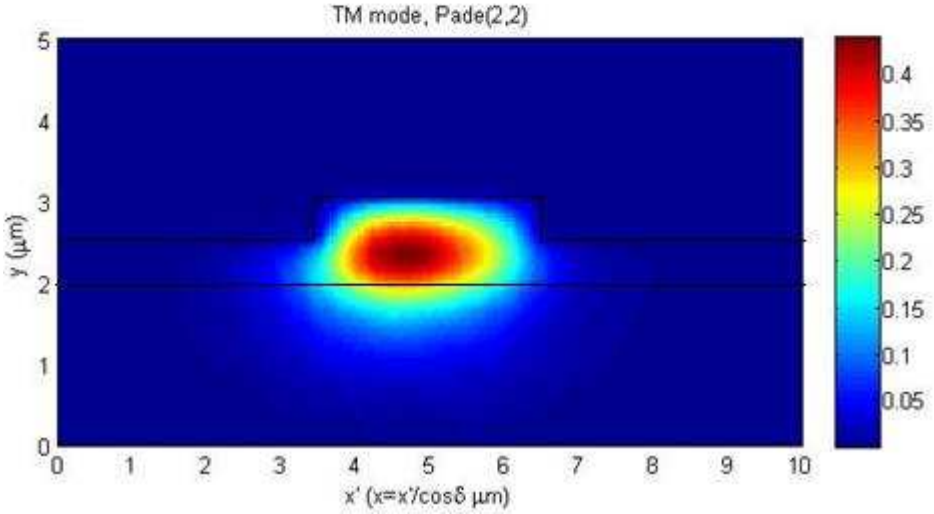
TM mode, Pade(2,2)
y (μm)
x' (x=x'/cosδ μm)
0
1
2
3
4
5
6
7
8
9
10
0.4
0.35
0.3
0.25
0.2
0.15
0.1
0.05

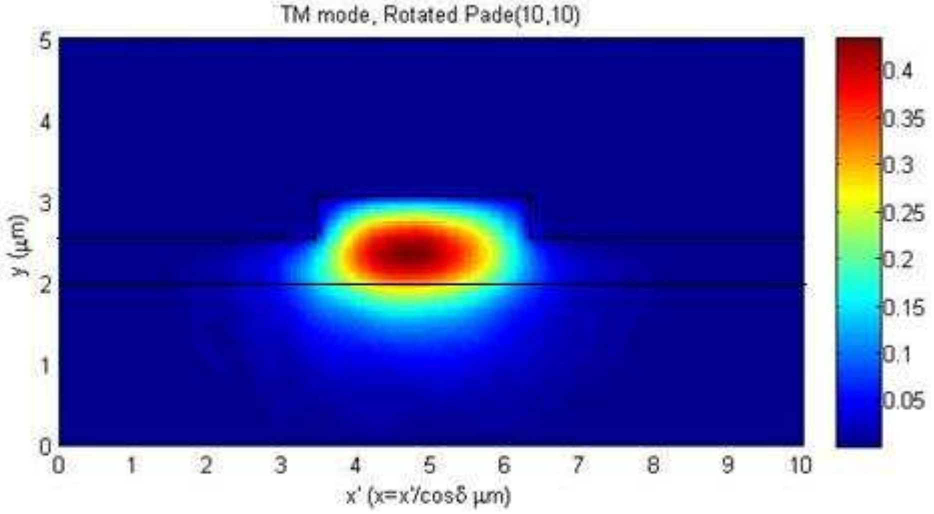
TM mode, Rotated Pade(10,10)
y (μm)
x' (x=x'/cosδ μm)
0
1
2
3
4
5
6
7
8
9
10
0.4
0.35
0.3
0.25
0.2
0.15
0.1
0.05